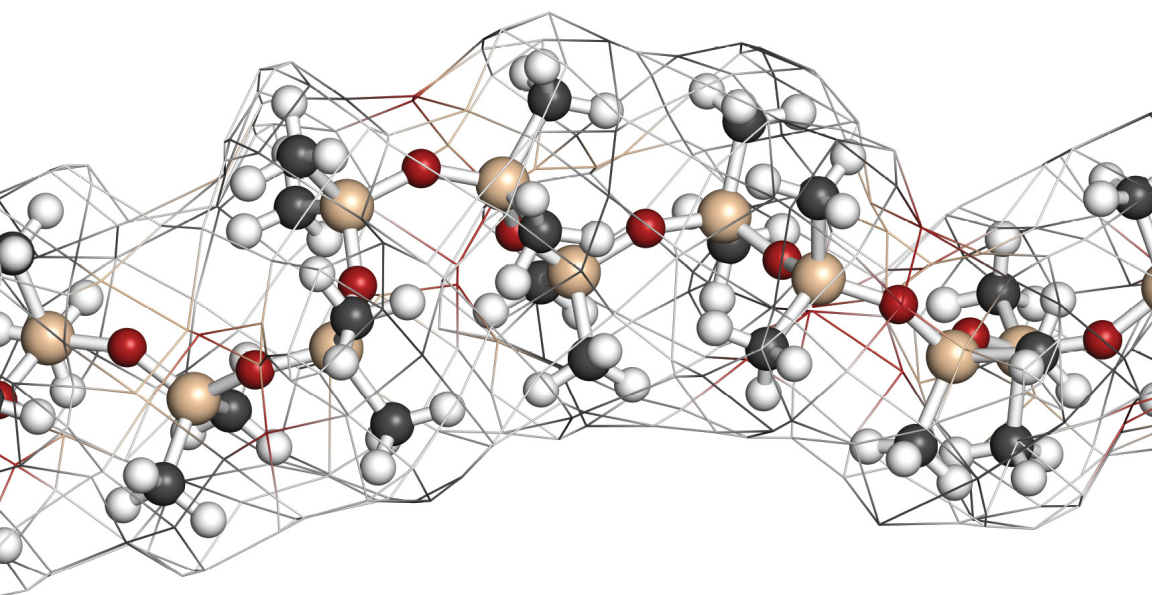


POLYMER SCIENCE AND TECHNOLOGY

Polydimethylsiloxane

Structure and Applications



Philip N. Carlsen
Editor

NOVA

POLYMER SCIENCE AND TECHNOLOGY

POLYDIMETHYLSILOXANE

STRUCTURE AND APPLICATIONS

No part of this digital document may be reproduced, stored in a retrieval system or transmitted in any form or by any means. The publisher has taken reasonable care in the preparation of this digital document, but makes no expressed or implied warranty of any kind and assumes no responsibility for any errors or omissions. No liability is assumed for incidental or consequential damages in connection with or arising out of information contained herein. This digital document is sold with the clear understanding that the publisher is not engaged in rendering legal, medical or any other professional services.

POLYMER SCIENCE AND TECHNOLOGY

Additional books and e-books in this series can be found
on Nova's website under the Series tab.

POLYMER SCIENCE AND TECHNOLOGY

POLYDIMETHYLSILOXANE
STRUCTURE AND APPLICATIONS

PHILIP N. CARLSEN
EDITOR



Copyright © 2020 by Nova Science Publishers, Inc.

All rights reserved. No part of this book may be reproduced, stored in a retrieval system or transmitted in any form or by any means: electronic, electrostatic, magnetic, tape, mechanical photocopying, recording or otherwise without the written permission of the Publisher.

We have partnered with Copyright Clearance Center to make it easy for you to obtain permissions to reuse content from this publication. Simply navigate to this publication's page on Nova's website and locate the "Get Permission" button below the title description. This button is linked directly to the title's permission page on copyright.com. Alternatively, you can visit copyright.com and search by title, ISBN, or ISSN.

For further questions about using the service on copyright.com, please contact:

Copyright Clearance Center

Phone: +1-(978) 750-8400

Fax: +1-(978) 750-4470

E-mail: info@copyright.com.

NOTICE TO THE READER

The Publisher has taken reasonable care in the preparation of this book, but makes no expressed or implied warranty of any kind and assumes no responsibility for any errors or omissions. No liability is assumed for incidental or consequential damages in connection with or arising out of information contained in this book. The Publisher shall not be liable for any special, consequential, or exemplary damages resulting, in whole or in part, from the readers' use of, or reliance upon, this material. Any parts of this book based on government reports are so indicated and copyright is claimed for those parts to the extent applicable to compilations of such works.

Independent verification should be sought for any data, advice or recommendations contained in this book. In addition, no responsibility is assumed by the Publisher for any injury and/or damage to persons or property arising from any methods, products, instructions, ideas or otherwise contained in this publication.

This publication is designed to provide accurate and authoritative information with regard to the subject matter covered herein. It is sold with the clear understanding that the Publisher is not engaged in rendering legal or any other professional services. If legal or any other expert assistance is required, the services of a competent person should be sought. FROM A DECLARATION OF PARTICIPANTS JOINTLY ADOPTED BY A COMMITTEE OF THE AMERICAN BAR ASSOCIATION AND A COMMITTEE OF PUBLISHERS.

Additional color graphics may be available in the e-book version of this book.

Library of Congress Cataloging-in-Publication Data

ISBN: 978-1-53617-590-5

Library of Congress Control Number: 2020933202

Published by Nova Science Publishers, Inc. † New York

CONTENTS

| | | |
|------------------|---|------------|
| Preface | | vii |
| Chapter 1 | Dielectric Properties and Relaxation of Polydimethylsiloxane Composites <i>J. Macutkevic, V. Samulionis, J. Belovickis, J. Banys and O. Shenderova</i> | 1 |
| Chapter 2 | Applications of Polydimethylsiloxane: Microstructure of Functional Surface for Observation of Biological Cell Behavior <i>Shigehiro Hashimoto</i> | 29 |
| Chapter 3 | PDMS in Urinary Tract Devices: Applications, Problems and Potential Solutions <i>M. Gomes, L. C. Gomes, R. Teixeira-Santos and F. J. Mergulhão</i> | 95 |
| Chapter 4 | Polydimethylsiloxane (PDMS): A Promising Material for Biological Applications <i>Sajede Saeidifard, Foozieh Sohrabi and Seyedeh Mehri Hamidi</i> | 145 |

| | | |
|------------------|--|------------|
| Chapter 5 | Study of TiO ₂ -PDMS as an Adsorbent in Solid Phase Microextraction of Aromatic Compounds | 179 |
| | <i>Erbin G. Uc-Cayetano, Ilse Ileana Cárdenas-Bates, Pablo Acereto-Escoffié and Cristian Carrera-Figueiras</i> | |
| Chapter 6 | Polydimethylsiloxane (PDMS): A Favorable Material for Active Plasmonic Applications | 199 |
| | <i>H. Mbarak, S. M. Hamidi and E. Mohajerani</i> | |
| Index | | 217 |

PREFACE

Polydimethylsiloxane is a non-conducting, silicone-based elastomer that is of widespread interest due to its flexibility and ease of micromolding for the rapid prototyping of microdevices and systems. Polydimethylsiloxane: Structure and Applications discusses the results of electric investigations of onion-like carbon (OLC)/polydimethylsiloxane composites addressing very wide frequency and temperature ranges.

Several kinds of devices for the observation of the behaviour of biological cells are discussed: micro-ridges, micro-grooves, micro-markers, and micro-slits, and the methodology to make each morphology by polydimethylsiloxane is described.

The authors reviews the main applications of polydimethylsiloxane in urinary tract devices and the associated complications. As new solutions are needed to reduce bacterial adhesion and biofilm formation on polydimethylsiloxane -based devices, a testing platform is described to evaluate surface performance in both urinary catheters and ureteral stents.

Also examined are the properties which make polydimethylsiloxane an excellent candidate for understanding complex biological behaviors, including its transparency for applying optical methods, biocompatibility and nontoxicity, high conformity with cells and other biostructures, gas permeability for the transfer of nutrients and oxygen, and flexibility.

In the subsequent study, a hybrid material of titanium dioxide and polydimethylsiloxane is obtained and characterized using a sol-gel and

electrospraying method. These results indicate that the hybrid material may be viable as an adsorbent, and that the optimization of the process could reduce both cost and analysis time.

In order to further the applications of polydimethylsiloxane, the closing study describes the steps in the fabrication of its plasmonic structure, and also examines the switching effect of the sample.

Chapter 1 - Polydimethylsiloxane (PDMS) is a non-conducting silicone-based elastomer that has been of widespread interest due to its flexibility and ease of micromolding for rapid prototyping of microdevices and systems. PDMS based composites filled with conductive fillers (at concentrations above the percolation threshold) can be used as flexible shielding materials, transparent self-cleaning coatings, triboelectric nanogenerators and stretchable conductors. However, before PDMS composites are ready for practical applications several unsolved problems related with the homogenous distribution of particles within the PDMS and the thermal stability of the PDMS matrix should be solved. In this chapter results of electric investigations of onion-like carbon (OLC)/polydimethylsiloxane composites will be presented addressing very wide frequency (20 Hz – 3 THz) and temperature (26 – 500 K) ranges. The percolation threshold in these composites strongly depends on the OLC aggregate sizes and was lowest for the composites with the smallest OLC aggregate sizes (~ 40nm). These results will be compared with PDMS composites filled with other nanoparticles. The temperature dependent electrical properties of PDMS composites will be explained in this chapter. Interestingly, the transition into the insulator state of the composites occurred at higher temperatures. The transition temperature increases with OLC aggregate concentration. Above the percolation threshold, the electrical conductivity in the composites occurs mainly due to electron tunneling between OLC clusters and quasi-one-dimensional hopping inside the clusters. The hopping almost vanishes at frequencies above 100 GHz where the phonon contribution dominates. The impact of ZnO nanoparticles on ultrasonic and dielectric properties of PDMS based nanocomposites over a wide temperature range will be also presented in the chapter. The complex dielectric permittivity was measured as a

function of the frequency at various temperatures and it was shown that the magnitude and position of the dielectric loss peak on the temperature scale depend on the concentration of fillers in PDMS/ZnO composites. The temperature dependence of ultrasonic wave attenuation showed attenuation peaks similar to those obtained by means of dielectric spectroscopy. These peaks are attributed to the dynamic glass transition and obey the Vogel-Fulcher-Tammann (VFT) equation. Values of the static glass transition temperature obtained analysing the dielectric and ultrasonic data are consistent and increase with the concentration of ZnO. The ultrasonic wave attenuation and velocity in these composites depend on the filler concentration. This investigation is motivated by the recently discovered superior electromagnetic attenuation of some types of PDMS based composites, demonstrating a promising high potential of PDMS for the design of flexible electromagnetic shielding materials over a broad microwave frequency range. On the other hand, the provision of high shielding effectiveness at low concentration of nanocarbon additives is an extremely important problem due to the requirements that coatings be low-cost and preserve (or even improve) the basic thermo mechanical properties of the polymer matrix, such as viscosity, good pigment wetting, resistance to pigment settling, and compatibility with human tissue, while, at the same time, imparting high mechanical performance and good chemical resistance.

Chapter 2 - Polydimethylsiloxane (PDMS) is frequently used for the base material for microcircuit chips. It can be applied for the base material for micro-machining to make the micro-surface morphology. The typical size of a biological cell, on the other hand, is micrometer. It is difficult to control dimension of micrometer with the conventional micro-machining technology. The micromachining with PDMS enables the surface design with the dimension of micrometer. Although the surface of PDMS is hydrophobic, it can be hydrophilized by the oxygen plasma ashing. The affinity of the surface to the biological fluid can be improved by the albumin coating. In this chapter, several kinds of devices, which are applied to observe the behaviour of biological cells, are exemplified: micro-ridges, micro-grooves, micro-markers, and micro-slits. Methodology

to make each morphology by PDMS is described: photolithography, and etching. The effectiveness of each kind of device is evaluated by experiments with several types of biological cells. The technology will contribute to several applications in the field of the biomedical engineering: medical diagnostics, and regenerative medicine.

Chapter 3 - PDMS is one of the most widely used polymers for the fabrication of biomedical devices. Of particular relevance is the application of PDMS in urinary tract devices such as urinary catheters and ureteral stents. As these devices are being used by a growing number of patients and indwelling times are increasing in an aging population, the incidence of urinary tract infections is rising. These infections have implications on the quality of life of the patients and represent a severe burden on healthcare systems. This chapter reviews the main uses of PDMS in urinary tract devices and associated complications. As new solutions are needed to reduce bacterial adhesion and biofilm formation on PDMS-based devices, a testing platform is described to evaluate surface performance in both urinary catheters and ureteral stents. Examples of these solutions are also discussed in a quest for more efficient urinary tract devices.

Chapter 4 - The development of PDMS structures emerges versatile and practical applications into industry, biology, medicine, and chemistry. This material is magnificently introduced in biological and medical researches due to its analogous to confined scales of cells and biomolecules dimensions, transparency for applying optical methods, biocompatibility and nontoxicity, possibility of applying different approaches for making the surface hydrophilic and cell adhesive, high conformality with cells and other biostructures, gas permeability for transfer of nutrients and oxygen, and flexibility. So, these properties make PDMS an excellent candidate for understanding the complex biological behaviors, which may be impossible to be investigated by other techniques, and for cutting-edge bio-applications. Therefore, there is a growing interest in utilizing PDMS, driven by the demand of versatile strategies to cell-based assays biosensors, drug delivery, chemical biology applications, and cell differentiation. Besides, combining the plasmonic and PDMS

structures has led to the generation of various approaches for thermal therapy, drug delivery, imaging and sensing applications.

Chapter 5 - In this study, a hybrid material of titanium dioxide and polydimethylsiloxane (TiO₂-PDMS) was obtained and characterized using a sol-gel and electrospraying method. The micrographs revealed the formation of spherical microparticles 3.8 μm in diameter. Infrared spectroscopy (FTIR) showed bands at 920 and 612 cm⁻¹, indicating the formation of Ti-O-Si and Ti-O-Ti-O bonds. The contact angle was 103°, which corresponds to a nonpolar material. TiO₂-PDMS presented a decomposition start temperature at 240°C, obtained by thermogravimetric analysis (TGA). Subsequently, its adsorption capacity was evaluated for the removal of benzene and naphthalene using solid-phase microextraction (SPME) with a liquid chromatography-ultraviolet detector (HPLC-UV). Different polarity elution solvents were compared, and the adsorption capacity was determined at different concentrations while maintaining a fixed amount of adsorbing material. The micrographs revealed the formation of uniform spherical microparticles of 3.8 ± 0.7 μm. The FTIR analysis of the hybrid composite material showed bands at 920 and 612 cm⁻¹, indicating the formation of Ti-O-Si and Ti-O-Ti bonds. The highest extraction percentages for benzene and naphthalene were 47 and 84%, respectively, with a relationship of analytes to synthesized absorbent material of 2 ppm in 25 mg. These results indicate that the hybrid material obtained could be viable as an adsorbent and that the optimization of the process could reduce both cost and analysis time.

Chapter 6 - Polydimethylsiloxane (PDMS), as a common silicone polymer, has attracted the attention of many researchers due to its own characteristics that make it desirable for use in different applications. This promising material is applied in a variety of fields including mechanics, electronics, medicines, cosmetics and fibers. According to its flexibility, low cost, optical transparency, long service life, good dielectric properties and ease of fabrication, the use of PDMS is expanded to new and exciting applications, especially in active plasmonic devices. The fabrication of PDMS-based 2D plasmonic grating switch is realized in a straightforward method, enabling the active control over the plasmonic properties. In order

to advance the applications of PDMS, a significant part of this chapter is devoted to introduce first the polymer (PDMS) and its properties, then describes the design steps of fabrication of the plasmonic structure and finally presents the switching effect of the sample showing the relevance of PDMS in this application.

Chapter 1

DIELECTRIC PROPERTIES AND RELAXATION OF POLYDIMETHYLSILOXANE COMPOSITES

J. Macutkevic^{1,}, V. Samulionis¹, J. Belovickis¹,
J. Banys¹ and O. Shenderova²*

¹Vilnius University, Vilnius, Lithuania

²Adamas Nanotechnology, Raleigh, North Carolina, US

ABSTRACT

Polydimethylsiloxane (PDMS) is a non-conducting silicone-based elastomer that has been of widespread interest due to its flexibility and ease of micromolding for rapid prototyping of microdevices and systems. PDMS based composites filled with conductive fillers (at concentrations above the percolation threshold) can be used as flexible shielding materials, transparent self-cleaning coatings, triboelectric nanogenerators and stretchable conductors. However, before PDMS composites are ready for practical applications several unsolved problems related with the homogenous distribution of particles within the PDMS and the thermal stability of the PDMS matrix should be solved.

In this chapter results of electric investigations of onion-like carbon (OLC)/polydimethylsiloxane composites will be presented addressing very wide frequency (20 Hz – 3 THz) and temperature (26 – 500 K)

* Corresponding Author's E-mail: jan.macutkevic@gmail.com.

ranges. The percolation threshold in these composites strongly depends on the OLC aggregate sizes and was lowest for the composites with the smallest OLC aggregate sizes (~ 40nm). These results will be compared with PDMS composites filled with other nanoparticles. The temperature dependent electrical properties of PDMS composites will be explained in this chapter. Interestingly, the transition into the insulator state of the composites occurred at higher temperatures. The transition temperature increases with OLC aggregate concentration. Above the percolation threshold, the electrical conductivity in the composites occurs mainly due to electron tunneling between OLC clusters and quasi-one-dimensional hopping inside the clusters. The hopping almost vanishes at frequencies above 100 GHz where the phonon contribution dominates.

The impact of ZnO nanoparticles on ultrasonic and dielectric properties of PDMS based nanocomposites over a wide temperature range will be also presented in the chapter. The complex dielectric permittivity was measured as a function of the frequency at various temperatures and it was shown that the magnitude and position of the dielectric loss peak on the temperature scale depend on the concentration of fillers in PDMS/ZnO composites. The temperature dependence of ultrasonic wave attenuation showed attenuation peaks similar to those obtained by means of dielectric spectroscopy. These peaks are attributed to the dynamic glass transition and obey the Vogel-Fulcher-Tammann (VFT) equation. Values of the static glass transition temperature obtained analysing the dielectric and ultrasonic data are consistent and increase with the concentration of ZnO. The ultrasonic wave attenuation and velocity in these composites depend on the filler concentration.

This investigation is motivated by the recently discovered superior electromagnetic attenuation of some types of PDMS based composites, demonstrating a promising high potential of PDMS for the design of flexible electromagnetic shielding materials over a broad microwave frequency range. On the other hand, the provision of high shielding effectiveness at low concentration of nanocarbon additives is an extremely important problem due to the requirements that coatings be low-cost and preserve (or even improve) the basic thermo mechanical properties of the polymer matrix, such as viscosity, good pigment wetting, resistance to pigment settling, and compatibility with human tissue, while, at the same time, imparting high mechanical performance and good chemical resistance.

INTRODUCTION

Polydimethylsiloxane (PDMS) is a non-conducting silicone-based elastomer that has been of widespread interest due to its flexibility and ease of micromolding for rapid prototyping of microdevices and systems. The chemical formula for PDMS is $\text{CH}_3[\text{Si}(\text{CH}_3)_2\text{O}]_n\text{Si}(\text{CH}_3)_3$, where n is the number of repeating monomer $[\text{SiO}(\text{CH}_3)_2]$ units. PDMS based composites filled with conductive fillers (at concentrations above percolation threshold) can be used as flexible shielding materials, transparent self-cleaning coatings, triboelectric nanogenerators and stretchable conductors. However, before implementation in practical applications several unsolved problems related with the homogenous distribution of particles inside PDMS and the thermals stability of the PDMS matrix should be solved.

The most simple form of the dielectric dispersion is the Debye like dispersion [1]:

$$\varepsilon'(\nu) = \varepsilon_{\infty r} + \frac{\Delta\varepsilon}{1+(\omega\tau)^2}, \quad (1)$$

$$\varepsilon''(\nu) = \Delta\varepsilon \frac{\omega\tau}{1+(\omega\tau)^2}. \quad (2)$$

However, in polymers as a rule the dielectric dispersion is much broader than 1.14 decades as it would be based upon the Debye formula. The plausible assumption is that the relaxation dielectric dispersion $\varepsilon^*(\omega) = \varepsilon' - i\varepsilon''$ in polymers (which are disordered materials) can be represented as a superposition of the independent individual Debye-like processes:

$$\varepsilon'(\nu) = \varepsilon_{\infty r} + \Delta\varepsilon \int_{-\infty}^{\infty} \frac{f(\tau)d\lg\tau}{1+(\omega\tau)^2}, \quad (3)$$

$$\varepsilon''(\nu) = \varepsilon_{\infty r} + \Delta\varepsilon \int_{-\infty}^{\infty} \frac{\omega\tau f(\tau)d\lg\tau}{1+(\omega\tau)^2}. \quad (4)$$

These two expressions actually are the Fredholm integral equations of the first kind for the relaxation time distribution $f(\tau)$ definition. Such

integral equations are known to be an ill-posed problem. Such normalization condition for $f(\tau)$ must fulfilled:

$$\int_{-\infty}^{\infty} f(\tau) d \ln g(\tau) = 1 \quad (5)$$

From the distribution function the decay function $\Phi(t)$ can be obtained:

$$\Phi(t) = \int_{-\infty}^{\infty} f(\ln(\tau)) e^{-\frac{t}{\tau}} d \ln(\tau). \quad (6)$$

Simplistic solutions way of Eqs. (3) and (4) is the guess the $f(\tau)$ function. A most popular predefined distribution of relaxation times is the Cole-Cole distribution [2]:

$$f(\tau) = \frac{\sin(\alpha_{cc}\pi)}{\cosh\left[(1-\alpha_{cc})\ln\frac{2\pi\tau_{cc}}{\tau}\right] - \cos(\alpha_{cc}\pi)}, \quad (7)$$

there $0 \leq \alpha_{cc} \leq 1$ are the parameters of width of Cole-Cole distributions functions, τ_{cc} is the mean and most probable Cole-Cole relaxation time. From Eqs. (3), (4) and (7) easily can be obtained:

$$\varepsilon^* = \varepsilon_{\infty r} + \frac{\Delta\varepsilon}{1+(i\omega\tau_{cc})^{1-\alpha_{cc}}}. \quad (8)$$

This formula is used very often for polymers [3]; extremely often for various preliminary (and therefore often narrowband) dielectric studies of new polymers and polymer based composites. However, for PDMS composites filled with silica the Cole-Cole equation (8) is not valid; instead some authors use three Cole-Cole functions [4]. Another example of an empirical symmetric function for $\varepsilon''(\omega)$ is the Fuoss-Kirkwood equation [5, 6] which is the generalized form of Debye response and formulated directly for the imaginary part of $\varepsilon^*(\omega)$:

$$\varepsilon''(\omega) = \varepsilon''_p (\operatorname{sech}(m \ln(\omega\tau))) = \frac{2\varepsilon''_p (\omega\tau)^m}{1+(\omega\tau)^{2m}}, \quad (9)$$

where ε''_p is the value of $\varepsilon''(\omega)$ at the peak frequency ω_p . In this case, $\varepsilon''_p = m^* \Delta\varepsilon/2$ and $\omega_p = 1/\tau$. This equation implies (9) power laws with exponent $-m$ at high frequencies and m at low frequencies. In this case, the distribution function is:

$$f(\tau) = \frac{m}{\pi} \frac{\cosh\left(\frac{m\pi}{2}\right) \cosh(m\omega)}{\sinh^2(m\omega) + \cos^2\left(\frac{m\pi}{2}\right)}, \quad \omega = \log(\tau_p/\tau). \quad (10)$$

The simplest case of the asymmetric distribution function is the Cole-Davidson distribution function [7]:

$$f(\tau) = \frac{\sin(\gamma\pi)}{\pi} \left(\frac{\tau}{\tau_{cd} - \tau} \right) \text{ for } \tau < \tau_{cd}, \quad (11)$$

and $f(\tau) = 0$ for $\tau > \tau_{cd}$, where τ_{cd} is the most probable relaxation time of the Cole-Davidson distribution function and $0 < \gamma \leq 1$ parameter of asymmetry of this functions. From Eqs. (3), (4) and (11) we have [7]:

$$\varepsilon^* = \varepsilon_{\infty r} + \frac{\Delta\varepsilon}{(1 + i\omega\tau_{cd})^\gamma}. \quad (12)$$

This function describes well the properties of an epoxy resin matrix with iron microparticles [8].

More general descriptions of the broad and asymmetric dielectric dispersion is the combination of the Cole-Cole and the Cole-Davidson-Havriliak-Negami function [9]:

$$\varepsilon^* = \varepsilon_{\infty r} + \frac{\Delta\varepsilon}{(1 + (i\omega\tau_{cc})^{1-\alpha_{cc}})^\gamma}. \quad (13)$$

Havriliak and Negami [9] derived the distribution function $f(\tau)$ by means of complex analysis:

$$f(\tau) = \frac{1}{\pi} \frac{\sin(\gamma\theta) \left(\frac{\tau}{\tau_{hn}}\right)^{(1-\alpha_{cc})\gamma}}{\left(\frac{\tau}{\tau_{hn}}\right)^{2(1-\alpha_{cc})} + 2\left(\frac{\tau}{\tau_{hn}}\right)^{(1-\alpha_{cc})} \cos(\pi(1-\alpha_{cc})) + 1}^{\gamma/2}, \quad (14)$$

with

$$\theta = \arctan\left(\frac{\sin(\pi(1-\alpha_{cc}))}{\left(\frac{\tau}{\tau_{nn}}\right)^{1-\alpha_{cc}} + \cos(\pi(1-\alpha_{cc}))}\right). \quad (15)$$

Together with the ColeCole equation (8), the Havriliak-Negami functions are widely used dielectric relaxation functions for polymers and polymeric composites [9-13].

A very important problem is the physical meaning of Havriliak-Negami functions and their parameters. The experimental data shows that α_{cc} and γ are strictly dependent on temperature, structure, composition and other controlled physical parameters. However, in many works the obtained parameters α_{cc} and γ are discussed very little (only how the form of dielectric dispersion is related with these parameters). When experimental data is of good quality (and only one relaxation process is manifest) the change of dielectric dispersion form is visual from the dielectric spectra $\varepsilon^*(\omega)$. Several attempts have been made to understand the physical meaning of Havriliak-Negami dielectric response functions [14].

In time-domain, the frequently used so-called “stretched exponential” or the Kolrausch-Williams-Watts (KWW) function is [15]:

$$\Phi(t) = \exp\left[-\left(\frac{t}{\tau_{ww}}\right)^\beta\right]. \quad (16)$$

The dielectric function then is:

$$\varepsilon^*(\omega) = \Delta\varepsilon \int_0^\infty \left[-\frac{d\Phi(t)}{dt}\right] e^{-i\omega t} dt, \quad (17)$$

and the distribution of relaxation times is:

$$f(\tau) = \frac{1}{\pi} \int e^{-x} e^{4\cos(\pi\beta)} \sin(usin(\pi\beta)) dx, \text{ with } u = \left(\frac{x\tau}{\tau_0}\right)^\beta. \quad (18)$$

Many physical models of KWW dielectric dispersions are proposed: the localized state model, the proton model, the dipole interaction model and more others [16]. Therefore, the KWW function physical meaning is better understood than the physical meaning of others predefined functions. Recently the empirical relationship between the KWW and Havriliak-Negami functions was discovered [16]:

$$\ln \left[\frac{\tau_{hn}}{\tau_{ww}} \right] = 2.6(1 - \beta)^{0.5} e^{-3\beta},$$

$$\alpha_{cc}\gamma = \beta^{1.23}. \quad (19)$$

Therefore, physical meaning of the Havriliak-Negami distributions sometimes can be related with physical meaning of the KWW models. There are many other predefined functions of distribution of relaxation times such as Joncher [15].

In order to reveal the influence of the nanoparticles concentration and their size, the dielectric permittivity and the electrical conductivity at some fixed frequency and room temperature can be plotted as a function of concentration. Below the percolation threshold the effective permittivity ϵ' at fixed frequency can be fitted according to the classical law [17]:

$$\epsilon' = \epsilon_m \left(\frac{p_c - p}{p_c} \right)^{-q}, \quad (20)$$

where ϵ_m is the dielectric permittivity of polymer matrix, p_c is the critical volume fraction, q is the critical index. Or fitting can be achieved using a simpler equation

$$\epsilon' = \epsilon_m (p_c - p)^{-q}. \quad (21)$$

At concentrations close to the percolation threshold, percolation theory predicts the value of the exponent close to 2 in any three-dimensional medium [18]. In onion like carbon (OLC)/PDMS composites the percolation threshold decreases with OLC aggregate size and it is 6.7 vol%

for 40 OLC aggregates [19]. Such critical volume fraction is lower than should be expected from theory for round particles [18].

ELECTRICAL TRANSPORT AT HIGH TEMPERTATURES

Temperature dependence of the dielectric permittivity and the electrical conductivity of OLC/PDMS composites with 100 nm OLC inclusions at 10 wt% is presented in Figure 1 at different frequencies from room temperature up to 500 K.

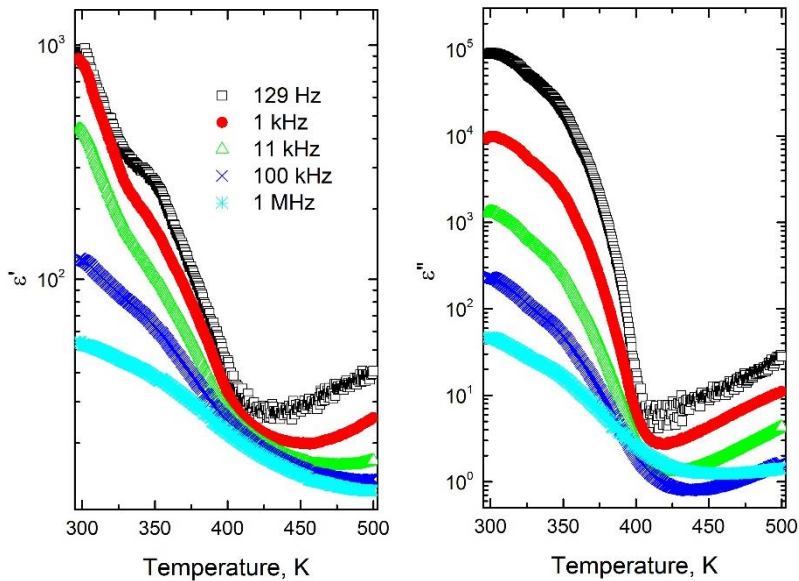


Figure 1. Temperature dependence of complex dielectric permittivity for OLC/PDMS composites (with 100 nm OLC 10 wt%) inclusions at different frequencies.

Both the dielectric permittivity and the electrical conductivity decrease during heating, however the most pronounced decrease occurs at temperatures above 450 K and at lower frequencies (below 11 kHz). In order to understand the phenomena the electrical conductivity was plotted as a function of frequency at various representative temperatures in Figure

2. During heating not only was the electrical conductivity decreased, but the shape of the conductivity spectrum was also substantially changed. A frequency independent conductivity (DC conductivity) is observed at lower frequencies and at lower temperatures.

Above 470 K no DC conductivity is observed in the conductivity spectra of the investigated composites. The frequency spectra of the conductivity was fitted with the fundamental equation [20]:

$$\sigma = \sigma_{DC} + A\omega^s \quad (22)$$

where σ_{DC} is the DC conductivity and $A\omega^s$ is the AC conductivity. Equation (22) is consistent with the Jonscher universal dielectric response and the parameter s has the same physical meaning as the Jonscher exponent [15]. DC conductivity values for all composites above the percolation threshold are presented in Figure 3a. From this fit, it is possible to calculate the critical frequency f_{cr} , at which the value of the conductivity $\sigma(\omega)$ deviates from the DC plateau. The experimental value for f_{cr} has been defined as the frequency at which the value of the conductivity is 10% higher than the DC conductivity value. The results are plotted in Figure 3b. It can be clearly seen that both the DC conductivity and the critical frequency f_{cr} are almost temperature independent at lower temperatures and rapidly decrease close to a specific temperature, which depends on the OLC aggregate size and concentration.

Above this temperature no DC conductivity occurs in the composites, therefore a metal-insulator phase transition is observed. Note that the complex effective permittivity of a pure PDSM polymer matrix only very slowly increases with temperature; no anomaly is revealed and its value remains quite low ($\epsilon' < 5$ and $\epsilon'' < 1.5$) in the temperature region 300 – 500 K. The transition temperature increases with OLC concentration and OLC aggregate size. DC conductivity and the static effective permittivity ϵ_s are connected with the critical frequency f_{cr} according to the relations:

$$f_{cr} = \sigma_{DC}/\epsilon_0\epsilon_s, \quad (23)$$

where z is an exponent, which characterizes the relation between the capacitive and conductive networks in the composite. For the composites under study, σ_{DC} and f_{cr} are almost temperature independent at temperatures far from the metal-insulator transition temperature, thus in this temperature region z is almost zero. Close to the metal-insulator transition temperature both DC conductivity and critical frequency rapidly decreases and the critical exponent is ~ 1.5 in this temperature region for all composites. This indicates a strong dependence on the gaps (the distances between OLC clusters) of both effective permittivity and electrical conductivity close to the metal- insulator transition temperature [21].

$$\sigma_{DC} \sim f_{cr}^z, \quad (24)$$

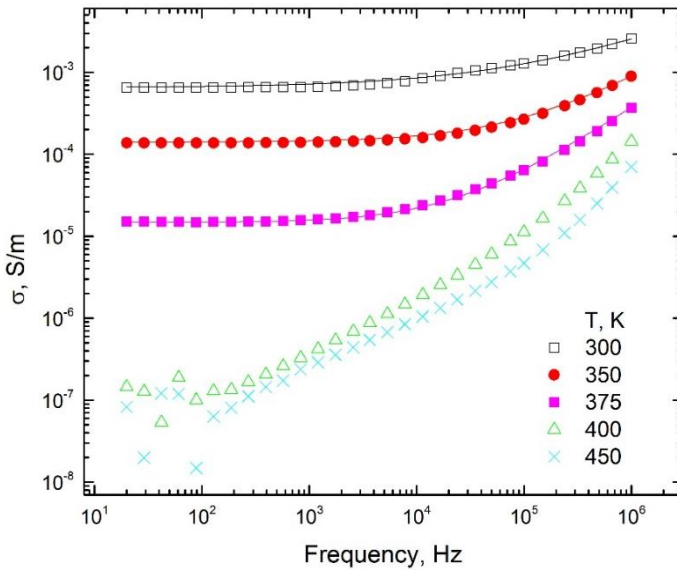


Figure 2. Frequency dependence of electrical conductivity for OLC/PDMS composites (with 100 nm OLC 10 wt%) inclusions at different frequencies.

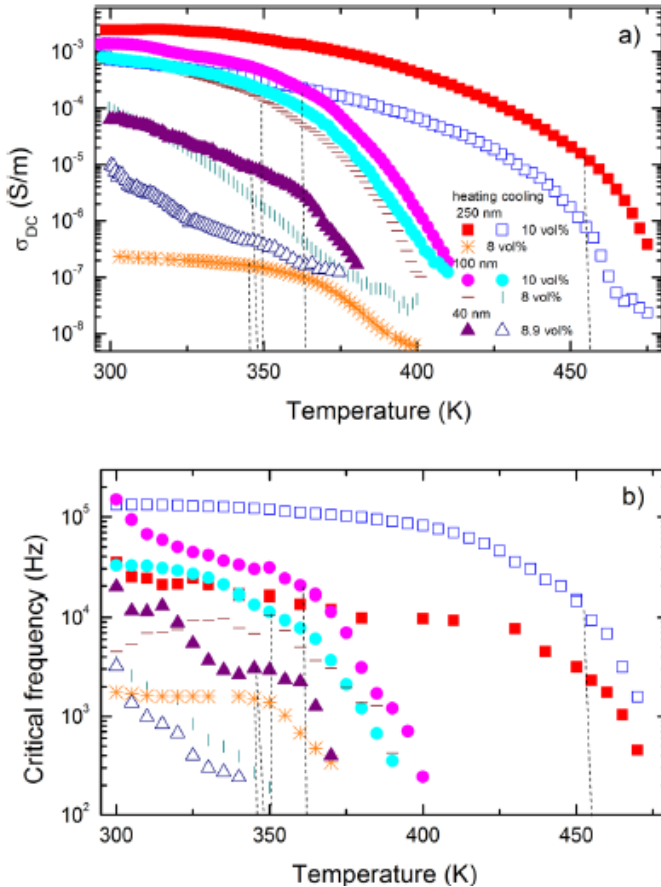


Figure 3. Temperature dependence of OLC/PDMS composites DC conductivity a) and critical frequency (high temperature region). The dotted lines indicate a limit between a “slow” decreasing of DC conductivity and critical frequency and a “rapid” decreasing of these parameters. Reproduced from [J. Macutkevicius, I. Kranauskaitė, J. Banys, S. Moseenkov, V. Kuznetsov, O. Shenderova, Metal-insulator transition and size dependent electrical percolation in onion-like carbon/polydimethylsiloxane composites, *Journal of Applied Physics* 115, 213702 (2014)], with the permission of AIP Publishing.

Upon heating both the electrical conductivity and the effective permittivity decrease due to the very different thermal expansion properties of the pure PDMS polymer matrix and OLC. The volume of OLC clusters remains almost the same, while the polymer matrix volume increases

rapidly with heating. At low frequencies the electrical conductivity in the investigated composites can occur via several mechanisms: 1) electron hopping in the infinite OLC clusters, 2) serial transport by hopping in finite clusters and tunneling between these finite clusters, 3) tunneling between finite and infinite clusters. Due to the rapid polymer matrix expansion only tunneling conductivity decreases because the distance for electron tunneling is increased. At higher temperatures (above the metal-dielectric transition temperature) the DC electrical conductivity disappears when the mean distance between the OLC clusters exceeds a critical value, at which no more tunneling is possible. Thus electrical transport in the OLC/PDMS composites is governed by a 2d mechanism.

With increasing OLC concentration or aggregate size the mean distance between the OLC clusters decreases and therefore the electrical conductivity is increased. The volume concentration of OLC clusters φ_i can be calculated as

$$\varphi_i = V_{\text{OLC}} / (V_{\text{OLC}} + V_{\text{PDMS}}), \quad (25)$$

where V_{OLC} is the volume of OLC in the composite and V_{PDMS} is the volume of matrix in the composite. Assuming, that V_{OLC} is almost temperature independent, φ_i could be proportional to $1/V_{\text{PDMS}}$. Thus, the volume concentration decreases upon heating and when it reaches a critical value, a transition into the insulator state occurs, which is followed by vanishing of both DC conductivity and critical frequency. This is clearly seen in Figure 3 where a slow decrease of both conductivity and critical frequency is observed upon heating, as well as a rapid decrease close to the metal-insulator temperature. Moreover, the rapid decrease of the conductivity, which occurs close to the transition temperature, (Figure 3) is similar to the concentration dependence of the conductivity close to the percolation threshold. Therefore, the transition into an insulator state can be explained by the decrease of OLC volume concentration below some critical concentration. The critical volume concentration depends on the OLC type, therefore the metal-insulator transition occurs at higher temperatures for bigger OLC aggregates [19].

For low OLC concentrations (8 vol% of 250 nm OLC aggregates) the metal-insulator transition is irreversible, i.e., after annealing above the transition temperature the value of composite effective permittivity remains low upon cooling (Figure 3). In this case the destroyed OLC network does not recover with polymer matrix shrinkage upon cooling and the composite is an isolator at room temperature after annealing. At higher OLC concentrations, the behavior of the DC conductivity and the critical frequency is reversible (Figure 3), i.e., upon cooling the values of DC conductivity and critical frequency are partially recovered.

A decrease in conductivity of percolative composites during heating was observed in other composites [21], however in these composites no metal-insulator transition occurred due to finite matrix conductivity at higher temperature. In contrast no DC conductivity and not any electric or dielectric anomaly was observed in the PDMS polymer up to 500 K. Above room temperature the metal-insulator transition usually occurs in vanadium oxide related compounds [22], however in our case the phase transition temperature can be easily changed by changing the OLC filler concentration and type. Moreover, in vanadium oxide related materials the high temperature phase is conductive and low temperature is non-conductive [22], while in our composites the high temperature phase is not conductive. This is due to the fact that in OLC/PDMS composites at higher temperatures the distances between the OLC clusters is too big and tunneling electrical conductivity does not occur in the composite. Thus, the OLC/PDMS composites can be useful in various applications, where a temperature dependent behavior is required.

ELECTRICAL TRANSPORT AT LOW TEMPERTATURES

At low temperatures (below 170 K) both the effective permittivity and the electrical conductivity decrease upon cooling. Not only the DC conductivity changes upon cooling, but also the shape of the conductivity spectra is changed (Figure 4).

Therefore, conductivity spectra $\sigma(\nu)$ were fitted with the Eq. (21). Obtained parameters are presented in Figures 5.

However, below 100 K not only the DC conductivity but also the shape of the conductivity spectra is temperature dependent (Figure 4). This means that the critical frequency is also temperature dependent.

We assumed that the temperature dependence of the DC conductivity at lower temperatures (below 100 K) can be fitted by the general Mott expression for variable range hopping (Figure 5) [23]:

$$\sigma_{dc} = \sigma_0 \exp(- (T_M/T)^{1/n}), \quad (26)$$

where T_M is a constant depending on the density of state and localization length of the system, $n = 1 + d$ (d is dimensionality of the system). A similar behavior is also valid for the critical frequency f_{cr} (Figure 5b) [23]:

$$f_{cr} = f_{cr\infty} \exp(- (T_M/T)^{1/n}), \quad (27)$$

where $f_{cr\infty}$ is the frequency at very high temperatures. Obtained parameters are discussed in [19]. The value of n is close to 1 for all investigated composites; this is typical for pure OLC powder [24].

For temperatures below 170 K, the DC conductivity data fit well to the fluctuation induced tunneling model [19]:

$$\sigma_{dc} = \sigma_0 \exp(- (T_1/(T + T_0))), \quad (28)$$

where T_1 represents the energy required for an electron to cross the insulator gap between the conductive particles aggregates, and T_0 is the temperature above which thermally activated conduction over the barriers begins to occur. According to the tunneling model [21, 25]:

$$T_1 = wA\beta_0/8\pi k, \quad (29)$$

$$T_0 = 2T_1/\pi\chi w, \tag{30}$$

where $\chi = (2mV_0)^{0.5}/h$ and $\beta_0 = 4V_0/ew$, m and e being the electron mass and charge, respectively, V_0 is the potential barrier height, w is the interparticle distance (gap width), and A is the area of capacitance formed by the junction. Obtained From Eqs. (6) and (7) it follows that T_1/T_0 is proportional to the gap width w , which is approximately proportional to $p^{-1/3}$ [26]. Thus, the ratio T_1/T_0 should decrease with the OLC concentration, as was observed in the composites with 100 nm OLC aggregates.

Thus, electrical transport in OLC/PDMS composites occurs via electron tunneling between OLC aggregates and a quasi-one-dimensional hopping inside the OLC clusters.

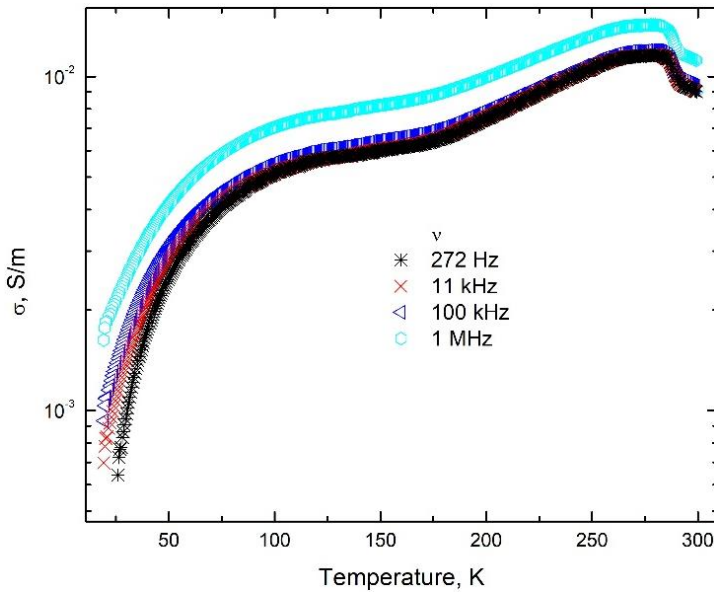


Figure 4. Temperature dependence of electrical conductivity for OLC/PDMS composites (with 100 nm OLC 10 wt%) inclusions at different frequencies.

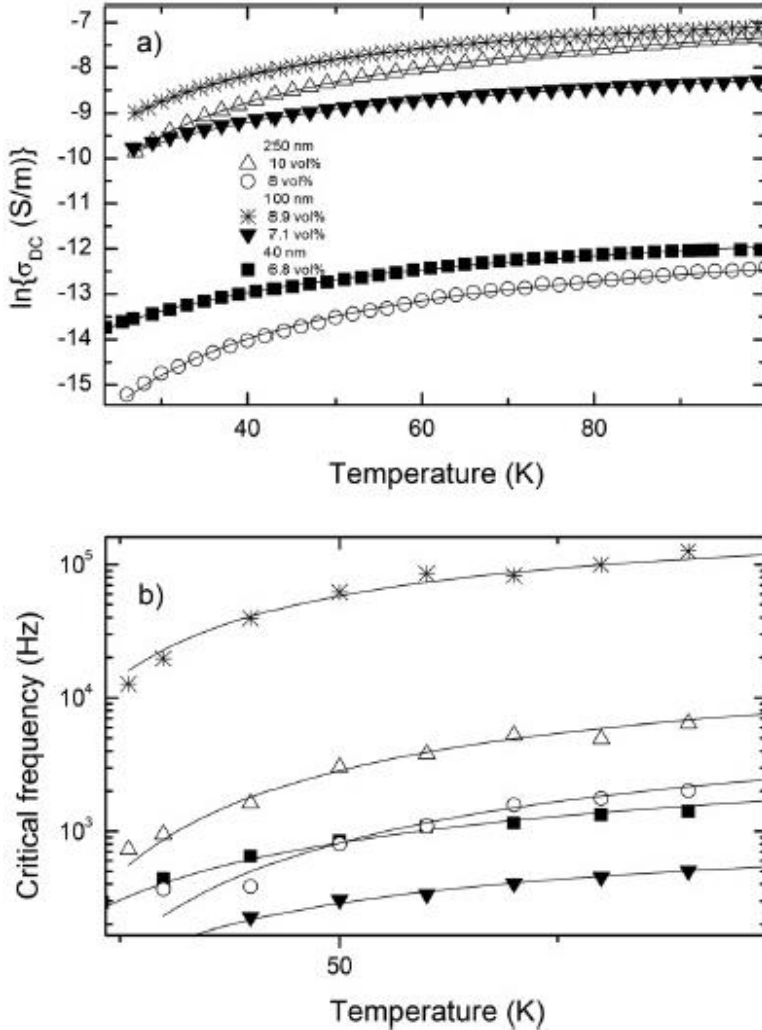


Figure 5. Temperature dependence of OLC/PDMS composites DC conductivity a) and critical frequency b) with Mott law fit (low temperatures region). Reproduced from [J. Macutkevici, I. Kranauskaite, J. Banys, S. Moseenkov, V. Kuznetsov, O. Shenderova, Metal-insulator transition and size dependent electrical percolation in onion-like carbon/polydimethylsiloxane composites, *Journal of Applied Physics* 115, 213702 (2014)], with the permission of AIP Publishing.

RELAXATION IN ZNO/PDMS COMPOSITES

Temperature dependences of the complex dielectric permittivity at different frequencies for PDMS with 10 wt% ZnO are presented in Figure 6. These dependences exhibit an anomalous behaviour at low temperatures (close to 175 K).

The behaviour is attributed to the glass transition, often indicated as a α relaxation, due to a relatively large-scale cooperative motion of many backbone segments in the amorphous phase of PDMS [27, 4]. Similar behaviour of the dielectric permittivity is observed in other PDMS composites with ZnO inclusions.

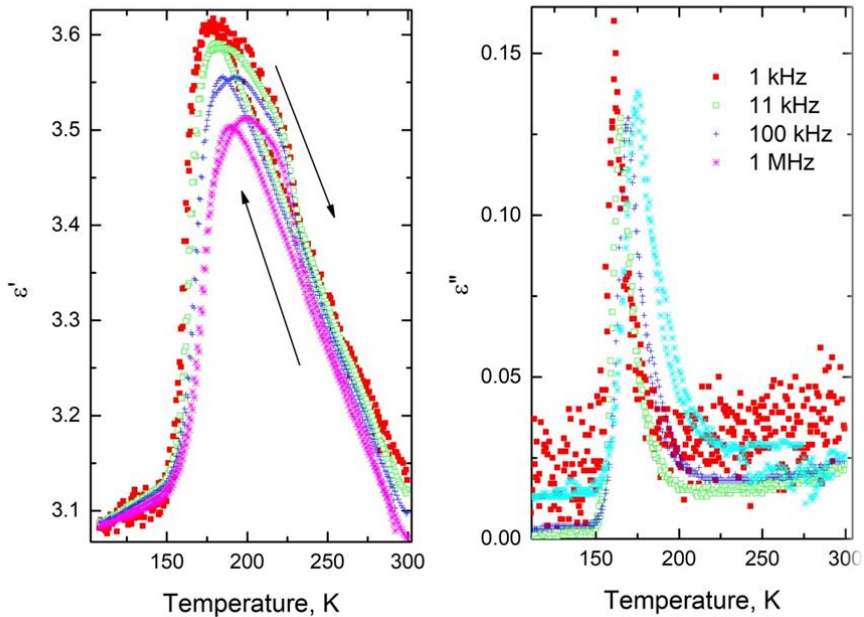


Figure 6. Temperature dependence of the complex dielectric permittivity for PDMS with 10 wt% ZnO at different frequencies.

The similar behaviour of the dielectric permittivity of pure PDMS has been previously observed by H. Adachi et al., [28] J. Ouyang et al. [29] and was attributed to the subsequent growth of spherulites in the

amorphous region. Therefore, our cooling rate is slow enough (1 K/min) and enables crystal nucleation within the polymer. The presence of ZnO nanoparticles strongly affects the crystallization rate and decreases the slope of $\varepsilon'(T)$ [30].

It is clearly visible that the peak of the dielectric loss maximum (T_{\max}) is shifted towards higher temperatures with increasing frequency (Figure 6). The dielectric dispersion and the peak of dielectric losses have been observed close to the temperature of the glass transition in all investigated composites [30]. Figure 7 shows the frequency dependence of the imaginary part of the dielectric permittivity for 10 wt.% ZnO in PDMS close to the glass transition temperature T_g . The curves of losses show a relaxation peak in the frequency range of 1 kHz – 1 MHz. The dielectric dispersion is caused by the α relaxation in PDMS, which origin is related to the local segmental dynamics [28, 30].

In Figure 8 experimental dependences of the longitudinal wave velocity and the ultrasonic wave attenuation on temperature and the concentration dependence of the ultrasonic wave attenuation (inset) are demonstrated. It is clearly observed that at low temperatures the ultrasonic velocity is noticeably dependent on the loading of ZnO nanofillers (Figure 8). The larger the concentration of ZnO nanoparticles embedded in the polymer matrix, the higher the observed velocity values in the composites. It might be due to the large difference between elastic coefficients of zinc oxide and polymer material [4, 31].

The peak corresponding to the maximum ultrasound wave attenuation within the composites is extended rightwards, depending from the concentration of ZnO (Figure 8). This is consistent with our observation in the dielectric behaviour of the composites (Figure 6) and could be due to the crystallization process, which is affected by specific interactions between the filler and the polymer matrix [4, 30]. This suggests that the molecular mobility of the polymer matrix is affected by the presence of embedded nanoparticles. ZnO fillers reduce the flexibility of PDMS backbone and, as a consequence, more heat is needed for the transition from the glassy to the soft state.

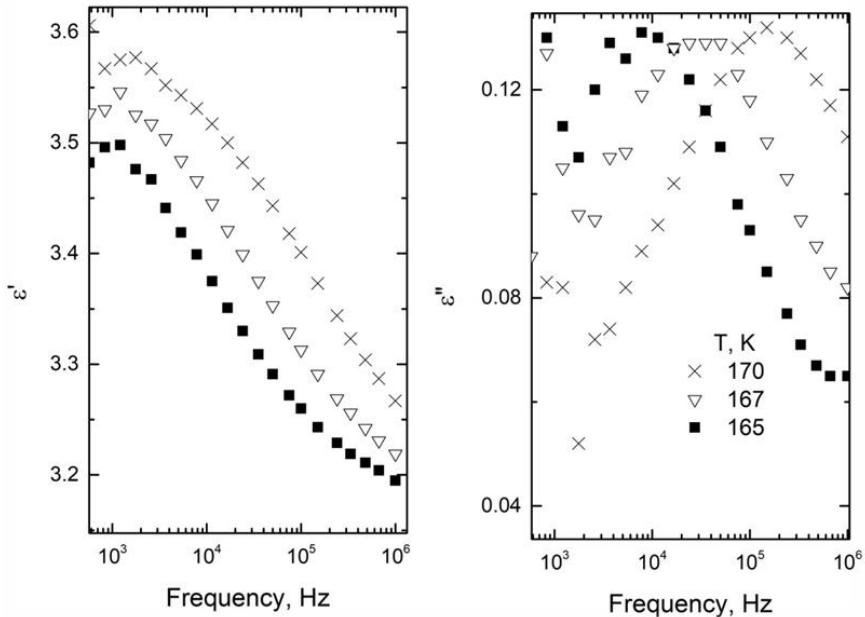


Figure 7. Frequency dependence of the complex dielectric permittivity for PDMS with 10 wt% ZnO at different frequencies.

An experimental dependence of the ultrasonic attenuation on ZnO content in PDMS nanocomposites is depicted by the inset in Figure 8. The attenuation of ultrasonic waves within the composite at room temperature linearly depends on the concentration of ZnO nanofillers. Similar results are obtained earlier in PDMS/OLC composites [33]. To explain such dependence, we assume that adding ZnO nanoparticles to PDMS increases the dynamic heterogeneity in the composite, that is an important factor for the ultrasonic attenuation.

A similar thermal hysteresis was also observed in the temperature dependence of the imaginary part of the complex dielectric permittivity [34]. The hysteresis is caused by the first order phase transition (crystallization/melting), which was previously observed upon heating by the differential scanning calorimetry of PDMS [32, 34]. The nanocomposites crystallize during slow cooling (at cooling rates not higher as 1 K/min) [35]. Upon heating, due to chain rearrangements and the decrease of the melt viscosity, PDMS also crystallizes from the amorphous

phase [35]. Complex melting occurs in PDMS during the heating cycle over the range 220-230 K in good agreement with previous investigations of PDMS polymer [36, 37].

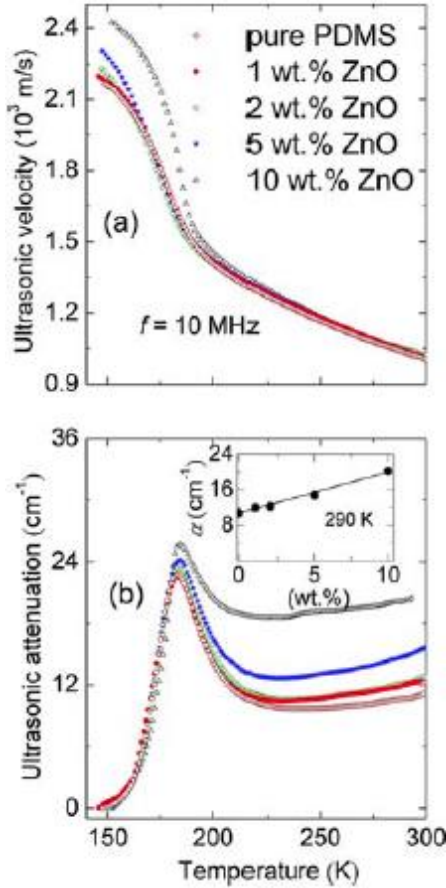


Figure 8. Temperature dependences of the ultrasonic velocity (left), the ultrasonic wave attenuation (right) for pure PDMS (a) and composites with 5 wt.% (b) and 10 wt.% (c) of ZnO inclusions. Solid symbols: on cooling, open symbols: on heating. J. Belovickis, J. Macutkevic, S. Svirskas, V. Samulionis, J. Banys, O. Shenderova, V. Borjanovic: Ultrasonic and dielectric relaxation in PDMS/ZnO nanocomposite. *Physica Status Solidi B*. 2015. 252. pp. 2778-2783. 2015. Copyright Wiley-VCH Verlag GmbH & Co. KGaA. Reproduced with permission.

ZnO nanoparticles can serve as nuclei, capable of the supporting crystal growth within the composite. As the amount of nanoparticles affects the crystallite size and the degree of the crystallinity, the melting is also enhanced by the presence of ZnO nanoparticles resulting in the appearance of the hysteresis.

The temperature dependences of the ultrasonic wave attenuation and the velocity are different on cooling and heating cycles (Figure 8). The hysteresis becomes more pronounced for higher nanofiller concentrations. The peak increases and shifts to higher temperatures with the frequency.

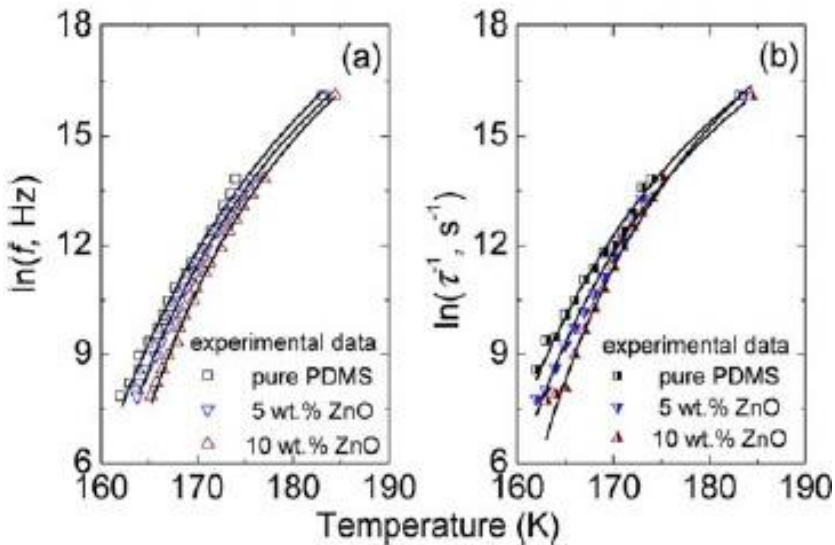


Figure 9. Measurements of frequency versus the dielectric losses maximum temperature (a) and relaxation frequency $f_r = 1/\tau$ obtained from the best fit of the Cole-Cole spectral function (b) for pure PDMS and composites with ZnO inclusions on cooling. Lines are the best fit according to the Vogel-Fulcher law (Eq. (31)). J. Belovickis, J. Macutkevicius, S. Svirskas, V. Samulionis, J. Banys, O. Shenderova, V. Borjanovic: Ultrasonic and dielectric relaxation in PDMS/ZnO nanocomposite. *Physica Status Solidi B*. 2015. 252. pp. 2778-2783. 2015. Copyright Wiley-VCH Verlag GmbH & Co. KGaA. Reproduced with permission.

The shift can be characterized by the Vogel-Fulcher (VF) relation [38-39]:

$$f = f_0 e^{\frac{-E_{VF}}{k_b(T_{\max} - T_{ref})}}, \quad (31)$$

where k_b is the Boltzmann constant, f_0 is the frequency approached with $T_{\max} \rightarrow \infty$ and T_{ref} is the temperature of glass transition in the polymer as cooling rate becomes infinitely slow.

Note, that the apparent activation energy used in the VF equation E_{VF} relates to the activation energy used in the Arrhenius law E_{Ar} , as $E_{VF} = E_{Ar}(1 - T/T_g)$, denoting an elastic shear energy around the local relaxation due to the change of an activation volume [40-41]. Figure. 9a shows experimental and fitted values of frequency versus the dielectric loss maxima temperature according to the (VF) equation (Eq. (31)) for pure PDMS and the composites on cooling. The value for 10 MHz frequency is obtained from the previously described ultrasonic measurements.

The frequency dependence of the imaginary part of dielectric permittivity was analyzed by the Cole-Cole function Eq. [8]. Obtained values of the relaxation time τ at various temperatures were converted to the relaxation frequency values f_r according to $f_r = 1/\tau$.

The temperature dependence of the relaxation frequency fit very well the VF equation (Figure 9b). It was determined, that the glass transition temperature increases with the concentration of ZnO nanoparticles, while the concentration behaviour of the activation energy is less expressed. The increase of the glass transition temperature is due to the reduced mobility of the polymer backbone close to ZnO nanoparticles [42-44].

The ultrasonic attenuation peak can be described using the relaxation theory of elasticity [45]:

$$\alpha = \frac{\Delta V}{V^2} \frac{\omega^2 \tau_u}{1 + \omega^2 \tau_u^2}, \quad (32)$$

where V and ΔV are the longitudinal ultrasonic velocity in the composite and its magnitude of downward step at a certain temperature, respectively, τ_u is the ultrasonic relaxation time. Here we assume that the relaxation time can be expressed by such VF relation:

$$\tau_u = \tau_0 e^{\frac{E_{F2}}{k_B(T-T_{ref2})}}, \quad (33)$$

where τ_0 is the relaxation time, when $T \rightarrow \infty$. In order to include the temperature dependence of the ultrasonic losses in acoustic bonds and buffers, a linear temperature dependence with two terms (A and α_0) can be added:

$$\alpha = \frac{\Delta V}{V^2} \frac{\omega^2 \tau_u}{1 + \omega^2 \tau_u^2} + AT + \alpha_0. \quad (34)$$

Obtained values of both of T_{ref} and T_{ref2} are very similar [30].

Thus mechanical and dielectric properties of PDMS/ZnO composites are strongly dependent on the concentration of ZnO, i.e., a composite containing higher concentration of fillers has a lower dielectric and higher mechanical loss peaks. Dielectric spectroscopic measurements in the PDMS/ZnO composites combined with ultrasonic measurements revealed the existence of the dielectric hysteresis between cooling and heating cycles and it is strongly dependent on the concentration of ZnO nanoparticles, acting as crystallization nuclei. The growth of spherulites (few hundred microns) can explain the increased scattering-attenuation in PDMS matrix for higher ZnO concentrations. The analysis of the dielectric losses maximum according to the VF law and the ultrasonic attenuation data shows that the glass transition temperature increases with increase of ZnO concentration in the composites. It has been shown that the ultrasonic and the dielectric relaxation processes can be described by Voge-Fulcher law.

REFERENCES

- [1] Debye, P. (1954). *Polar molecules*, Dover, New York.
- [2] Cole, K. S. & Cole, R. H. (1941). Dispersion and absorption in dielectrics: alternating current characteristics. *J. Chem. Phys.*, 9, 341-351.

- [3] Bergman, R., Alvarez, F., Alegria, A. & Colmenero, J. (1998). Dielectric relaxation in PMMA revisited. *Journal of Chemical Physics*, *109*, 7546-7555.
- [4] Fragiadakis, D., Pissis, P. & Bokobza, L. (2005) Glass transition and molecular dynamics in poly(dimethylsiloxane)/silica nanocomposites. *Polymer*, *46*, 6001-6008.
- [5] Fuoss, R. M. & Kirkwood, J. G. (1941). Electrical properties of solids. VIII. Dipole moments in polyvinyl chloride-diphenyl systems. *J. Am. Chem. Soc.*, *63*, 385-394.
- [6] Diaz-Calleja, R., Garcia-Bernabe, A., Pagueguy, C., Gargallo, L. & Radic, D. (2001). Dielectric relaxations of poly(2-norbornyl methacrylate) and poly(3-methyl-2-norbornyl methacrylate). *Polymer*, *42*, 8907-8910.
- [7] Davidson, D. W. & Cole, R. H. (1951). Dielectric relaxation in glycerol, propylene glycol, and n-propanol. *J. Chem. Phys.*, *19*, 1484-1490.
- [8] Psarras, G. C., Manolakaki, E. & Tsangaris, G. M. (2003). Dielectric dispersion and ac conductivity in iron-particles loaded-polymer. *Composites Part A – Applied Science and Manufacturing*, *34*, 1187-1198.
- [9] Havriliak, S. & Negami, S. (1967). A complex plane representation of dielectric and mechanical processes in some polymers. *Polymer*, *8*, 161-210.
- [10] Robles-Hernandez, B., Monnier, X., Pomposo, J. A., Gonzalez-Burgos, M. & Cangialosi Alegria, A. (2019). Glassy dynamics of an all-polymer nanocomposite based on polystyrene single-chain nanoparticles. *Macromolecules*, *52*, 6868-6877.
- [11] Duarte, D. M., Tu, W. K., Dzienia, A. & Adrjanowicz, K. (2019) Study on the effect of side-chain group on the segmental dynamics of selected methacrylate polymers at ambient and high pressures. *Polymer*, *183*, 121860.
- [12] Ding, R., Torres, S. W., Bowen, D. E. & Bowler, N. (2018). Dynamics of polycyclic aromatic hydrocarbon compound-epoxy composites: A dielectric study. *Polymer*, *136*, 6-16.

- [13] Carrol, B., Cheng, S. W. & Sokolov, A. P. (2017). Analyzing the interfacial layer properties in polymer nanocomposites by broadband dielectric spectroscopy. *Macromolecules*, *50*, 6149-6163.
- [14] Kliem, H. (2005). Kohlraush relaxations: new aspects about the everlasting story. *IEEE Transactions on Dielectrics and Electrical Insulation*, *12*, 709-717.
- [15] Jonscher, A. K. (1983). *Dielectric relaxation in solids*, Chelsea Dielectric Press, London.
- [16] Alvarez, F., Alegria, A. & Colmenero, J. (1991). Relationship between the time-domain Kohlraush-Williams-Watts and frequency domain Havriliak-Negami relaxation functions *Phys. Rev. B*, *44*, 7306-7312.
- [17] Liang, J. & Yang, Q. (2007). Aggregate structure and percolation behavior in polymer/carbon black conductive composites. *Journal of Applied Physics*, *102*, 083508.
- [18] Nan, C. W. (1993). Physics of inhomogeneous inorganic materials. *Progress in Materials Science*, *37*, 1-116.
- [19] Macutkevic, J. Kranauskaite, I., Banys, J., Moseenkov, S., Kuznetsov, V. & Shenderova, O. (2014). Metal-insulator transition and size dependent electrical percolation in onion-like carbon/polydimethylsiloxane composites. *Journal of Applied Physics*, *115*, 213702.
- [20] Almond, G., Duncan, G. K. & West, A. R. (1983). The determination of hopping rates and carrier concentrations in ionics conductors by a new analysis of ac conductivity. *Solid State Ionics*, *8*, 159-164.
- [21] Mdahari, A., Carmona, F., Brosseau, C. & Delhaes, P. (2008) Direct current electrical and microwave properties of polymer-multiwalled carbon nanotubes composites. *Journal of Applied Physics*, *103*, 054303.
- [22] Zylbersztein, A. & Mott, N. F. (1975). Metal-insulator transition in vanadium dioxide. *Physical Review B*, *11*, 11, 4383.
- [23] Mott, N. F. & Davis, E. A. (1971). *Electronic processes in non-crystalline solids* (Oxford University, London).

- [24] Kuznetsov, V. L., Butenko, Yu. V., Chuvilin, A. L., Romanenko, A. I. & Okotrub, A. V. (2001). Electrical resistivity of graphitized ultra-disperse fiamond and onion-like carbon. *Chemical Physics Letters*, 336, 397-404.
- [25] Ksenevich, V. K., Odzhaev, V. B., Martunas, Z., Seliuta, D., Valusis, G., Galibert, J., Melnikov, A. A., Wieck, A. D., Novitski, D., Kozlov, M. E. & Samuilov, V. A. (2008). Localization and nonlinear transport in single walled carbon nanotubes fibers. *Journal of Aplied Physics*, 104, 073724.
- [26] Ezquerra, T. A., Kulesza, M. & Balta-Calleja, F. J. (1991). Electrical transport in polythylene-graphite composite materials. *Synthetic Metals*, 41, 915-920.
- [27] Youssef, M. H. (2003). Influence of sulfur content and curing time on the glass transition parameters in SBR vulcanizates: an ultrasonic study. *Polymer Testing*, 22, 235-242.
- [28] Adachi, H., Adachi, K., Ishida, Y. & Kotaka, T. (1979). Dielectric relaxation of polydimethylsiloxane. *Journal of Polymer Science Part B: Polymer Physics*, 17, 851–857.
- [29] Ouyang, J., Pan, Y., Zhou, S. & Goh, S. H. (2006). Supramolecular assembled C-60-containing carboxylated poly(dimethylsiloxane) composites. *Polymer*, 47, 6140-6148.
- [30] Belovickis, J., Macutkevici, J., Svirskas, S., Samulionis, V., Banys, J., Shenderova, O. & Borjanovic, V. (2015) Ultrasonic and dielectric relaxation in PDMS/ZnO nanocomposite. *Physica Status Solidi B*, 252, 2778-2783.
- [31] Roland, C. M. & Casalini, R. (2003). Temperature dependence of local segmental motion in polystyrene and its variation with molecular weight. *Journal of chemical physics*, 119, 1838-1842.
- [32] Bateman, T. B. (1962). Elastic moduli of single-crystal zinc oxide. *J. Appl. Phys.*, 33, 3309-3312.
- [33] Klonos, P., Panagopolou, A., Kyritsis, S., Bokobza, L. & Pissis, P. (2011). Dielectric studies of segmental dynamics in poly (dimethylsiloxane)/titania nanocomposites. *Journal of Non-Crystalline Solids*, 357, 610-614.

- [34] Samulionis, V., Macutkevicius, J., Banys, J. & Belovickis, J. (2014). Ultrasonic studies of onion-like carbon polydimethylsiloxane composites. *2014 IEEE International Ultrasonic Symposium (IUS)*, 1986-1987.
- [35] Belovickis, J., Macutkevicius, J., Svirskas, S., Samulionis, V., Banys, J., Shenderova, O. & Borjanovic, V. (2015). Dielectric spectroscopy of polymer based PDMS nanocomposites with ZnO nanoparticles. *Ferroelectrics*, 479, 82-89.
- [36] Dollase, T., Wilhelm, M., Spiess, H. W., Yagen, Y., Yerushalmi-Rozen, R. & Gottlieb, M. (2003). Effect of interfaces on the crystallization behaviour of PDMS. (2003) *Interface Science*, 11, 199-209.
- [37] Valle-Carrandi, L., Alegria, A. & Colmenero, J. (2010). PDMS behaviour under confinement in strongly segregated mesophases of PS-PDMS diblock copolymers. *European Physical Journal Special Topics*, 189, 257-261.
- [38] Bai, Y. & Jin, L. (2008). Characterization of frequency-dependent glass transition temperature by Vogel-Fulcher relationship. *Journal of Physics D, Applied Physics*, 41, 152008.
- [39] Vogel, H. (1921). The law of the relationship between viscosity of liquids and the temperature. *Physikalische Zeitschrift*, 22, 645-646.
- [40] Trachenko, K. (2011). Understanding the spin glass transition as a dynamic phenomenon. *Journal of Physics-Condensed Matter*, 23, 366003.
- [41] Pirc, R. & Blinc, R. (2007). Vogel-Fulcher freezing in relaxor ferroelectrics. *Physical Review B*, 76, 020101.
- [42] Bisticic, L., Borjanovic, V., Mikac, L. & Dananic, V. (2013). Vibrational spectroscopic studies of poly(dimethylsiloxane)-ZnO nanocomposites. *Vibrational Spectroscopy*, 68, 1-10.
- [43] Sushko, R., Filimon, M., Dannert, R., Elens, P., Sanctuary, R. & Baller, J. (2014). Anomalous glass transition behaviour of SBR-Al₂O₃ nanocomposites at small filler concentrations. *Nanotechnology*, 25, 425704.

- [44] Ansorge, S. & Papailiou, K. (2015). Mechanical properties of silicone rubber under high loadings of alumina trihydrate filler. *Journal of Elastomers & Plastics*, 47, 1-29.
- [45] Valevicius, V., Samulionis, V. & Banys, J. (1994) Ultrasonic dispersion in the phase transition region of ferroelectric materials. *J. Alloys Compd.*, 369, 211–212.

Chapter 2

**APPLICATIONS OF
POLYDIMETHYLSILOXANE:
MICROSTRUCTURE OF FUNCTIONAL
SURFACE FOR OBSERVATION OF
BIOLOGICAL CELL BEHAVIOR**

*Shigehiro Hashimoto**

Department of Mechanical Engineering, Kogakuin University,
Tokyo, Japan

ABSTRACT

Polydimethylsiloxane (PDMS) is frequently used for the base material for microcircuit chips. It can be applied for the base material for micro-machining to make the micro-surface morphology. The typical size of a biological cell, on the other hand, is micrometer. It is difficult to control dimension of micrometer with the conventional micro-machining technology. The micromachining with PDMS enables the surface design with the dimension of micrometer.

* Corresponding Author's E-mail: shashimoto@cc.kogakuin.ac.jp.

Although the surface of PDMS is hydrophobic, it can be hydrophilized by the oxygen plasma ashing. The affinity of the surface to the biological fluid can be improved by the albumin coating. In this chapter, several kinds of devices, which are applied to observe the behaviour of biological cells, are exemplified: micro-ridges, micro-grooves, micro-markers, and micro-slits. Methodology to make each morphology by PDMS is described: photolithography, and etching. The effectiveness of each kind of device is evaluated by experiments with several types of biological cells. The technology will contribute to several applications in the field of the biomedical engineering: medical diagnostics, and regenerative medicine.

Keywords: polydimethylsiloxane, micro-machining, biological cell, ridge, groove, marker, and slit

1. INTRODUCTION

Polydimethylsiloxane (PDMS) is frequently used for the base material in the field of electronics for microcircuit chips. The material is easy to be used for molding. It can be applied for the base material for micro-machining to make the micro-surface structure. The typical size of the biological cell, on the other hand, is micrometer. It is difficult to control dimension of micrometer with the conventional micro-machining technology. The micromachining with PDMS enables the surface design around the dimension of micrometer with the specially designed process.

The plate of PDMS with the micro-machined surface is able to maintain the transparency. Through the plate, the micro-machined inner surface can be observed by the optical microscope. The surface of PDMS can be hydrophilized by the oxygen plasma ashing. The affinity of the surface to the biological fluid can be improved by albumin coating. The micro-machined surface of PDMS can be used for the scaffold for the cell culture. The rigidity of the surface of PDMS dipped in the medium is enough to maintain the micro-morphology of the scaffold.

In this chapter, several kinds of devices, which are applied to observe the behavior of biological cells, are exemplified: micro-patterns for cell orientation, micro-grooves for cell capture, micro-markers for cell tracings,

and micro-slits for cell sorting. In each section, methodology to make each morphology by PDMS is described: photolithography, and etching. The effectiveness of each kind of device is evaluated by experiments with several types of biological cells.

The control technique of orientation of cells might be applied to the alternative system to the animal experiment for tissue technology: making the engineered pseudo-environment, or the partial biological tissue *in vitro*.

2. METHODS

Several micropattern of PDMS were manufactured for application to biological cells. For comparison between cell types, several types of cells were used in the test: C2C12 (mouse myoblast cell line originated with cross-striated muscle of C3H mouse), Hepa1-6 (mouse hepatoma cell line of C57L mouse), 3T3-L1 (mouse fat precursor cells, cell line of 3T3 mouse), Neuro-2a (a mouse neural crest-derived cell line), L929 (fibroblast connective tissue of C3H mouse), MC3T3-E1 (osteoblast precursor cell line derived from mouse calvaria), and HUVEC (human umbilical vein endothelial cells). D-MEM (Dulbecco's Modified Eagle's Medium) containing 10% FBS (decomplemented fetal bovine serum) and 1% penicillin/ streptomycin was used for the culture medium. In the case of L929, E-MEM (Eagle's minimal essential medium) was used. In the case of MC3T3-E1, alpha-MEM (alpha modified Eagle's minimal essential medium) was used. In the case of HUVEC, EBM-2 (Endothelial Cell Basal Medium) containing EGM-2 (Endothelial Cell Growth Medium) and 2% decomplemented FBS was used. In the case of the flow test, the cells were exfoliated from the bottom of the culture dish with trypsin, and were suspended in the culture medium.

The swine erythrocyte also was used in the test for comparison. After centrifugation, erythrocytes were suspended in the phosphate buffer solution to make a suspension of cells at the volume ratio of 0.1 percent.

2.1. Micro Pattern for Orientation

PDMS has advantage as the material which can be used in the micromachining to make micro-morphology on the surface. The orientation of the biological cell, on the other hand, depends on the surface morphology of the scaffold. In this section, several kinds of micro patterns on the scaffold have been exemplified to control the orientation of the biological cells.

2.1.1. Micro-Ridgeline

2.1.1.1. Height of Micro-Ridge for Orientation

To study on the minimum height of the micro-ridge to control the orientation of biological cells, several parallel lines of micro-ridges were made on the disk of transparent PDMS. The width, the interval and the length of each rectangular ridge were 3 μm , 7 μm , and 2 mm respectively. Variation was made on the height of the ridge between 0.3 μm and 3.5 μm .

The silicon wafer was used for the surface mold for the disk in the photolithography process. The surface of the wafer was cleaned by the following process. The surface was exposed to the oxygen gas in the reactive ion etching system for five minutes (the oxygen plasma ashing). It was then cleaned in the ultrasonic cleaner with 2-propanol, with the hydrogen peroxide solution, and with the ultrapure water. The wafer was dried on the hot plate at 373 K for five minutes.

The photoresist material of OFPR-800 was coated on the wafer with 2 μm thick at 5000 rpm with the spin coater. The photoresist material was baked in the oven at 383 K for 90 seconds. The pattern of lines was drawn on the wafer with the laser drawing system. To control the dimension of the lines on the mold with the laser drawing system, the parameters were selected as follows: the wavelength of 408 nm, and the power of 20 mW. After the drawing, the photoresist material was baked again in the oven at 393 K for five minutes. The photoresist was developed with tetra-methyl-ammonium hydroxide (NMD-3). The wafer was rinsed with the distilled water. To increase the adhesiveness of the coating, the wafer was baked at

393 K for five minutes. The wafer was etched with the plasma gas using the reactive ion etching system to make lines of the micro-groove. The alternative switching mode between C_4F_8 gas and SF_6 gas was applied on the disk. To exfoliate the residual photoresist material from the surface, the wafer was exposed to the oxygen gas. The dimension of the micro-grooves of the mold was measured with the laser microscope. Each mold had several groups of ridges dispersed on the disk. Each mold had its own unified height of the ridges. The surface of the wafer with micro pattern was coated with 1 μm thickness of parylene as the release agent.

After the wafer was enclosed with the peripheral wall of the polyimide tape, PDMS with the curing agent was poured on the mold of the wafer. The volume ratio of the curing agent was ten percent of PDMS. After degassing, PDMS was baked at 383 K for one hour in the oven. After the baked disk of PDMS was exfoliated from the mold, the disk was sterilized in the autoclave. The disk with the micro ridges at several positions was cut into the plate of 35 mm diameter to be set at the bottom of the dish. The plate was exposed to the oxygen gas for one minute in the reactive ion etching system to be characterized as hydrophilic. To maintain the hydrophilic property, the plate was preserved in the ultrapure water, before the cell culture. The contact angles were measured between the surface of PDMS and the medium by the contact angle analyzer, before and after the oxygen plasma ashing.

The culture dish, which consists of 6 cylindrical wells of 35 mm diameter, was used for cell culture. Each PDMS disk, which has micro ridges on the upper surface, was placed in the bottom of each well, and preserved in medium of D-MEM. C2C12 was used in the experiment. Cells were seeded on the culture plate with the medium of D-MEM at the density of 1.5×10^3 cells/cm². FBS was added to the medium with the volume rate of 10 percent. Cells were cultured in the incubator to maintain both the temperature of 310 K and the carbon dioxide partial pressure of 5 percent for one week.

The deformation of cells near the micro ridges was observed with the inverted phase-contrast microscope every three hours in 24 hours. The

angle between the longitudinal axis of the cell adjacent to the ridge and the longitudinal direction of the ridge was measured.

2.1.1.2. Behavior of Cell on Micro-Ridge

Several parallel lines of micro ridges were made at the center on the disk of transparent PDMS. The height, the interval, and the length of the rectangular ridge were 1 μm , 3 μm , and 0.5 mm, respectively. To compare the effect of interval of ridges on the behavior of each cell, variation was made on the width of the ridge: 1 μm , 3 μm , and 5 μm . Each pattern was drawn in the square area of 0.5 mm \times 0.5 mm, which was the quarter part of the square area of 1.0 mm \times 1.0 mm. One of the quarter areas had the smooth surface, and had no ridge for comparison.

The silicon wafer was used for the surface mold for the disk at the photolithography process. The surface of the wafer was cleaned by the spin-dryer. Hexamethyldisilazane (HMDS) was coated at 3000 rpm for thirty seconds with the spin coater. The photoresist material of OFPR-800 of 1.7 μm thick was coated on the wafer with the spin coater. The photoresist material was baked on the heated plate at 373 K for 90 seconds. The pattern for the micro-grooves was drawn on the wafer with the laser drawing system. To save the 1 μm thickness of parylene coating, the dimensions of the width of the three kinds of grooves on the mold were 3 μm , 5 μm , and 7 μm , respectively. The pattern was baked on the heated plate at 393 K for five minutes. The photoresist was developed with NMD-3 for 60 seconds. The wafer was rinsed with the distilled water, and dried by the spin-dryer. To increase the adhesiveness of the coating, the wafer was baked at 393 K for five minutes. The wafer was etched with the plasma gas using the reactive ion etching system to make lines of the micro-grooves of 1 μm depth. The gas of sulfur hexafluoride (with argon and oxygen) was applied on the wafer at 15 Pa for three minutes. To exfoliate the residual photoresist material from the surface, the wafer was exposed to the oxygen gas using the compact etcher. The dimensions of the three kinds of the micro-grooves of the mold were measured with the laser microscope. The morphology along the transverse lines of the grooves was traced. The morphology of the micro-grooves was also observed by the

scanning electron microscope (SEM). The surface of the wafer with micro-patterns was coated with 1 μm thickness of parylene.

PDMS was poured with the curing agent on the wafer. After degassing, PDMS was baked in the oven. The baked disk of PDMS of 0.25 mm thickness was exfoliated from the mold, and sterilized in the autoclave. The disk with the micro-ridges was used for the bottom of the dish. Another disk of PDMS, which has the donut shape (50 mm outer diameter, 5.5 mm thickness) with the hole of 33 mm diameter, was made for the peripheral wall of the dish. These two disks were contacted with the affinity between them. The dish of PDMS was exposed to the oxygen gas for one minute in the reactive ion etching system to be characterized as hydrophilic. The dish was preserved in the ultrapure water to keep the hydrophilic property of the surface, before the cell culture.

The centrifugal force was used to apply the tangential force field on the surface of the scaffold. The hysteresis effect of the force field on the single osteoblast cell (MC3T3-E1) attached on the scaffold was investigated. To examine the effect of the direction of the force field on the cell at the specific alignment, the orientation of the cell was controlled by the striped pattern on the surface of the scaffold. The micro striped pattern was made in three partial rectangular areas of 0.4 mm \times 1.6 mm on the PDMS plate of the scaffold by photolithography technique. The height, the width, and the interval of the quadrangular ridges were 0.7 μm , 3 μm , and 3 μm , respectively. Each area has its own specific direction of the striped pattern. Namely, variation was made on the angle between the longitudinal direction of the ridge and the direction of the centrifugal force in the two-dimensional scaffold surface: 0 degree (parallel), 45 degree, and 90 degree (perpendicular). Three partial areas are made on the same surface of the scaffold plate in the parallel position, so that the behavior of cells on each area can be compared simultaneously. The pattern of each area was also used as the marker to trace each cell.

PDMS was poured with the curing agent on the mold. After degassing, PDMS was baked at 338 K for one hour in the oven. The baked plate of PDMS (1 mm thickness) was exfoliated from the mold of the slide glass plate. The PDMS plate was cut to make the plate of 15 mm \times 10 mm \times 1

mm, and stuck on the glass plate of 50 mm × 13 mm × 1 mm. The surface of the PDMS plate was exposed to the oxygen gas in the reactive ion etching system for thirty seconds just before the cell culture.

2.1.2. Micro-Checked Pattern

The checked convexo-concave pattern was designed with micro quadrangular prisms at the square area of 1 mm × 1 mm on the disk of glass for the scaffold by the lithography technique. Each prism had the following dimension. The length of the top rectangular surface was 10 μm length. Variation was made on the width of the top square of the prism: 5 μm, 8 μm, and 10 μm. The variation of the width makes the variation on the aspect ratio of the top rectangular surface of the prism: 1, 1.25, and 2. The arctangent of the each ratio is 0.79 rad, 0.89 rad, and 1.1 rad. Each pattern was drawn in the square area of 0.5 mm × 0.5 mm, which was the quarter part of the square area of 1.0 mm × 1.0 mm on the scaffold. Photomasks were used to trace the micro checked pattern on the mold. The photomasks were made by two kinds of etching process: wet and dry.

After the disk of Tempax glass was enclosed with the peripheral wall of polyimide tape, degassed PDMS was poured with the curing agent. PDMS was baked at 373 K for one hour in the oven. The culture plate was exposed to the oxygen gas in the reactive ion etching system to be characterized as hydrophilic. C2C12 was used in the test.

2.1.3. Taper-Stripe Pattern for Durotactic Migration

To observe the durotactic migration of the cell depend on the surface hardness, the taper-alternative-stripe pattern of scaffold was designed on the plate of PDMS for the flat scaffold by the photolithography technique. A part of each band had gradual reduction at the width: from 0.2 mm to 0.1 mm, or from 0.15 mm to 0.05 mm. The surface of the scaffold consisted of bands made of two alternate materials: PDMS, and SU-8 (epoxy based negative photoresist material).

The pattern of the mold was controlled by the photomask. The dimension of the morphology of the surface of the photomask was observed by the laser microscope.

The borosilicate glass disk was used for the base of the mold. The surface of the glass disk was cleaned by the oxygen plasma ashing. After the negative photoresist material of the high viscosity (SU-8 10) was coated on the disk by the spin coater, the photoresist was baked in the oven at 368 K. After the photomask with the taper-stripe patterns was mounted on the surface (SU-8 10), the photoresist was exposed to the ultraviolet light through the mask in the mask aligner. The photoresist was baked in the oven at 368 K. The photoresist was developed with SU-8 developer. The glass surface with the micro pattern was rinsed with IPA (2-propanol), and the pure water. The morphology of the surface of the mold was measured across the stripes by the stylus of the contact profilometer.

PDMS was poured with the curing agent on the mold. PDMS was baked at 373 K in the oven. The baked disk of PDMS (3 mm thickness) was exfoliated from the mold, and was sectioned into the disk (diameter of 25 mm; with the micro pattern). The disk was exposed to the oxygen gas to be characterized as hydrophilic. On the micro pattern of the disk, another disk without micro pattern, which has two holes, was attached. The photoresist material of the low viscosity (SU-8 2) was injected by the capillary effect into the space. The space was kept by the micro pattern, between two disks through the holes. After the disks with the photoresist material of the low viscosity (SU-8 2) was baked at 393 K for five hours in the oven, the PDMS disk part with no micro pattern was exfoliated, and discarded. Before the cell cultivation, the surface of the culture plate was hydrophilized by the oxygen plasma ashing.

In each test, cells (C2C12) were seeded on the micro pattern of the disk placed in the culture dish at the density of 2000 cells/cm². The culture dish was kept in the incubator. The migration tendency of each cell was checked at the time lapse image by the phase contrast microscope during the cell culture.

2.2. Micro-Groove for Capture

Several types of micro-grooves were designed on the bottom surface of the flow channel: the hole of the cylindrical column, the hole of the half-cylindrical column, and the groove of the quadrangular prism. Variation was made on the angle between the longitudinal axis of the quadrangular prism and the direction of the flow: 0 degree (parallel), 45 degree, and 90 degree (perpendicular). The manufactured micro-grooves were contained in the flow channel and applied for the trap of the flowing biological cell.

2.2.1. Hole of Cylindrical Column

Several micro-traps of the cylindrical hole of 0.01 mm depth (diameter between 0.01 mm and 0.04 mm) was fabricated on PDMS disk with the photolithography technique. A silicon wafer is used for the surface mold. The surface of the wafer is cleaned three times: with the isopropyl alcohol for ten minutes, with hydrogen peroxide solution for ten minutes, and ultrapure water for ten minutes. After the wafer was dried on the hot plate at 383 K for 10 minutes, it was exposed to the oxygen gas in the reactive ion etching system to be characterized as hydrophilic.

The photoresist material of SU8-10 was coated on the wafer with 0.015 mm thick at 1000 rpm with the spin coater. The photoresist was baked on the heated plate with two processes: at 338 K for 3 minutes, before at 368 K for 7 minutes. To make columns on the mold, the pattern of holes was drawn on the wafer with the laser drawing system. The pattern was baked on the heated plate with two processes: at 338 K for 1 minute, before at 368 K for 3 minutes. The photoresist was developed with SU8 developer for five minutes to make micro-columns, where the laser beam was radiated. After the wafer was rinsed with the distilled water, it was dried on the heated plate. To decrease remaining stress and to increase the adhesiveness of the coating, the wafer was baked at 423 K for 5 minutes. After developing, the dimension of the micro-columns on the mold was measured with the laser microscope. The convex mold with micro pattern was used for the lower disk of PDMS to make the micro-

holes. The surface of the wafer was coated with 1 μm thickness of parylene as the release agent.

PDMS was poured with the curing agent on the wafer. After degassing, PDMS was baked at 353 K for two hours in the oven. Each diameter of two PDMS disks is 50 mm. The thicknesses of the upper and the lower disks are 10 mm and 2 mm, respectively. At the upper disk, two holes of 5 mm diameter were machined by the punching tool. The silicone tubes are stuck at the holes without adhesives.

The one-way flow system was designed to control the wall shear rate at the disk of PDMS. The system consists of the flow chamber, the micro syringe pump, tubes and the microscope. The plastic tubes (3 mm internal diameter and of 5 mm external diameter) were used for the connector to the flow chamber. The flow channel consisted of two transparent PDMS disks and the thin sheet of silicone rubber. The thin sheet (0.1 mm thick) of silicone rubber, which had the rectangular void space of 1 mm \times 20 mm, was sandwiched between the PDMS plates. The void space formed the channel of 20 mm length \times 1 mm width \times 0.1 mm depth. The three plates stuck together with their surface affinity without adhesives. The inner surface of the channel was exposed to the oxygen gas (the oxygen plasma ashing), before the parts of the flow channel were assembled. Immediately after the characterization, the flow path of the channel was rinsed with the saline solution, and the suspension of cells was introduced, successively. One of the tubes was connected to the plastic syringe pump. The room temperature was maintained at 25 degrees Celsius. The channel was placed on the inverted phase-contrast microscope.

Two types of biological cells were used in the test alternatively: L929 or C2C12. The suspension of cells was introduced to the channel at the constant flow. Variation was made on the flow rate between $0.3 \times 10^{-10} \text{ m}^3/\text{s}$ and $2.8 \times 10^{-10} \text{ m}^3/\text{s}$. The flow path was carefully examined to avoid mixing of air bubbles, which might stir the medium in the flow chamber and might induce exfoliation of cells. The behavior of cells on the plate of the chamber was observed with the microscope.

2.2.2. Hole of Half-Cylindrical Column

To keep the captured cell for longer time, the shape of each hole was changed from cylinder to half-cylinder. Several micro traps of the half cylindrical hole of 2 μm depth were fabricated on the surface of PDMS disk with the photolithography technique. The diameter of the half cylinder was 0.02 mm. Sixteen holes were arranged in two lines. The interval between holes was 0.02 mm. Variation was made on the direction of the half cylindrical holes (Figure 10). A rectangular flow channel was constructed with the silicone film, which was sandwiched by two transparent PDMS disks.

The silicon wafer was used for the surface mold for the disk. The diameter and the thickness of the wafer are 50 mm and 0.30 mm, respectively. After the surface of the wafer was cleaned, it was exposed to the oxygen gas (the oxygen plasma ashing).

The photoresist material of low viscosity (SU8-2) was coated on the wafer with 2 μm thick at 2000 rpm for 30 s with the spin coater. The photoresist material was baked on the heated plate. The pattern of holes to make half cylindrical columns on the mold was drawn on the wafer with the laser drawing system. The pattern was baked on the heated plate.

The photoresist material was developed with SU8 developer for five minutes to make micro columns, where the laser beam was radiated. After the wafer was rinsed with the distilled water, it was dried on the heated plate. To decrease remaining stress and to increase the adhesiveness of the coating, the wafer was baked at 423 K for 5 minutes. The convex mold with micro pattern was used for the lower disk of PDMS to make the micro-holes on the surface. The surface of the wafer was coated with 1 μm thickness of parylene.

PDMS was poured with the curing agent on the wafer. After degassing, PDMS was baked at 353 K for two hours in the oven. The diameter of two PDMS disks was 50 mm. The thicknesses of the upper and the lower disks were 10 mm and 2 mm, respectively. At the upper disk, two holes of 5 mm diameter were machined by the punching tool. The silicone tubes were stuck at the holes without adhesives.

The one-way flow system was designed to control the wall shear rate at the disk of PDMS. The flow channel consisted of two transparent PDMS disks and the thin sheet of silicone rubber. The thin sheet (0.1 mm thick) of silicone rubber, which has the rectangular void space of 1 mm × 20 mm, was sandwiched between the PDMS plates. The void space formed the channel of 20 mm length × 1 mm width × 0.1 mm depth. The three plates stuck together with their surface affinity without adhesives. The inner surface of the channel was exposed to the oxygen gas to be characterized as hydrophilic before assembly.

Immediately after the characterization, the flow path of the chamber was rinsed with the saline solution, and the suspension of cells was injected, successively. One of the tubes was connected to the syringe pump. The room temperature was maintained at 25 degrees Celsius. The chamber was placed on the stage of the inverted phase-contrast microscope.

Two types of biological cells were used in the test alternatively: C2C12, or MC3T3-E1. The suspension was introduced to the chamber at the constant flow with the micro syringe pump. Variation was made on the flow rate: 2.8×10^{-10} m³/s and 8.3×10^{-10} m³/s.

2.2.3. Groove of Quadrangular Prism

Six grooves were arranged in two lines. Each groove had the rectangular shape: 2 μm depth, 0.025 mm width and 0.2 mm length. The interval between grooves was 0.2 mm. Variation was made on the angle between the longitudinal direction of the groove and the flow direction: 0 degree (parallel), 45 degree, and 90 degree (perpendicular).

A silicon wafer was used for a surface mold for the disk. The diameter and the thickness of the wafer are 50 mm and 0.30 mm, respectively. The photoresist material of low viscosity (SU8-2) was coated on the wafer with 2 μm thick at 2000 rpm for 30 s with the spin coater. The photoresist baked on the heated plate with two processes: at 338 K for 1 minute, before at 358 K for 3 minutes. The pattern for grooves on the mold was drawn on the wafer with the laser drawing system. The pattern was baked on the heated plate.

The photoresist material was developed with SU8 developer for six minutes to make the micro rectangular ridges, where the laser beam was radiated. The wafer was rinsed with the isopropyl alcohol and the ultrapure water, before dried with the air gun. The convex mold with the micro patterns was used for the lower disk of PDMS to make the micro-grooves on the surface for trapping cells. The surface of the wafer was coated with 1 μm thickness of parylene. After the wafer was enclosed with the peripheral wall of the polyimide tape, PDMS was poured with the curing agent on the wafer. After degassing, PDMS was baked at 383 K.

The one-way flow system has been designed to control the shear rate at the wall of PDMS. The system consists of the flow channel, the micro syringe pump, tubes and the microscope. The flow channel consists of two transparent PDMS disks and the thin sheet of silicone rubber. The thin sheet (0.1 mm thick) of silicone rubber, which has the rectangular void of 5 mm \times 30 mm, was sandwiched between two transparent PDMS plates. The void forms the channel of 30 mm length \times 5 mm width \times 0.1 mm depth. The lower PDMS disk, which has the micro grooves at the center of the upper surface, was placed on the inner bottom of the culture dish of 50 mm diameter. At the upper disk, two holes of 5 mm diameter were machined by the punching tool. The silicone tube was inserted to each hole of the upper PDMS disk. To seal the leak at the gap between elements, the liquid of PDMS was pasted on the junction of elements, and baked at 333 K for 90 minutes in the oven. One of the tubes was connected to the syringe pump, and the other tube was connected to the reservoir of the suspension. The flow channel was placed on the stage of the inverted phase-contrast microscope.

Two types of biological cells were used in the test alternatively: C2C12, or 3T3-L1. The suspension of 4000 cells/cm³ was introduced to the channel at the constant flow rate of 2.8×10^{-11} m³/s with the micro syringe pump.

2.2.4. Oblique Groove of Quadrangular Prism

Because the trapping time of the cell at the hole depends on the several factors including the flowing position, the character of each cell is hardly

distinguished by the capture. At the oblique groove (2.2.3.), on the other hand, the moving direction of the cell was shifted at the groove independent of the flowing position. For trapping cells, micro grooves of the rectangular shapes (4.5 μm depth, and 0.2 mm length) were fabricated on the surface of PDMS plate with the photolithography technique. Several grooves were arranged on the same wall for the bottom of the micro flow channel. The angle between the longitudinal direction of the groove and the flow direction was 0.79 rad. At the groove arrangement from upstream to downstream, variation was made on the width of the groove: 0.03 mm, 0.04 mm, and 0.05 mm.

For the lower plate of the flow channel, the slide glass plate was used for the base of the mold. The surface of the glass plate was hydrophilized by the oxygen plasma ashing. The epoxy based negative photoresist material (SU8-5) was coated on the glass at 2700 rpm for 120 s with the spin coater. The photoresist was baked in the oven at 338 K for three minutes, and at 368 K for seven minutes successively. The photoresist was exposed to the ultraviolet light through the photomask in the mask aligner. The photoresist was baked in the oven at 363 K for seven minutes. The photoresist was developed with SU8 developer to make micro rectangular ridges, where the laser beam was radiated. The glass surface with the micro pattern was rinsed with IPA. The plate was dried by the spin-dryer with N_2 gas. PDMS was poured with the curing agent on the plate. After degassing, PDMS was baked at 368 K for twenty minutes in the oven.

For the upper plate of the flow channel, the polyimide tape (0.055 mm thickness, 1 mm width, and 25 mm length) was pasted at the center of the poly-methyl-methacrylate plate for the mold. PDMS was poured with the curing agent on the plate. After degassing, PDMS was baked at 368 K for twenty minutes in the oven. Two holes (diameter of 5 mm) with the interval of 20 mm were made for the inlet and the outlet of the flow channel.

Both the upper and the lower plates were exposed to the oxygen gas in the reactive ion etching system (the oxygen plasma ashing). Immediately after ashing, the upper disk was adhered (plasma bonding) to the lower disk to make the flow path (0.055 mm height \times 1 mm width \times 25 mm

length) between them. C2C12 was used in the test. For comparison, a group of cells (malnourished cells) was kept in the cryopreservation solution in the incubator for one week without medium change.

2.3. Micro-Marker for Tracings

Micro-machined patterns on the scaffold surface can be the marker to trace behaviour of each cell. The scaffold of the transparent film with micro pattern markers was designed to trace the contractile movement of myotube under the electric stimulation *in vitro*. The scaffold was made of the thin film, of which the back side had the arrangement of micro-protrusions. On PDMS film, the protrusions were made by the photolithography technique. Each protrusion had the hemisphere shape (4 μm diameter, 2 μm height). The pitch between adjacent protrusions was 0.03 mm. The thickness of the base film of PDMS was 6.4 μm . The side without protrusions was used for the scaffold of the cell culture. The protrusions played the role of the position marker. The array of protrusions was made in the square area of 3 mm \times 3 mm at the center of the film. The mold for the thin film of the scaffold with micro protrusions was made on the surface of the glass plate by the photolithography technique with the photomask photoresist of OFPR-800LB.

PDMS was mixed with the curing agent. The volume ratio of PDMS to curing agent is ten to one. After degassing, PDMS was poured on the mold, which was placed on the spin coater, to make the thin film of scaffold with the micro pattern. The PDMS ring, which was hydrophilized by the oxygen plasma ashing, was placed on the thin film of PDMS. The PDMS film with the PDMS ring was baked with the ring in the oven at 368 K for thirty minutes. After residual PDMS film outside of PDMS ring was cut off, PDMS film with PDMS ring was carefully peeled off from the mold using acetone. After rinsed by the pure water, PDMS film was sandwiched by another PDMS ring, and dried in the oven at 333 K for one hour. For the test, C2C12 was used. Myoblasts were cultured on the thin film and differentiated into myotubes.

2.4. Micro-Slit for Sorting

Micro-machining using PDMS is effective to make micro-slits. The deformability of the biological cell is related to its function. The micro-slit plays an important role to sort biological cells *in vivo*. In this section, the micro-slit is manufactured by two kinds of ways: between micro pillars, and between ridges.

2.4.1. Micro-Slit between Pillars

2.4.1.1. Slit for Erythrocytes

The micro slits with the micro width (between 2 μm and 4 μm) between micro cylindrical columns of 0.05 mm diameter were designed on the disk of transparent PDMS. The silicon wafer was used for the mold for the disk. The photoresist material of OFPR-800 was coated on the wafer with 2 μm thick at 5000 rpm for 30 s with the spin coater. The photoresist material was baked on the heated plate at 383 K for 90 s. The pattern of holes was drawn on the coated wafer with the laser drawing system. Several cylindrical holes with the diameter of 0.05 mm were arranged on the line with the small interval between 3 μm and 5 μm . The photoresist material was developed with NMD-3 for several minutes. The wafer was rinsed with the distilled water, and dried on the heated plate. To increase the adhesiveness of the coating, the wafer was baked at 383 K for 5 minutes.

The wafer was etched with the plasma gas using the reactive ion etching system to make the micro cylindrical holes. The switching mode between C_4F_8 gas and SF_6 gas was applied on the disk. The residual photoresist material was exfoliated in the separating solution. The wafer was dipped in IPA, before rinsed with the distilled water. Then, the wafer with the holes was dried on the hot plate, and used for the concave mold to make micro cylindrical columns in the following process.

The surface of the wafer with the micro pattern was coated with 1 μm thickness of parylene. PDMS was poured with the curing agent on the wafer. After degassing, PDMS was baked at 383 K for one hour in the

oven. The baked disk of PDMS was exfoliated from the mold. The dimension of the manufactured slit was observed with the scanning electron microscope.

The one-way flow system was designed to observe the behavior of cells through the micro slits *in vitro*. The system consists of the flow chamber, the micro syringe pump, tubes and the microscope. The flow chamber consists of two transparent PDMS disks and the thin sheet of silicone rubber. The thickness of the sheet is 0.1 mm. A rectangular open space of 1 mm \times 20 mm was cut off in the sheet, and sandwiched between the PDMS plates. The open space forms the flow channel of 20 mm length \times 1 mm width \times 0.1 mm depth.

The three parts stuck together with their surface affinity without adhesives. The thicknesses of the upper and the lower disks were 10 mm and 2 mm, respectively. The PDMS disk, which has micro columns on the upper surface, was placed at the inner bottom side. The upper PDMS disk had no micro pattern, and had two holes of 5 mm diameter machined by the punching tool. The silicone tubes were stuck at the holes without adhesives for the inlet and the outlet.

2.4.1.2. Slit for C2C12 and Hepa1-6

The micro slits for cells were designed between micro cylindrical pillars. The dimension of each micro cylindrical pillar was as follows: 0.025 mm diameter, and 0.06 mm height. Cylindrical pillars were arranged along the four lines by the photolithography technique. Each line was perpendicular to the flow direction of the channel. The pitch between lines was 0.5 mm. Each line had its own uniform gaps (the width of the slit) between pillars. The gaps were 0.025 mm at the first line. The gaps were 0.020 mm at the second line. The gaps were 0.015 mm at the third line. The gaps were 0.010 mm at the fourth line.

The micro slits were located at the middle part of the flow path (1 mm width, 30 mm length, and 0.06 mm height) between parallel plates (the upper plate of PDMS, and the lower plate of glass). The upper plate had two holes of 5 mm diameter for the inlet and for the outlet for the flow of the cell suspension.

The slide glass plate (38 mm length, 26 mm width, and 1.0 mm thickness) was used for the base of the photomask. The disk was dipped in the pure water and cleaned by the ultrasonic washer. After the surface of the glass plate was hydrophilized by the oxygen plasma ashing, titanium was deposited on the surface of the glass plate with 100 nm thickness in the electron beam vapor deposition apparatus. After the oxygen ashing, HMDS was coated on the titanium coated glass plate by the spin coater to improve affinity to the photoresist material. After the positive photoresist material of OFPR-800LB was coated on the surface with the spin coater, the photoresist was baked in the oven at 368 K. After the pattern for the slit was drawn on the mask with the laser drawing system, the photoresist was baked in the oven. The photoresist was developed with NMD-3 for one minute, rinsed with the distilled water, and dried by the spin-dryer. After confirmation of free of residual resists by the microscope, the titanium coated plate was etched with the plasma gas using the reactive ion etching system. For etching, the gas of SF₆ with Ar was applied at 100 W at 4 Pa for five minutes. The residual OFPR-800LB was removed by acetone. The plate was dipped in the distilled water in one minute, in ethanol for one minute, and dried by the spin-dryer.

The slide glass was used for the base of micro cylindrical pillars, after cleaning with acetone. The surface of the glass plate was hydrophilized by the oxygen plasma ashing. After the negative photoresist material of high viscosity (SU8-100) was coated on the slide glass at 3000 rpm for 30 s with the spin coater, the photoresist was baked at the hotplate at 338 K for three hours. The photoresist was exposed to the ultraviolet light through the mask in the mask aligner. The photoresist was baked at the hotplate in two processes: at 338 K for one minute, and at 368 K for ten minutes. The photoresist was developed with SU-8 Developer. The glass surface with the micro pattern was rinsed with IPA, and with pure water. The pattern was baked at the hotplate at 393 K for five minutes. At the end of the process, the micro morphology of the surface with the micro-pillars was observed by the scanning electron microscope.

PDMS was poured with the curing agent on the mold. After degassing, PDMS was baked at 333 K for one hour in the oven. The baked plate of

PDMS (3 mm thickness) was exfoliated from the slide glass plate. Another PDMS plate was cut to make the rectangular upper plate for the flow channel. Two holes with the interval of 25 mm were punched by the punching tool to make the inlet and the outlet. Adjusting the position of holes to make the flow channel, the upper plate was stuck on the lower plate with micro pattern. The rectangular parallelepiped channel was formed between plates. The two plates stuck together with their surface affinity. The flow channel was placed on the stage of the inverted phase-contrast microscope.

Two kinds of biological cells were used in the flow test alternatively: C2C12, or Hepa1-6. Before the test, the surface of the flow channel was hydrophilized by the oxygen plasma ashing. The channel was filled with the 4% bovine albumin aqueous solution, and placed in the incubator for one hour to coat stable proteins on the inner surface of the channel. The channel was washed out with the saline solution, and filled with the saline solution. The flow path was carefully examined to avoid mixing of air bubbles, which might stir the medium in the flow channel.

The suspension of cells was added into the inlet port of the flow channel. The suspension of cells was introduced to the slits by the pressure difference between the inlet and the outlet, which was kept by the gravitational level of the medium.

The cell passing through the slit was observed by the microscope, and recorded by the video camera, which is set at the eyepiece. The passing behavior of each cell through the slit was observed.

2.4.2. Micro-Slit between Weir Walls

The single micro slit was fabricated between weir-walls on the glass plate using the photolithography technique: 0.1 mm length and 0.055 mm height. Variation was made on the width of the slit: 0.010 mm, and 0.015 mm to make wider variation of the strain at the cell in the experiment.

The single micro slit was set in the flow path between parallel plates. The dimensions of the cross section of the flow channel were 2 mm width, 30 mm length, and 0.055 mm height. The upper plate had two holes of 5 mm diameter for the inlet and for the outlet of the flow of the cell

suspension. The upper plate with the micro slit was made by two kinds of molds, which were made by the following process.

The slide glass plate was used for the base of the mold (Figure 1). The polyimide tape (0.055 mm thickness, 10 mm width) was pasted at the center of the glass plate. The tape was cut by the ultra-short pulse laser to make the mold for the upper part of the flow channel with the single slit.

After the mold of the slide glass plate was enclosed with the peripheral wall of polyimide tape, PDMS was poured with the curing agent on the mold. After degassing, PDMS was baked at 368 K for 15 min in the oven. The baked plate of PDMS (4 mm thickness) was exfoliated from the mold of the slide glass plate. The PDMS plate was cut to make the rectangular upper plate for the flow channel. Two holes (diameter of 5 mm) with the interval of 25 mm were punched by the punching tool to make the inlet and the outlet. The morphology of the slit was observed by the scanning electron microscope.

The slide glass plate was used for the base of the lower plate. After PDMS was coated on the glass plate with the spin coater, it was baked in the oven at 368 K for ten minutes. The surface of the lower plate was hydrophilized by the oxygen plasma ashing.

By the surface affinity, the upper plate was stuck on the lower plate to make the flow channel. The rectangular parallelepiped channel of 30 mm length \times 2 mm width \times 0.05 mm height was formed between upper and lower plates. The two plates stuck together with their surface affinity. The flow channel was placed on the stage of the inverted phase contrast microscope.

Two types of biological cells were used in the test alternatively: C2C12, or Hepa1-6. The inner surface of the flow channel was hydrophilized by the oxygen plasma ashing, and prefilled with the bovine serum albumin aqueous solution. The flow occurred by the pressure difference between the inlet and the outlet, which was kept by the gravitational level of the medium (< 3 mm).

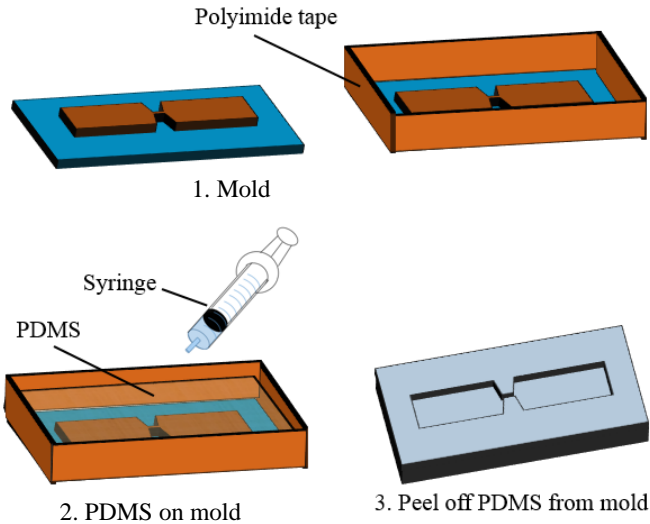


Figure 1. Machining process of upper plate with slit [1].

2.4.3. Micro-Slit between Rectangular Ridge and Plate

The slit was designed between the transparent PDMS plate and the borosilicate glass plate. The upper plate of PDMS had the rectangular ridge of 0.05 mm height, 0.10 mm (L) width, and 2 mm length. The lower plate of glass had the rectangular groove of 0.010 mm (H) depth, 2 mm width, and 20 mm length, which had the narrow part of 0.8 mm (W) width. The width had enough dimension for the cells to slip through. These plates made contact to make slits (width (W) of 0.8 mm, length (L) of 0.1 mm and height (H) of 0.010 mm) between them (Figure 2).

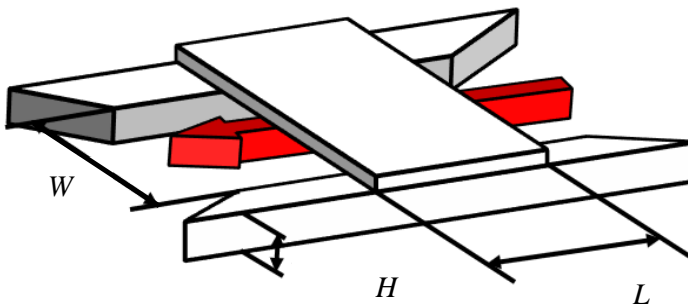


Figure 2. Micro-slit between rectangular ridge and plate [2].

The glass plate of 0.2 mm thick was used for the base of the photomask for the upper plate. Before the vapor deposition of titanium, the surface of the glass plate was hydrophilized by the oxygen plasma ashing. Titanium was coated on the surface with 150 nm thick in the electron beam vapor deposition apparatus. The positive photoresist material of OFPR-800LB was coated on the titanium at the plate with the spin coater. The photoresist was baked on the heated plate at 368 K. The pattern was drawn on the mask with the laser drawing system. The pattern was baked on the heated plate at 368 K. The photoresist was developed with NMD-3 for 5 minutes. The plate was rinsed by the ultrapure water, and dried by the spin-dryer. The titanium coating plate was etched with the plasma gas (SF_6 , Ar) using the reactive ion etching system. The residual OFPR-800LB on the surface was exfoliated by acetone.

A glass plate (38 mm \times 26 mm \times 1 mm) was used for the surface mold for the upper plate. The plate was cleaned by the ultrasonic cleaner with alkaline solution, and rinsed by the ultrapure water. The surface of the glass plate was hydrophilized by the oxygen plasma ashing. The negative photoresist material of high viscosity (SU8-10) was coated on the glass plate at 1000 rpm for 30 s with the spin coater. After the photoresist was baked on the heated plate at 338 K for two minutes, the plate was baked on the heated plate at 368 K for seven minutes. SU8-10 was coated on the plate at 1000 rpm for 30 s with the spin coater again. After the photoresist was prebaked on the heated plate at 338 K for five minutes, the plate was baked on the heated plate at 368 K for one hour. The photomask was mounted on the surface of SU8-10, and the photoresist was exposed to the ultraviolet light through the mask in the mask aligner. After the photoresist was prebaked on the heated plate at 338 K for one minute, the plate was baked on the heated plate at 368 K for five minutes. The photoresist was developed with SU-8 developer. The glass surface with the micro pattern was rinsed with IPA, and with the ultrapure water. The plate was dried by the spin-dryer. The plate was baked on the heated plate at 368 K for three minutes.

PDMS was poured together with the curing agent on the mold. After degassing, PDMS was baked at 373 K for one hour in the oven. The baked

plate of PDMS was exfoliated from the mold. Two holes of 8 mm diameter were machined with the punching tool at the upper disk to make the inlet and the outlet for the flow channel.

The glass plate of 0.2 mm thick was used for the base of the photomask for the lower plate. Before the vapor deposition of titanium, the surface of the glass plate was hydrophilized by the oxygen plasma ashing. Titanium was coated on the surface with 150 nm thick in the electron beam vapor deposition apparatus. The part of Titanium coating was covered with the polyimide tape to make the flow channel of 2 mm width (narrow part: 0.8 mm width) \times 20 mm length. The titanium coating disk was etched with the plasma gas (SF_6 , Ar) using the reactive ion etching system. After the etching, the polyimide tape was exfoliated.

A glass plate for the lower plate was cleaned by the ultrasonic cleaner with alkaline solution, and rinsed by the ultrapure water. The surface of the glass plate was hydrophilized by the oxygen plasma ashing. The negative photoresist material of high viscosity (SU8-10) was coated on the glass plate at 2000 rpm for 30 s with the spin coater. After the photoresist was baked on the heated plate at 338 K for three minutes, the plate was baked on the heated plate at 368 K for seven minutes. The photomask was mounted on the surface of SU8-10, and the photoresist was exposed to the ultraviolet light through the mask in the mask aligner. After the photoresist was prebaked on the heated plate at 338 K for one minute, the plate was baked on the heated plate at 368 K for five minutes. The photoresist was developed with SU-8 developer for three minutes. The glass surface was rinsed with IPA for two minutes, and with the ultrapure water. The plate was dried by the spin-dryer.

The upper plate of PDMS was rinsed with IPA, and with the ultrapure water. The plate was dried by the spin-dryer. The surface of the PDMS plate was hydrophilized by the oxygen plasma ashing. The plate was rinsed with aminopropyl-triethoxysilane for five minutes, and with the ultrapure water. The plate was dried in the oven at 338 K for three minutes. The upper plate of PDMS was adhered on the lower plate of SU8-10 to make the slit, and was baked on the heated plate at 338 K for five minutes.

Several kinds of cells were used in the flow test: C2C12, Hepa1-6, HUVEC, MC3T3-E1, and Neuro-2a. After the bovine serum albumin solution was prefilled in the flow channel, the suspension of the cells was poured at the inlet of the flow channel. The behavior of cells near the slit was observed with the inverted phase-contrast microscope at 298 K. The microscopic movie images of thirty frames per second at the shutter speed of 1/2000 s were recorded by the camera. At the images, the outline of each cell was traced with “Image J,” and the projected area was calculated. The deformation ratio was detected by the projected area of the cell in the slit compared with that before the slit. The velocity of the cell passing through the slit was calculated at the movie by “Kinovea.” Most of cells passed through the slit in a few seconds. The velocity ratio was calculated at each cell by the velocity in the slit compared with that before the slit.

3. RESULTS

Results of both manufactured micro-devices of PDMS and the test of each device applied to biological cells are described in each section.

3.1. Micro-Pattern for Orientation

Dimension of each type of micro-pattern manufactured on the scaffold surface was confirmed by the laser-microscopic image. Cells were cultured on the scaffold surface with each type of micro-pattern to observe the orientation of each cell.

3.1.1. *Micro-Ridgeline*

3.1.1.1. Height of Micro-Ridge for Orientation

The hydrophilic property of the scaffold surface was confirmed by the contact angle. Figure 3 shows the contact between the surface of PDMS and the medium. The figure shows that the contact angle decreases (from

θ_1 to θ_2) after the oxygen plasma ashing on the surface of PDMS. The contact angle decreases, when the surface of PDMS becomes hydrophilic.

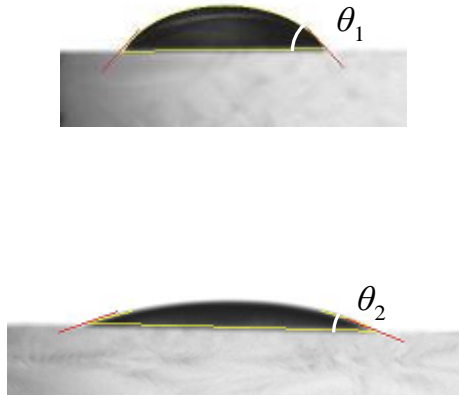


Figure 3. Contact angle of drop of medium on PDMS before (θ_1) and after (θ_2) oxygen plasma ashing [3].

Each cell stayed on the top of the ridge lower than $2.5 \mu\text{m}$, and extended the pseudopodium along the longitudinal direction of the ridge. Cells, on the other hand, fell down into the groove of the interval of $7 \mu\text{m}$ between the ridges higher than $3 \mu\text{m}$, and extended along the longitudinal direction of the groove. Near the end of the ridge, some cells extended the pseudopodium into the space between ridges.

The angle (θ) between the longitudinal axis of each cell and the longitudinal direction of the parallel micro-ridge was able to be measured through transparent PDMS by the optical microscope during the cell culture (Figure 4).

The mean value of the angle (30 cells for each height) is shown with the standard deviation in Figure 5. The mean value will be 45 degree with even distribution of angles. Most of the angles distributed in the area lower than 45 degree, which showed the tendency of the orientation of each cell along the longitudinal direction of the parallel ridge-lines. Every cell was forced to be aligned to the longitudinal direction of the groove between the ridges of the height of $3.5 \mu\text{m}$ (every angle is zero at $3.5 \mu\text{m}$ in Figure 5). The mean value was smaller than 45 degree on the parallel ridges with the

height of 0.7 μm . The major axis of the adhered cell tended to align to the longitudinal direction of the parallel lines of micro-ridges (width of 3 μm , interval of 7 μm) higher than 0.7 μm . The height of 0.7 μm was used for the minimum value for the micro-ridges to control the orientation of cells on the surface of the scaffold in the other section.

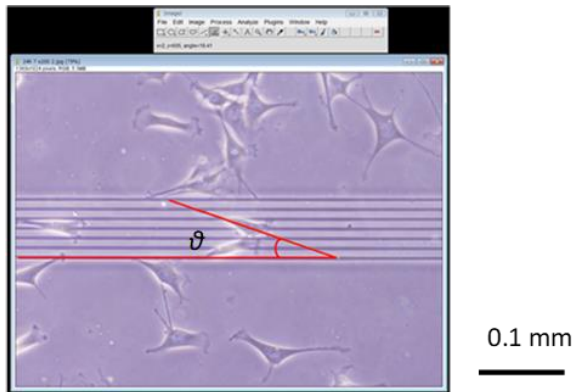


Figure 4. Angle (θ) between longitudinal axis of C2C12 and longitudinal direction of ridge [3].

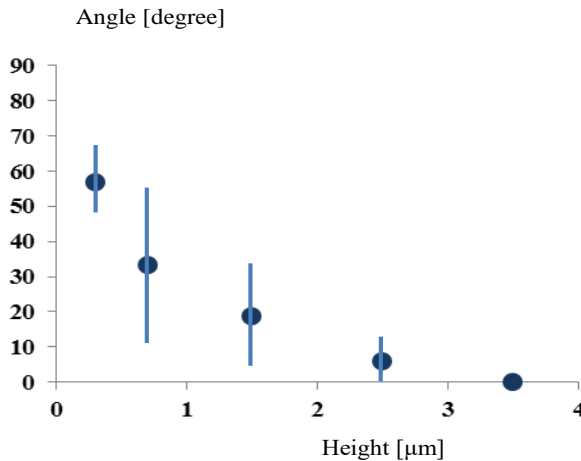


Figure 5. Mean angle (point) between longitudinal axis of C2C12 and longitudinal direction of ridge in relation to height of ridge. Each vertical bar shows standard deviation [3].

3.1.1.2. Behavior of Cell on Micro-Ridge

SEM image shows successfully manufactured regular morphology of the surface of the mold for the scaffold surface of PDMS (Figure 6). The dimensions of the micro pattern measured by the laser-microscope were as follows: 1.3 μm of the depth, 1 μm of the width. Variations made on the interval between ridges were confirmed as 3 μm , 5 μm , and 7 μm .

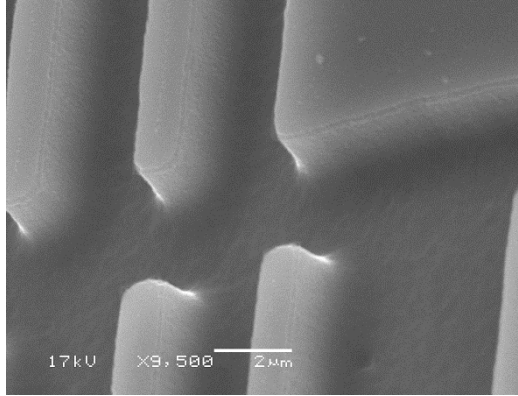


Figure 6. SEM image of lines of grooves on mold. Perspective view [4].

The tracing of the scaffold surface morphology across the lines of ridges of PDMS measured by the laser microscope showed the height of 1 μm , and width of 3 μm . The tracing also showed the variation on the interval for comparison: between 1 μm and 7 μm . Most of cells extended along the lines of ridges. Some cells of L929 bridged between ridges. The most of cells of Neuro-2a were rounded on the micro pattern, although several cells extended the neurite on the smooth surface. The most of cells of 3T3-L1 extended along the lines of ridges, although cells extended to random direction on the smooth surface. C2C12 extended at the ridges of the interval between 1 μm and 4 μm .

By the time laps images, continuous activity of each cell was easily traced through the transparent scaffold with surface-micro-ridges: migration, deformation, and proliferation. Each cell repetitively extended pseudopods. Each cell tended to tilt to the perpendicular direction to the centrifugal force after proliferation. Each cell tended to align along the

longitudinal direction of the striped pattern, which was parallel to the centrifugal force direction. The tendency was relieved in 12 hours after the centrifugal force stimulation. Each cell even tended to align along the longitudinal direction of the striped pattern, which is perpendicular to the centrifugal force direction. The tendency continued for 24 hours after the centrifugal force stimulation. Each cell was elongated to the longitudinal direction of the striped pattern by the hysteresis of the exposure to the tangential centrifugal force field more frequently at 100 G than at 50 G.

Each cell was elongated within 12 hours after adhesion to the scaffold. Each cell tended to be rounded after the centrifugal force stimulation. The number of rounded cells on the ridges decreased immediately after centrifugation. The elongation tendency was apparent, when the longitudinal direction of the micro ridge was parallel to the direction of centrifuge. Each cell extended along the striped pattern more frequently in 6 hours after the centrifugal force stimulation, although the tendency decreased in 12 hours after the centrifugal force stimulation. At proliferation, each cell tended to elongate to the direction perpendicular to the hysteretic tangential force direction.

3.1.2. Micro-Checked Pattern

The tracings of the laser microscope showed that the height of the micro pattern on the mold was 0.7 μm , which was equal to the minimum height of the ridge to control the orientation of the single cell (see 3.1.1.1.). The checkered convexo-concave pattern of micro quadrangular prisms was successfully made with the top of each square of 0.01 mm \times 0.01 mm (Figure 7). On the pattern of 0.7 μm height, observation of cells was easy without the much light scattering through the micro-pattern.

Each cell tended to extend to the direction of the neighbor prism. The tendency made orientation of cells to the diagonal direction of the quadrangular prism. The orientation can be controlled by the aspect ratio of each square in the checkered pattern. The orientation of myotubes developed after 12 days of culture.

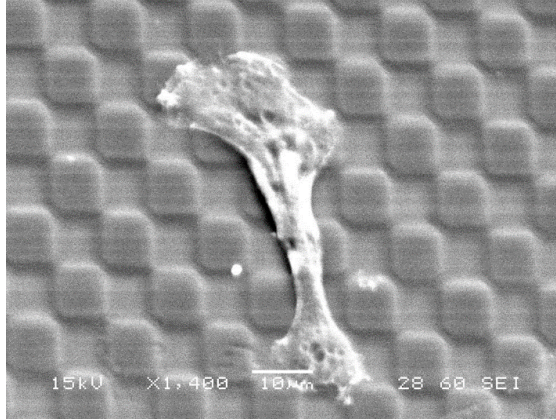


Figure 7. SEM image of surface of scaffold with checkered micro-pattern. C2C12 adheres to the pattern [5].

3.1.3. Taper-stripe pattern for durotactic migration

The taper-alternative-stripe pattern of SU-8 (wider on the left hand) or PDMS (wider on the right hand) was successfully made on the surface of the scaffold for the cell culture. The ratios of SU-8 area at left side and at right side are 48% and 32%, respectively. The tendency of the migration of cells can be analyzed by comparison between the left side and the right side.

Because of the difference of the surface hardness between PDMS and SU-8, the dimension of the taper-alternative-striped pattern on the scaffold surface was able to be sensed as the intended step (1 μm) by the surface scanning-stylus with the indentation load of 3×10^{-5} N.

C2C12 was cultivated on the micro pattern for 24 hours. The contour of each cell was traced to calculate the total area of cells on each band: SU-8 (yellow), and PDMS (dark red) (Figure 8). Migration tended to be active in the wide band of SU-8. Each cell tended to migrate to the area of SU-8 from PDMS.

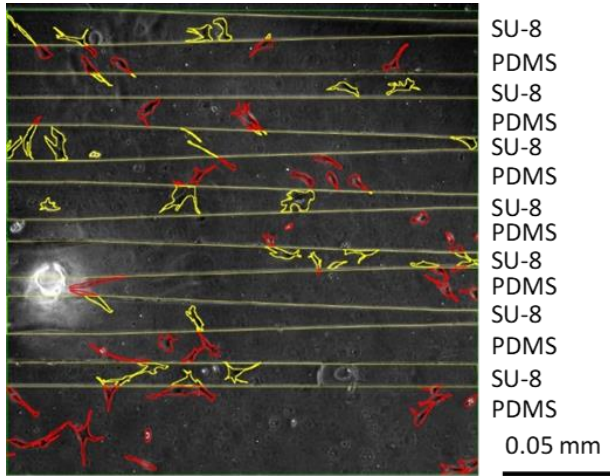


Figure 8. C2C12 cultured on micro pattern for 24 hours. Traced contour of each cell: on SU-8 (yellow), and on PDMS (dark-red) [6].

3.2. Micro-Groove for Capture

The dimension of each kind of manufactured micro-groove was confirmed by the laser microscopic image. The grooves were contained in the flow channel, and applied to capture the flowing cell.

3.2.1. Hole of Cylindrical Column

The laser measurement of surface morphology of the mold showed that the diameter ranged from 0.01 mm to 0.04 mm, same as the designed dimension. The laser measurement also showed that the mean height of micro columns on the mold was 0.01 mm.

The observed behavior of each cell was as follows (Figure 9). The diameter of each cell suspended in the medium was approximately 0.01 mm. When cells flowed at the flow rate between $3 \times 10^{-11} \text{ m}^3/\text{s}$ and $7 \times 10^{-11} \text{ m}^3/\text{s}$, every cell rolled on the bottom surface of the flow channel and was trapped in the hole. When cells flowed at the flow rate of $1.4 \times 10^{-10} \text{ m}^3/\text{s}$, some of cells were trapped in the holes. Other cells, on the other hand, passed over the holes. When cells flowed at the flow rate of $2.8 \times 10^{-10} \text{ m}^3/\text{s}$,

every cell passed over the holes on the surface of the disk. Several cells, which were captured in a hole, flowed out from the hole with the flow.

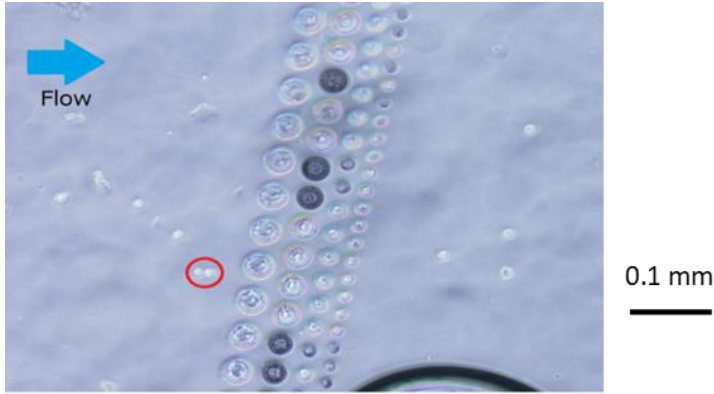


Figure 9. L929 (circle) flows over holes of cylindrical column [7].

3.2.2. Hole of Half-Cylindrical Column

The laser measurement of surface morphology of the mold showed that the diameter of half cylindrical column was 0.02 mm, same as the designed dimension. The laser measurement also showed that the mean height of micro columns was 1.5 μm .

The flow tests showed the following results. The moving cells over the holes were able to be observed with the microscope at the test system. The diameter of the suspended cell was approximately 0.01 mm. The trapped time of the cell was able to be measured compared with the movement of floating cell. In the case of C2C12, one of the cells was trapped in the hole for 5 seconds at the flow rate of $2.8 \times 10^{-10} \text{ m}^3/\text{s}$. Another cell was trapped in the hole for 8 seconds at the flow rate of $8.3 \times 10^{-10} \text{ m}^3/\text{s}$ (Figure 10). In the case of MC3T3-E1, one of the cells was trapped in the hole for one second at the flow rate of $2.8 \times 10^{-10} \text{ m}^3/\text{s}$. Every cell rolled over the hole in the flow rate at $8.3 \times 10^{-10} \text{ m}^3/\text{s}$. The time of trapped in the hole was longer with C2C12 than with MC3T3-E1.

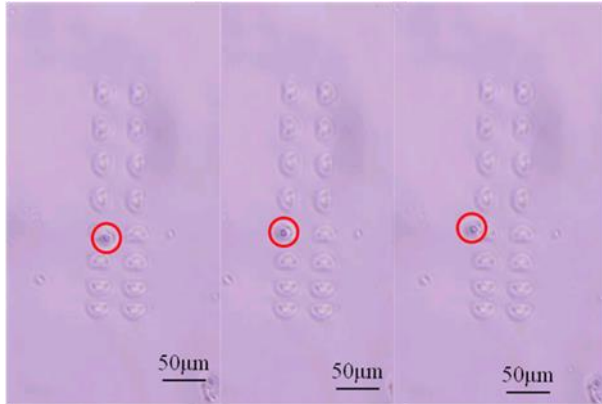


Figure 10. C2C12 (circle) enters (left), is trapped for 8 s (middle), and exits from hole (right). Flow ($8.3 \times 10^{-10} \text{ m}^3/\text{s}$) from right to left [8].

3.2.3. Groove of Quadrangular Prism

The grooves of the quadrangular prism were successfully manufactured: the depth of $2.0 \mu\text{m}$, the width of 0.025 mm , the length of 0.2 mm (Figure 11). The trapped time of the cell was able to be measured compared with the movement of floating cell in the main flow. When the air bubble was trapped in the groove, every cell moved along the boundary of the groove. Some cells moved along the fringe of the groove. C2C12 tended to be trapped in the micro groove for the longer period than 3T3-L1.

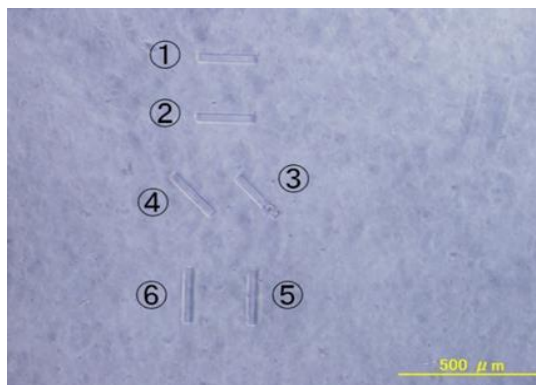


Figure 11. Manufactured three pairs of grooves: phase-contrast microscopic image [9].

3.2.4. Oblique Groove of Quadrangular Prism

The dimension of the width of each groove were confirmed at the microscopic image same as the designed value. The density of the normal C2C12 was 1.065 g/cm^3 . The density of the malnourished C2C12 was lower than 1.06 g/cm^3 . The malnourished C2C12 did not adhere to the scaffold within 30 minutes in the incubator. The diameter of each cell was in the range between $13.1 \text{ }\mu\text{m}$ and $21.7 \text{ }\mu\text{m}$. The velocity of each cell immediately before the groove was in the range between 0.038 mm/s and 0.80 mm/s according to the pressure difference between the inlet and the outlet. The velocity decreased with the time, because the pressure head at the inlet decreased with time.

The shifted distance was in the range shorter than $11.1 \text{ }\mu\text{m}$. Data of the shifted distance of C2C12 were collected in relation to the diameter (D) of each cell. The shifted distance at the groove ($0.03 \text{ mm} < \text{the width of the groove } (w) < 0.05 \text{ mm}$) scattered between $4 \text{ }\mu\text{m}$ and $12 \text{ }\mu\text{m}$, when the diameter of each cell was in the range between $12 \text{ }\mu\text{m}$ to $20 \text{ }\mu\text{m}$. The value of the shifted distance tended to increase with the width of the groove.

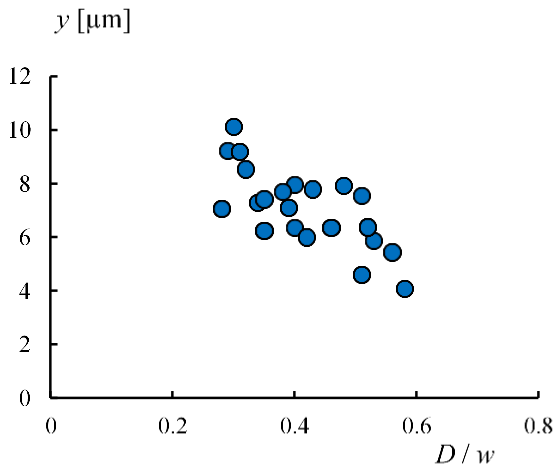


Figure 12. Shifted distance (y [μm]) vs. D/w : $0.1 \text{ mm/s} < v_x < 0.2 \text{ mm/s}$ [10].

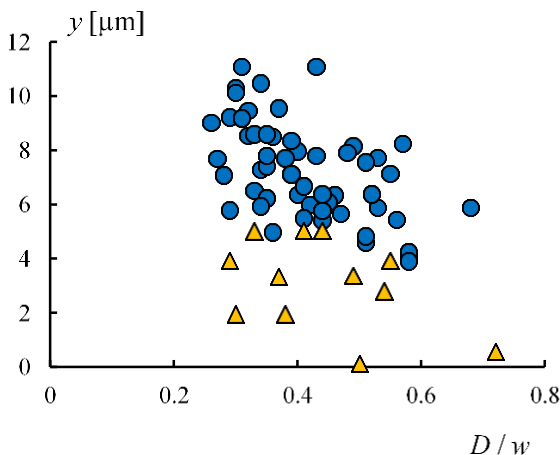


Figure 13. Shifted distance (y [μm]) vs. D/w : normal cell (circle), and malnourished cell (triangle) [10].

Figure 12 shows the shifted distance (y) in relation to D/w , when the velocity of cell (v_x) was between 0.1 mm/s and 0.2 mm/s. The ratio of D/w was unity, when the diameter of the cell (D) was equal to the width of the groove (w). The shifted distance (y) tended to decrease with the increase of the ratio of D/w . When the diameter of the cell (D) was big compared with the width of the groove (w), the travel along the groove was shortened. Data of malnourished cells were added in Figure 13. The shifted distance (y) of the malnourished cell was shorter than that of the normal cell.

3.3. Micro-Marker for Tracings

The laser microscopic image of the photomask showed that the diameter of each hole was 4 μm , and the pitch between adjacent holes was 0.03 mm. The thickness of the film (6.4 μm) of the scaffold was estimated by the measurement at the step of the mold with the stylus. The measurement by the stylus on the mold showed that the depth of the hole was 2 μm , which corresponded to the height of protrusions on the film.

The thin film with micro markers was successfully made of PDMS, and had enough transparency for observation of myotubes by the inverted

phase-contrast microscope. Figure 14 shows the scanning electron microscope image of micro protrusions array on the film. Each protrusion had the hemisphere shape, and the pitch between adjacent protrusions was 0.03 mm. The myoblasts (C2C12) were able to be cultured on the film of the scaffold to be differentiated into myotubes (Figure 15). The markers of micro protrusions on the counter side of the film were able to be observed by adjusting the focus on the microscope.

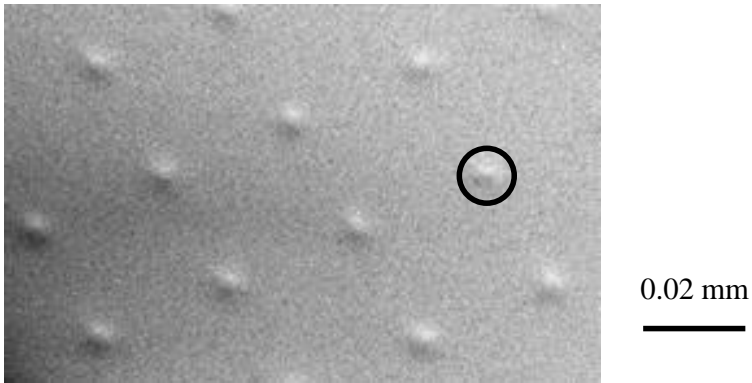


Figure 14. SEM image of micro protrusions (circle) array on PDMS film [11].

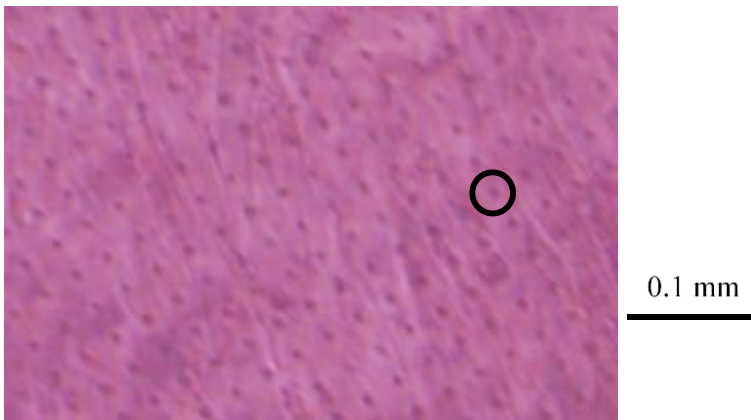


Figure 15. Myotubes on the film with markers (circle): culture day 12 [11].

When the electric pulses (amplitude of 30 V, 0.06 A) were applied between electrodes of the titanium wire dipped in the medium, the repetitive contractions of myotubes synchronous to the period of the electric pulses were able to be observed through the transparent scaffold by the microscope. The tracings of the distances between adjacent micro pattern markers on the film of the scaffold showed the local strain amplitudes of 0.01. The cyclic strain occurred both in the parallel and in the perpendicular directions to the longitudinal axis of the myotube.

3.4. Micro-Slit for Sorting

3.4.1. Micro-Slit between Pillars

The slit of 2 μm was successfully made between micro cylindrical columns of PDMS. The morphology of the slit was confirmed by the image of SEM (Figure 16). In Figure 17, the medium flows from left to right at the mean velocity of 2.8 mm/s. Every deformed erythrocyte passed through the slit.

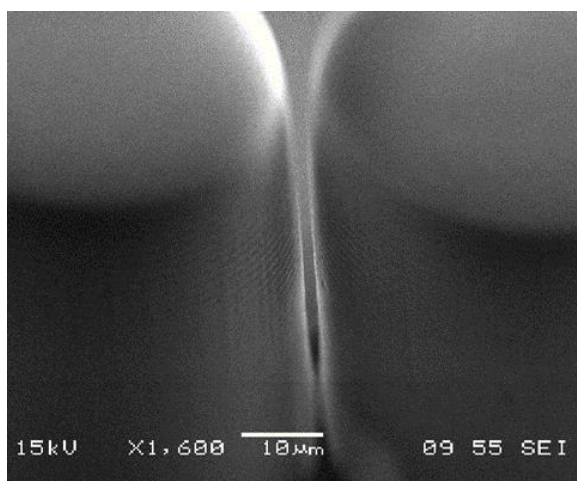


Figure 16. SEM image of micro slit between micro cylindrical columns [12].

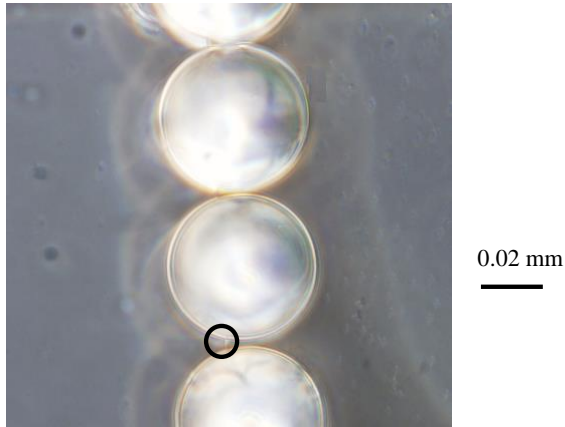


Figure 17. Erythrocyte (circle) passes through micro slits. The diameter of each column is 0.05 mm [12].

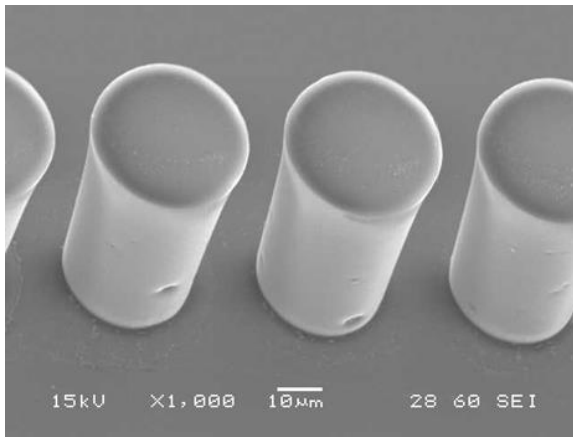


Figure 18. SEM image of micro slits between micro cylindrical columns [13].

Figure 18 shows SEM image of the micro pillars. The morphology of the gap between pillars kept rectangular slit. The micro pillars stood perpendicular to the surface of the glass slide.

Figure 19 exemplifies C2C12 passing through the slit (0.01 mm of width) between micro pillars. The cell approached to the slit, was captured between micro pillars, deformed to pass through the slit, and slipped out from the slit. Several cells were caught in the slits of 0.01 mm. Most of cells, on the other hand, passed through the slits wider than 0.015 mm. The

diameter of each cell suspended in the saline solution distributed around 0.02 mm.

The passing time of C2C12 was shorter than that of Hepa1-6. The passing time distributed wider at C2C12 than at Hepa1-6. Among the passed cells, the maximum deformation ratio was higher at C2C12 than at Hepa1-6. C2C12 took longer time to be deformed to the higher deformation ratio.

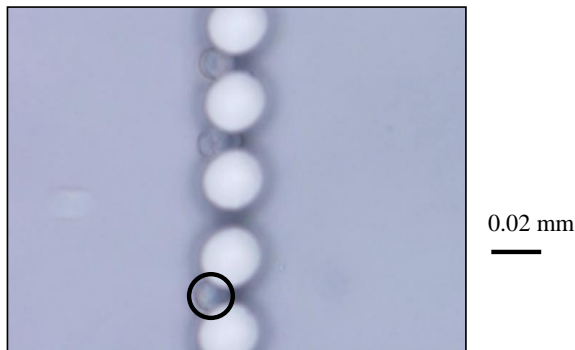


Figure 19. C2C12 (circle) passes through slit between micro cylindrical pillars: diameter of cylinder is 0.025 mm: flow from left to right [13].

3.4.2. Micro-Slit between Weir Walls

Figure 20 shows SEM image of the slit (the rectangular groove) between weir-walls. The top opening side of the groove was covered by the counter plate to make the slit. Figure 21 exemplifies the microscopic image of C2C12 passing through the slit. The cell approached to the slit, entered in the slit, moved through the slit, and moved away from the slit.

Hepa1-6 did not pass through the slit of 0.010 mm width. Some myoblasts passed through the slit of 0.010 mm width with the higher deformation ratio at the higher flow rate. At the higher flow rate, C2C12 passed through the slit with the higher deformation ratio. At the wider slit of 0.015 mm width, on the other hand, even the cell of the bigger diameter passed through the slit at the lower flow rate. Neuro-2a tended to adhere to the wall of the flow channel. The movement of Neuro-2a passing through the slit was difficult to be observed.

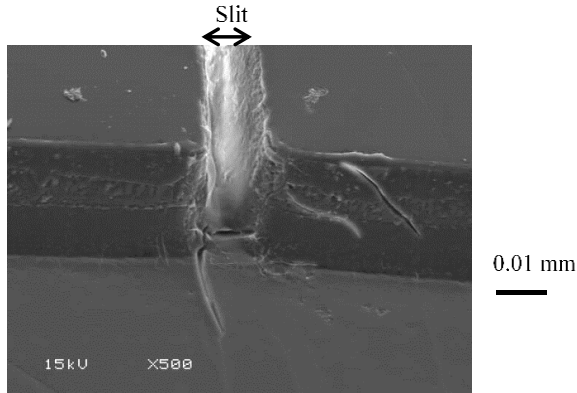


Figure 20. SEM image of slit [1].

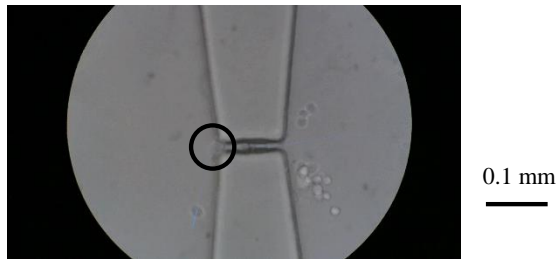


Figure 21. Hepa1-6 (circle) passing through slit: flow from left to right [14].

3.4.3. *Micro-Slit between Rectangular Ridge and Plate*

Figure 22 shows the dimension of the manufactured ridge of the upper part measured by the laser microscope. The mean value of the height was $55\ \mu\text{m}$. The mean value of thickness of the sheet of silicone rubber was $57\ \mu\text{m}$. Figure 23 exemplifies the swine erythrocyte passing through the slit. The cell flowed from left to right. The velocity of the cell moving through the slit was not accelerated compared with the decrease of cross section of the flow path, because of the friction between the deformed cell and the wall of the slit. C2C12 was not able to pass through the same slit.

The tracing across the ridge on the upper disk of PDMS measured by the laser microscope showed that the height of the ridge was $61\ \mu\text{m}$, which made the height of the flow channel. The tracings across the ridge on the lower disk measured by the laser microscope showed that the height of the

ridge was 11 μm , which made the height of the slit. Figure 24 shows the micro slit between ridges observed by the inverted phase-contrast microscope.

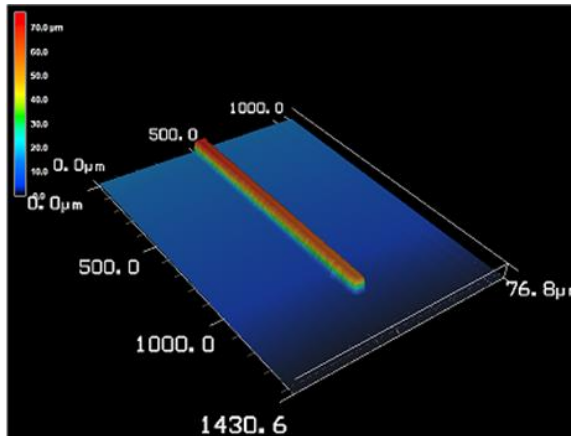


Figure 22. Laser microscopic image of the rectangular ridge [μm] [15].

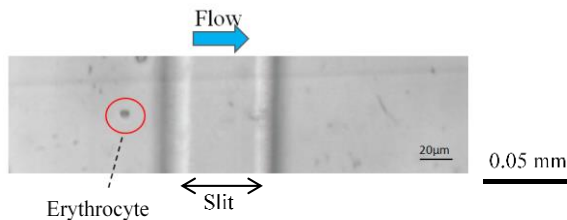


Figure 23. Erythrocyte approaches to slit (length: 50 μm). Flow from left to right [15].

The velocity in the slit was low with Neuro-2a. Some cells of C2C12 passed the slit at the higher velocity with the small deformation ratio. The deformation ratio tended to increase with the increase of the velocity of the cell (HUVEC, Hepa1-6). HUVEC elongated to the direction of flow during the movement through the slit. Erythrocyte and Hepa1-6, on the other hand, were deformed into the flat circular disk during the movement through the slit (Figure 25).

The tracing across the ridge on the lower disk measured by the stylus profiler showed that the height of the ridge was 10 μm , which made the

height of the slit. Some cells of C2C12 got caught at the inlet of the slit. Others passed through the slit.

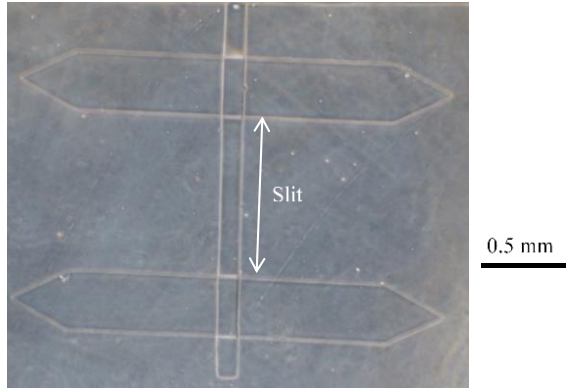


Figure 24. Micro slit (width: 0.8 mm) between ridges [16].



Figure 25. Cell (circle) passing through slit (length: 0.1 mm): flow from left to right [17].

The bigger cell made the larger projected area in the slit with the higher deformation ratio. The ratio of the cross-sectional area between the flow channel (0.064 mm height \times 2 mm width) and the slit (0.01 mm height \times 0.8 mm width) was 16. The ratio was confirmed by the mean velocity ratio of the erythrocyte, which flowed through the slit.

At the most of cells of Hepa1-6, the velocity of the cell in the slit was much lower than that before the slit. At C2C12, the velocity of the cell in

the slit was lower than that before the slit in the case of the higher velocity before the slit. At MC3T3-E1, on the other hand, the velocity of the cell in the slit was sometimes higher than that before the slit.

As the deformation ratio increased, the velocity ratio decreased. The tendency was remarkable at MC3T3-E1. Every velocity ratio of each cell was lower than three.

4. DISCUSSION

Biological cells adhere on the matrix of collagen *in vivo*. In the previous studies, the scaffold of cells was designed to simulate the biological matrix: fibers, or networks. A lot of chemical treatments have been tried on the scaffold to control the behavior of cells.

In this chapter, the micromachined PDMS is applied to the surface of the scaffold with the micro-morphology of quantitatively controlled dimension. This kind of methods has advantage to analyze the physical properties of the biological cells.

4.1. Micro-Pattern for Orientation

Control methodology (the acceleration technique) for orientation, proliferation and differentiation of cells would be applied to the regenerative tissue technology. The electrical stimulation affected cells [18]. The shear flow governs the orientation of endothelial cells [19]. The mechanical stress exfoliates several cells, which makes vacancy around the adhered cell. The mechanical stimulation can decrease proliferation of cells. The mechanical stress, on the other hand, can accelerate differentiation of C2C12 into myotubes. The differentiation can be optimization of cells to the changing environment. Cells are responsive to the micro morphology of the scaffold.

4.1.1. Micro-Ridgeline

The biological cell is sensitive to the property of the surface of the scaffold. The hydrophilic property of the scaffold can be confirmed by the small contact angle. The micro pattern was designed to control the orientation of cell in the tissue *in vitro* [20]. The adhesion of cell was controlled with hydrophilic-hydrophobic micro-domains of polymer [21]. The tissue was designed to control interaction between cell and polymer *in vitro* [22]. Control methodology for orientation and proliferation of myoblasts has a potential to be applied to a bio-actuator [23].

To make orientation of cells in the cultured tissue, several morphologies were applied to the cell culture: a micro capillary, and a sub-millimeter groove. In these experiments, the cells orient along the wall, and cells are forced to be aligned to the longitudinal direction of the space sandwiched between walls.

In the previous studies, cells were cultured on various morphological pattern of scaffold. In the conventional preparation, the morphology of the scaffold surface was controlled with the dimension of sub-millimeter. In this chapter, the dimension of sub-micrometer at the morphology of the scaffold surface has been controlled by the photolithography technique.

The biological cells, on the other hand, can sense micro morphology of the surface smaller than their own dimension through their cytoskeleton or membrane [24]. The effect of the curvature of grooves of micro-meter order on the behavior of cell was studied in the previous study [25]. Morphology of nanometer order of the surface can affect behavior of cells [26].

In the most of previous studies, there were two ways to design the micro-structure of scaffold for cell culture: nanometer-structure with molecular-structure, and sub-millimeter-structure with surface machining. Between these two dimensions, micrometer-structure can be controlled on the surface of PDMS with the photolithography technique. In this chapter, the effect of micrometer order of morphology on the orientation of cells has been highlighted.

The experimental results show that each cell moves and extends along the ridge. Although the single ridge is not enough to make orientation of

cells, multiple ridges affect orientation of cells. The experimental results with C2C12 show that cells adhere on the top of the ridge and align in the longitudinal direction of the micro ridges with the height between 1.5 μm and 2.5 μm . The ridge, which is lower than 0.3 μm , is not enough to make orientation of the cell. The ridge, which is higher than 3 μm , is too high for the cell to stay on the top of the ridge. Between the higher ridges, the cells fall down into the valley between ridges, and extend along the valley. Near the higher single ridge, the cells tend to align along to the wall of the ridge.

The surface morphology of micrometer level affects cells behavior. The differentiation of cells can be accelerated with micro ridges. The alignment of cells affects that of neighbor cells. A cell tends to rotate to make the parallel alignment to the neighbor cell. A cell can change the alignment through proliferation. The alignment of the single cell governs orientation of cells in the tissue.

To study about the effect of surface micro morphology of the solid scaffold on the alignment of the cell, the alignment of the longitudinal direction of the cell was measured after adhesion of the cell *in vitro*. If cells proliferate to the confluent state, interaction between cells is dominant. In that case, each environmental effect on orientation of cells cannot be distinguished each other. Sparsely seeding of cells is preferable for the study about each effect on the individual single cell.

In the differentiation of C2C12, cells fuse and make myotubes. The alignment of cells governs the alignment of the myotube. In the case of the solid surface of the scaffold, the micro grooves can give a space for the flow of the medium between the cell and the scaffold. That can make better condition to grow the tissue. The behavior of the cell on the lines of ridges depends on the cell types: extended, or got rounded.

The gravity in the fluid is reduced by the buoyancy [27]. Measurement of the density of cells by the phthalate ester method showed that the density of cells was between $1.06 \times 10^3 \text{ kg/m}^3$ and $1.07 \times 10^3 \text{ kg/m}^3$. When the cells floating in the medium of the density of $1.00 \times 10^3 \text{ kg/m}^3$, the effective centrifugal force ratio calculated from the difference of two density is 6.5 G at centrifuge of 100 G.

Each cell deforms and migrates randomly on the uniform scaffold. The behavior of the cell depends on the direction of the hyper-gravitational field. Each cell changes its own direction during migration. The migration depends on the morphology of the scaffold surface. When a cell cannot keep adhesion under stimulation, the cell deforms to be a sphere. When the cell rounds, the contact between the cell and the scaffold decreases. The cell easily exfoliates from the scaffold at the small contact area. After the cell rounds at proliferation, alignment of cells along the longitudinal direction of the striped pattern is relieved. The typical cell cycle of proliferation is 24 hours. The elongated cell, on the other hand, tends to align along the longitudinal direction of the striped pattern of ridges on the scaffold surface.

The cell on the striped pattern not parallel to the centrifugal force stimulation hardly makes contact to the scaffold surface at 100 G by centrifugation. The hysteresis of centrifugation affects each cell to increase the contact area with the surface of the scaffold. Each cell tends to align along the pattern on the scaffold surface at the higher tangential force field than at the lower tangential force field. Cells tend to migrate to the direction to keep away from the area of the stripes perpendicular to the centrifugal force direction. Cells passively follow the direction in the strong tangential force field: migration, and deformation. Immediately after the centrifugation, cell can start to show active responses to the mechanical stimulation. The mild tangential force field induces the active reflection of myoblasts to tilt perpendicularly to decrease internal force of the cells. The cell shows adaptation against stimulation.

The stimulation leaves hysteresis in the cell. The hyper-gravitational stimulation affects the behavior of the cell after stimulation. The number of cells, which do not align to the longitudinal direction of ridges, tends to decrease by hysteresis of the hyper-gravitational stimulation. The tendency of the C2C12 to align along the longitudinal direction of ridges is enhanced on the ridge perpendicular to the direction of the excess gravity by the centrifuge.

A microstriped pattern can be used to orient a single cell on the scaffold prior to stimulation. The average diameter of the floating cell in

the medium is 20 μm . A cell can migrate over the ridge of the height of 0.7 μm . The micro striped pattern on the scaffold can also be the position marker to trace the behavior of each cell.

To apply continuous uniform mechanical stimulation to the cells, the centrifugal force field is useful [28]. The response of biological system to the microgravity field was studied using the space satellite [29]. The muscle tissue decreases in the micro gravitational field [30]. In the hypergravitational field, on the other hand, the differentiation of C2C12 can be accelerated. The myotube can align to the direction perpendicular to the centrifugal field [31]. The muscle tissue can increase in the hypergravity [32]. The hyper-gravitational field thickens the myotubes *in vitro*.

4.1.2. Micro-Checked Pattern

Each myoblast makes orientation along the longitudinal direction of the rectangular top surface of the micro quadrangular prisms (Figure 26). C2C12 migrates and extends along the longitudinal axis of the ridges. These action depends on the alignment of the neighbor prism. The micro checked pattern can control the orientation of cells. The orientation of the single cell can accelerate subsequent orientation of cells in the tissue. Myotube tends to make orientation following the neighbor myotube [33].

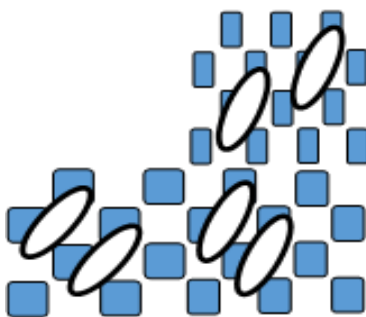


Figure 26. Orientation of cell on checked pattern [34].

4.1.3. Taper-Striped Pattern for Durotactic Migration

The cell can sense the rigidity of the scaffold surface. The taper-striped pattern with variation of mechanical property can be successfully

manufactured on the scaffold surface with the aid of the photolithography technique. The introduction of another material of the liquid phase by the capillary effect into the groove space, which is sandwiched between surfaces of the base and the cap, is effective technique to make variations of mechanical property according to the surface micro pattern.

Because few cells show orientation at the border between bands, the height of the step between bands was confirmed lower than 1 μm . The gap of the step between bands was small enough for the random migration of each cell. The value, which the stylus shows, was related to the difference of compliance (rigidity) of the surface between two bands. The tracing showed that the compliance of the band of PDMS is higher than that of SU-8 [35].

Cells were seeded at the low density on the scaffold to trace the response of sparsely populated single cell. In the confluent state, interaction between cells governs the behavior of cells.

4.2. Micro-Groove for Capture

Several kinds of systems were designed for the cell sorting *in vitro*. There are several methods to sort biological cells. The microfluidic system was applied to sort cells [36], and to trap biological cells. Non-invasive way is preferable to sort cells with minimum damage. Non-destructive cell sorting systems were also designed in several studies [37]. The flow cytometry is one of the technologies, which is used for cell sorting. Cells suspended in the fluid are analyzed by the laser.

Fluorescence technique was used in the sorting systems [38]. The fluorescently labelled components in the cell are analyzed by the light emission. The label-free methods were designed with microfluidic systems [39, 40]. Some of them were designed to capture cancer cells: using the microfluidic system [41], and using the micropatterns [42]. The system also was used to study on the local environment around the cultured cell. The photolithography technique was applied to fabricate the microfluidic channel. The morphology of micro channel simulated the lymph system in

the circulatory system *in vivo*. In several studies, permeability of the membrane was controlled related to designing artificial vessels.

The micro-pattern of the surface has been applied to study the surface effect of adhesion of cells [43]. The property of the surface governs the affinity between the surface and the cell. Because of the change of the property of the outer surface of the membrane of the cell, the damaged cell will show different behavior on the micro groove. The experimental results will contribute to analyze adhesive mechanism of cancer cell during metastasis. The micro trap can simulate the adhesive mechanism of flowing cells. The sorting technique can be applied to selection of cells for regenerative medicine and diagnostics of disease.

In 2.2.1., the depth of the micro holes was 0.01 mm of the cylindrical hole. In 2.2.2., the depth of the micro holes was 2 μm , which was smaller than diameter of the cell. The deeper hole has advantage to catch the cell. The shallow trap, on the other hand, has an advantage to distinguish cells. The duration of the trapped time of the cell is related to several factors: adhesiveness between the cell and the surface of the micro pattern, deformability of the cell, and specific gravity. The asymmetrical hole can be more suitable for the trap of the cell than the symmetrical hole.

The movement of cell travelling on the wall was modified by the oblique micro groove on the bottom wall under the cell velocity lower than 1 mm/s. The angle of 45 degrees between the longitudinal direction of the groove and the flow direction was effective to shift the streamline of the cell. The shift movement along the oblique groove depends on the several parameters: the diameter of cells, the width of the groove, the velocity of the cell, and the cell types. As the diameter of the cell decreases, the traveling length along the groove increases. The movement can be related not only to the diameter but also to the deformability of the cell.

The movement of flowing cell at the bottom surface of the flow channel relates to the specific gravity of the cell: the density ratio between the cell and the medium. The shifted distance of malnourished cells by the oblique groove was smaller than that of normal cells.

The cell density in the suspension is very low in this section to reduce the interaction between the cells. Cells can be sorted by the traveling length along the micro groove.

4.3. Micro-Marker for Tracings

The contraction of the specimen of muscle tissue was measured by laser preparation [44]. The local movement should be observed to analyze the force of contraction at the single myotube.

In another study, cells were cultured on the micro pillars to measure the contraction movement by the deformation of the micro pillar [45]. The deformability of the micro pillar depends on its height. The micromorphology of the surface of the scaffold, however, affects the behavior of myoblast [46]. To separate the effect of micromorphology on the myoblast from the contraction of the myotube, the micro-protrusions were used as the markers on the counter side of the scaffold in this section.

The photolithography technique can be applied to control compliance of the surface [47]. Several studies showed that the harder scaffold accelerated differentiation of cells. The sheet lined with micro-protrusions array has distribution about local micro compliance at the counter side of the scaffold. The myoblast made the orientation on the scaffold sheet at any direction regardless of the position of the micro-protrusions on the counter side of the sheet.

To minimize the optical scattering through the transparent scaffold sheet, the height of the micro-protrusions is lowered. The film of the scaffold should deform synchronously with the myotube to detect the contraction force of the myotube. The surface of the scaffold was hydrogenized by oxygen ashing. The surface of the thin film of the scaffold had enough affinity to the myotube to keep adhesion during contraction of the myotube. Interaction between cell and PDMS was examined according to the property: hydrophobic, and hydrophilic [48]. The behavior (adhesion and motility) of cell on PDMS was investigated [49]. The thickness of the PDMS film of the scaffold was made as thin as

possible [50] to have enough compliance to follow the contraction with the small force of myotubes [51].

The contractile force of myotube at the electric stimulation estimated by the movement of the markers of the film is 1 mN, calculated by the following parameters: the elastic modulus of 2 MPa [45], the strain of 0.01, and the cross-sectional area of 0.06 mm². The movement of myotube can be measured along the longitudinal direction of the myotube using the arrangement of micro markers.

4.4. Micro-Slit for Sorting

The effects of flow on cells were investigated in many studies. An erythrocyte has flexibility and deforms in the shear flow. It also passes through micro-circulation, of which the dimension is smaller than the diameter of the erythrocyte. An erythrocyte deforms as the shear stress increases. The deformability of erythrocyte can be described by the mechanical parameters: the maximum deformation, and the specific stress [52]. The deformability of erythrocyte changes with aging. The sublethal damage can be detected by the abnormal deformation: cyclic deformation in the shear field [53]. The fatigue of erythrocytes can be evaluated by mechanical parameters: the shear stress, and the exposure time multiplied by the shear rate [54]. It was also evaluated by the behavior of cells through the narrow path.

After the circulation through the blood vessels for days, the erythrocyte is trapped in the micro-circulation systems *in vivo*. The erythrocyte, on the other hand, passes through the micro slit narrower than 1 μm in the spleen. The fine architecture of the red pulp of the spleen was investigated [55]. The continuity between capillaries and splenic sinuses was examined with the microscope. The special morphology relates to the function for sorting erythrocytes. In many studies, the typical diameter of the micro cylindrical channel, which simulates the capillary blood vessel, is around 5 μm .

Preparation of the slit with the controlled dimension of sub-micrometer is not easy. Deformability can be measured during passing through the

narrow slit. The micro-slit is also useful for diagnostics on the biological cell. The low Reynolds number can be realized at the microfluidic systems, which has an advantage to analyze the mechanical property of cells in the flow quantitatively. Reynolds number (Re) is calculated by Equation 1.

$$Re = \rho v w / \eta \quad (1)$$

In Equation 1, ρ is density of the fluid, v is the mean flow velocity, w is the width of the flow channel, and η is the viscosity of the fluid (the medium). Re is 1, when ρ , v , w , and η are 10^3 kg m^{-3} , $1 \times 10^{-3} \text{ m/s}$, $2 \times 10^{-3} \text{ m}$, and $2 \times 10^{-3} \text{ Pa s}$, respectively. The turbulent flow may not occur in the flow of small value of Reynolds number.

The velocity profile between the parallel walls can be approximated to parabolic, when the distance between two parallel walls is small compared with the width of the channel. The shear rate (γ , [s^{-1}]) on the wall of the disk is calculated by Equation 2.

$$\gamma = 6 q / (b D^2) \quad (2)$$

In Equation 2, q is the flow rate [$\text{m}^3 \text{ s}^{-1}$], b is the width of the canal [m] and D is distance [m] between two parallel walls. The wall shear rate γ is 16 s^{-1} , when D , b , q , are 0.1 mm , 1 mm , and $0.3 \times 10^{-10} \text{ m}^3/\text{s}$, respectively.

4.4.1. Micro-Slit between Pillars

For the reason of the photolithography process, the edge of the ridge was not sharp, but it had the edge with the small width at the top. The biological system, on the other hand, might have the sharper edge ($1 \mu\text{m}$). A cell passes easily through the slit with the shorter travel distance ($1 \mu\text{m}$) *in vivo*. The cell has to struggle to pass through the slit in the experimental device with the longer travel distance (Figure 2: L).

A cell makes three-dimensional deformation. The combination of two ways of observation is effective to trace the three-dimensional deformation: the slit between pillars, and the slit between ridges. The

rectangular shape of slit smaller than 0.01 mm height (Figure 2: *H*) was successfully manufactured with the micromachining technique.

The shorter passing time of C2C12 at the smaller deformation ratio indicated that the frictional resistance with the surface of the wall might be smaller at C2C12 than Hepa1-6. The capture of the cell at the slit depends on several factors: the dimension of the slit, the dimension of the cell, the deformation of the cell, the wall shear stress (the shear rate) at the slit, and the affinity of the cell to the wall of the slit. Related to the affinity, the following procedure was effective to make the property of the inner surface of the flow-channel stable. The channel was pre-filled with the 4% bovine serum albumin aqueous solution, and placed in the incubator for one hour.

The adhesion of the cell to the inner surface of the channel in the flow depends on the morphology of the wall and on the wall shear stress. The vacancy of the cell arrangement on the tissue wall of flow path can cause the capture of cells. The capture also depends on the property of the cell. The mechanism of adhesion was applied to sorting of cells [56]. The experimental results can contribute to analyze adhesive mechanism of cancer cell during metastasis. The micro trap can simulate adhesive mechanism of flowing cells.

4.4.2. Micro-Slit between Weir Walls

In parallel multiple slits system, the driving force of the cell passing through each slit changes with the clogging at some of the slit. In the parallel slits system, the media flow velocity cannot be controlled at each slit separately. The single slit has an advantage to trace the media flow simply at the slit. The single slit preparation of sub-micrometer is not easy. The slit of the narrow width (0.010 mm, and 0.015 mm) was machined by micromachining techniques: the ultra-short pulse laser, and photolithography. The results of the dimension by the machining was acceptable for the slit to observe the movement of each cell. The higher flow rate was necessary for the bigger cell (the bigger diameter with the higher strain) to pass through the slit. The deformation of the harder part of the cell was necessary to pass through the narrower slit.

The resistance of the flow channel with the narrow slit is very high. The resistance of the flow channel increases, when the cells clogged the slits. Internal pressure of the flow channel should be carefully controlled, otherwise leakage or cavitation would occur. The flow control by the difference of the pressure head is easier than by the syringe pump. The flow path is carefully examined to avoid mixing of air bubbles, which stirs the medium in the flow channel. The small pressure difference (0.03 Pa) between the inlet and the outlet of the flow channel was maintained by the difference of the level of the fluid between the inlet and the outlet.

The diameter (5 mm) of the inlet port was much larger than cross sectional area of the slit to keep the level of the inlet port in the longer period. The flow rate can be confirmed by the flow speed of the cell during the microscopic observation. The surface was not completely flat at the wall of the slit, which might increase frictional resistance. The micro-roughness at the wall of the slit might affect the movement of each cell passing through.

4.4.3. Micro-Slit between Rectangular Ridge and Plate

The lower ridge had the curvature of 0.01 mm at the tip of the side wall, which can reduce turbulence of the flow in the channel. The height of the slit (Figure 2: H) was successfully maintained everywhere over the width (Figure 2: W) of the slit despite of the elasticity of PDMS. The machined micro ridge had enough hardness to maintain dimension of the slit.

The height of the slit was confirmed by the change of the diameter of the deformed cell during slipping through the slit. The height of the slit was selected as the dimension slightly smaller than the diameter of the cell (C2C12, Hepa1-6, and HUVEC). The dimension of the width of the slit was selected 0.87 mm, which was wide enough for the deformed cell to slip through.

At the coupling, adjusting the position of micro ridges precisely each other between the counter plates is not easy. At the parallel position, the slit cannot be made, when the position shifts even with the very short

distance each other. To adjust easily the position of each micro ridge at the counter wall, the tops of the ridges are set perpendicularly each other.

The deformability of the cell is related to the density of intra-cellular contents. While the cell passed through the slit, the cell kept the circle shape at the two-dimensional projected image. HUVEC elongates along the streamline on the blood vessel wall *in vivo*. Endothelial cells cover the inner surface of the vessel wall, and are exposed to the blood flow every time *in vivo*. HUVEC has the high sensitivity to the flow direction. HUVEC may have the inner structure to elongate to the direction of the flow. Both C2C12 and Hepa1-6, on the other hand, might have the inner structure to keep the circular disk under the flow. Hepa1-6 may have high passive deformability to the moving velocity.

The biological cells are sorted according to the shape, and deformability *in vivo*. Several cells pass through the micro slit. Some fragments, which pass through the slit, are decomposed. Some cells, which cannot pass through the narrow channel, are captured.

The most of biological cells kept the spherical shape, when they are flowing in the medium. The micro slit was designed with the narrower dimension (Figure 2: *H*) than that in the study with capillaries to observe the deformation of cells. In this section, the deformation was evaluated with the ratio of the two-dimensional projected area of the cell during the slit-passing. Some cells of HUVEC passed through the slit at the higher velocity with the small deformation ratio. Several bigger cells of Hepa1-6 passed through the slit at the higher velocity with the large deformation ratio.

The velocity of each cell was lower than that of the media due to the friction between the cell and the wall of the slit. The cell of the larger diameter is forced to be deformed at the higher deformation ratio in the slit. The higher deformation ratio makes the larger projected area in the slit. The higher deformation ratio can increase the frictional resistance at the slit.

CONCLUSION

Several kinds of devices (micro-ridges, micro-grooves, micro-markers, and micro-slits) for the observation of the behaviour of biological cells were successfully manufactured with PDMS by micro-machining: photolithography, and etching. Surface morphology and compliance of PDMS can be controlled by the micro-machining process. The property of the surface of PDMS can be controlled by the additional processes: the oxygen plasma ashing, and the dipping in the protein aqueous solution. The effectiveness of each kind of device was evaluated by experiments with several types of biological cells.

Dimension of the surface morphology was checked using the biological cells, which has the 20 μm diameter suspended in the medium. To make orientation of cells on the scaffold, the minimum height of the microridge is one thirtieth of the cell size. The micro-pattern can be applied to trace the hysteresis effect of the mechanical force field on the orientation of each type of cell. The micro-pattern with the dimension smaller than cell size is effective to make orientation of each cell to make a tissue. The shifted distance of each cell along the oblique shallow groove in flow channel depends on the ratio of the cell diameter per the width of the groove. The malnourished cell can be distinguished by the shifted distances in the flow. The contraction movement of the myotube can be traced by the micro-protrusions marker on the backside of the thin film scaffold of 6 μm thick (PDMS). The micro slit with the dimension smaller than cell size can detect deformation characteristics of each type of cell. PDMS can be applied to make the microstructure of the functional surface for observation of the biological cell. The technology will contribute to several applications in the field of the biomedical engineering: medical diagnostics, and regenerative medicine.

ACKNOWLEDGMENTS

The author thanks to Dr. Haruka Hino, Dr. Yusuke Takahashi, Mr. Fumihiko Sato, Mr. Atsushi Mizoi, Mr. Hiromi Sugimoto, Mr. Kenta Sugimoto, Mr. Takuya Tamura, Mr. Kenta Noda, Mr. Hiroaki Nakajima, Mr. Tsutomu Horie, Mr. Shuhei Shimegi, Mr. Kenichi Kitagawa, Mr. Reona Nomoto, Mr. Shoma Nishino, Mr. Tatsuki Azuma, Mr. Nariaki Noguchi, Mr. Takeshi Yamaguchi, Mr. Yusuke Nakano, Mr. Keisuke Kakishima, Mr. Yuki Takiguchi, Mr. Akira Hayasaka, Mr. Yuji Endo, and Mr. Daiki Watanabe for their assistance of the experiments.

REFERENCES

- [1] Hashimoto, S., Takahashi, Y., Nakano, Y., Hasegawa, D., Takiguchi, Y. and Yasuda, T. (2018). Observation of cell passing through single micro slit between weir-walls. *Proc. 22nd World Multi-Conference on Systemics Cybernetics and Informatics*, 2: 120–125.
- [2] Hashimoto, S., Kakishima, K. and Takahashi, Y. (2019). Cell deformation passing through slit between micro-machined surfaces in vitro: comparison among cell types. *Proc. 23rd World Multi-Conference on Systemics Cybernetics and Informatics*, 4: 100–105.
- [3] Hino, H., Hashimoto, S. and Sato, F. (2014). Effect of micro ridges on orientation of cultured cell. *Journal of Systemics Cybernetics and Informatics*, 12 (3): 47–53.
- [4] Hino, H., Hashimoto, S., Nishino, S., Nakajima, H., Takahashi, Y. and Sugimoto, H. (2015). Behavior of cell on vibrating micro ridges. *Journal of Systemics Cybernetics and Informatics*, 13 (3): 9–16.
- [5] Sugimoto, K., Takahashi, Y., Hashimoto, S. and Hino, H. (2017). Effect of aspect ratio of checkered convexo-concave micro-pattern on orientation of cultured single cell. *Proc. 21st World Multi-Conference on Systemics Cybernetics and Informatics*, 2: 221–226.
- [6] Hashimoto, S., Sugimoto, K. and Takahashi, Y. (2018). Design of scaffold with taper-striped pattern to observe durotactic migration of

- cell. *Proc. 22nd World Multi-Conference on Systemics Cybernetics and Informatics*, 2: 96–101.
- [7] Hashimoto, S., Nomoto, R., Shimegi, S., Sato, F., Yasuda, T. and Fujie, H. (2013). Micro trap for flowing cell. *Proc. 17th World Multi-Conference on Systemics Cybernetics and Informatics*, 1: 1–6.
- [8] Hashimoto, S., Takahashi, Y., Hino, H., Nomoto, R. and Yasuda, T. (2014). Micro hole for trapping flowing cell. *Proc. 18th World Multi-Conference on Systemics Cybernetics and Informatics*, 2: 114–119.
- [9] Takahashi, Y., Hashimoto, S., Hino, H., Mizoi, A. and Noguchi, N. (2015). Micro groove for trapping of flowing cell. *Journal of Systemics Cybernetics and Informatics*, 13 (3): 1–8.
- [10] Hashimoto, S., Hayasaka, A. and Endo, Y. (2019). Sorting of cells with flow channel: movement of flowing myoblast cell at oblique micro grooves. *Proc. 23rd World Multi-Conference on Systemics Cybernetics and Informatics*, 4: 82–87.
- [11] Takahashi, Y., Hashimoto, S., Sugimoto, K., Watanabe, D. and Hino, H. (2017). Measurement of contractile force of myotube on scaffold of thin film with micro-pattern-markers. *Journal of Systemics Cybernetics and Informatics*, 15(4): 1–8.
- [12] Hashimoto, S., Horie, T., Sato, F., Yasuda, T. and Fujie, H. (2013). Behavior of cells through micro slit. *Proc. 17th World Multi-Conference on Systemics Cybernetics and Informatics*, 1: 7–12.
- [13] Takahashi, Y., Hashimoto, S., Hino, H. and Sugimoto, H. (2017). Measurement of deformability of cell by slits between micro cylindrical pillars. *Proc. 21st World Multi-Conference on Systemics Cybernetics and Informatics*, 2: 245–250.
- [14] Takahashi, Y., Hashimoto, S., Mizoi, A., Hino, H., Yamaguchi, T. and Yasuda, T. (2017). Measurement of deformability of biological cell passing through single micro slit between walls. *Proc. 21st World Multi-Conference on Systemics Cybernetics and Informatics*, 2: 233–238.
- [15] Hashimoto, S., Mizoi, A., Hino, H., Noda, K., Kitagawa, K. and Yasuda, T. (2014). Behavior of cell passing through micro slit. *Proc.*

- 18th World Multi-Conference on Systemics Cybernetics and Informatics*, 2: 126–131.
- [16] Takahashi, Y., Hashimoto, S., Mizoi, A. and Hino, H. (2017). Deformation of cell passing through micro slit between micro ridges fabricated by photolithography technique. *Journal of Systemics Cybernetics and Informatics*, 15 (3): 1–9.
- [17] Hashimoto, S., Takahashi, Y., Kakishima, K. and Takiguchi, Y. (2018). Slit between micro machined plates for observation of passing cell: deformation and velocity. *Proc. 22nd World Multi-Conference on Systemics Cybernetics and Informatics*, 2: 102–107.
- [18] Au, H. T. H., Cheng, I., Chowdhury, M. F. and Radisic, M. (2007). Interactive effects of surface topography and pulsatile electrical field stimulation on orientation and elongation of fibroblasts and cardiomyocytes. *Biomaterials*, 28(29): 4277–4293.
- [19] Levesque, M. J. and Nerem, R. M. (1985). The elongation and orientation of cultured endothelial cells in response to shear stress. *Journal of Biomechanical Engineering*, 107(4): 341–347.
- [20] Sun, J. G., Tang, J. and Ding, J. D. (2009). Cell orientation on a stripe-micropatterned surface. *Chinese Science Bulletin*, 54(18): 3154–3159.
- [21] Okano, T., Nishiyama, S., Shinohara, I., Akaike, T., Sakurai, Y., Kataoka, K. and Tsuruta, T. (1981). Effect of hydrophilic and hydrophobic microdomains on mode of interaction between block polymer and blood platelets. *Journal of Biomedical Materials Research*, 15(3): 393–402.
- [22] Shimizu, T., Yamato, M., Kikuchi, A. and Okano, T. (2003). Cell sheet engineering for myocardial tissue reconstruction. *Biomaterials*, 24(13): 2309–2316.
- [23] Akiyama, Y., Terada, R., Hashimoto, M., Hoshino, T., Furukawa, Y. and Morishima, K. (2010). Rod-shaped tissue engineered skeletal muscle with artificial anchors to utilize as a bio-actuator. *Journal of Biomechanical Science and Engineering*, 5(3): 236–244.
- [24] Davidson, P., Bigerelle, M., Bounichane, B., Giazson, M. and Anselme, K. (2010). Definition of a simple statistical parameter for

- the quantification of orientation in two dimensions: application to cells on grooves of nanometric depths. *Acta Biomaterialia*, 6, 2590–2598.
- [25] Mathur, A., Moore, S. W., Sheetz, M. P. and Hone, J. (2012). The role of feature curvature in contact guidance. *Acta Biomaterialia*, 8: 2595–2601.
- [26] Lu, J., Rao, M. P., MacDonald, N. C., Khang, D. and Webster, T. J. (2008). Improved endothelial cell adhesion and proliferation on patterned titanium surfaces with rationally designed, micrometer to nanometer features. *Acta Biomaterialia*, 4: 192–201.
- [27] Endo, Y., Hashimoto, S. and Tamura, T. (2019). Alignment and deformation of MC3T3-E1 cultured on micro striped pattern after stimulation of tangential force field. *Proc. 23rd World Multi-Conference on Systemics Cybernetics and Informatics*, 4: 76–81.
- [28] Ciofani, G., Ricotti, L., Rigosa, J., Mencias, A., Mattoli, V. and Monici, M. (2012). Hypergravity effects on myoblast proliferation and differentiation. *Journal of Bioscience and Bioengineering*, 113(2): 258–261.
- [29] Hughes-Fulford, M. and Lewis, L. M. (1996). Effect of microgravity on osteoblast growth activation. *Experimental Cell Research*, 224(1): 103–109.
- [30] Lalani, R., BhaSIn, S., Byhower, F., Tarnuzzer, R., Grant, M., Shen, R., Asa, S., Ezzat, S. and Gonzalez-Cadavid, F. N. (2000). Myostatin and insulin-like growth factor-I and -II expression in the muscle of rats exposed to the microgravity environment of the neuro lab space shuttle flight. *Journal of Endocrinology*, 167(3): 417–428.
- [31] Hashimoto, S. and Okada, M. (2011). Orientation of cells cultured in vortex flow with swinging plate in vitro. *Journal of Systemics Cybernetics and Informatics*, 9(3): 1–7.
- [32] Tschopp, A. and Cogoli, A. (1983). Hypergravity promotes cell proliferation. *Experientia*, 39(12): 1323–1329.
- [33] Lam, M. T., Sim, S., Zhu, X. and Takayama, S. (2006). The effect of continuous wavy micropatterns on silicone substrates on the

- alignment of skeletal muscle myoblasts and myotubes. *Biomaterials*, 27(24): 4340–4347.
- [34] Sugimoto, K., Takahashi, Y., Hino, H. and Hashimoto, S. (2016). Effect of aspect ratio of checkered (Ichimatsu) convexo-concave micro-pattern on orientation of cultured cells. *Proc. 20th World Multi-Conference on Systemics Cybernetics and Informatics*, 2: 141–146.
- [35] Yu, H., Balogun, O., Li, B., Murray, T. W. and Zhang, X. (2004). Building embedded microchannels using a single layered SU-8, and determining Young's modulus using a laser acoustic technique. *Journal of Micromechanics and Microengineering*, 14(11): 1576–1584.
- [36] Fu, A. Y., Spence, C., Scherer, A., Arnold, F. H. and Quake, S. R. (1999). A microfabricated fluorescence-activated cell sorter. *Nature Biotechnology*, 17; 1109–1111.
- [37] Takahashi, K., Hattori, A., Suzuki, I., Ichiki, T. and Yasuda, K. (2004). Non-destructive on-chip cell sorting system with real-time microscopic image processing. *Journal of Nanobiotechnology*, 2(5): 2004, pp. 1–8.
- [38] Mayer, G., Ahmed, M. S. L., Dolf, A., Endl, E., Knolle, P. A. and Famulok, M. (2010). Fluorescence-activated cell sorting for aptamer SELEX with cell mixtures. *Nature Protocols*, 5(12): 1993–2004.
- [39] Gossett, D. R., Weaver, W. M., Mach, A. J., Hur, S. C., Tse, H. T. K., Lee, W., Amini, H. and DiCarlo, D. (2010). Label-free cell separation and sorting in microfluidic systems. *Analytical and Bioanalytical Chemistry*, 397: 3249–3267.
- [40] Carey, T. R., Cotner, K. L., Li, B. and Sohn, L. L. (2019). Developments in label-free microfluidic methods for single-cell analysis and sorting. *WIREs Nanomedicine and Nanobiotechnology*, 11(e1529): 1–17.
- [41] Liu, Z., Huang, F., Du, J., Shu, W., Feng, H., Xu, X. and Y. Chen, Y. (2013). Rapid isolation of cancer cells using microfluidic deterministic lateral displacement structure. *Biomicrofluidics*, 7(011801): 1–10.

- [42] Ou, Y. C., Hsu, C. W., Yang, L. J., Han, H. C., Liu, Y. W. and Chen, C. Y. (2008). Attachment of tumor cells to the micropatterns of glutaraldehyde (GA)-crosslinked gelatin. *Sensors and Materials*, 20(8): 435–446.
- [43] Raghavan, S., Desai, R. A., Kwon, Y., Mrksich, M. and Chen, C. S. (2010). Micropatterned dynamically adhesive substrates for cell migration. *Langmuir*, 26: 17733–17738.
- [44] Hashimoto, S., Takase, J., et al., (2008). Measurement of mechatronic property of biological gel with micro-vibrating electrode at ultrasonic frequency. *Journal of Systemics Cybernetics and Informatics*, 6(5): 93–98.
- [45] Ghassemi, S., Meacci, G., Liu, S., Gondarenko, A. A., Mathur, A., Roca-Cusachs, P., Sheetz, M. P. and Hone, J. (2012). Cells test substrate rigidity by local contractions on submicrometer pillars. *Proceedings of the National Academy of Sciences of the United States of America*, 109(14): 5328–5333.
- [46] Kaji, H., Ishibashi, T., Nagamine, K., Kanzaki, M. and Nishizawa, M. (2010). Electrically induced contraction of C2C12 myotubes cultured on a porous membrane-based substrate with muscle tissue-like stiffness. *Biomaterials*, 31(27): 6981–6986.
- [47] Liu, M., Sun, J., Sun, Y., Bock, C. and Chen, Q. (2009). Thickness-dependent mechanical properties of polydimethylsiloxane membranes. *Journal of Micromechanics and Microengineering*, 19(3): 1–4.
- [48] Nakazawa, K., Izumi, Y. and Mori, R. (2009). Morphological and functional studies of rat hepatocytes on a hydrophobic or hydrophilic polydimethylsiloxane surface. *Acta Biomaterialia*, 5(2): 613–620.
- [49] Fuard, D., Tzvetkova-Chevolleau, T., Decossas, S., Tracqui, P. and Schiavone, P. (2008). Optimization of poly-di-methyl-siloxane (PDMS) substrates for studying cellular adhesion and motility. *Microelectronic Engineering*, 85(5-6): 1289–1293.
- [50] Thangawng, A. L., Ruoff, R. S., Swartz, M. A. and Glucksberg, M. R. (2007). An ultra-thin PDMS membrane as a bio/micro-nano

- interface: fabrication and characterization. *Biomedical Microdevices*, 9(4): 587–595.
- [51] Engler, A. J., Griffin, M. A., Sen, S., Bönnemann, C. G., Sweeney, H. L. and Discher, D. E. (2004). Myotubes differentiate optimally on substrates with tissue-like stiffness: pathological implications for soft or stiff microenvironments. *The Journal of Cell Biology*, 166(6): 877–887.
- [52] Hashimoto, S., Otani, H. and Imamura, H., et al., (2005). Effect of aging on deformability of erythrocytes in shear flow. *Journal of Systemics Cybernetics and Informatics*, 3(1): 90–93.
- [53] Hashimoto, S. (2014). Detect of sublethal damage with cyclic deformation of erythrocyte in shear flow. *Journal of Systemics Cybernetics and Informatics*, 12(3): 41–46.
- [54] Hashimoto, S. (1989). Erythrocyte destruction under periodically fluctuating shear rate; comparative study with constant shear rate. *Artificial Organs*, 13: 458–463.
- [55] Steiniger, B., Bette, M. and Schwarzbach, H. (2011). The open microcirculation in human spleens: a three-dimensional approach. *Journal of Histochemistry Cytochemistry*, 59(6): 639–648.
- [56] King, M. R., Western, L. T., Rana, K. and Liesveld, J. L. (2009). Biomolecular surfaces for the capture and reprogramming of circulating tumor cells. *Journal of Bionic Engineering*, 6(4): 311–317.

BIOGRAPHICAL SKETCH

Shigehiro Hashimoto

Affiliation: Dean, Faculty of Engineering, Kogakuin University, Tokyo, Japan.

Education: Bachelor of Engineering in Mechanical Physics (1979), and Master of Engineering at Tokyo Institute of Technology (1981), Tokyo, Doctor of Medicine at Kitasato University (1987), Sagamihara, and Doctor of Engineering at Tokyo Institute of Technology (1990), Tokyo.

Research and Professional Experience: Research Associate in School of Medicine (1981-1989), and Assistant Professor in School of Medicine (1989 -1994), at Kitasato University.

Associate Professor in the Department of Electronics (1994-2001), and Professor at Osaka Institute of Technology (2001-2011). Creator of the first Department of Biomedical Engineering in Japan at Osaka Institute of Technology (2005), Director of Medical Engineering Research Center (2005-2011).

Professor at Kogakuin University (2011-), Associate to President and Dean of Admissions Center at Kogakuin University, Tokyo (2012-2018), Dean, Faculty of Engineering, Kogakuin University, Tokyo, Japan (2018-).

Professional Appointments:

- The Society of Life Support Engineering (Director),
- Japanese Society for Artificial Organs (Councilor).

Honors:

- International Association of Advanced Materials Award (2019),
- William G. Lesso Memorial Award (International Institute of Informatics and Systemics, 2016)

Publications from the Last 3 Years:

- 1) Shigehiro Hashimoto, Hiromi Sugimoto, Haruka Hino, Effect of Couette Type of Shear Stress Field with Axial Shear Slope on Deformation and Migration of Cell: Comparison Between C2C12

- and HUVEC, *Journal of Systemics Cybernetics and Informatics*, Vol. 17(2), pp. 4-10, 2019.
- 2) Shigehiro Hashimoto, Cross Cultural Seminar Inspires Multidisciplinary Learning: From Biomedical Engineering to Gerontechnology, *Journal of Systemics Cybernetics and Informatics*, Vol. 16(4), pp. 1-7, 2018.
 - 3) Yusuke Takahashi, Shigehiro Hashimoto, Manabu Watanabe, Daisuke Hasegawa, Dielectrophoretic Movement of Cell around Surface Electrodes in Flow Channel, *Journal of Systemics Cybernetics and Informatics*, Vol. 16(3), pp. 81-87, 2018.
 - 4) Shigehiro Hashimoto, Hiromi Sugimoto, Haruka Hino, Behavior of Cell in Uniform Shear Flow Field between Rotating Cone and Stationary Plate, *Journal of Systemics Cybernetics and Informatics*, Vol. 16(2), pp.1-7, 2018.
 - 5) Shigehiro Hashimoto, Multidisciplinary Learning Extends Communication Skill, and Helps Cross Cultural Understandings: Biomedical Engineering, *Journal of Systemics Cybernetics and Informatics*, Vol. 15(6), pp.106-112, 2017.
 - 6) Haruka Hino, Shigehiro Hashimoto, Yusuke Shinozaki, Hiromi Sugimoto, Yusuke Takahashi, Effect of Flow on Cultured Cell at Micro-pattern of Ridge Lines, *Journal of Systemics Cybernetics and Informatics*, Vol. 15(5), pp.1-7, 2017.
 - 7) Yusuke Takahashi, Shigehiro Hashimoto, Kenta Sugimoto, Daiki Watanabe, Haruka Hino, Measurement of Contractile Force of Myotube on Scaffold of Thin Film with Micro-pattern-markers by Electric Stimulation, *Journal of Systemics Cybernetics and Informatics*, Vol. 15(4), pp.1-8, 2017.
 - 8) Yusuke Takahashi, Shigehiro Hashimoto, Atsushi Mizoi, Haruka Hino, Deformation of Cell Passing through Micro Slit between Micro Ridges Fabricated by Photolithography Technique, *Journal of Systemics Cybernetics and Informatics*, Vol. 15(3), pp.1-9, 2017.
 - 9) Haruka Hino, Shigehiro Hashimoto, et al., Electric Measurement of Cultured Myoblast Oriented on Scaffold with Micro-pattern,

Proc. 21st World Multi-Conference on Systemics Cybernetics and Informatics, Vol. 2, pp. 209-214, 2017.

- 10) Takuya Tamura, Haruka Hino, Shigehiro Hashimoto, Hiromi Sugimoto, Yusuke Takahashi, Cell Behavior After Stimulation of Excess Gravity, *Proc. 21st World Multi-Conference on Systemics Cybernetics and Informatics*, Vol. 2, pp. 263-268, 2017.
- 11) Yusuke Takahashi, Kenta Sugimoto, Shigehiro Hashimoto, Haruka Hino, Effect of Mechanical Property of Scaffold Surface with Micro Hybrid Striped Pattern on Cell Migration, *Proc. 21st World Multi-Conference on Systemics Cybernetics and Informatics*, Vol. 2, pp. 227-232, 2017.

Chapter 3

**PDMS IN URINARY TRACT DEVICES:
APPLICATIONS, PROBLEMS
AND POTENTIAL SOLUTIONS**

***M. Gomes, L. C. Gomes, R. Teixeira-Santos
and F. J. Mergulhão****

LEPABE - Laboratory for Process Engineering, Environment,
Biotechnology and Energy, Faculty of Engineering, University of Porto,
Rua Dr. Roberto Frias, Portugal

ABSTRACT

PDMS is one of the most widely used polymers for the fabrication of biomedical devices. Of particular relevance is the application of PDMS in urinary tract devices such as urinary catheters and ureteral stents. As these devices are being used by a growing number of patients and indwelling times are increasing in an aging population, the incidence of urinary tract infections is rising. These infections have implications on the quality of life of the patients and represent a severe burden on healthcare systems.

* Corresponding Author's E-mail: filipem@fe.up.pt.

This chapter reviews the main uses of PDMS in urinary tract devices and associated complications. As new solutions are needed to reduce bacterial adhesion and biofilm formation on PDMS-based devices, a testing platform is described to evaluate surface performance in both urinary catheters and ureteral stents. Examples of these solutions are also discussed in a quest for more efficient urinary tract devices.

Keywords: PDMS-based surfaces, urinary catheters, ureteral stents, urinary tract infections, antibiofilm coatings, flow systems

ABBREVIATIONS

| | |
|-------|---|
| 3D | three-dimensional |
| AgNP | silver nanoparticles |
| AMP | antimicrobial peptide |
| CAUTI | catheter-associated urinary tract infection |
| CFD | computational fluid dynamics |
| CFU | colony forming unit |
| CLSM | confocal laser scanning microscopy |
| DAPI | 4'-6-diamidino-2-phenylindole |
| ECDC | European Centre for Disease Prevention and Control |
| EPS | extracellular polymeric substance |
| FDA | Food and Drug Administration |
| GA | gallic acid |
| HAI | healthcare-associated infection |
| IAR | initial adhesion rate |
| L-AmB | liposomal amphotericin B |
| MRD | modified Robbins device |
| MRSA | methicillin-resistant <i>Staphylococcus aureus</i> |
| PC | phosphoryl-choline |
| PCA | plate count agar |
| PDA | polydopamine |
| PEG | polyethylene glycol |

| | |
|--------|--|
| PLC(P) | polycaprolactone polymer |
| PPFC | parallel plate flow chamber |
| PTFE | polytetrafluoroethylene |
| SD | standard deviation |
| SMZ | sulfamethoxazole |
| TANP | tetraetherlipid-silver nanoparticle-norfloracin-poly lactide |
| TMP | trimethoprim |
| UTD | urinary tract device |
| UTI | urinary tract infection |
| UV | ultraviolet |
| VRE | vancomycin-resistant enterococci |

1. INTRODUCTION

Since the 1960s, silicone materials have been extensively applied in the medical field due to their high biocompatibility [1, 2]. Polydimethylsiloxane (PDMS) is one of the most used class of commercially available silicone polymers [3, 4]. This polymer is non-toxic, biological and chemically inert, optically clear, elastomeric, gas-permeable, hydrophobic, mechanically resistant, and inexpensive [4, 5]. Moreover, the risk of PDMS biodegradation and migration appears to be inexistent [6]. Therefore, the high biocompatibility and stability of PDMS contributed to its success in several medical applications, including the development of urinary tract devices (UTDs) [4, 7].

The several benefits of silicone compared to other available biomaterials have made it the material of choice for the construction of urinary tract devices [8]. However, despite of its outstanding properties, silicone is prone to bacterial adhesion and biofilm formation [9, 10]. The complications associated with the use of indwelling urinary catheters and ureteral stents have driven the technological evolution in the surface coatings. Up to date, numerous studies have described different coating

strategies changing the PDMS physicochemical properties or conferring it antimicrobial potential.

In this chapter, the PDMS-based surfaces developed to prevent urinary tract infections (UTIs) will be reviewed. Additionally, different flow systems available for surface evaluation will be discussed and their importance will be evidenced with an experimental approach to study bacterial adhesion and biofilm formation under hydrodynamic conditions that mimic those found in urinary catheters and ureteral stents.

2. PDMS IN URINARY TRACT DEVICES

Urinary tract devices, including urinary catheters and ureteral stents, are some of the most widely used medical devices in hospitals and healthcare facilities. The first urinary devices were constructed using metallic materials such as copper, tin, bronze and gold [9]. However, in the last decades, metals were replaced by polyvinylchloride, polyurethanes, silicone and latex rubbers in order to reduce their rigidity [8-10]. Over the years, polymeric materials have been improved towards higher biocompatibility, tensile strength, softness and elasticity, and biological and chemical resistance [9, 11, 12]. Table 1 lists the advantages and disadvantages of different biomaterials used in the manufacture of UTDs.

Silicone presents several advantages compared to other polymeric materials. Due to the nontoxic and inert nature of silicone, this polymer displays higher tissue compatibility than latex or polyvinylchloride. Simultaneously, it is non-irritating and non-sensitizing, having low surface tension and moderate resistance to abrasion and external compression. Conversely to latex, silicone is UV and chemical resistant and is more thermally stable than polyurethane. However, although this biomaterial reveals desirable properties for a urinary device, silicone has a low drainage efficacy. In terms of encrustation, there is a reduced incidence of struvite and calcium phosphate hydroxyapatite stones, whereas encrustation by calcium carbonate and calcium oxalate stones is more frequent. Moreover, similarly to latex and polyurethane, silicone is prone

to bacterial adhesion [8-10]. Despite having some disadvantages, silicone has become the “gold standard” material for urinary devices [9-12].

**Table 1. Biomaterials used for urinary tract devices:
Advantages and disadvantages**

| Material | Advantages | Disadvantages |
|--------------------|--|--|
| Silicone | Biocompatible Non-irritating and non-sensitizing Chemically and thermally stable UV resistant Low surface tension Moderate resistance to abrasion Improves surface lubrication Long lifetime before encrustation and blockage Highly resistant to external compression Decreased struvite and calcium phosphate stones incidence Inexpensive | Can be uncomfortable due to its rigidity Prone to premature device failure Prone to bacterial adhesion Decreased drainage efficacy Prone to encrustation by calcium carbonate and calcium oxalate stones |
| Latex | Can be modified by hydrogel or Teflon coatings Inexpensive Easily manipulated High tensile strength | Poor biocompatibility Poor UV and chemical resistance Poor tissue adherence Can promote biofilm formation and encrustation Causes allergic reactions |
| Polyurethane | Excellent biocompatibility Soft and smooth Resistant to external forces | Sensitivity to heat Cannot be autoclaved Prone to bacterial adhesion Prone to encrustation by calcium carbonate and calcium oxalate stones |
| Polyvinyl-chloride | Long lifetime Chemically stable Inexpensive | Reduced flexibility Public health concerns due to additives that can leach <i>in vivo</i> |

Compiled using data from [8-11].

Based on these evidences, several authors have studied the efficacy of PDMS urinary catheters on the prevention of catheter-associated infections. Moola and Konno conducted a systematic review about the management of indwelling urethral catheters to prevent UTIs where uncoated silicone catheters were compared with other types of catheters

[13]. According to this study, there were no differences between PDMS and latex urethral catheters. However, the use of PDMS catheters was associated with an overall infection rate of 2.1% at 24 h, 6.8% at 48 h, and 20% at 96 h [13]. Stenzenlius et al. reported similar results for PDMS urinary catheters (an incidence of bacteriuria of 5.5%) after a mean period of 2 days of catheterization [14]. Additionally, Thibon and co-workers demonstrated that silicone Foley catheters had a cumulative bacteriuria incidence of 11.9% [15]. Lastly, Moola and Konno also registered an incidence of bacteriuria and funguria per 1000 catheter days of 38.6% for silicon catheters [13].

Regarding PDMS ureteral stents, there are few data demonstrating their efficacy. According to Hoe, although silicone stents are tolerated by patients and associated with low complication rates, 28% of inserted stents failed [16]. Conversely, a study carried out by Tunney et al. demonstrated that silicone has a higher resistance to encrustation compared to other materials [17].

Thus, the complications associated with silicone urinary tract devices warn of the need to develop new PDMS-based surfaces to avoid bacterial colonization and encrustation.

3. PROBLEMS ASSOCIATED TO URINARY TRACT DEVICES

Urinary tract devices have been widely applied in the treatment and mitigation of some diseases, improving the quality of life of the patients. However, despite all care and preventive measures taken to avoid contamination during the insertion of these devices, UTIs are increasingly common.

UTIs are one of the most common healthcare-associated infections (HAIs), being responsible for about 17% of hospital-acquired bacteremia [18]. In fact, the HAI annual incidence reports pointed to a prevalence of 36% and 27% of hospital-wide UTIs in the United States and Europe, respectively [19, 20]. Furthermore, the same authors found that UTIs were responsible for a mortality rate of 2.3% [20]. In 2017, the European Centre

for Disease Prevention and Control (ECDC) also noticed a UTI emergence of 2% among the patients hosted in intensive care units for more than two days; 98% of these UTI episodes were associated with the use of a urinary catheter [21].

Urinary catheters are considered the most common indwelling devices. Currently, in the United States, over 30 million urinary catheters are inserted per year [22]. Previous studies carried out in several European and US hospitals reported about 15-25% of patients experiencing catheterization during their hospital permanence. The emergence of catheter-associated urinary tract infections (CAUTIs) is increasingly common, representing approximately 75% of hospital-acquired or nosocomial UTIs [23, 24]. Moreover, when compared to other 20 types of medical devices, catheters revealed an infection incidence of 33% [22]. The likelihood of developing CAUTIs increases with the duration of catheterization. Studies described that the incidence of CAUTIs among patients undergoing non-Foley or short-term urinary catheterization (< 7 days) was 10-50%, increasing to 90-100% in long-term catheterization (> 28 days) [25, 26].

Ureteral stents are also commonly used devices in modern urology practice. Like catheters, stents are very prone to contamination and colonization by different pathogens. Actually, 31% of the patients with ureteral stents develop UTIs [27], and 45–100% of patients have bacteriuria [28]. As with any biomedical device, exposure time is a risk factor for bacterial/fungal colonization. In fact, a previous research found that the incidence of stent colonization and bacteriuria increases from 69% in patients with temporary stents to 100% in patients carrying chronic indwelling stents [29].

Besides these alarming numbers, there is also an increasing cost associated with UTIs. In the United States, the problems related to UTIs have an estimated cost of \$1.6 - \$3.5 billion each year [30]. Regarding CAUTI, the annual treatment costs are over \$350 million [31] and £1–2.5 billion [32] in the United States and the United Kingdom, respectively. In relation to stent-associated UTI, the total economic costs are approximately \$15 per patient per day [33].

The successful treatment of catheter and stent-associated UTIs requires the background knowledge of the pathogens involved in the infection. Different microorganisms have been responsible for the colonization of UTDs. Some of the most commonly observed are *Escherichia coli*, *Staphylococcus aureus*, *Pseudomonas aeruginosa*, *Proteus* spp., *Klebsiella pneumoniae*, *Staphylococcus epidermidis*, *Enterococcus* spp., and *Candida* spp. [9, 34, 35]. These microorganisms commonly attach to indwelling medical devices, forming biofilms. These are complex three-dimensional (3D) structures composed by sessile microbial communities surrounded by a matrix of self-produced extracellular polymeric substances (EPS), including proteins, polysaccharides, nucleic acids, and molecules involved in cell-cell communication [36, 37].

Biofilm formation is, along with encrustation, the main reason why device-associated infections are considered so recalcitrant. Although they are two distinct phenomena generated by different factors, they can overlap and, consequently, worsen the infection. The development of new surface materials/techniques to overcome these infections requires the full comprehension of both phenomena.

Biofilm growth is governed by a number of physical, chemical and biological processes, and begins with the reversibly microbial adhesion to a conditioned surface either by physical forces or bacterial appendages (pili or flagella) [38]. Physical forces associated with this weak bacterial adhesion include van der Waals forces, as well as hydrophobic, steric and electrostatic interactions [39]. The rate of cell adhesion depends not only on the type and number of free-swimming cells, but also on the physicochemical characteristics of the material used in the implanted device, the fluid behaviour, and other environmental factors, such as temperature and pH [40]. When bacterial appendages overcome the physical repulsive forces [41], an irreversible attachment between bacterial surface structures and substratum occurs and microorganisms start to communicate with each other via quorum sensing by the production of autoinducer signals. In a maturation stage, a significant growth of the biofilm population occurs, with an increase of biofilm thickness up to 200

μm [42]. The final stage of biofilm development includes the detachment of bacteria, which may then colonize new areas [38].

Ureteral stents and urinary catheters are usually colonized both on extraluminal and intraluminal sides. While in an initial phase, biofilms are composed of single-species populations, in a further stage, multispecies communities are commonly detected. Overall, the chronicity of the infections associated with implanted biomedical devices is attributed to the growing resistance of the pathogens to antimicrobial agents, which is strongly related to the slow penetration of drugs within the EPS matrix, as well as the presence of persister cells that stay in a transitory dormant state and induce recurrent infections [43, 44]. The increasing antimicrobial resistance has limited the strategies to prevent and control UTIs.

Encrustation, on the other hand, results from the colonization of indwelling devices by urease-positive pathogens. Despite being mainly caused by *Proteus mirabilis* [45], other species can be involved in the formation of these encrustations, namely *Morganella morganii*, *P. aeruginosa*, *K. pneumoniae* and *Proteus vulgaris*. During the process of blockage, urease catalyzes the hydrolysis of urea into ammonia and carbamate, increasing urinary pH and, consequently, promoting stone formation by salt precipitation (calcium phosphate and struvite crystals) and potentially leading to complete occlusion of the catheter/stent through encrustation [46]. Apart from blocking the stent lumen, these encrustations potentiate further bacterial adhesion and biofilm formation, frequently resulting in complete device failure [47].

The complications associated with indwelling devices have been the main driving force for the development of alternative materials with antimicrobial and antifouling properties.

4. PDMS-BASED SURFACES TO PREVENT INFECTIONS IN URINARY TRACT DEVICES

In the last decades, a series of improvements have been performed in urinary catheters aiming to reduce pathogen colonization. As described in

previous sections, PDMS is prone to bacterial adhesion essentially due to its hydrophobic properties. In order to overcome this drawback, several coating strategies have been developed, conferring antimicrobial potential to PDMS or modifying its physicochemical properties, aiming to prevent bacterial adhesion and biofilm formation. Table 2 describes the antibiofilm strategies of different PDMS coatings and their potential against several bacterial and fungal species. PDMS coatings were grouped into four categories: (1) release of antimicrobial agents, (2) contact-killing, (3) anti-adhesive, and (4) biofilm architecture disruption.

Bactericidal/fungicidal strategies include the use of silver and antimicrobial agents or disinfectants (Table 2). Up to date, several studies have reported the effectiveness of silver/PDMS-coated catheters in the prevention and control of catheter-associated infections. The mechanisms of action of silver are already well characterized and include impairment of microbial membrane function by loss of membrane potential, protein dysfunction, and oxidative stress [8, 48]. Moreover, silver is one of the few antimicrobial agents approved by the Food and Drug Administration (FDA) for urinary catheter applications [8].

In the early 2000s, Ahearn et al. exploited the efficacy of silver/hydrogel-coated PDMS catheters against a broad range of microorganisms. Coated catheters reduced the adhesion by 73% for *Citrobacter diversus*, 65% for *Enterobacter cloacae*, 71-93% for *Enterococcus* spp., 70% for *E. coli*, 30% for *K. pneumoniae*, 70% for *P. mirabilis*, 92% for *P. aeruginosa*, and 96% for *Staphylococcus saprophyticus* compared to uncoated catheters [49]. Silver ions have also been applied as PDMS coatings, improving their potential against bacterial adhesion and biofilm growth [50]. Likewise, silver nanoparticles (AgNPs) decreased biofilm formation by *E. coli*, *P. mirabilis* and *K. pneumoniae*, preventing urinary tract infections [51]. Indeed, AgNPs are one of the most attractive types of catheter coatings. Dayyoub et al. prepared a PDMS hydrophobic film composed by tetraether lipids-coated silver nanoparticles distributed in poly(lactic-co-glycolic acid) loaded with norfloxacin, and tested it against a broad variety of bacterial species. In this study, adhered cells decreased about 48% on coated PDMS films compared to the uncoated PDMS [52]. In turn, Heidari

and co-workers evaluated silver/poly(p-xylylene)-coated catheters and observed a reduction in *E. coli* and *Staphylococcus cohnii* biofilms [53]. Recently, the efficacy of silver-polytetrafluoroethylene (Ag-PTFE) nanocomposites was evaluated against *E. coli*, *P. mirabilis* and *S. aureus*. Results showed that Ag-PTFE-coated catheters reduced bacterial adhesion and yielded strong antibiofilm activity (97%) [54, 55]. However, despite its broad-spectrum antimicrobial activity, silver-impregnated catheters can easily lose their properties in the long term and trigger bacterial resistance in intermittent catheterization [8].

Antimicrobial coatings were introduced as a good option to inhibit or delay the onset of biofilm formation. Up to date, several antimicrobial or disinfectant agents have been impregnated into silicone urinary catheters. In 2000, Simhi et al. demonstrated that PDMS impregnated with a secondary metabolite produced by *Myxococcus xanthus* significantly reduced the number of *E. coli* cells adhered to the surface [56]. Similar results were obtained for silicone catheters coated with gendine. This disinfectant was able to reduce the number of viable cells adhered to internal and external catheter surfaces, except for *P. aeruginosa* [57]. In turn, triclosan-coated catheters presented high resistance to encrustation and blockage by *P. mirabilis* and prevented the colonization by MRSA and carbapenemases-producing *E. coli* for 12 consecutive weeks [58, 59]. Rifampicin and sparfloxacin-coated catheters also prevented bacterial colonization [58].

In 2015, Gonçalves and co-workers showed the strong effect of PDMS coated with poly(catechin) conjugated with trimethoprim and sulfamethoxazole on the reduction of adhered Gram-negative and Gram-positive bacteria [60]. Likewise, the antimicrobial film composed by norfloxacin revealed a potent bactericidal activity, killing 99.9% of the adhered bacteria [52]. Lastly, Alves et al. proved that liposomal amphotericin B impregnated on silicone catheters reduced *Candida albicans* attachment by 3 Log CFU [21]. The success of this type of coating is usually attributed to the high-local concentrations of antimicrobial agents released at the potential site of colonization and their high effectiveness to target the pathogen [8]. Nevertheless, the continued

use of antimicrobial drugs may lead to bacterial resistance that compromises the application of these coatings [61].

In the last decade, antimicrobial peptides (AMPs) have emerged as contact-killing coatings for urinary catheters. This type of coating displays broad-spectrum activity targeting the pathogens through multiple pathways [8]. In 2014, Lim et al. described two arginine/lysine/tryptophane-rich antimicrobial peptides, RK1 and RK2. Catheters coated with these AMPs exhibited excellent antimicrobial activity towards *E. coli*, *S. aureus* and *C. albicans* [62]. *C. albicans* biofilm formation was also substantially inhibited (75-90%) by coumarin-linker-(ACHC- β 3hVal- β 3hLys)₃-loaded catheters [63]. The synthetic AMP CWR11 was able to reduce the bacterial attachment on a PDMS surface by 92% for *E. coli*, *P. aeruginosa* and *S. aureus* [64]. Recently, Lim et al. developed a new antimicrobial peptide (HHC36) into anhydrous polycaprolactone polymer-based dual-layer coated [PLC(P)-POPC(P)]. The coated PDMS catheters reduced bacterial adherence on catheter surfaces by 100% [65]. Although AMPs have a strong activity towards bacteria and fungi and low level of induced resistance compared to other antimicrobial agents, they may be toxic at high doses [61].

Since microbial adhesion depends on the charge, roughness and topography of the surface, anti-adhesive surfaces have optimised the physicochemical properties in order to prevent the initial microbial adhesion and thus reduce the biofilm development. Several polymers such as polyethylene glycol (PEG), hydrogels, zwitterionic polymers and cationic polymers have been applied as antifouling coatings for PDMS catheters. The polyethylene glycol capability to adsorb nonspecific proteins has been reported by several authors [8, 66, 67]. In 2001, Park et al. developed PEG-modified PDMS surfaces and evaluated them against *E. coli* and *S. epidermidis*. Bacterial adhesion decreased approximately 1 Log CFU on PDMS modified with monomethoxy poly(ethylene glycol) [68]. Despite PEG-coated materials are effectively resistant to nonspecific protein adsorption and short-term bacterial adhesion, this kind of coating has limited success in preventing biofilm formation [67]. Moreover, the

potential immunogenicity of PEG has also been reported as a relevant weakness [8].

Similarly to PEG, hydrogel coatings increase surface hydrophilicity, inhibiting nonspecific protein adsorption. In 2002, Park and co-workers demonstrated the antifouling efficacy of a new hydrogel based on poly(ethylene oxide)-poly(polytetramethylene oxide) copolymer-coated silicone catheter. The hydrogel-coated silicone catheter was able to extend the catheter patency up to 20 h versus 7.8 h with the control [69]. Recently, Yong et al. reported that the addition of a N-halamine monomer (a biocide) to the hydrogel coating deactivated both *E. coli* and *S. aureus* after 30 min of contact and reduced biofilm formation by 90% [70]. Moreover, Chung et al. in a prospective interventional study demonstrated the effectiveness of hydrogel-coated catheters in the prevention of CAUTIs [71].

Polyzwitterion coatings also resist to non-specific protein adsorption through electrostatic and steric repulsion [8]. In 2014, Diaz Blanco et al. developed a new coating based on PDMS grafted with gallic acid (GA), activated by laccases triggering the polymerization of zwitterionic sulfobetaine methacrylate monomers. Catheters coated with this film demonstrated a strong ability to resist bacterial adhesion and biofilm formation by *P. aeruginosa* and *S. aureus* [72]. Additionally, Vatterott et al. produced a new copolymer constituted by a 2-(dimethylamino)ethyl methacrylate derivate and poly(sulfobetaine methacrylate) (PTMAEMA-co-PSPE). Multilayer coatings on PDMS reduced *S. aureus* adhesion by 40% [73]. Sulfobetaine acrylamide covalently conjugated with polydopamine films-deposited copper ions coating also exhibited high fouling resistance and antimicrobial properties towards *E. coli* and *S. epidermidis*, as confirmed by the low number of adhered bacteria [74]. In turn, PDMS coated with a copolymer formed by polyacrylate [ethylene glycol dicyclopentenyl ether acrylate-co-di(ethyleneglycol) methyl ether methacrylate] was able to inhibit *E. coli* and *P. mirabilis* biofilm formation by up to 95% [75]. Based on these data, polyzwitterion coatings appear to be an effective anti-biofouling strategy.

Table 2. Antibiofilm coatings applied on PDMS-based urinary catheters

| Antibiofilm strategy | Coating | Species | Major conclusions | Year | Reference |
|-------------------------------------|--|--|--|------|-----------|
| Bactericidal/ Fungicidal | Silver Hydrogel/silver | <i>C. diversus</i> <i>E. cloacae</i> <i>E. faecalis</i> <i>E. faecium</i> <i>E. coli</i> <i>K. pneumoniae</i> <i>P. mirabilis</i> <i>P. aeruginosa</i> <i>S. saprophyticus</i> | Mean percentage reduction of adhesion to hydrogel/silver-silicone catheters versus silicone catheters was 72.5% for <i>C. diversus</i> , 64.6% for <i>E. cloacae</i> , 70.6-92.5% for <i>Enterococcus</i> spp., 70.3% for <i>E. coli</i> , 30.1% for <i>K. pneumoniae</i> , 70.3% for <i>P. mirabilis</i> , 91.8% for <i>P. aeruginosa</i> , and 95.5% for <i>S. saprophyticus</i> . | 2000 | [49] |
| | Silver | <i>E. coli</i> <i>K. pneumoniae</i> <i>P. mirabilis</i> | Silver-coated catheters significantly decreased bacterial adhesion (ratio of means: 0.63, $p = 0.0083$) and biofilm formation (ratio of means: 3.01, $p = 0.0488$) when compared to non-silver-coated catheters. | 2015 | [50] |
| | Silver nanoparticles | <i>K. pneumoniae</i> <i>P. mirabilis</i> | Silver-coated catheters decreased biofilm formation by 6 Log for <i>E. coli</i> on day 10 ($p = 0.032$); 4 Log for <i>P. mirabilis</i> ($p = 0.003$) and 1 Log for <i>K. pneumoniae</i> , both on day 14 ($p = 0.036$). | 2016 | [51] |
| | Silver with poly(p-xylylene) | <i>E. coli</i> <i>S. cohnii</i> | The supernatant of the silver/poly(p-xylylene)-coated catheters significantly reduced biofilm formation, similar to the antibiotic control (penicillin-streptomycin). | 2017 | [53] |
| | Tetraether lipids-coated silver nanoparticles distributed in a hydrophobic film of poly(lactic-co- | <i>E. coli</i> <i>P. aeruginosa</i> <i>P. mirabilis</i> <i>S. aureus</i> | Adhered cells decreased about 48% on coated silicone films compared to the control. | 2017 | [52] |

| Antibiofilm strategy | Coating | Species | Major conclusions | Year | Reference |
|-------------------------------------|---|--|---|------|-----------|
| Bactericidal/ Fungicidal | Silver glycolic acid) loaded with norfloxacin Silver-polytetrafluoroethylene nanocomposites | <i>S. epidermidis</i> <i>E. faecalis</i> <i>E. coli</i> <i>S. aureus</i> <i>P. mirabilis</i> | The Ag-PTFE-coated catheters reduced bacterial adhesion and exhibited strong antibiofilm activity (97.4%) compared with the silicone catheters. Coated catheters resisted encrustation to 78 ± 5.66 h and 89.5 ± 3.54 h with an initial concentration of 10^6 and 10^3 cells/mL in the bladder, respectively, versus 33.3 ± 1.1 h and 36.2 ± 1.1 h achieved by control catheters. | 2019 | [54, 55] |
| | Antimicrobial agents/Disinfectants Macrocyclic secondary metabolite produced by <i>M. xanthus</i> | <i>E. coli</i> | The secondary metabolite significantly reduced the number of adhered bacteria on the silicone surface (approximately less 7.0×10^6 cell/cm ² compared to control). | 2000 | [56] |
| | Gendine (a combination of Gentian Violet and chlorhexidine) | <i>E. coli</i> <i>P. aeruginosa</i> MRSA <i>C. parapsilosis</i> <i>P. mirabilis</i> | The gendine-coated catheters significantly reduced the number of viable organisms adhering to their internal and external surfaces, except for <i>P. aeruginosa</i> , when compared to the uncoated control ($p < 0.01$). | 2005 | [57] |
| | Hydrogel impregnated with triclosan, iodine and polyhexamethylene biguanide | <i>P. mirabilis</i> | Only catheters containing triclosan showed enhanced resistance to encrustation and blockage by <i>P. mirabilis</i> (up to > 7 days). | 2010 | [59] |
| | Poly(catechin) conjugated with trimethoprim and sulfamethoxazole | <i>E. coli</i> <i>P. aeruginosa</i> <i>P. mirabilis</i> <i>S. aureus</i> | The most significant reduction in adhesion was observed with poly(catechin)-TMP (85% for Gram-negative and 87% for Gram-positive bacteria) and with poly(catechin)-TMP-SMZ (85% for Gram-negative and 91% for Gram-positive bacteria). | 2015 | [60] |

Table 2. (Continued)

| Antibiofilm strategy | Coating | Species | Major conclusions | Year | Reference |
|---|---|---|--|--------------|------------------|
| Bactericidal/ Fungicidal | Antimicrobial agents/Disinfectants | | | | |
| | Tetraether lipids-coated silver nanoparticles distributed in a hydrophobic film of poly (lactic-co-glycolic acid) loaded with norfloxacin | <i>S. epidermidis</i> <i>B. subtilis</i> <i>E. coli</i> <i>P. aeruginosa</i> <i>P. mirabilis</i> <i>S. aureus</i> <i>S. epidermidis</i> <i>E. faecalis</i> | The antimicrobial film killed 99.952% of the adhered bacteria. | 2017 | [52] |
| | Rifampicin, triclosan and sparfloxacin Liposomal amphotericin B | <i>E. coli</i> (NDM-1) MRSA <i>C. albicans</i> | Antimicrobial urinary catheter prevented colonisation by MRSA and carbapenemases-producing <i>E. coli</i> for 12 weeks. L-AmB immobilized reduced fungal attachment by approximately 3 Log. | 2019 2019 | [58] [21] |
| Contact-killing | Antimicrobial peptide (AMP) | | | | |
| | Arginine/lysine/tryptophane-rich antimicrobial peptides: RK1 (RWKRWRRKK) and RK2 (RKKRWRRKK) | <i>E. coli</i> <i>S. aureus</i> <i>C. albicans</i> | The peptide-coated silicone surfaces exhibited excellent microbial killing activity towards bacteria and fungi (> 70%). | 2014 | [62] |
| | Synthetic antimicrobial peptide: CWR11 (CWFWKWRRRRR-NH2) | <i>E. coli</i> <i>P. aeruginosa</i> <i>S. aureus</i> | Bacterial attachment on the PDMS-CWR11 surface was significantly reduced by 92%. | 2015 | [64] |
| Coumarin-linker-(ACHC-β3hVal-β3hLys)3 (β-peptide 1) | <i>C. albicans</i> | B-peptide-loaded catheters substantial reduced <i>C. albicans</i> biofilm formation by 75-90%. | 2016 | [63] | |

| Antibiofilm strategy | Coating | Species | Major conclusions | Year | Reference |
|------------------------|--|--|---|------|-----------|
| Contact-killing | Antimicrobial peptide (AMP) Antimicrobial peptides (HHC36) into anhydrous polycaprolactone (PCL) polymer-based dual layer coating PCL(P)-POPC(P) | <i>E. coli</i> <i>P. aeruginosa</i> <i>S. aureus</i> | The PCL(P)-POPC(P)-coated silicone urinary catheters significantly inhibited planktonic bacteria and reduced bacteria adherence on catheter surface by 100%. | 2018 | [65] |
| Anti-adhesive | Poly(ethylene glycol) (PEG) Monomethoxy poly(ethylene glycol) (MPEG) grafts | <i>E. coli</i> <i>S. epidermidis</i> | Bacterial adhesion significantly decreased after PDMS-based polyurethanes were modified with monomethoxy PEG (from 4.0×10^4 to 5.0×10^3 CFU/cm ²). | 2001 | [68] |
| | Hydrogel Hydrogel (multiblock copolymer) based on poly(ethylene oxide)-poly(polytetramethylene oxide) copolymer | <i>P. mirabilis</i> | The performance of the hydrogel-coated silicone catheter was extended up to 20 ± 3.1 h versus 7.8 ± 3.1 h with the control. | 2002 | [69] |
| | Hydrogel impregnated with N-halamine monomer | <i>E. coli</i> <i>S. aureus</i> | The addition of a biocidal N-halamine monomer to the hydrogel coating deactivated both <i>S. aureus</i> and <i>E. coli</i> within 30 min of contact and reduced biofilm formation by 90%. | 2019 | [70] |
| | Polyzwitterion PDMS was plasma-activated and preaminated, allowing subsequent laccase-catalyzed grafting of the natural phenolic compound GA. | <i>P. aeruginosa</i> <i>S. aureus</i> | Biofilm formation on PDMS-coated samples was reduced by about 80% compared to the <i>P. aeruginosa</i> biofilm produced on the urethra part of uncoated catheters, and by about 90% in the case of <i>S. aureus</i> biofilm produced on the catheter balloon. | 2014 | [72] |

Table 2. (Continued)

| Antibiofilm strategy | Coating | Species | Major conclusions | Year | Reference |
|----------------------|--|--|---|-------------------------|-------------------------|
| Anti-adhesive | <p>Polyzwitterion</p> <p>The tethered GA residues were activated by laccases to phenoxy radicals, triggering an enzymatically initiated radical polymerization of zwitterionic sulfobetaine methacrylate monomers.grafting of the natural phenolic compound GA. The tethered GA residues were activated by laccases to phenoxy radicals, triggering an enzymatically initiated radical polymerization of zwitterionic sulfobetaine methacrylate monomers.</p> | | | | |
| | <p>PTMAEMA-co-PSPE</p> <p>Polyacrylate [ethylene glycol dicyclopentenyl ether acrylate - co-di(ethyleneglycol) methyl ether methacrylate]</p> | <p><i>S. aureus</i></p> <p><i>E. coli</i></p> <p><i>P. mirabilis</i></p> | <p>Multilayer films not only reduced the bacterial adhesion by 40% relative to uncoated PDMS, but also killed the bacteria adhered to the surface.</p> <p>Coated PDMS inhibited <i>E. coli</i> and <i>P. mirabilis</i> biofilms by up to 95% when compared with uncoated PDMS after 10 days of continuous bacterial exposure.</p> | <p>2016</p> <p>2017</p> | <p>[73]</p> <p>[75]</p> |

| Antibiofilm strategy | Coating | Species | Major conclusions | Year | Reference |
|----------------------|---|---|--|------|-----------|
| Anti-adhesive | <p>Polyzwitterion</p> <p>Copper ions deposited on polydopamine films with covalent conjugation of sulfobetaine acrylamide (pDA-SBAA)</p> | <p><i>E. coli</i></p> <p><i>S. epidermidis</i></p> | <p>r-pDA-SBAA coatings exhibited fouling resistance and antimicrobial properties which were confirmed by low adherent bacterial numbers ($\approx 1 \times 10^5$ cell/cm²) and high dead fraction (0.8).</p> | 2019 | [74] |
| | <p>Cationic polymers</p> <p><i>N</i>-acetyl-d-glucosamine-1-phosphate acetyltransferase inhibitors plus protamine sulphate</p> | <p><i>P. aeruginosa</i></p> <p><i>S. epidermidis</i></p> | <p>Confocal microscopy confirmed that coated-silicone catheters were almost free from bacterial colonization.</p> | 2006 | [76] |
| | <p>Polydopamine- poly(2-methacryloyloxyethyl)trimethylammonium chloride (pDA-g-pMTAC)</p> | <p><i>E. coli</i></p> <p><i>P. aeruginosa</i></p> | <p>The pDA-g-pMTAC-coated catheters showed a significant reduction in bacterial adhesion (50% for <i>E. coli</i> and 90% for <i>P. aeruginosa</i>).</p> | 2016 | [77] |
| Antifouling | <p>Cationic polymers</p> <p>Isobornyl methacrylate/diethylene glycol ethyl ether methacrylate (IBMA/DEGMA) (3-acrylamidopropyl) trimethylammonium chloride (AMPTMA) with trimethylammonium chloride (AMPTMA)</p> | <p><i>E. coli</i></p> <p><i>P. aeruginosa</i></p> <p><i>S. aureus</i></p> | <p>IBMA/DEGMA polymer demonstrated a bacterial coverage of less than 0.5%.</p> | 2016 | [78] |

Table 2. (Continued)

| Antibiofilm strategy | Coating | Species | Major conclusions | Year | Reference |
|------------------------------------|--|--|---|------|-----------|
| Antifouling | <p>Cationic polymers with quaternized polyethylenimine methacrylate (Q-PEI-MA) together with (polyethylene glycol dimethacrylate, PEGDMA)</p> | <p><i>E. coli</i> <i>P. aeruginosa</i> <i>S. aureus</i> MRSA VRE</p> | <p>AMPTMA/PEGDMA film coating exhibited good antibiofilm and antimicrobial effect against MRSA, with 99.4% <i>in vitro</i> reduction and 98.9% <i>in vivo</i> reduction. AMPTMA/PEGDMA/Q-PEI-MA film coating had significant efficacy against VRE, with 96.8% <i>in vitro</i> reduction and 94.5% <i>in vivo</i> reduction.</p> | 2017 | [79] |
| | <p>Dodecyl methacrylate/poly(ethylene glycol) methacrylate-and an acrylic acid (Poly(DMAmPEGMA-AA))</p> | <p><i>E. coli</i> <i>S. aureus</i></p> | <p>Polymer-coated surface displayed significantly reduced attachment of bacteria (> ~8-fold) compared to the non-coated substrates.</p> | 2017 | [80] |
| | <p>Other polymers Calixarene polymer</p> | <p><i>E. coli</i> <i>P. mirabilis</i></p> | <p>Biofilm formation was significantly reduced in the coated silicone samples compared to uncoated control ($p = 0.02$).</p> | 2018 | [81] |
| Disruption of biofilm architecture | <p>Enzymes for EPS disruption Acyase and α-amylase</p> | <p><i>E. coli</i> <i>P. aeruginosa</i> <i>S. aureus</i></p> | <p>Assembly of both enzymes in hybrid nanocoatings resulted in stronger biofilm inhibition (30%) under both static and dynamic conditions. The quorum quenching and matrix-degrading enzyme assemblies delayed biofilm growth up to 7 days.</p> | 2015 | [82] |
| | <p>Acyase</p> | <p><i>P. aeruginosa</i></p> | <p>Biofilm formation was inhibited by 80% in the balloon part, while the urethra part inserted into the bladder model was able to inhibit biofilm formation by 45%.</p> | 2015 | [83] |

Table 3. Antibiofilm coatings applied on PDMS-based ureteral stents

| Antibiofilm strategy | Coating | Species | Major conclusions | Year | Reference |
|--------------------------|---|---|--|------|-----------|
| Bactericidal | Silver Silver and hydrogel | <i>E. coli</i> <i>E. faecalis</i> | The surface material had no direct influence on bacterial adhesion. | 1997 | [84] |
| | Tetraetherlipid-silver nanoparticle-norfloxacin-poly lactide coating (TANP) | <i>E. coli</i> <i>P. aeruginosa</i> <i>S. aureus</i> <i>S. epidermidis</i> <i>E. faecalis</i> | TANP-coated samples displayed a reduction in the precipitate concentration (> 20%) and biofilm volume (80%). | 2018 | [85] |
| Antifouling | PEG Mimics mussel adhesive protein conjugated to polyethylene glycol (mPEG-DOPA3) | <i>E. coli</i> <i>P. mirabilis</i> <i>E. faecalis</i> | The mPEG-DOPA3 coating significantly resisted the attachment of all uropathogens tested, with a maximum 231-fold reduction in adherence compared to uncoated disks. | 2008 | [86] |
| Anti-encrustation | Hydrophilic polymers Phosphoryl-choline | <i>P. mirabilis</i> | PC-coated stents showed lower encrustation compared with uncoated stents. PC-coating did not reduce microbial colonization or encrustation of the surfaces of these devices. There was some evidence that PC-coating makes these devices less vulnerable to these processes. | 2002 | [87] |

Cationic polymers can also be anti-adhesive coating agents. Contrary to what was described before, this type of coating adsorbs both proteins and bacterial cells by attraction through the negatively charged bacterial membrane, exerting an anti-adhesive and antimicrobial effect [8]. Burton et al. developed a coating of *N*-acetyl-d-glucosamine-1-phosphate acetyltransferase inhibitors with protamine sulphate and evaluated its efficacy against *P. aeruginosa* and *S. epidermidis*. In this study, the coated silicone catheters were almost free of bacteria [76]. Likewise, the polydopamine-poly (2-methacryloxyethyl) trimethylammonium chloride showed a significant reduction in bacterial adhesion of 50% for *E. coli* and 90% for *P. aeruginosa* [77]. Adlington et al. demonstrated that the cationic polymer IBMA/DEGMA-coated PDMS displayed a bacterial coverage of less than 0.5% for *E. coli*, *P. aeruginosa* and *S. aureus* [78]. Recently, Zhou and colleagues developed two methacrylate polymers with excellent *in vitro* and *in vivo* antibiofilm and antimicrobial activities [79]. Lastly, poly(DMAmPEGMA-AA)-coated PDMS surfaces significantly inhibited bacterial attachment by 8 Log CFU compared to uncoated surfaces [80]. Another type of polymers, such as calixarene polymers, were reported as effective coatings to prevent biofilm formation by *E. coli* and *P. mirabilis* on PDMS surfaces [81].

Currently, different strategies are emerging aiming to disrupt the architecture of biofilm through matrix degradation or quorum sensing interruption. A study conducted by Ivanova et al. demonstrated the potential of acylase and α -amylase enzymes against extracellular polymeric substances. Assembly of both enzymes in hybrid coatings resulted in a strong biofilm inhibition (about 30%) for *E. coli*, *P. aeruginosa*, and *S. aureus*. Moreover, the quorum quenching and matrix-degrading enzymes delayed biofilm growth up to 7 days [82]. The same authors showed that acylase-coated PDMS catheters inhibited *P. aeruginosa* biofilm formation by 80% in the balloon part of the catheter, and by 40% into the urethra part [83]. These results revealed that enzymatic catheter coatings are promising to inhibit or delay biofilm formation.

Unlike in urinary catheters, antibiofilm coatings for ureteral stents were less exploited. Table 3 lists antibiofilm strategies based on distinct PDMS coatings and their effectiveness against several bacterial species. In 1997, Cormio et al. verified that PDMS stents coated with silver/hydrogel had no

direct influence on bacterial adhesion [84]. However, Frant et al. recently developed a new tetraetherlipid-silver nanoparticle-norfloxacin-poly lactide (TANP) coating and tested its antibiofilm potential towards *E. coli*, *P. aeruginosa*, *S. aureus*, *S. epidermidis*, and *E. faecalis*. TANP-coated stents reduced the precipitate concentration on silicone surfaces by up to 20% and the biofilm volume decreased 80%, showing the effectiveness of the coatings [85].

In 2008, Ko et al. introduced a new approach inspired in marine mussels to prevent biofilm formation. The biomimetic mussel adhesive protein conjugated to polyethylene glycol coating significantly resisted attachment of uropathogens, with a maximum 231-fold reduction in adherence compared to the control [86]. Lastly, the application of hydrophilic polymers such as phosphoryl-choline on silicone stents did not reduce microbial colonization or encrustation [87].

Although a wide range of antibiofilm coatings for PDMS-based urinary devices is currently available, there is a growing need to develop new effective and stable coatings to prevent or delay biofilm formation.

The development of biomimetic polymeric superhydrophobic surfaces generated an increasing interest due to their outstanding anti-biofouling properties. A strategy to combat microbial biofouling consists in modifying the topographical structure of the surface at nanometer to micrometer levels avoiding cell attachment, colonization and, ultimately, biofilm formation. Some authors, inspired on the nature, physically modified surfaces creating micropatterns to control the hydration layer and turn them superhydrophobic. This technology allows the development of surfaces that mimic the texture of shark skin or the self-cleaning properties of lotus leaves [88, 89]. In 2014, Bixler and co-workers produced PDMS-microstructured surfaces inspired by rice leaves and butterfly wings, and tested their anti-biofouling effectiveness against *E. coli*. Data demonstrated that the modified surface resulted in a coverage area reduction of 28%, suggesting the importance of surface geometrical features on fouling resistance [90]. Although these novel bioinspired surfaces have shown promising antifouling activity, their application in the medical field and,

particularly, in the construction of urinary tract devices needs further research.

5. FLOW SYSTEMS FOR SURFACE EVALUATION

A wide variety of *in vitro* biofilm model systems have been established to evaluate the efficacy of antimicrobial and antifouling surfaces under flow conditions. Indeed, this type of experimental set-up is more advantageous compared with static experiments, allowing a better representation of the hydrodynamic conditions that occur in different parts of the human body. Furthermore, it is well known that fluid flow affects not only cell adherence to the surface material, but also biofilm formation and its structure [91]. In this section, we briefly summarize the commonly used platforms for the *in vitro* assessment of cell adhesion and biofilm formation under flow conditions, with an emphasis on two types of flow systems - the modified Robbins device (MRD) and the parallel plate flow chamber (PPFC) [92-94]. Each reactor presents advantages and disadvantages that must be considered before use.

5.1. Drip Flow Reactor

The drip flow reactor has been used to mimic the flow inside indwelling medical devices and to evaluate potential antimicrobial materials [95, 96]. These reactors consist in a device with four completely separate parallel chambers with vented lids (each chamber contains a coupon where the biofilm can form) and are recommended for visualization and quantification of biofilms formed at low shear stress conditions [97]. These reactors require small space, are easy to operate, and allow noninvasive sample analysis. However, they present some disadvantages as the low number of sampling surfaces and the heterogeneity of biofilm development on the coupons due to hydrodynamics [98].

5.2. Rotary Biofilm Reactors

Three different types of rotary biofilm reactors are also commonly used in the assessment of material and fluid flow effects on biofilm development: the rotary annular reactor, the rotary disk reactor and the concentric cylinder reactor. These reactors have different designs. The rotary annular reactor is composed by a stationary outer cylinder and a rotating inner cylinder whose rotation frequency can be controlled so that a well-mixed liquid phase, turbulent flow and constant shear stress fields may be obtained [99]. The rotary disk reactor contains a disk that holds several coupons and is connected to a magnet that allows the regulation of the rotational speed [100]. The concentric cylinder reactor is composed of four cylindrical sections that can be rotated at variable speeds within four concentric chambers [101]. The last one can be used to test different cell suspensions, since each chamber of the concentric cylinder reactor contains independent feeding and sampling ports. The primary limitation of these reactors is related to the low number of individual strains that can be tested simultaneously (one microorganism per experiment in the rotary annular reactor and disk reactor, and up to four in the concentric cylinder reactor).

5.3. Microfluidics

Microfluidics can also be used to demonstrate the combined effect of several factors on the development of medically relevant biofilms [102-104]. Microfluidic systems allow the precise manipulation of the fluid contained in the microchannels, and their main advantages include the low volume requirements, the precise gradient generation, the easy handling due to their small dimensions, and the capacity to mimic microscale events, such as drug delivery systems [105-107].

5.4. Flow Cells

Flow cells have been widely used to study bacterial cell adhesion and biofilm formation under hydrodynamic conditions that mimic the urinary tract [92, 108, 109]. Originally developed by Jim Robbins and Bill McCoy, and later patented by the Shell Oil Company, the Robbins device consists of a tube incorporating several threaded holes where different coupons are fixed on the end of screws placed into the liquid stream. These coupons are parallel aligned to the fluid flow and can be independently removed to be further analyzed [110, 111]. MRD is a new version of the original Robbins device that is essentially composed by a square-channel tube with equally-spaced sampling plugs where the coupons are mounted without disturbing the flow characteristics [112]. It has an entry section long enough to allow the flow to stabilize before reach the coupons and, consequently, a constant shear stress is maintained along all the platform [113], which is extremely important to minimize the differences between the coupons. In fact, it is well known that the transport rate of oxygen, cells and nutrients to the coupon surface is strongly dependent on the fluid hydrodynamics [114]. Moreover, it can support biofilm growth for several weeks without stoppage, which constitutes an important advantage of the MRD over the original Robbins device [115, 116]. Our research group has been using a custom-made semi-circular flow cell whose hydrodynamics was fully characterized by computational fluid dynamics (CFD) [117], and which can be operated at low or high flow rates in order to mimic the biofilms formed in medical devices or industrial pipes and equipment, respectively [115, 117]. This flow cell was constructed so as to have an enough inlet length for full flow development, and a large surface area on which the hydrodynamic conditions remain constant for a wide range of flow velocities. The flow cell system is mainly composed by a recirculating tank, one vertical semi-circular flow cell (about a meter high), and peristaltic and centrifugal pumps.

5.6. Parallel Plate Flow Chamber

Contrary to the flow systems previously described, the PPFC was designed to allow real-time observation of microbial adhesion and biofilm development. Several authors have frequently applied PPFCs to monitor biofilm formation [118, 119]. This platform can contain one or two glass viewing ports that enable the use of a microscope and a camera for image capture and further monitorization of bacterial adhesion to the material. PPFCs are usually smaller than flow cells and cheaper to build. They can also be used to conduct experiments in parallel under the same operational conditions, which enables a higher throughput.

6. ADHESION AND BIOFILM FORMATION IN URINARY CATHETERS AND URETERAL STENTS: EXPERIMENTAL APPROACH

A PPFC was used in this work to evaluate the transition from initial *E. coli* adhesion to the complex structure of the biofilm formed on PDMS, one of the most widely used materials for the manufacture of UTDs. This *in vitro* flow system was fully characterized by CFD [92] and showed to be adequate to mimic the flow conditions found in different biomedical systems [120, 121], including urinary catheters and ureteral stents. The numerical simulations revealed that the average shear strain rate value of 15 s^{-1} reported for urinary flow in catheters [122] can be attained in the PPFC system at a flow rate of 2 mL/s. On the other hand, shear stress values between 0.01 and 0.038 Pa were described for problematic zones in ureteral stents [123]. The average shear stress in critical areas that are prone to encrustation (0.024 Pa) can be obtained by operating the PPFC system at a flow rate of 4 mL/s. Therefore, the PPFC was selected for this study because it can replicate relevant hydrodynamic conditions of UTDs and allows direct observation of bacterial adhesion to PDMS in real-time by conventional light *microscopy*, as well as offline monitoring of biofilm development on the same substrate.

6.1. PPFC System

The PPFC system used in the present work is represented in Figure 1. The flow chamber had a rectangular cross section of 0.8×1.6 cm and a length of 25.4 cm, and contained a bottom and a top opening for the introduction of the test surfaces. This setup generated a window of 6.7×1.6 cm through which bacterial adhesion within the chamber may be visualized. The PPFC was coupled to a jacketed glass tank connected to a centrifugal pump and a valve by a silicone tubing system. The valve allowed the bacterial suspension to circulate through the system at a controlled flow rate, in this case, 2 or 4 mL/s in order to obtain wall shear forces similar to those found in urinary catheters or ureteral stents, respectively. A recirculating water bath was connected to the tank jacket to enable temperature control at 37°C to mimic human body conditions.

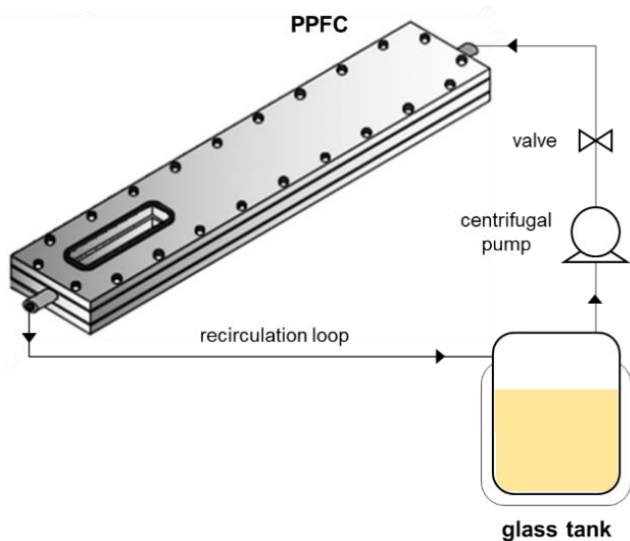


Figure 1. Schematic representation of the PPFC system.

Before performing adhesion or biofilm formation assays, the PPFC system was sterilized by recirculating a sodium hypochlorite solution (3% v/v, 3 cycles of 15 min each). Then, it was washed with sterile water and placed inside a laminar flow chamber for 30 min of UV sterilization. All

the surfaces (glass microscopic slides for the top and PDMS slides for the bottom of the PPFC) were sterilized by spraying with absolute ethanol for 5 min.

6.2. Synthesis and Thermodynamic Characterization of PDMS

The PDMS surfaces were prepared according to the procedure fully described by Moreira et al. [92]. Briefly, glass microscope slides ($W \times D \times H = 76 \times 26 \times 1$ mm, VWR) were washed with a commercial detergent (Sonasol Pril, Henkel Ibérica SA) and immersed in a sodium hypochlorite solution. The clean slides were then coated with PDMS. The PDMS (Sylgard 184 Part A, Dow Corning) was first submitted to an ultrasound treatment to eliminate air bubbles. The curing agent (Sylgard 184 Part B, Dow Corning) was added to the PDMS at a 1:10 ratio and the mixture was deposited as a thin layer (with a uniform thickness of 10 μm) on the top of glass slides by spin coating.

Surface and bacterial hydrophobicity (ΔG_{sws}^{TOT} and ΔG_{bwb}^{TOT} , respectively) were evaluated according to the approach of van Oss et al. [124-126]. The contact angles were determined by the sessile drop method in a contact angle meter (Dataphysics OCA 15 Plus, Germany) using water, formamide and α -bromonaphtalene as reference liquids. In this approach, the ΔG values can be calculated from the surface tension components by Equation (1):

$$\Delta G^{TOT} = -2 \left(\sqrt{\gamma_s^{LW}} - \sqrt{\gamma_w^{LW}} \right)^2 + 4 \left(\sqrt{\gamma_s^+ \gamma_w^-} + \sqrt{\gamma_s^- \gamma_w^+} - \sqrt{\gamma_s^+ \gamma_s^-} - \sqrt{\gamma_w^+ \gamma_w^-} \right) \quad (1)$$

If $\Delta G^{TOT} < 0$ mJ/m², the material is considered hydrophobic; if $\Delta G^{TOT} > 0$ mJ/m², the material is hydrophilic.

The free energy of adhesion between a surface and bacteria (ΔG_{bws}^{TOT}) can be calculated by Equation (2):

$$\Delta G_{bws}^{TOT} = \gamma_{sb}^{LW} - \gamma_{sw}^{LW} - \gamma_{bw}^{LW} + 2 \left[\sqrt{\gamma_w^+} (\sqrt{\gamma_s^-} + \sqrt{\gamma_b^-} - \sqrt{\gamma_w^-}) + \sqrt{\gamma_w^-} (\sqrt{\gamma_s^+} + \sqrt{\gamma_b^+} - \sqrt{\gamma_w^+}) - \sqrt{\gamma_s^+ \gamma_b^-} - \sqrt{\gamma_s^- \gamma_b^+} \right] \quad (2)$$

Thermodynamically, if $\Delta G_{bws}^{TOT} < 0$ mJ/m², adhesion is favored, while adhesion is not expected to occur if $\Delta G_{bws}^{TOT} > 0$ mJ/m².

Table 4. Contact angles with water (θ_w), formamide (θ_F) and α -bromonaphthalene (θ_B), surface tension parameters, free energy of interaction (ΔG_{sws}^{TOT} or ΔG_{bwb}^{TOT}) of the bacteria (*b*) and surface (*s*) when immersed in water (*w*), and free energy of adhesion (ΔG_{bws}^{TOT}) between the bacteria and the surface

| | Contact angle (°) | | | Surface tension parameters (mJ/m ²) | | | | Hydrophobicity (mJ/m ²) | Free energy of adhesion (mJ/m ²) |
|-----------------|-------------------|----------------|---------------|---|------------|------------|---------------|--|--|
| | θ_w | θ_F | θ_B | γ^{LW} | γ^+ | γ^- | γ^{AB} | ΔG_{sws}^{TOT} or ΔG_{bwb}^{TOT} | ΔG_{bws}^{TOT} |
| <i>Surface</i> | | | | | | | | | |
| PDMS | 113.6 ± 0.6 | 111.2 ± 0.6 | 87.6 ± 1.8 | 12.0 | 0.0 | 4.5 | 0.0 | -61.8 | 32.6 |
| <i>Bacteria</i> | | | | | | | | | |
| <i>E. coli</i> | 19.1 ± 0.9 | 73.3 ± 0.7 | 58.5 ± 2.0 | 25.7 | 0.0 | 123.2 | 0.0 | 121.9 | n/a |

Note: n/a - not applicable.

Values are means ± SDs of three independent experiments.

Table 4 presents the results of the thermodynamic analysis of PDMS coating and *E. coli* cells based on contact angle measurements. It was observed that PDMS is hydrophobic ($\Delta G^{TOT} < 0$ mJ/m²), whereas *E. coli* cells are hydrophilic ($\Delta G^{TOT} > 0$ mJ/m²). From the water contact angle (θ_w , Table 4), PDMS can also be classified as non-wettable since θ_w exceeded 110° [127]. Regarding the polar surface components (γ^+ and γ^-), results showed that PDMS and *E. coli* cells have monopolar surfaces, being electron donors. From a thermodynamic point of view (Table 4), the

adhesion of *E. coli* to PDMS was not expected to occur ($\Delta G_{bws}^{TOT} > 0$ mJ/m²).

6.3. Initial Adhesion Assays

For the adhesion assays, the PPFC was mounted in a microscope (Nikon Eclipse LV100, Japan) to monitor cell attachment to PDMS in real-time during 25 min. An *E. coli* JM109(DE3) suspension of 7.6×10^7 cells/mL in citrate buffer 0.05 M was prepared and recirculated through the PPFC system at 2 or 4 mL/s. Citrate buffer was used to avoid any surface conditioning effects that may arise with using conventional culture medium. Images were acquired every 60 s with a camera (Nikon DS-Ri 1, Japan) connected to the microscope. The microscopic images were analyzed by ImageJ software (version 1.38e) to determine the number of adherent cells per square centimeter at each time point for each tested flow rate.

Figure 2 shows the initial adhesion results obtained for PDMS for each flow rate (2 and 4 mL/s). It is possible to observe that the number of adhered cells increased with time for both flow rates, having achieved an average value of 1.15×10^6 cells/cm² after 25 min of experiment. Moreover, the number of adhered cells was mostly similar between flow rates during the experimental time ($P > 0.05$ for 92% of the time points). Indeed, the initial adhesion rates (IAR) obtained from linear regression of the data presented in Figure 2 were very similar: 4.25×10^4 cells/(cm² s) for the flow rate of 2 mL/s and 3.83×10^4 cells/(cm² s) for the flow rate of 4 mL/s. Usually, increased flow velocities result in higher adhesion due to the increased cell transport to the surface [128]. However, it was not surprising that doubling the flow rate did not increase the number of attached cells because the higher shear forces may have contributed to higher cell detachment or be high enough to hamper the process of initial reversible adhesion [92, 129].

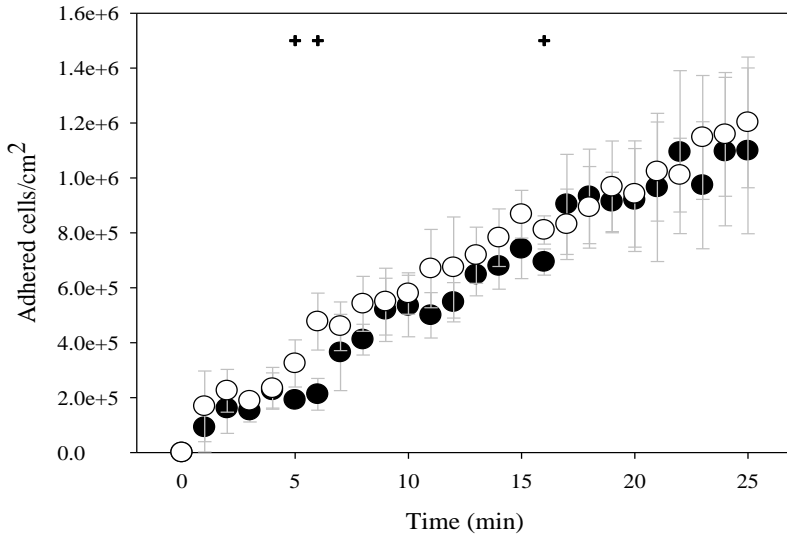


Figure 2. *E. coli* adhesion to PDMS surface at a flow rate of 2 mL/s (●; mimicking urinary catheters) and 4 mL/s (○; mimicking ureteral stents). The means \pm standard deviations (SDs) for three independent experiments for each condition are illustrated. Statistically significant differences for a confidence level greater than 95% ($P < 0.05$) are indicated by +.

6.4. Biofilm Formation Assays

Biofilm formation experiments using the PPFC system previously described (Section 6.1) were carried out for 24 h. Note that it has been reported that biofilms developed in UTDs are completely mature after 24 h [130]. Synthetic urine was the culture medium chosen to prepare the *E. coli* suspension [109], which recirculated through the PPFC at 2 and 4 mL/s in order to mimic the urine flow behaviour in urinary catheters and ureteral stents, respectively. After 24 h of biofilm growth, the PPFC was opened and the cells adhered on PDMS were removed through the swabbing method [131].

The total number of sessile cells on PDMS was determined by epifluorescence microscopy by staining the biofilm suspension with 4'-diamidino-2-phenylindole (DAPI; Merck, Germany) [132], while the cell culturability was assessed by spreading the biofilm suspension on plate

count agar (PCA, Oxoid, England) and incubating at 37°C for colony-forming unit (CFU) enumeration. Results of total and culturable cell quantification for both hydrodynamic conditions are shown in Figure 3. There were no statistically significant differences in the number of total and culturable cells between the two flow rates ($P > 0.05$). The 24-h biofilms formed on PDMS slides had on average 1.2×10^8 total cells/cm² and about 26% of these cells were culturable, regardless of the flow rate tested. These first results seem to indicate that the similar cell amount in *E. coli* biofilms developed under two different flow rates could be associated with the similar initial adhesion rates also obtained (Figure 2).

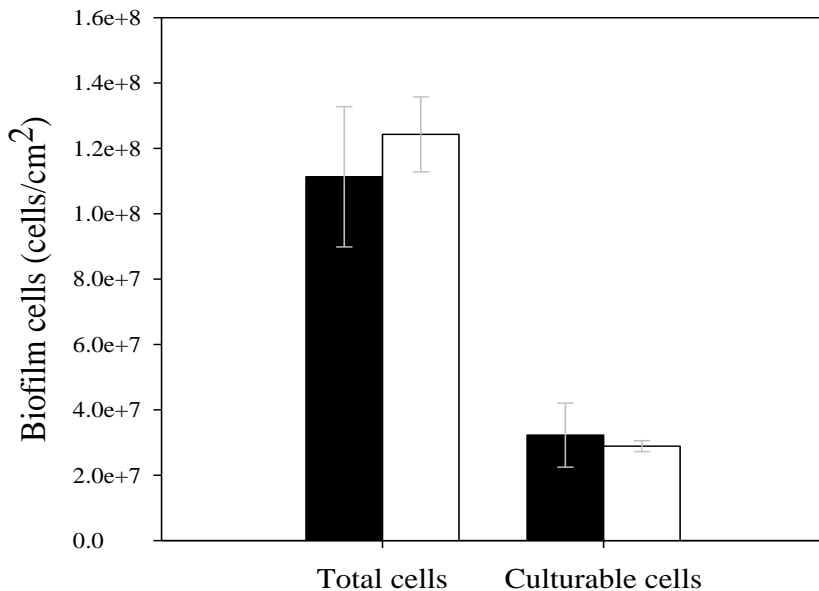


Figure 3. Number of total and culturable *E. coli* cells on PDMS after 24 h of biofilm formation at a flow rate of 2 mL/s (■; mimicking urinary catheters) and 4 mL/s (□; mimicking ureteral stents). The means \pm SDs for three independent experiments for each condition are presented.

The analysis of the biofilm cell number was complemented by their observation (Figure 4) and quantification (Figure 5) by confocal laser scanning microscopy (CLSM).

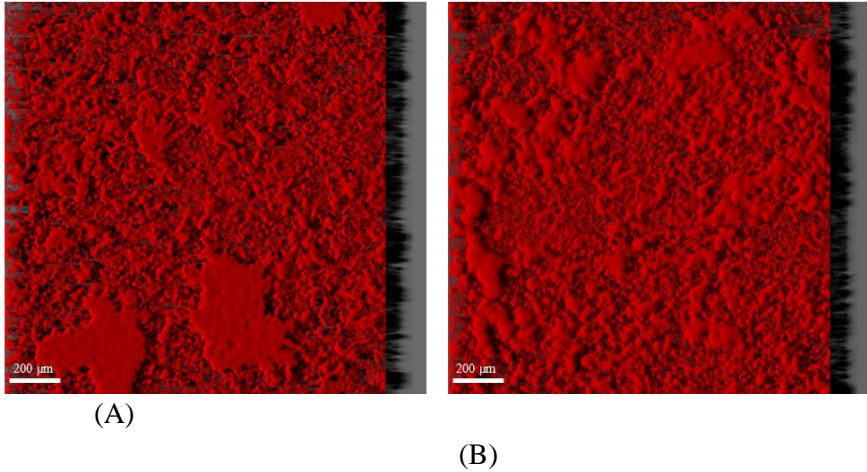


Figure 4. 3D projections of 24-h *E. coli* biofilms formed on PDMS at a flow rate of 2 mL/s (A; mimicking urinary catheters) and 4 mL/s (B; mimicking ureteral stents). These representative images were obtained from confocal z stacks using IMARIS software and present an aerial view of biofilm structures, with the shadow projection on the right. White bars correspond to 200 μm .

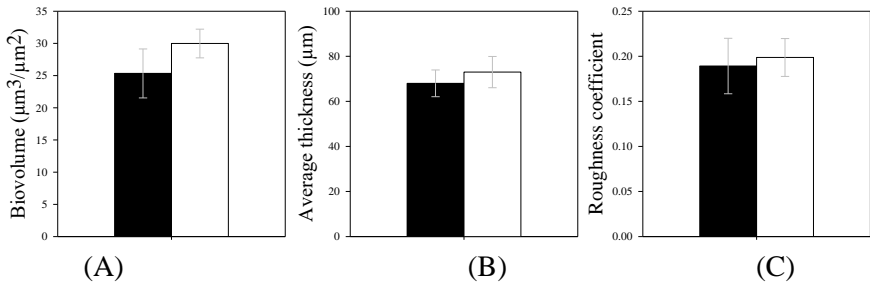


Figure 5. Biovolume (A), average thickness (B) and roughness coefficient (C) of 24-h *E. coli* biofilms formed on PDMS at a flow rate of 2 mL/s (■; mimicking urinary catheters) and 4 mL/s (□; mimicking ureteral stents). These quantitative parameters were obtained from confocal image series using the COMSTAT2 tool associated with the ImageJ software. The means \pm SDs for three independent experiments for each condition are presented.

This microscopic technique is a valuable tool for the study of biofilms developed on different surface materials, including those used in medical devices [133], as it allows the 3D visualization of fully hydrated, living specimens. In this work, the 24-h biofilms formed on PDMS surfaces placed inside the flow chamber were counterstained with Syto61

(Invitrogen, USA), a cell-permeant fluorescent nucleic acid stain, and observed using a Leica TCS SP5 II CLSM (Leica Microsystems, Germany). Three-dimensional projections of biofilm structures were reconstructed using the “Easy 3D” tool of IMARIS 8.4.1 software (Bitplane, Switzerland) directly from the *xyz* images series. Figure 4 presents representative CLSM images of biofilms developed on PDMS when exposed to a flow rate of 2 (Figure 4A) and 4 mL/s (Figure 4B). The two images are clearly similar, with thick biofilms with a dense and smooth appearance obtained at both flow rates.

Regarding quantification of biofilm structures, the COMSTAT2 tool associated with the ImageJ software was used to measure the biovolume ($\mu\text{m}^3/\mu\text{m}^2$), the average biofilm thickness (μm) and the roughness coefficient (Figure 5). Briefly, the biovolume is the overall volume occupied by the biofilm and an estimate of the biomass in the biofilm [134]. The average biofilm thickness provides a measure of the spatial size of the biofilm, while the roughness coefficient is a measure of variation in biofilm thickness across the field of view, giving an indication of biofilm heterogeneity [134].

The biovolume, thickness and roughness of the biofilm were maintained with increasing flow rate ($P > 0.05$, Figure 5), which reinforced the visual inspection of the biofilm structures (Figure 4).

When comparing all parameters obtained for the biofilm formed under two distinct hydrodynamic conditions (one that mimicked urine flow within urinary catheters and another that simulated fluid in ureteral stents), they were consistent with each other and follow the trend dictated by the adhesion results. Therefore, this study performed with the PPFC system suggests that the profile of initial adhesion can be used to estimate biofilm growth in urinary tract medical devices such as urinary catheters and ureteral stents.

CONCLUSION

PDMS has been widely used in the manufacture of urinary catheters and ureteral stents due to its outstanding properties. However, serious

complications are still arising due to biofilm formation on the surface of these indwelling devices. In the last years, numerous studies have been conducted in order to improve the antimicrobial and antifouling properties of PDMS-based surfaces. According to collected data, different strategies including the release of antimicrobial agents, contact-killing and anti-adhesive coatings, and surfaces that cause disruption of biofilm architecture by matrix degradation or quorum sensing interruption, have been proposed to prevent or delay biofilm formation on PDMS surfaces.

Despite the multiplicity of antibiofilm coatings for PDMS-based urinary devices, there is a need to develop new effective strategies, particularly for ureteral stents, where research in antibiofilm coatings is far less developed.

Flow cells are attractive *in vitro* platforms to evaluate biofilm growth on potential antimicrobial and antifouling surfaces under dynamic conditions. The experimental approach explored in this chapter showed the importance of using PPFCs in the investigation of cell adhesion and biofilm formation. Additionally, the PPFC results revealed that initial bacterial adhesion can be used to estimate biofilm growth in urinary tract devices such as urinary catheters and ureteral stents.

ACKNOWLEDGMENTS

This work was financially supported by: Base Funding - UIDB/00511/2020 of the Laboratory for Process Engineering, Environment, Biotechnology and Energy – LEPABE - funded by national funds through the FCT/MCTES (PIDDAC); and by project POCI-01-0145-FEDER-029589 funded by FEDER funds through COMPETE2020 – Programa Operacional Competitividade e Internacionalização (POCI) and by national funds (PIDDAC) through FCT/MCTES. R. Teixeira-Santos acknowledges the receipt of a Junior Researcher fellowship from this project. L. C. Gomes acknowledges the Junior Researcher contract (CEECIND/01700/2017) funded by national funds through FCT, I. P.

Support from the EU COST Actions ENBA (CA15216) and ENIUS (CA16217) is acknowledged.

REFERENCES

- [1] Kim, J. H., Park, H., and Seo, S. W. 2017. "In situ synthesis of silver nanoparticles on the surface of PDMS with high antibacterial activity and biosafety toward an implantable medical device." *Nano converg* 4:33.
- [2] Curtis, J. and Colas, A. 2013. "Chapter II.5.18 - Medical Applications of Silicones." In *Biomaterials Science (Third Edition)*, edited by B.D. Ratner, et al., 1106-1116. Academic Press.
- [3] Kendrick, T. C., Parbhoo, B. M., and White, J. W. 1989. "25 - Polymerization of Cyclosiloxanes." In *Comprehensive Polymer Science and Supplements*, edited by G. Allen and J.C. Bevington, 459-523. Amsterdam: Pergamon.
- [4] Shen, Q., Shan, Y., Lü, Y., Xue, P. et al. 2019. "Enhanced Antibacterial Activity of Poly (dimethylsiloxane) Membranes by Incorporating SiO₂ Microspheres Generated Silver Nanoparticles." *Nanomaterials (Basel, Switzerland)* 9:705.
- [5] Bhattacharjee, N., Urrios, A., Kang, S., and Folch, A. 2016. "The upcoming 3D-printing revolution in microfluidics." *Lab on a chip* 16:1720-1742.
- [6] ter Meulen, P. H., Berghmans, L. C. M., and van Kerrebroeck, P. E. V. A. 2003. "Systematic Review: Efficacy of Silicone Microimplants (Macroplastique®) Therapy for Stress Urinary Incontinence in Adult Women." *Eur Urol* 44:573-582.
- [7] Keskin, D., Mokabbar, T., Pei, Y., and Van Rijn, P. 2018. "The Relationship between Bulk Silicone and Benzophenone-Initiated Hydrogel Coating Properties." *Polymers (Basel)* 10:534.
- [8] Zhu, Z., Wang, Z., Li, S., and Yuan, X. 2019. "Antimicrobial strategies for urinary catheters." *J Biomed Mater Res A* 107:445-467.

- [9] Singha, P., Locklin, J., and Handa, H. 2017. "A review of the recent advances in antimicrobial coatings for urinary catheters." *Acta Biomater* 50:20-40.
- [10] Todd, A. M. and Knudsen, B. E. 2017. "Ureteral Stent Materials." In *Ureteric Stenting*, edited by R. Kulkarni, 83-90. Wiley.
- [11] Lawrence, E. L. and Turner, I. G. 2005. "Materials for urinary catheters: a review of their history and development in the UK." *Med Eng Phys* 27:443-453.
- [12] Liatsikos, E., Kallidonis, P., Stolzenburg, J. U., and Karnabatidis, D. 2009. "Ureteral stents: past, present and future." *Expert Rev Med Devices* 6:313-324.
- [13] Moola, S. and Konno, R. 2010. "A systematic review of the management of short-term indwelling urethral catheters to prevent urinary tract infections." *JBI Libr Syst Rev* 8:695-729.
- [14] Stenzelius, K., Persson, S., Olsson, U. B., and Stjarneblad, M. 2011. "Noble metal alloy-coated latex versus silicone Foley catheter in short-term catheterization: a randomized controlled study." *Scand J Urol Nephrol* 45:258-264.
- [15] Thibon, P., Le Coutour, X., Leroyer, R., and Fabry, J. 2000. "Randomized multi-centre trial of the effects of a catheter coated with hydrogel and silver salts on the incidence of hospital-acquired urinary tract infections." *J Hosp Infect* 45:117-124.
- [16] Hoe, J. W. 1989. "Antegrade double J ureteral stenting for ureteric strictures: use of silicone stents." *Australas Radiol* 33:385-389.
- [17] Tunney, M. M., Keane, P. F., Jones, D. S., and Gorman, S. P. 1996. "Comparative assessment of ureteral stent biomaterial encrustation." *Biomaterials* 17:1541-1546.
- [18] Weinstein, M. P., Towns, M. L., Quartey, S. M., Mirrett, S. et al. 1997. "The clinical significance of positive blood cultures in the 1990s: a prospective comprehensive evaluation of the microbiology, epidemiology, and outcome of bacteremia and fungemia in adults." *Clin Infect Dis* 24:584-602.
- [19] 2008. *Annual Epidemiological Report on Communicable Diseases in Europe 2008*. European Centre for Disease Prevention and Control.

- [20] Klevens, R. M., Edwards, J. R., Richards, C. L., Horan, T. C. et al. 2007. "Estimating health care-associated infections and deaths in U.S. hospitals, 2002." *Public Health Reports (Washington, D.C.:1974)* 122:160-166.
- [21] Alves, D., Vaz, A. T., Grainha, T., Rodrigues, C. F. et al. 2019. "Design of an Antifungal Surface Embedding Liposomal Amphotericin B Through a Mussel Adhesive-Inspired Coating Strategy." *Front Chem* 7:431.
- [22] Darouiche, Rabih O. 2001. "Device-Associated Infections: A Macroproblem that Starts with Microadherence." *Clin Infect Dis* 33:1567-1572.
- [23] Zarb, P., Coignard, B., Griskeviciene, J., Muller, A. et al. 2012. "The European Centre for Disease Prevention and Control (ECDC) pilot point prevalence survey of healthcare-associated infections and antimicrobial use." *Euro surveillance : bulletin Europeen sur les maladies transmissibles = European communicable disease bulletin* 17:20316.
- [24] Magill, S. S., Edwards, J. R., Bamberg, W., Beldavs, Z. G. et al. 2014. "Multistate point-prevalence survey of health care-associated infections." *N Engl J Med* 370:1198-1208.
- [25] Donlan, R. M. 2001. "Biofilms and device-associated infections." *Emerg Infect Dis* 7:277-281.
- [26] Mulhall, A. B., Chapman, R. G., and Crow, R. A. 1988. "Bacteriuria during indwelling urethral catheterization." *J Hosp Infect* 11:253-262.
- [27] Richter, S., Ringel, A., Shalev, M., and Nissenkorn, I. 2000. "The indwelling ureteric stent: a 'friendly' procedure with unfriendly high morbidity." *BJU International* 85:408-411.
- [28] Nicolle, L. E. 2005. "Complicated urinary tract infection in adults." *Can J Infect Dis Med Microbiol* 16:349-360.
- [29] Riedl, C. R., Plas, E., Hübner, W. A., Zimmerl, H. et al. 1999. "Bacterial colonization of ureteral stents." *Eur Urol* 36:53-59.

- [30] Foxman, B. 2002. "Epidemiology of urinary tract infections: incidence, morbidity, and economic costs." *Am J Med* 113 Suppl:5S-13S.
- [31] Scott II, R. D. 2009. *The direct medical costs of healthcare-associated infections in the US hospitals and the benefits of prevention.*
- [32] Feneley, R., Hopley, I., and Wells, P. 2015. "Urinary catheters: history, current status, adverse events and research agenda." *J Med Eng Technol* 39:459-470.
- [33] Staubli, S. E. L., Mordasini, L., Engeler, D. S., Sauter, R. et al. 2016. "Economic Aspects of Morbidity Caused by Ureteral Stents." *Urol Int* 97:91-97.
- [34] Maki, D. G. and Tambyah, P. A. 2001. "Engineering out the risk for infection with urinary catheters." *Emerg Infect Dis* 7:342-347.
- [35] Jacobsen, S. M., Stickler, D. J., Mobley, H. L. T., and Shirliff, M. E. 2008. "Complicated catheter-associated urinary tract infections due to *Escherichia coli* and *Proteus mirabilis*." *Clin Microbiol Rev* 21:26-59.
- [36] Costerton, J. W., Stewart, P. S., and Greenberg, E. P. 1999. "Bacterial biofilms: a common cause of persistent infections." *Science* (New York, N.Y.) 284:1318-1322.
- [37] Flemming, H.-C. and Wingender, J. 2010. "The biofilm matrix." *Nat Rev Microbiol* 8:623-633.
- [38] Garrett, T. R., Bhakoo, M., and Zhang, Z. 2008. "Bacterial adhesion and biofilms on surfaces." *Prog Nat Sci* 18:1049-1056.
- [39] Briandet, R., Herry, J.-M., and Bellon-Fontaine, M.-N. 2001. "Determination of the van der Waals, electron donor and electron acceptor surface tension components of static Gram-positive microbial biofilms." *Colloids Surf B Biointerfaces* 21:299-310.
- [40] Katsikogianni, M. and Missirlis, Y. 2004. "Concise review of mechanisms of bacterial adhesion to biomaterials and of techniques used in estimating bacteria-material interactions." *Eur Cells Mater* 8:37-57.

- [41] De Weger, L. A., van der Vlugt, C. I., Wijfjes, A. H., Bakker, P. A. et al. 1987. "Flagella of a plant-growth-stimulating *Pseudomonas fluorescens* strain are required for colonization of potato roots." *J Bacteriol* 169:2769-2773.
- [42] Ganderton, L., Chawla, J., Winters, C., Wimpenny, J. et al. 1992. "Scanning electron microscopy of bacterial biofilms on indwelling bladder catheters." *Eur J Clin Microbiol Infect Dis* 11:789-796.
- [43] Stewart, P. S. and Costerton, J. W. 2001. "Antibiotic resistance of bacteria in biofilms." *Lancet* (London, England) 358:135-138.
- [44] Lewis, K. 2007. "Persister cells, dormancy and infectious disease." *Nat Rev Microbiol* 5:48-56.
- [45] Morris, N. S. and Stickler, D. J. 1998. "Encrustation of indwelling urethral catheters by *Proteus mirabilis* biofilms growing in human urine." *J Hosp Infect* 39:227-234.
- [46] Broomfield, R. J., Morgan, S. D., Khan, A., and Stickler, D. J. 2009. "Crystalline bacterial biofilm formation on urinary catheters by urease-producing urinary tract pathogens: a simple method of control." *J Med. Microbiol* 58:1367-1375.
- [47] Tenke, P., Köves, B., Nagy, K., Hultgren, S. J. et al. 2012. "Update on biofilm infections in the urinary tract." *World J Urol* 30:51-57.
- [48] Dakal, T. C., Kumar, A., Majumdar, R. S., and Yadav, V. 2016. "Mechanistic Basis of Antimicrobial Actions of Silver Nanoparticles." *Front Microbiol* 7:1831.
- [49] Ahearn, D. G., Grace, D. T., Jennings, M. J., Borazjani, R. N. et al. 2000. "Effects of hydrogel/silver coatings on in vitro adhesion to catheters of bacteria associated with urinary tract infections." *Curr Microbiol* 41:120-125.
- [50] Ogilvie, A. T., Brisson, B. A., Singh, A., and Weese, J. S. 2015. "In vitro evaluation of the impact of silver coating on *Escherichia coli* adherence to urinary catheters." *Can Vet J* 56:490-494.
- [51] Cooper, I. R., Pollini, M., and Paladini, F. 2016. "The potential of photo-deposited silver coatings on Foley catheters to prevent urinary tract infections." *Mater Sci Eng C* 69:414-420.

- [52] Dayyoub, E., Frant, M., Pinnapireddy, S. R., Liefelth, K. et al. 2017. "Antibacterial and anti-encrustation biodegradable polymer coating for urinary catheter." *Int J Pharm* 531:205-214.
- [53] Heidari Zare, H., Juhart, V., Vass, A., Franz, G. et al. 2017. "Efficacy of silver/hydrophilic poly(p-xylylene) on preventing bacterial growth and biofilm formation in urinary catheters." *Biointerphases* 12:011001.
- [54] Zhang, S., Wang, L., Liang, X., Vorstius, J. et al. 2019. "Enhanced Antibacterial and Antiadhesive Activities of Silver-PTFE Nanocomposite Coating for Urinary Catheters." *ACS Biomater Sci Eng* 5:2804-2814.
- [55] Wang, L., Zhang, S., Keatch, R., Corner, G. et al. 2019. "In-vitro antibacterial and anti-encrustation performance of silver-polytetrafluoroethylene nanocomposite coated urinary catheters." *J Hosp Infect* 103:55-63.
- [56] Simhi, E., van der Mei, H. C., Ron, E. Z., Rosenberg, E. et al. 2000. "Effect of the adhesive antibiotic TA on adhesion and initial growth of *E. coli* on silicone rubber." *FEMS Microbiol Lett* 192:97-100.
- [57] Chaiban, G., Hanna, H., Dvorak, T., and Raad, I. 2005. "A rapid method of impregnating endotracheal tubes and urinary catheters with gendine: a novel antiseptic agent." *J Antimicrob Chemoth* 55:51-56.
- [58] Belfield, K., Chen, X., Smith, E. F., Ashraf, W. et al. 2019. "An antimicrobial impregnated urinary catheter that reduces mineral encrustation and prevents colonisation by multi-drug resistant organisms for up to 12 weeks." *Acta Biomater* 90:157-168.
- [59] Kazmierska, K. A., Thompson, R., Morris, N., Long, A. et al. 2010. "In Vitro Multicompartmental Bladder Model for Assessing Blockage of Urinary Catheters: Effect of Hydrogel Coating on Dynamics of *Proteus mirabilis* Growth." *Urology* 76:515.e15-515.e20.
- [60] Gonçalves, I., Abreu, A. S., Matamá, T., Ribeiro, A. et al. 2015. "Enzymatic synthesis of poly(catechin)-antibiotic conjugates: an

- antimicrobial approach for indwelling catheters." *Appl Microbiol Biotechnol* 99:637-651.
- [61] Adlhart, C., Verran, J., Azevedo, N. F., Olmez, H. et al. 2018. "Surface modifications for antimicrobial effects in the healthcare setting: a critical overview." *J Hosp Infect* 99:239-249.
- [62] Li, X., Li, P., Saravanan, R., Basu, A. et al. 2014. "Antimicrobial functionalization of silicone surfaces with engineered short peptides having broad spectrum antimicrobial and salt-resistant properties." *Acta Biomater* 10:258-266.
- [63] Raman, N., Lee, M.-R., Rodríguez López, A. d. L., Palecek, S. P. et al. 2016. "Antifungal activity of a β -peptide in synthetic urine media: Toward materials-based approaches to reducing catheter-associated urinary tract fungal infections." *Acta Biomater* 43:240-250.
- [64] Lim, K., Chua, R. R. Y., Ho, B., Tambyah, P. A. et al. 2015. "Development of a catheter functionalized by a polydopamine peptide coating with antimicrobial and antibiofilm properties." *Acta Biomater* 15:127-138.
- [65] Lim, K., Saravanan, R., Chong, K. K. L., Goh, S. H. M. et al. 2018. "Anhydrous polymer-based coating with sustainable controlled release functionality for facile, efficacious impregnation, and delivery of antimicrobial peptides." *Biotechnol Bioeng* 115:2000-2012.
- [66] Xu, L. C. and Siedlecki, C. A. 2017. "Protein adsorption, platelet adhesion, and bacterial adhesion to polyethylene-glycol-textured polyurethane biomaterial surfaces." *J Biomed Mater Res B Appl Biomater* 105:668-678.
- [67] Cheng, G., Zhang, Z., Chen, S., Bryers, J. D. et al. 2007. "Inhibition of bacterial adhesion and biofilm formation on zwitterionic surfaces." *Biomaterials* 28:4192-4199.
- [68] Park, J. H., Lee, K. B., Kwon, I. C., and Bae, Y. H. 2001. "PDMS-based polyurethanes with MPEG grafts: mechanical properties, bacterial repellency, and release behavior of rifampicin." *J Biomater Sci Polym Ed* 12:629-645.

- [69] Park, J. H., Cho, Y. W., Kwon, I. C., Jeong, S. Y. et al. 2002. "Assessment of PEO/PTMO multiblock copolymer/segmented polyurethane blends as coating materials for urinary catheters: in vitro bacterial adhesion and encrustation behavior." *Biomaterials* 23:3991-4000.
- [70] Yong, Y., Qiao, M., Chiu, A., Fuchs, S. et al. 2019. "Conformal Hydrogel Coatings on Catheters To Reduce Biofouling." *Langmuir* 35:1927-1934.
- [71] Chung, P. H., Wong, C. W., Lai, C. K., Siu, H. K. et al. 2017. "A prospective interventional study to examine the effect of a silver alloy and hydrogel-coated catheter on the incidence of catheter-associated urinary tract infection." *Hong Kong Med J* 23:239-245.
- [72] Diaz Blanco, C., Ortner, A., Dimitrov, R., Navarro, A. et al. 2014. "Building an Antifouling Zwitterionic Coating on Urinary Catheters Using an Enzymatically Triggered Bottom-Up Approach." *ACS Appl Mater Interfaces* 6:11385-11393.
- [73] Vaterrodt, A., Thallinger, B., Daumann, K., Koch, D. et al. 2016. "Antifouling and Antibacterial Multifunctional Polyzwitterion/Enzyme Coating on Silicone Catheter Material Prepared by Electrostatic Layer-by-Layer Assembly." *Langmuir* 32:1347-1359.
- [74] Fan, Y.-J., Pham, M. T., and Huang, C.-J. 2019. "Development of Antimicrobial and Antifouling Universal Coating via Rapid Deposition of Polydopamine and Zwitterionization." *Langmuir* 35:1642-1651.
- [75] Tyler, B. J., Hook, A., Pelster, A., Williams, P. et al. 2017. "Development and characterization of a stable adhesive bond between a poly(dimethylsiloxane) catheter material and a bacterial biofilm resistant acrylate polymer coating." *Biointerphases* 12:02C412.
- [76] Burton, E., Gawande, P. V., Yakandawala, N., LoVetri, K. et al. 2006. "Antibiofilm activity of GlmU enzyme inhibitors against catheter-associated uropathogens." *Antimicrob Agents Chemother* 50:1835-1840.

- [77] Thompson, V. C., Adamson, P. J., Dilag, J., Uswatte Uswatte Liyanage, D. B. et al. 2016. "Biocompatible anti-microbial coatings for urinary catheters." *RSC Adv* 6:53303-53309.
- [78] Adlington, K., Nguyen, N. T., Eaves, E., Yang, J. et al. 2016. "Application of Targeted Molecular and Material Property Optimization to Bacterial Attachment-Resistant (Meth)acrylate Polymers." *Biomacromolecules* 17:2830-2838.
- [79] Zhou, C., Wu, Y., Thappeta, K. R. V., Subramanian, J. T. L. et al. 2017. "In Vivo Anti-Biofilm and Anti-Bacterial Non-Leachable Coating Thermally Polymerized on Cylindrical Catheter." *ACS Appl Mater Interfaces* 9:36269-36280.
- [80] Keum, H., Kim, J. Y., Yu, B., Yu, S. J. et al. 2017. "Prevention of Bacterial Colonization on Catheters by a One-Step Coating Process Involving an Antibiofouling Polymer in Water." *ACS Appl Mater Interfaces* 9:19736-19745.
- [81] Guildford, A., Morris, C., Kitt, O., and Cooper, I. 2018. "The effect of urinary Foley catheter substrate material on the antimicrobial potential of calixerene-based molecules." *J Appl Microbiol* 124:1047-1059.
- [82] Ivanova, K., Fernandes, M. M., Francesko, A., Mendoza, E. et al. 2015. "Quorum-Quenching and Matrix-Degrading Enzymes in Multilayer Coatings Synergistically Prevent Bacterial Biofilm Formation on Urinary Catheters." *ACS Appl Mater Interfaces* 7:27066-27077.
- [83] Ivanova, K., Fernandes, M. M., Mendoza, E., and Tzanov, T. 2015. "Enzyme multilayer coatings inhibit *Pseudomonas aeruginosa* biofilm formation on urinary catheters." *Appl Microbiol Biotechnol* 99:4373-4385.
- [84] Cormio, L., LaForgia, P., LaForgia, D., Siitonen, A. et al. 1997. "Is it possible to prevent bacterial adhesion onto ureteric stents?" *Urol Res* 25:213-216.
- [85] Frant, M., Dayyoub, E., Bakowsky, U., and Liefieith, K. 2018. "Evaluation of a ureteral catheter coating by means of a BioEncrustation in vitro model." *Int J Pharm* 546:86-96.

- [86] Ko, R., Cadieux, P. A., Dalsin, J. L., Lee, B. P. et al. 2008. "First prize: Novel uropathogen-resistant coatings inspired by marine mussels." *J Endourol* 22:1153-1160.
- [87] Stickler, D. J., Evans, A., Morris, N., and Hughes, G. 2002. "Strategies for the control of catheter encrustation." *Int J Antimicrob Agents* 19:499-506.
- [88] Graham, V. M. and Cady, C. N. 2014. "Nano and Microscale Topographies for the Prevention of Bacterial Surface Fouling." *Coatings* 4:37-59.
- [89] Wen, G., Guo, Z., and Liu, W. 2017. "Biomimetic polymeric superhydrophobic surfaces and nanostructures: from fabrication to applications." *Nanoscale* 9:3338-3366.
- [90] Bixler, G. D., Theiss, A., Bhushan, B., and Lee, S. C. 2014. "Anti-fouling properties of microstructured surfaces bio-inspired by rice leaves and butterfly wings." *J Colloid Interface Sci* 419:114-133.
- [91] Pereira, M. O., Kuehn, M., Wuertz, S., Neu, T. et al. 2002. "Effect of flow regime on the architecture of a *Pseudomonas fluorescens* biofilm." *Biotechnol Bioeng* 78:164-171.
- [92] Moreira, J. M. R., Araújo, J. D., Miranda, J. M., Simões, M. et al. 2014. "The effects of surface properties on *Escherichia coli* adhesion are modulated by shear stress." *Colloids Surf B Biointerfaces* 123:1-7.
- [93] Millsap, K. W., Reid, G., van der Mei, H. C., and Busscher, H. J. 1997. "Adhesion of *Lactobacillus* species in urine and phosphate buffer to silicone rubber and glass under flow." *Biomaterials* 18:87-91.
- [94] McClaine, J. W. and Ford, R. M. 2002. "Characterizing the adhesion of motile and nonmotile *Escherichia coli* to a glass surface using a parallel-plate flow chamber." *Biotechnol Bioeng* 78:179-189.
- [95] Ammons, M. C. B., Ward, L. S., and James, G. A. 2011. "Anti-biofilm efficacy of a lactoferrin/xylitol wound hydrogel used in combination with silver wound dressings." *Int Wound J* 8:268-273.

- [96] Carlson, R. P., Taffs, R., Davison, W. M., and Stewart, P. S. 2008. "Anti-biofilm properties of chitosan-coated surfaces." *J Biomater Sci Polym Ed* 19:1035-1046.
- [97] Goeres, D. M., Hamilton, M. A., Beck, N. A., Buckingham-Meyer, K. et al. 2009. "A method for growing a biofilm under low shear at the air-liquid interface using the drip flow biofilm reactor." *Nat Protoc* 4:783-788.
- [98] Azeredo, J., Azevedo, N. F., Briandet, R., Cerca, N. et al. 2017. "Critical review on biofilm methods." *Crit Rev Microbiol* 43:313-351.
- [99] Lawrence, J. R., Swerhone, G. D., and Neu, T. R. 2000. "A simple rotating annular reactor for replicated biofilm studies." *J Microbiol Methods* 42:215-224.
- [100] Coenye, T. and Nelis, H. J. 2010. "In vitro and in vivo model systems to study microbial biofilm formation." *J Microbiol Methods* 83:89-105.
- [101] Willcock, L., Gilbert, P., Holah, J., Wirtanen, G. et al. 2000. "A new technique for the performance evaluation of clean-in-place disinfection of biofilms." *J Ind Microbiol Biotechnol* 25:235-241.
- [102] Lee, J. H., Kaplan, J. B., and Lee, W. Y. 2008. "Microfluidic devices for studying growth and detachment of *Staphylococcus epidermidis* biofilms." *Biomed Microdevices* 10:489-498.
- [103] Tremblay, Y. D., Vogeleer, P., Jacques, M., and Harel, J. 2015. "High-throughput microfluidic method to study biofilm formation and host-pathogen interactions in pathogenic *Escherichia coli*." *Appl Environ Microbiol* 81:2827-2840.
- [104] Shields, R. C. and Burne, R. A. 2016. "Growth of *Streptococcus mutans* in Biofilms Alters Peptide Signaling at the Sub-population Level." *Front Microbiol* 7:1075.
- [105] Situma, C., Hashimoto, M., and Soper, S. A. 2006. "Merging microfluidics with microarray-based bioassays." *Biomol Eng* 23:213-231.

- [106] Wessel, A. K., Hmelo, L., Parsek, M. R., and Whiteley, M. 2013. "Going local: technologies for exploring bacterial micro-environments." *Nat Rev Microbiol* 11:337-348.
- [107] Abaci, H., Drazer, G., and Gerecht, S. 2013. "Recapitulating the vascular microenvironment in microfluidic platforms." *Nano LIFE* 03:1340001.
- [108] Nickel, J. C., Ruseska, I., Wright, J. B., and Costerton, J. W. 1985. "Tobramycin resistance of *Pseudomonas aeruginosa* cells growing as a biofilm on urinary catheter material." *Antimicrob Agents Chemother* 27:619-624.
- [109] Azevedo, A. S., Almeida, C., Gomes, L. C., Ferreira, C. et al. 2017. "An in vitro model of catheter-associated urinary tract infections to investigate the role of uncommon bacteria on the *Escherichia coli* microbial consortium." *Biochem Eng J* 118:64-69.
- [110] Salanitro, J. and Hokanson, J. 1990. "Tubular Biofilm Reactor."
- [111] McCoy, W. F., Bryers, J. D., Robbins, J., and Costerton, J. W. 1981. "Observations of fouling biofilm formation." *Can J Microbiol* 27:910-917.
- [112] Linton, C. J., Sherriff, A., and Millar, M. R. 1999. "Use of a modified Robbins device to directly compare the adhesion of *Staphylococcus epidermidis* RP62A to surfaces." *J Appl Microbiol* 86:194-202.
- [113] Teodósio, J. S., Silva, F. C., Moreira, J. M. R., Simões, M. et al. 2013. "Flow cells as quasi-ideal systems for biofouling simulation of industrial piping systems." *Biofouling* 29:953-966.
- [114] Simões, M., Pereira, M. O., Sillankorva, S., Azeredo, J. et al. 2007. "The effect of hydrodynamic conditions on the phenotype of *Pseudomonas fluorescens* biofilms." *Biofouling* 23:249-258.
- [115] Teodósio, J. S., Simões, M., Melo, L. F., and Mergulhão, F. J. 2011. "Flow cell hydrodynamics and their effects on *E. coli* biofilm formation under different nutrient conditions and turbulent flow." *Biofouling* 27:1-11.

- [116] Teodósio, J. S., Simões, M., and Mergulhão, F. J. 2012. "The influence of nonconjugative *Escherichia coli* plasmids on biofilm formation and resistance." *J Appl Microbiol* 113:373-382.
- [117] Teodósio, J. S., Simões, M., Alves, M. A., Melo, L. F. et al. 2012. "Setup and validation of flow cell systems for biofouling simulation in industrial settings." *Sci World J* 2012:10.
- [118] Chin, M. Y. H., Busscher, H. J., Evans, R., Noar, J. et al. 2006. "Early biofilm formation and the effects of antimicrobial agents on orthodontic bonding materials in a parallel plate flow chamber." *Eur J Orthod* 28:1-7.
- [119] van der Borden, A. J., van der Werf, H., van der Mei, H. C., and Busscher, H. J. 2004. "Electric current-induced detachment of *Staphylococcus epidermidis* biofilms from surgical stainless steel." *Appl Environ Microbiol* 70:6871-6874.
- [120] Lopez-Mila, B., Alves, P., Riedel, T., Dittrich, B. et al. 2018. "Effect of shear stress on the reduction of bacterial adhesion to antifouling polymers." *Bioinspir Biomim* 13:065001.
- [121] Alves, P., Nir, S., Reches, M., and Mergulhão, F. 2018. "The effects of fluid composition and shear conditions on bacterial adhesion to an antifouling peptide-coated surface." *MRS Commun* 8:938-946.
- [122] Velraeds, M. M., van de Belt-Gritter, B., van der Mei, H. C., Reid, G. et al. 1998. "Interference in initial adhesion of uropathogenic bacteria and yeasts to silicone rubber by a *Lactobacillus acidophilus* biosurfactant." *J Med Microbiol* 47:1081-1085.
- [123] Mosayyebi, A., Yue, Q. Y., Somani, B. K., Zhang, X. et al. 2018. "Particle accumulation in ureteral stents is governed by fluid dynamics: in vitro study using a "stent-on-chip" model." *J Endourol* 32:639-646.
- [124] Van Oss, C. J., Chaudhury, M. K., and Good, R. J. 1987. "Monopolar surfaces." *Adv Colloid Interface Sci* 28:35-64.
- [125] Van Oss, C. J., Good, R. J., and Chaudhury, M. K. 1988. "Additive and nonadditive surface tension components and the interpretation of contact angles." *Langmuir* 4:884-891.

- [126] Van Oss, C. J., Ju, L., Chaudhury, M. K., and Good, R. J. 1989. "Estimation of the polar parameters of the surface tension of liquids by contact angle measurements on gels." *J Colloid Interface Sci* 128:313-319.
- [127] Aryal, B. and Neuner, G. 2009. "Leaf wettability decreases along an extreme altitudinal gradient." *Oecologia* 162:1.
- [128] Sjollema, J., Busscher, H. J., and Weerkamp, A. H. 1988. "Deposition of oral streptococci and polystyrene latices onto glass in a parallel plate flow cell." *Biofouling* 1:101-112.
- [129] Bakker, D. P., van der Plaats, A., Verkerke, G. J., Busscher, H. J. et al. 2003. "Comparison of velocity profiles for different flow chamber designs used in studies of microbial adhesion to surfaces." *Appl Environ Microbiol* 69:6280-6287.
- [130] Koseoglu, H., Aslan, G., Esen, N., Sen, B. H. et al. 2006. "Ultrastructural stages of biofilm development of *Escherichia coli* on urethral catheters and effects of antibiotics on biofilm formation." *Urology* 68:942-946.
- [131] Barbosa, J., Cuppini, M., Flach, J., Steffens, C. et al. 2016. "Removal of *Escherichia coli* in boning knives with different sanitizers." *LWT - Food Sci Technol* 71:309-315.
- [132] Gomes, L. C., Silva, L. N., Simoes, M., Melo, L. F. et al. 2015. "*Escherichia coli* adhesion, biofilm development and antibiotic susceptibility on biomedical materials." *J Biomed Mater Res A* 103:1414-1423.
- [133] Adair, C. G., Gorman, S. P., Byers, L. B., Jones, D. S. et al. 2000. "Confocal Laser Scanning Microscopy for Examination of Microbial Biofilms." In *Handbook of Bacterial Adhesion: Principles, Methods, and Applications*, edited by Y.H. An and R.J. Friedman, 249-257. Totowa, NJ: Humana Press.
- [134] Heydorn, A., Nielsen, A. T., Hentzer, M., Sternberg, C. et al. 2000. "Quantification of biofilm structures by the novel computer program COMSTAT." *Microbiology* 146 (Pt 10):2395-2407.

Chapter 4

**POLYDIMETHYLSILOXANE (PDMS):
A PROMISING MATERIAL
FOR BIOLOGICAL APPLICATIONS**

*Sajede Saeidifard, Foozieh Sohrabi
and Seyedeh Mehri Hamidi**

Magneto-plasmonic lab, Laser and Plasma Research Institute,
Shahid Beheshti University, Tehran, Iran

ABSTRACT

The development of PDMS structures emerges versatile and practical applications into industry, biology, medicine, and chemistry. This material is magnificently introduced in biological and medical researches due to its analogous to confined scales of cells and biomolecules dimensions, transparency for applying optical methods, biocompatibility and nontoxicity, possibility of applying different approaches for making the surface hydrophilic and cell adhesive, high conformality with cells and other biostructures, gas permeability for transfer of nutrients and oxygen, and flexibility. So, these properties make PDMS an excellent candidate for understanding the complex biological behaviors, which may be impossible to be investigated by other techniques, and for cutting-edge

* Corresponding Author's E-mail: m_hamidi@sbu.ac.ir.

bio-applications. Therefore, there is a growing interest in utilizing PDMS, driven by the demand of versatile strategies to cell-based assays biosensors, drug delivery, chemical biology applications, and cell differentiation. Besides, combining the plasmonic and PDMS structures has led to the generation of various approaches for thermal therapy, drug delivery, imaging and sensing applications.

1. INTRODUCTION

The continuous growth and development of new materials and novel structures creates up-to-date applications. During the past decades, emergence of novel substances and modern technology led to explosive growth of microfluidic as a potential field in multifunctional technologies such as biochemical [1-3], biological [3-6], clinical [7, 8] and medical studied [2, 9, 10]. By considering the capability of these systems to confine the liquids on the micrometer or even smaller scales close to the cell dimensions, this technology has exhibited great potential for understanding the sophisticated or impossible biological function [11-14]. Furthermore, microfluidic-based fabrication techniques are an enabling tool for mimicking the tissues and organs [15, 16]. The existing crucial challenges in tissue engineering such as the shortage of an organized system for conduction of oxygen and nutrients, and analysis of position, orientation, and metabolic of ambient cells in vasculature networks were solved [3, 16-19]. Currently, the majority of these devices are fabricated from inorganic materials in industry such as in silica or glass [6, 20-22], metals [23, 24], and semiconductors [25, 26]. These materials would be selected for ease of deposition, high thermo-conductivity, excellent strength, and mature processing. However, hardness of them, high cost of fabrication, resistance to organic solvent for functionalization, and not being gas permeable have kept them away from various applications like long-term cell culture [6, 27]. On the other hand, the motivation of elimination of such limitations leads to the introduction of elastomers and plastics as a promising and efficient mean for broader biological applications [20, 27-30]. The vast variety of polymers makes them an excellent candidate for bio-molecular studies [30-33], drug delivery [34-37], and bio-sensing [38-40]. Based on

physical properties of the polymers, they are classified into three groups of elastomers, thermoplastics and thermosets as follows:

- A. *Elastomers*: Elastomers are loosely cross-linked polymers, which are particularly entangled. By applying external force to this material, they can be stretched easily, but return to their original shapes when the force or stress is removed. They display weak inter-molecular forces and their Young's modulus is low. Polydimethylsiloxane (PDMS) is one of the most interesting elastomers because of the excellent optical transparency, ease of fabrication, bonding property to other substrates and elastomeric features. In spite of hydrophobic nature of PDMS, plasma exposure makes its surface hydrophilic. In contrast to glass, silicon, and other hard materials [(e.g., poly (methylmethacrylate) (PMMA) and polycarbonate (PC)], PDMS is gas permeable which is crucial for long-term cell culture and its surface is compatible for cell culture.
- B. *Thermoset polymers*: Thermosets consist of irreversible chains, which are bound together when they are cross-linked. Lack of melting and swelling are their obvious properties. These materials are not suitable for long time cell culture.
- C. *Thermoplastic polymers*: Thermoplastics are polymers which remold multiple times by reaching glass transition temperature. Their main feature is high cross-linking and preservation of their shape after cooling [6]. Higher cross-linking makes these material less flexible and more rigid than elastomers [41]. Unfortunately, not as convenient as PDMS, these polymers do not exhibit conformal contact with other surfaces such as biological cells [6]. Polystyrene (PS), PMMA and PC are the most common thermoplastic polymers. In addition, thermoplastic polymers such as poly(methylmethacrylate) (PMMA), polycarbonate (PC), polystyrene (PS) that are used as a resist in T-NIL hardly satisfy excellent mold releasing properties during the de-molding process

and simultaneously compromise adhesion of mold to the substrate. This creates defects in patterning process [42].

Consequently, among polymers, elastomers especially PDMS has showed great potential for microfluidic systems which are suitable for biological and cell culture applications. Due to the significant properties of PDMS, this material could open a new window for the investigation of cell interactions and behaviors in bio micro-technologies, which enables the simulation of *in vivo* structures in a minimized size [18, 43, 44]. Fortunately, in spite of other polymers such as thermoplastic and thermoset polymers, PDMS conveniently exhibits conformal contact with other surfaces even non-flat surfaces like biological cells [45, 46]. In addition, PDMS has attracted great attention because of its capability for patterning cells on large superficial areas that offers biocompatibility [6, 47, 48]. This material has high transparency, which is suitable for observations of morphological features of cells [48, 49]. Furthermore, the molecular weight of PDMS is low that provides portable point-of-care medical product [50]. In addition, mechanically flexible and bendable substrates compared with rigid substrates such as silicon and glass offers significant advantage in different medical and biological domain [6, 28]. Consequently, the integration of functional high-performance PDMS into biological applications makes it an excellent candidate for biosensors. In 2012, Perez Leonardo and his colleagues [51] developed a micro-pressure sensor in the electrode array, which is applicable in cochlear implant. Ease of patterning via soft lithography as a substantial approach for prototyping of PDMS systems is considered as minimized platforms for tests in chemistry and biology [52, 53]. On the other hand, the development of plasmonic systems as an active area has emerged growing integrated biosensors [54-57]. Combining the plasmonic nanostructures and microfabrication has allowed promising applications particularly powerful analytical tools with highly sensitive and real time detection of biosamples such as protein and biomolecules, which play a central role in various cellular activities [58-60]. Aiming to reflect the trend in PDMS, we focus on the progress of PDMS as a motivating research area after its debut in

1990s especially in biological domain. First, this study presents the development of biological, physical, and chemical characteristics of PDMS employed for biomedical applications and continuously its applications would be discussed.

2. BIOLOGICAL, PHYSICAL, AND CHEMICAL CHARACTERISTICS OF PDMS

2.1. Biocompatibility and Nontoxicity of PDMS

PDMS suggests new opportunities for plenty of structures with cell or subcellular size that makes it attractive for development of cell-based assays. Compared with the inorganic and silicon materials, PDMS was proved to be non-toxic and biocompatible. Ref. [61-63] provide the proof for this fact. Extensive nature of PDMS as a substances capable to sterilization and cell culture make it formidable and promising material for current and future biological applications. As we know, sterilization is one of the most prominent processes of cell culture that intensifies the isolation of cell lines and culture medium from unwanted growth of bacteria, microbes, etc. [64]. Alvaro Mata et al. [65] has implemented tests based on prevalent approaches for sterilization using ethanol (EtOH), ultraviolet light (UV), and steam autoclave (AS) and diverse PDMS (Sylgard 184) prepolymer and cross-linker were combined at various weight ratios (as *PDMS1*, *PDMS2*, *PDMS3*, *PDMS4* and *PDMS5*, corresponding to 5.7, 10.0, 14.3, 21.4, and 42.9 wt.% cross-linker, respectively). Since the evaluation of structure erosion depends on geometrical and surface properties, their SEM studies have not demonstrated any significant variation in patterns, roughness of surface, and hydrophobicity except for one specimen. Different formulations of PDMS have shown validity for biomedical applications. Furthermore, as the culture media contain nutrients and physical growth parameters necessary for microbial growth, Mata and et al. [65] have investigated the influence of cell culture media (α -MEM (Minimum Essential Medium), Gibco, Grand Island, NY) on chemical compounds of PDMS using analysis of X-Ray photoelectron

spectroscopy. Obtained results implies that surfaces of 5 PDMS specimens has not shown major distortion after media immersion except for the presence of nitrogen (N) (2.0% on *PDMS3* to 6.0% on *PDMS1*), and an increase in the O/Si ratio and it is likely for the deposition of existed ingredients upon exposure to the α -MEM Minimum Essential Medium such as amino acids [65]. In addition, PDMS has attracted a lot of attention since applying temperature gradients does not make it damaged. Specifically for the biological applications where the temperature between 40 to 95°C is required for processing of substances. Another point about PDMS that introduces this known material as a nontoxic biocompatible substance is based on this fact that approximately none of the references has declared any different types of toxicity for this material [66, 67]. Consequently, this material is suitable for the studies of tissue, cell [68-69] and proteins [70, 71] because of being nontoxic and gas permeable [44, 72]. Tables (1-3) demonstrate the effects of different toxicities including acute oral, acute dermal, inhalation, and skin irritation. As we observe, approximately no serious hazard was reported.

Table 1. The impact of PDMS rates on acute oral and acute dermal toxicity

| Toxicity type | Species | PDMS viscosity | Hazard rating, LD ₅₀ (mg kg ⁻¹) | References |
|-----------------------|---------------------------|----------------|--|------------|
| Acute oral toxicity | Rat | 1000 | ≥ 4800 | [66] |
| Acute oral toxicity | Rabbit/dog/cat | 140 | ≥ 9800 | [66] |
| Acute dermal toxicity | Rabbit (Male New Zealand) | 350 | No adverse effect at 24h, LD ₅₀ is ≥19400 mg kg ⁻¹ | [66] |
| Acute dermal toxicity | Rabbits | 0.65-1000000 | LD ₅₀ is ≥1020mg kg ⁻¹ | [67] |

Table 2. The effects of PDMS rates on inhalation toxicity [66]

| Toxicity type | Species | PDMS materials | Hazard rating, LD ₅₀ (mg kg ⁻¹) |
|---------------------|------------|--|--|
| Inhalation toxicity | Wistar rat | PDMS(10000 cs) aerosol in 25% solution in white spirit | No observed adverse effect, LC ₅₀ : 4h ≥ 11582 mg m ⁻³ |
| Inhalation toxicity | Wistar rat | Aerosol of 10000 cs PDMS fluid 25% solution in dichloromethane | No observed adverse effect, LC ₅₀ : 4h ≥ 695 mg m ⁻³ |

Table 3. Influence of PDMS on skin irritation [66]

| Toxicity type | Species | PDMS viscosity (cs) | Volume (ml) | Application type | No. of applications | Duration (days) | Effects |
|-----------------|------------|---------------------|-------------|---|---------------------|-----------------|----------------|
| Skin irritation | Rabbits | 100 | 0.5 | Applied to the ears under an occlusive dressing | 1 | 1 | Non irritating |
| Skin irritation | Guinea pig | 100 | 0.5 | Draize method, 10 times per day | 10(daily) | 15 | Non irritating |

2.2. Flexibility and Conformality to Non-Flat Surfaces

In spite of other materials such as glass, silicon, and hard plastics, PDMS has additional advantage that produce a Van der Waals contact (conformal contact) with smooth and non-flat surfaces such as proteins, cells, or biomolecules [73]. Comparatively, PDMS has displayed high conformality with most of the materials. Besides being conformal to non-flat and flat surfaces, flexible PDMS biostructures provide several advantages such as lower invasiveness, portable point-of-care medical product, light-weight, low cost, stretch ability, transparency, capability of implantation and compressed recognition structure [6]. Integration of simpler procedure of fabrication and manipulation of PDMS surface characteristics (e.g., replica molding, casting, injection molding, and embossing) onto mechanically flexible and bendable substrates compared with rigid substrates such as silicon and glass [70, 74-78] offer significant advantage in different biological fields especially where fragile materials would fail. Also, diverse fabrication methods including nanoimprint lithography, electron-beam lithography, dip-pen lithography, scanning probe lithography, and near-field optical lithography have been developed which can create two- or even three dimensional nanoscale structures. Among these methods, there is a growing interest in utilizing of nanoimprint lithography [79]. Nanoimprint lithography makes it possible

to replicate nanostructures from a nano- or micro-scale molds to a light/thermal sensitive polymer resist layer by light or heat. Particularly, nanoimprint lithography based on heat has shown greater demand due to its potential to replicate nanostructures in the polymer and sol-gel derived oxide films [77, 78, 80]. In 2017, Ramendra K. Pal et al. [28] reported a patterned conducting polymer PEDOT:PSS on thin photo curable PDMS membranes via an ink consisting of polymer and a bio-friendly silk protein carrier. This flexible PDMS-based biosensor has the capability of entrapping bio-recognition molecules such as dopamine and ascorbic acid besides glucose. Its flexibility is significantly crucial for applications with involvement of soft and mechanically compliant surfaces [28].

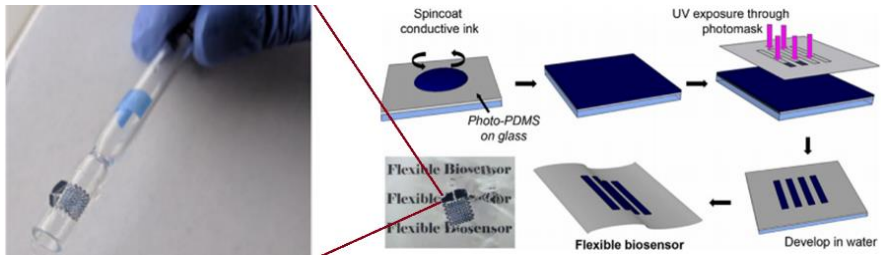


Figure 1. Fabrication of flexible PDMS-based biosensor for biomolecules recognition [28].

2.3. Transparency of PDMS

As we know visible, near infrared and infrared regimes (VIS-NIR and IR) are the most applicable spectrum in biotechnology for optical detection approaches. PDMS is transparent in over a large frequency domain of visible/UV regions (>95%) [81]. Fig.2 shows the spectrum of PDMS with the optical loss in dB/cm. As we see, in the range between 400 nm and 1100 nm approximately no significant loss is observable. This characteristic not only provides the reduction of losses but also makes it a suitable material for optical methods [82].

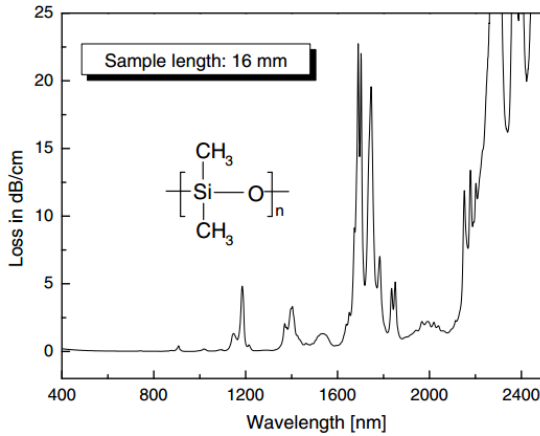


Figure 2. Loss in dB/cm in a PDMS sample [82].

2.4. Exposure to High Energy Treatment for Hydrophilicity

In spite of hydrophobic nature of PDMS (contact angle $\sim 110^\circ$ and water contact angle $\sim 108^\circ \pm 7^\circ$) [18, 83, 84], applying oxygen plasma, UV/ozone treatment, polyelectrolyte multilayers (PEMs), chemical vapor deposition, silanization to PDMS makes its surface hydrophilic or more significantly, let PDMS be sealed to diverse polymers [85, 86]. Table.4 describes the effect of these methods on hydrophobicity, stability, longevity, biocompatibility, and mechanical and optical properties of its surface.

However, hydrophilic microstructures offer numerous advantages with respect to the hydrophobic structures such as increasing cell adhesion to the surface or less air trapping during filling with aqueous solutions or mixtures of aqueous and organic solutions [8, 87]. This has led many groups to devise different methods to render the PDMS surface hydrophilic and resistant to biomolecules adsorption [85]. Alvaro Mata et al. [65] have improved the bonding quality of PDMS to other surfaces by oxygen plasma supply, while applying air recovery for the hydrophobicity.

3. PDMS IN BIOLOGICAL APPLICATIONS

In addition to above-mentioned properties, PDMS proposes the structures with intrinsic dimensions that are comparable with the length scales of eukaryotes and prokaryotic organisms, organelles, proteins, DNA and length scales for diffusion of CO₂ or O₂ into tissues [87]. There is a growing interest in utilizing PDMS, driven by the demand of versatile strategies to interface microfluidics with cell-based assay biosensors [69, 88-90], proteins [91-93], and DNA [94-97]. We organized some of these utilities into categories; summarize them below.

Table 4. Introduction of different approaches for making the PDMS surface hydrophilic and its effects on other parameters [8]

| Approach | WCA(θ) | Throughput/ Stability | Shelf Life (Longevity) | Biocom- patibility | Optical/ Mechanical effect |
|--|-----------|-----------------------------|--|-----------------------|----------------------------------|
| Plasma treatment | 50-60 | Current process | Low (≤3 days) | High | Cracking possible |
| Grafting-to (e.g., plasma, silanization) | ≤10-100 | Low-medium(2-7 added steps) | Medium (14-47 days) | Not reported | Likely not affected |
| Grafting-from (e.g., SLATRP) | 10-80 | Very low (many added steps) | Medium-High (up to 3 month) | Not reported | Likely not affected |
| Physisorption | 15-90 | Low(one-many added steps) | Typically low | Not reported | Likely not affected |
| Past studies with block copolymer(BCP) addition to other pre-I polymer additives | 63-104 | Very high; no added steps | Not reported; BCP or other additives dependent | Not reported | Likely not affected |
| A past study using PDMS-b-PEO addition | 21.5-80.9 | Very high; no added steps | 2 months | Not reported | Likely not affected |
| Current study-Addition of a PDMS- PEG BCP with optimized processing | ≤10-20 | Very high; no added steps | Very high(up to 20 months) | High | None when well-designed |

3.1. Chemical Biology

Several approaches have been proposed for introducing, pumping, isolation and manipulation of materials or cellular organism on the chips

such as electroosmosis and microvalve [99, 100]. However, these two methods introduce some obstacles to control. Quake et al. [101] have devised a method based on soft lithography that is able to fabricate pneumatically activated valves. PDMS systems provide the facility of studying the interactions between proteins, cells and molecules in a multiplexed format. In 2007, Zhuangzhi Wang's team successfully reported the use of PDMS channels and surface plasmon resonance (SPR) imaging method to study the responses of DNA aptamer-human Immunoglobulin E (IgE) [102]. Furthermore, controlling the laminar streams of fluids produces the gradients of biostructure mixtures. On the contrary, other techniques such as gradients with complicated profiles and gradients of gradients cannot provide the gradients of combinatorial layout including immobilized biomolecules on surface [103-105]. In other words, PDMS not only makes it possible to simulate the natural environment especially tissue extracellular matrices with similar geometries [106] but also allows to study the cell behavior in response to the biochemical signaling factors. Gunawan et al. [107] explored the migration and polarity of rat intestinal IEC-6 cells on gradients of extracellular matrix proteins as well as demonstration of laminin gradients on migration of rat IEC-6 intestinal crypt-like cells. Moreover, another useful property of PDMS networks is the isolation of single cells that makes it possible to survey the biochemistry and biophysics of single cells [101]. Ochsner's team have developed a 3D fabricated array to control endothelial cells. This system has the capability to be used for other basic biological studies and cell monitoring tests [108]. In 2019, Gao et al. [109] have presented a minimized model of cellular microenvironments via creation of arrays of microcavities coated by various proteins. Recently, Kenneth H. Hu et al. [110] have proposed a model in which precise spatiotemporal control was accomplished using an atomic force microscope (AFM) that delivered the ligands and blocked the cell-surface receptors.

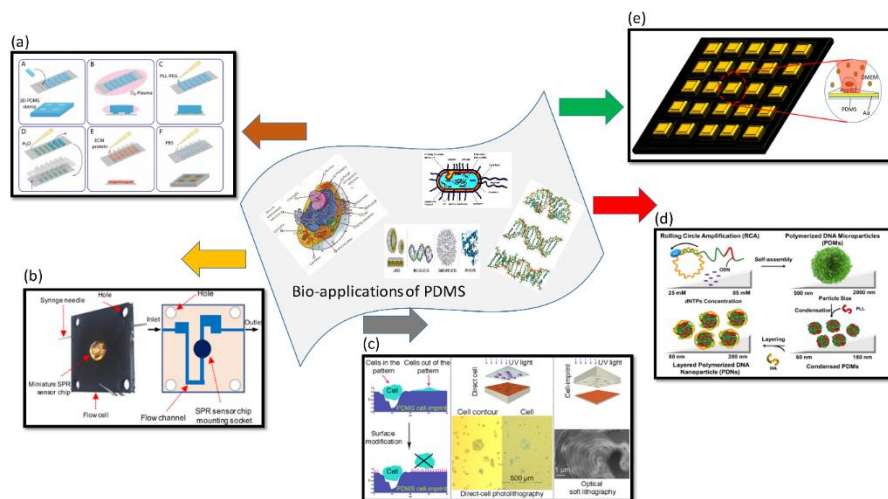


Figure 3. Bio applications of PDMS. From left to right: (a) Fabrication of a microstructured six-channel slide by microscale plasma-initiated protein patterning (μ PIPP) technique [2]. (b) Fabrication of Miniature Surface Plasmon Resonance Sensor for cell adhesion studies and the detection of the cellular interaction [98]. (c) New cell-imprint surface modification techniques based on cell-imprint surface modification techniques based on direct-cell photolithography and optical soft lithography using PDMS [47]. (d) Synthesis of size-tunable polymerized DNA nanoparticles (PDNs) for cancer-targeted drug delivery by sequential processes of rolling circle amplification, condensation, and layer-by-layer assembly [49]. (e) Fabrication of 2D plasmonic biosensor for study of membrane depolarization by infrared laser stimulation [79].

3.2. Drug Release

It is recognized that polymers coating on drug eluting stent (DES) enables controlled and local drug delivery [111]. In 2008, Simmons et al. [112] studied the biostability and biological operation of a siloxane-based polyurethane elastomer (E2A) that had accompanied a therapeutic drug known as dexamethasone acetate (DexA). The research has not reported any significant alteration in biocompatibility of the system (i.e., biostability). In 2010, A. Scott et al. [113] suggested PDMS composite embedded Au nanoparticles in various forms of gels, foams and films. They have utilized these nanocomposites for water filtration, eliminating pollution and releasing the dye fluorescent as a platform for drug delivery.

In 2018, a model for drug containing structures was suggested by Jenny Holländer et al. [114] in which they combined 3D printing technique and UV-assisted crosslinking technology using UV-LED light. In 2019, N.Nagai et al. [115] reported a drug filling system consisting of PDMS silicon reservoir and an injectable gelatin/chitosan gel (iGel) for retina patients. This drug was successfully tested and could be a promising tool to administer the drugs for long-term. In 2019, Keonwook Nam have devised a method for synthesis of size-tunable polymerized DNA nanoparticles for cancer drug delivery by successive procedure of rolling circle amplification(RCA), generation of polymerized DND micro particles (PDMs), their condensation and layering with targeting moiety [49].

3.3. Cell Differentiation

The construction and analysis of systems suitable for mimicking the organ reconstruction ready for implantation is essential [116, 117]. However, there are numerous factors to be considered in developing such networks and implants for example the charge of surface and being commercially available modified cell culture plates [48]. To overcome these problems, several groups have investigated populated cells on different patterned surfaces to conduct more desirable cell growth [17, 118]. PDMS has triggered valuable and excellent topographic modification, surface patterning, cell positioning on desired areas, promote contact with proper targets, and differentiation [48, 119]. In 2008, implemented surface modification of PDMS proposed by Sun-Jung Kim et al. [19] has controlled the proliferation and differentiation of umbilical cord blood-derived mesenchymal stem cells (UCB-MSCs). This study has opened up a new insight into stem cell therapy. In 2010, Bédier et al. [120] studied the effects of micropatterns and molecular coating for neuronal cells (Neuro2a cell line) growth and the differentiation on PDMS substrate. They utilized the carbon nanotube coating and optimal patterns which resulted in the differentiation rate close to 100%. In 2019, Kavand et al. [47] have presented a new approach for cell-imprint surface modification

in which direct-cell photolithography and standard optical contact lithography process were used to imprint mesenchymal stem cells.

3.4. Sensing

The development of a vehicle for real-time and non-invasive analysis of biostructures that would generate hazard health risks or could be susceptible to danger seems necessary. PDMS-based platform is one of the best elements for sensing these biological hazards that threaten health condition, or require to be displayed following status of patient [121-123]. In 2003, Paranjape et al. [121] fabricated a bi-layer PDMS dermal patch for transdermal glucose sensing. Asadishad et al. [124] have optically described the impact of addicting nicotine chemical on colon cells cultured on a 2D plasmonic chip. In 2013, Zuo et al. [20] integrated a hybrid layout with graphene-oxide biosensors that have showed great potential for the detection of a wide variety of bacterial and viral pathogens. In 2019, Nootchanatet et al. [98] has focused on the fabrication of a novel plasmonomechanical optical biosensor placed in a microfluidic channel as a new tool for cell adhesion studies and the detection of the cellular interaction. Recently, Asadishad et al. [125] have successfully investigated the effects of addicting methadone and tramadol drugs on mesenchyme cells that have receptors of pain.

3.5. Plasmonic Platforms

The ability of nanoimprint lithography for fabrication of structures with arbitrary geometries has considered as a mainstream of fabrication methods in semiconductor industry. The increasing development of new tools and techniques has brought this innovatory method into some areas of emerging fields of research from photonics to biotechnology [126, 127]. On the other hand, recent advances in plasmonics has attracted an outburst attention for a wide range of applications in biosensing [128-132], photo

thermal therapy [132-135], environmental and agricultural pollutants [136, 137], drug delivery [138-140], and imaging [141-143]. By considering the ability of this technology beyond diffraction limit, possibility of confinement of electromagnetic fields at subwavelength scale close to bio particles, being label-free and real-time, and signal enhancement, the implementation based on plasmonic resonance could open a new avenue for detection of bio particles and bio approaches at the molecular level [79, 131]. Nanoimprint lithography is becoming mature technology as a potential platform for patterning at the nanoscale with high throughput and controlled precision especially for manufacturing the grating coupled nanostructures that play an important role in bio-plasmonic platforms [144-149]. In addition, the challenges of grating fabrication have undoubtedly led to an upsurge in the investigation of various soft polymers as a patterned substrate and nanoimprint lithography as an attainable approach with high resolution, parallel, high throughput and moreover economical process [150]. As mentioned before, PDMS acts an excellent candidate for this purpose. Consequently, there is a plethora of examples in the literature that proves the potential effect of grating plasmonic structures and nano-biosensor tools for utilization in cell biology [151-154]. In 2016, Kahraman et al. [154] presented a convenient and novel model comprising the combination of soft lithography and nanosphere lithography in which they used size tunable and mechanically flexible PDMS latex coated by Ag. They have shown that high SERS enhancement could be a great promising mean for detection and characterization of proteins.

Combination of polymer compounds and nanostructures have indicated great potential for targeted drug delivery. Nanostructures could be used for broad range of applications where polymer network keeps the nanoparticles stabilized [113]. They use their harnessed photothermal and biocompatibility properties coupled with thermal and elastic characteristics of PDMS polymer [155, 156]. The photothermal effect could be adjusted by controlling the morphology of plasmonic structures [157]. Recently, the use of nanostructure-composited polymer as a plasmonic heat patch was proposed for bioapplications such as photothermal tumor therapy, bioimaging, and drug delivery [157-160]. In 2019, Saeidifard et al. [79]

have studied the membrane depolarization of Hep-G2 and mesenchymal cells cultured on 2D plasmonic chip by nanoimprint lithography under infrared laser irradiation without any need for functionalization. They have utilized photothermal impact of plasmonic layer coated on 2D chip for detection of the membrane activity which relied on changes of refractive index in the vicinity of the gold surface. Furthermore, neural cell activity based on different mechanisms could be assessed by nanostructures. Sohrabi et al. [161] have proposed a prototyping methodology by which they could record the neural activity of the cerebellum tissue slice cultured on a flexible plasmonic interface under electrical and chemical stimulations. In 2019, Asadishad et al. [162] have intensified the coupling of plasmonic hotspots of Au nanostructures and fluorophore from the green fluorescence proteins. In 2019, Nootchanat et al. [98] has fabricated SPR chips based on PDMS for detection of human immunoglobulin G.

CONCLUSION

In summary, we portrayed PDMS polymer as a bio-friendly composition whose physical, optical, mechanical, biological, and chemical properties make it an excellent candidate for biomedical, biochemical, and cell studies. PDMS is a particularly attractive material for fabrication of cell culture platform due to its flexibility, biocompatibility, transparency, permeability to gases, and ease of patterning. In addition, its high gas permeability and optical transparency enables easy on-chip cell culture and detection, respectively. Furthermore, advances in soft lithography has opened up possibility for surface patterning, thus facilitating desired forms and dimensions. Mentioned argues provide a number of advantageous features for drug delivery, cell differentiation, sensing, and biochemistry fields. In addition, the combination of PDMS and plasmonics has emerged as a promising concept for drug delivery, intensified photothermal effect, stimulation of cell, and optical imaging methods.

REFERENCES

- [1] Meldrum, D. R., & Holl, M. R. (2002). Microscale bioanalytical systems. *Science*, 297(5584), 1197-1198.
- [2] Ertl, P., & Rothbauer, M. (Eds.). (2018). *Cell-Based Microarrays*. Springer New York.
- [3] Yeo, L. Y., Chang, H. C., Chan, P. P., & Friend, J. R. (2011). Microfluidic devices for bioapplications. *Small*, 7(1), 12-48.
- [4] Munoz-Garcia, J., Babic, J., & Coudreuse, D. (2018). Drug delivery and temperature control in microfluidic chips during live-cell imaging experiments. In *Methods in cell biology* (Vol. 147, pp. 3-28). Academic Press.
- [5] Reyes, D. R., Iossifidis, D., Auroux, P. A., & Manz, A. (2002). Micro total analysis systems. 1. Introduction, theory, and technology. *Analytical chemistry*, 74(12), 2623-2636.
- [6] Ren, K., Zhou, J., & Wu, H. (2013). Materials for microfluidic chip fabrication. *Accounts of chemical research*, 46(11), 2396-2406.
- [7] Fonseca-Santos, B., Bonifácio, B. V., Baub, T. M., Gremião, M. P. D., & Chorilli, M. (2019). *In-Situ* Gelling Liquid Crystal Mucoadhesive Vehicle for Curcumin Buccal Administration and Its Potential Application in the Treatment of Oral Candidiasis. *Journal of biomedical nanotechnology*, 15(6), 1334-1344.
- [8] Gökaltun, A., Kang, Y. B. A., Yarmush, M. L., Usta, O. B., & Asatekin, A. (2019). Simple Surface Modification of Poly (dimethylsiloxane) via Surface Segregating Smart Polymers for Biomicrofluidics. *Scientific reports*, 9(1), 7377.
- [9] Zhang, H., & Chiao, M. (2015). Anti-fouling coatings of poly (dimethylsiloxane) devices for biological and biomedical applications. *Journal of medical and biological engineering*, 35(2), 143-155.
- [10] Wang, J. D., Douville, N. J., Takayama, S., & ElSayed, M. (2012). Quantitative analysis of molecular absorption into PDMS microfluidic channels. *Annals of biomedical engineering*, 40(9), 1862-1873.

- [11] Marre, S., & Jensen, K. F. (2010). Synthesis of micro and nanostructures in microfluidic systems. *Chemical Society Reviews*, 39(3), 1183-1202.
- [12] Blazej, R. G., Kumaresan, P., & Mathies, R. A. (2006). Microfabricated bioprocessor for integrated nanoliter-scale Sanger DNA sequencing. *Proceedings of the National Academy of Sciences*, 103(19), 7240-7245.
- [13] Mu, X., Zheng, W., Sun, J., Zhang, W., & Jiang, X. (2013). Microfluidics for manipulating cells. *Small*, 9(1), 9-21
- [14] Ren, K., Chen, Y., & Wu, H. (2014). New materials for microfluidics in biology. *Current opinion in biotechnology*, 25, 78-85.
- [15] Ghaemmaghami, A. M., Hancock, M. J., Harrington, H., Kaji, H., & Khademhosseini, A. (2012). Biomimetic tissues on a chip for drug discovery. *Drug discovery today*, 17(3-4), 173-181.
- [16] Chung, B. G., Lee, K. H., Khademhosseini, A., & Lee, S. H. (2012). Microfluidic fabrication of microengineered hydrogels and their application in tissue engineering. *Lab on a Chip*, 12(1), 45-59.
- [17] Leclerc, E., Corlu, A., Griscom, L., Baudoin, R., & Legallais, C. (2006). Guidance of liver and kidney organotypic cultures inside rectangular silicone microchannels. *Biomaterials*, 27(22), 4109-4119.
- [18] Toepke, M. W., & Beebe, D. J. (2006). PDMS absorption of small molecules and consequences in microfluidic applications. *Lab on a Chip*, 6(12), 1484-1486.
- [19] Kim, S. J., Lee, J. K., Kim, J. W., Jung, J. W., Seo, K., Park, S. B.,... & Lee, Y. S. (2008). Surface modification of polydimethylsiloxane (PDMS) induced proliferation and neural-like cells differentiation of umbilical cord blood-derived mesenchymal stem cells. *Journal of Materials Science: Materials in Medicine*, 19(8), 2953-2962.
- [20] Zuo, P., Li, X., Dominguez, D. C., & Ye, B. C. (2013). A PDMS/paper/glass hybrid microfluidic biochip integrated with aptamer-functionalized graphene oxide nano-biosensors for one-step multiplexed pathogen detection. *Lab on a Chip*, 13(19), 3921-3928.

- [21] Bu, M., Melvin, T., Ensell, G. J., Wilkinson, J. S., & Evans, A. G. (2004). A new masking technology for deep glass etching and its microfluidic application. *Sensors and Actuators A: Physical*, 115(2-3), 476-482.
- [22] Grosse, A., Grewe, M., & Fouckhardt, H. (2001). Deep wet etching of fused silica glass for hollow capillary optical leaky waveguides in microfluidic devices. *Journal of micromechanics and microengineering*, 11(3), 257.
- [23] Kim, D., Lee, Y., Lee, D. W., Choi, W., Yoo, K., & Lee, J. B. J. (2015). Hydrochloric acid-impregnated paper for gallium-based liquid metal microfluidics. *Sensors and Actuators B: Chemical*, 207, 199-205.
- [24] Allen, P. B., Rodriguez, I., Kuyper, C. L., Lorenz, R. M., Spicar-Mihalic, P., Kuo, J. S., & Chiu, D. T. (2003). Selective electroless and electrolytic deposition of metal for applications in microfluidics: Fabrication of a microthermocouple. *Analytical chemistry*, 75(7), 1578-1583.
- [25] Henning, A. K. (1998, March). Microfluidic mems. In *1998 IEEE Aerospace Conference Proceedings (Cat. No. 98TH8339)* (Vol. 1, pp. 471-486). IEEE.
- [26] Henning, A. K., Fitch, J. S., Harris, J. M., Dehan, E. B., Cozad, B. A., Christel, L.,... & Weber, W. A. (1998). Microfluidic MEMS for semiconductor processing. *IEEE Transactions on Components, Packaging, and Manufacturing Technology: Part B*, 21(4), 329-337.
- [27] Domachuk, P., Tsioris, K., Omenetto, F. G., & Kaplan, D. L. (2010). Bio-microfluidics: biomaterials and biomimetic designs. *Advanced materials*, 22(2), 249-260.
- [28] Pal, R. K., Pradhan, S., Narayanan, L., & Yadavalli, V. K. (2018). Micropatterned conductive polymer biosensors on flexible PDMS films. *Sensors and Actuators B: Chemical*, 259, 498-504.
- [29] Park, T., Lee, S., Seong, G. H., Choo, J., Lee, E. K., Kim, Y. S.,... & Lee, S. (2005). Highly sensitive signal detection of duplex dye-labelled DNA oligonucleotides in a PDMS microfluidic chip:

- confocal surface-enhanced Raman spectroscopic study. *Lab on a Chip*, 5(4), 437-442.
- [30] Liu, E. Y., Jung, S., Weitz, D. A., Yi, H., & Choi, C. H. (2018). High-throughput double emulsion-based microfluidic production of hydrogel microspheres with tunable chemical functionalities toward biomolecular conjugation. *Lab on a Chip*, 18(2), 323-334.
- [31] Jang, H., Pawate, A., Bhargava, R., & Kenis, P. (2019). Polymeric microfluidic continuous flow mixer combined with hyperspectral FT-IR imaging for studying rapid biomolecular events. *Lab on a Chip*.
- [32] Ismagilov, R. F., Tice, J. D., Gerdt, C. J., & Zheng, B. (2018). *U.S. Patent Application No. 15/926,985*.
- [33] Fathollahi, B., Stearns, D. G., & Whalen, W. (2019). *U.S. Patent No. 10,488,321*. Washington, DC: U.S. Patent and Trademark Office.
- [34] Chen, K., Merkel, T. J., Pandya, A., Napier, M. E., Luft, J. C., Daniel, W.,... & DeSimone, J. M. (2012). Low modulus biomimetic microgel particles with high loading of hemoglobin. *Biomacromolecules*, 13(9), 2748-2759.
- [35] Badruddoza, A. Z. M., Godfrin, P. D., Myerson, A. S., Trout, B. L., & Doyle, P. S. (2016). Core-Shell Composite Hydrogels for Controlled Nanocrystal Formation and Release of Hydrophobic Active Pharmaceutical Ingredients. *Advanced healthcare materials*, 5(15), 1960-1968.
- [36] Munoz-Garcia, J., Babic, J., & Coudreuse, D. (2018). Drug delivery and temperature control in microfluidic chips during live-cell imaging experiments. In *Methods in cell biology* (Vol. 147, pp. 3-28). Academic Press.
- [37] Iyer, M. A., & Eddington, D. T. (2019). Storing and releasing rhodamine as a model hydrophobic compound in polydimethylsiloxane microfluidic devices. *Lab on a Chip*, 19(4), 574-579.
- [38] Solis-Tinoco, V., Marquez, S., Quesada-Lopez, T., Villarroja, F., Homs-Corbera, A., & Lechuga, L. M. (2019). Building of a flexible microfluidic plasmid-nanomechanical biosensor for live cell analysis. *Sensors and Actuators B: Chemical*, 291, 48-57.

- [39] Hu, L., Ge, A., Wang, X., Wang, S., Yue, X., Wang, J.,... & Liu, B. F. (2018). Real-time monitoring of immune responses under pathogen invasion and drug interference by integrated microfluidic device coupled with worm-based biosensor. *Biosensors and Bioelectronics*, 110, 233-238.
- [40] Zirath, H., Rothbauer, M., Spitz, S., Bachmann, B., Jordan, C., Müller, B.,... & Holnthoner, W. (2018). Every breath you take: non-invasive real-time oxygen biosensing in two-and three-dimensional microfluidic cell models. *Frontiers in physiology*, 9, 815.
- [41] Lampman, S. (2003). *Characterization and failure analysis of plastics*. Asm International.
- [42] Guo, L. J. (2004). Recent progress in nanoimprint technology and its applications. *Journal of Physics D: Applied Physics*, 37(11), R123.
- [43] Shin, Y., Han, S., Jeon, J. S., Yamamoto, K., Zervantonakis, I. K., Sudo, R.,... & Chung, S. (2012). Microfluidic assay for simultaneous culture of multiple cell types on surfaces or within hydrogels. *Nature protocols*, 7(7), 1247.
- [44] Leclerc, E., Sakai, Y., & Fujii, T. (2004). Microfluidic PDMS (polydimethylsiloxane) bioreactor for large-scale culture of hepatocytes. *Biotechnology progress*, 20(3), 750-755.
- [45] Ng, J. M., Gitlin, I., Stroock, A. D., & Whitesides, G. M. (2002). Components for integrated poly (dimethylsiloxane) microfluidic systems. *Electrophoresis*, 23(20), 3461-3473.
- [46] Neils, C., Tyree, Z., Finlayson, B., & Folch, A. (2004). Combinatorial mixing of microfluidic streams. *Lab on a Chip*, 4(4), 342-350.
- [47] Kavand, H., van Lintel, H., Bakhshi Sichani, S., Bonakdar, S., Kavand, H., Koohsorkhi, J., & Renaud, P. (2019). Cell-Imprint Surface Modification by Contact Photolithography-Based Approaches: Direct-Cell Photolithography and Optical Soft Lithography Using PDMS Cell Imprints. *ACS applied materials & interfaces*, 11(11), 10559-10566.
- [48] Bani-Yaghoub, M., Tremblay, R., Voicu, R., Mealing, G., Monette, R., Py, C.,... & Sikorska, M. (2005). Neurogenesis and neuronal

- communication on micropatterned neurochips. *Biotechnology and bioengineering*, 92(3), 336-345.
- [49] Nam, K., Kim, T., Kim, Y. M., Yang, K., Choe, D., Mensah, L. B.,... & Roh, Y. H. (2019). Size-controlled synthesis of polymerized DNA nanoparticles for targeted anticancer drug delivery. *Chemical Communications*, 55(34), 4905-4908.
- [50] Kuo, A. C. (1999). Polymer data handbook. *Polymer Data Handbook*, 962.
- [51] Perez, L., Puers, R., & Volckaerts, B. *Fabrication of an Implantable Micro-pressure Sensor to Measure Deviation within the Cochlea*.
- [52] Xia, Y., & Whitesides, G. M. (1998). Soft lithography. *Annual review of materials science*, 28(1), 153-184.
- [53] Wyart, C., Ybert, C., Bourdieu, L., Herr, C., Prinz, C., & Chatenay, D. (2002). Constrained synaptic connectivity in functional mammalian neuronal networks grown on patterned surfaces. *Journal of neuroscience methods*, 117(2), 123-131.
- [54] Xiao, F., Li, Y., Zan, X., Liao, K., Xu, R., & Duan, H. (2012). Growth of metal-metal oxide nanostructures on freestanding graphene paper for flexible biosensors. *Advanced Functional Materials*, 22(12), 2487-2494.
- [55] Labroo, P., & Cui, Y. (2013). Flexible graphene bio-nanosensor for lactate. *Biosensors and Bioelectronics*, 41, 852-856.
- [56] Polavarapu, L., & Liz-Marzán, L. M. (2013). Towards low-cost flexible substrates for nanoplasmonic sensing. *Physical Chemistry Chemical Physics*, 15(15), 5288-5300.
- [57] Focsan, M., Craciun, A. M., Potara, M., Leordean, C., Vulpoi, A., Maniu, D., & Astilean, S. (2017). Flexible and tunable 3D gold nanocups platform as plasmonic biosensor for specific dual LSPR-SERS immuno-detection. *Scientific reports*, 7(1), 14240.
- [58] Yuca, E., & Tamerler, C. (2019). Self-Assembled Recombinant Proteins on Metallic Nanoparticles as Bimodal Imaging Probes. *JOM*, 71(4), 1281-1290.
- [59] Park, K., Woo, M. A., Lim, J. A., Kim, Y. R., Choi, S. W., & Lim, M. C. (2018). In situ synthesis of directional gold nanoparticle arrays

- along ridge cracks of PDMS wrinkles. *Colloids and Surfaces A: Physicochemical and Engineering Aspects*, 558, 186-191.
- [60] Zhao, D., Liu, Y., Zhang, Q., Zhang, Y., Zhang, W., Duan, Q.,... & Sang, S. (2019). Surface stress-based biosensor with stable conductive AuNPs network for biomolecules detection. *Applied Surface Science*.
- [61] Qin, D., Xia, Y., & Whitesides, G. M. (2010). Soft lithography for micro-and nanoscale patterning. *Nature protocols*, 5(3), 491.
- [62] Khanafer, K., Duprey, A., Schlicht, M., & Berger, R. (2009). Effects of strain rate, mixing ratio, and stress-strain definition on the mechanical behavior of the polydimethylsiloxane (PDMS) material as related to its biological applications. *Biomedical microdevices*, 11(2), 503.
- [63] Samel, B., Griss, P., & Stemme, G. (2007). A thermally responsive PDMS composite and its microfluidic applications. *Journal of Microelectromechanical systems*, 16(1), 50-57.
- [64] Davis, J. M. (Ed.). (2011). *Animal cell culture: essential methods*. John Wiley & Sons.
- [65] Mata, A., Fleischman, A. J., & Roy, S. (2005). Characterization of polydimethylsiloxane (PDMS) properties for biomedical micro/nanosystems. *Biomedical microdevices*, 7(4), 281-293.
- [66] *Joint Assessment of Commodity Chemicals No. 26, Linear Polydimethylsiloxanes* (viscosity $10 \pm 100,000$ centistokes). European Centre for Ecotoxicology and Toxicology of Chemicals, Brussels, 1994 (and references therein).
- [67] *MDMS of Silicone Fluid SWS101*. Wacker Silicone Corp., 1996.
- [68] Leclerc, E., Sakai, Y., & Fujii, T. (2003). Cell culture in 3-dimensional microfluidic structure of PDMS (polydimethylsiloxane). *Biomedical microdevices*, 5(2), 109-114.
- [69] Mi, Y., Chan, Y., Trau, D., Huang, P., & Chen, E. (2006). Micromolding of PDMS scaffolds and microwells for tissue culture and cell patterning: A new method of microfabrication by the self-assembled micropatterns of diblock copolymer micelles. *Polymer*, 47(14), 5124-5130.

- [70] Yamamoto, T., Fujii, T., & Nojima, T. (2002). PDMS–glass hybrid microreactor array with embedded temperature control device. Application to cell-free protein synthesis. *Lab on a Chip*, 2(4), 197-202.
- [71] Atsuta, K., Noji, H., & Takeuchi, S. (2004). Micro patterning of active proteins with perforated PDMS sheets (PDMS sieve). *Lab on a Chip*, 4(4), 333-336.
- [72] Singh, A., Freeman, B. D., & Pinnau, I. (1998). Pure and mixed gas acetone/nitrogen permeation properties of polydimethylsiloxane [PDMS]. *Journal of Polymer Science Part B: Polymer Physics*, 36(2), 289-301.
- [73] Chiu, D. T., Jeon, N. L., Huang, S., Kane, R. S., Wargo, C. J., Choi, I. S.,... & Whitesides, G. M. (2000). Patterned deposition of cells and proteins onto surfaces by using three-dimensional microfluidic systems. *Proceedings of the National Academy of Sciences*, 97(6), 2408-2413.
- [74] McDonald, J. C., & Whitesides, G. M. (2002). Poly (dimethylsiloxane) as a material for fabricating microfluidic devices. *Accounts of chemical research*, 35(7), 491-499.
- [75] McDonald, J. C., Duffy, D. C., Anderson, J. R., Chiu, D. T., Wu, H., Schueller, O. J., & Whitesides, G. M. (2000). Fabrication of microfluidic systems in poly (dimethylsiloxane). *ELECTROPHORESIS: An International Journal*, 21(1), 27-40.
- [76] Stroock, A. D., & Whitesides, G. M. (2003). Controlling flows in microchannels with patterned surface charge and topography. *Accounts of chemical research*, 36(8), 597-604.
- [77] Mbarak, H., Hamidi, S. M., Mohajerani, E., & Zaatar, Y. (2019). Electrically driven flexible 2D plasmonic structure based on a nematic liquid crystal. *Journal of Physics D: Applied Physics*, 52(41), 415106.
- [78] Haddawi, S. F., Mirahmadi, M., Mbarak, H., Kodeary, A. K., Ghasemi, M., & Hamidi, S. M. (2019). Footprint of plexcitonic states in low-power green–blue plasmonic random laser. *Applied Physics A*, 125(12), 843.

- [79] Saeidifard, S., Sohrabi, F., Ghazimoradi, M. H., Hamidi, S. M., Farivar, S., & Ansari, M. A. (2019). Two-dimensional plasmonic biosensing platform: Cellular activity detection under laser stimulation. *Journal of Applied Physics*, 126(10), 104701.
- [80] Kumari, S., Mohapatra, S., & Moirangthem, R. S. (2017). Development of flexible plasmonic plastic sensor using nanograting textured laminating film. *Materials Research Express*, 4(2), 025008.
- [81] Chang-Yen, D. A., Eich, R. K., & Gale, B. K. (2005). A monolithic PDMS waveguide system fabricated using soft-lithography techniques. *Journal of lightwave technology*, 23(6), 2088.
- [82] Cai, D. K., Neyer, A., Kuckuk, R., & Heise, H. M. (2008). Optical absorption in transparent PDMS materials applied for multimode waveguides fabrication. *Optical materials*, 30(7), 1157-1161.
- [83] Ren, K., Zhao, Y., Su, J., Ryan, D., & Wu, H. (2010). Convenient method for modifying poly (dimethylsiloxane) to be airtight and resistive against absorption of small molecules. *Analytical chemistry*, 82(14), 5965-5971.
- [84] Wu, M. H., Urban, J. P., Cui, Z., & Cui, Z. F. (2006). Development of PDMS microreactor with well-defined and homogenous culture environment for chondrocyte 3-D culture. *Biomedical microdevices*, 8(4), 331-340.
- [85] Gokaltun, A., Yarmush, M. L., Asatekin, A., & Usta, O. B. (2017). Recent advances in nonbiofouling PDMS surface modification strategies applicable to microfluidic technology. *Technology*, 5(01), 1-12.
- [86] Whitesides, G. M., Ostuni, E., Takayama, S., Jiang, X., & Ingber, D. E. (2001). Soft lithography in biology and biochemistry. *Annual review of biomedical engineering*, 3(1), 335-373.
- [87] Hu, S., Ren, X., Bachman, M., Sims, C. E., Li, G. P., & Allbritton, N. (2002). Surface modification of poly (dimethylsiloxane) microfluidic devices by ultraviolet polymer grafting. *Analytical chemistry*, 74(16), 4117-4123.

- [88] Sia, S. K., & Whitesides, G. M. (2003). Microfluidic devices fabricated in poly (dimethylsiloxane) for biological studies. *Electrophoresis*, 24(21), 3563-3576.
- [89] Fu, A. Y., Spence, C., Scherer, A., Arnold, F. H., & Quake, S. R. (1999). A microfabricated fluorescence-activated cell sorter. *Nature biotechnology*, 17(11), 1109.
- [90] Chumbimuni-Torres, K. Y., Coronado, R. E., Mfuh, A. M., Castro-Guerrero, C., Silva, M. F., Negrete, G. R.,... & Garcia, C. D. (2011). Adsorption of proteins to thin-films of PDMS and its effect on the adhesion of human endothelial cells. *RSC advances*, 1(4), 706-714.
- [91] Volcke, C., Gandhiraman, R. P., Basabe-Desmonts, L., Iacono, M., Gubala, V., Cecchet, F.,... & Williams, D. E. (2010). Protein pattern transfer for biosensor applications. *Biosensors and Bioelectronics*, 25(6), 1295-1300.
- [92] Wang, L., Lei, L., Ni, X. F., Shi, J., & Chen, Y. (2009). Patterning bio-molecules for cell attachment at single cell levels in PDMS microfluidic chips. *Microelectronic Engineering*, 86(4-6), 1462-1464.
- [93] Hu, G., Gao, Y., Sherman, P. M., & Li, D. (2005). A microfluidic chip for heterogeneous immunoassay using electrokinetical control. *Microfluidics and nanofluidics*, 1(4), 346-355.
- [94] Sims, P. A., Greenleaf, W. J., Duan, H., & Xie, X. S. (2011). Fluorogenic DNA sequencing in PDMS microreactors. *Nature methods*, 8(7), 575.
- [95] Fredonnet, J., Foncy, J., Lamarre, S., Cau, J. C., Trévisiol, E., Peyrade, J. P.,... & Séverac, C. (2013). Dynamic PDMS inking for DNA patterning by soft lithography. *Microelectronic Engineering*, 111, 379-383.
- [96] Pasquardini, L., Potrich, C., Quaglio, M., Lamberti, A., Guastella, S., Lunelli, L.,... & Pederzoli, C. (2011). Solid phase DNA extraction on PDMS and direct amplification. *Lab on a Chip*, 11(23), 4029-4035.
- [97] Khodakov, D. A., Thredgold, L. D., Lenahan, C. E., Andersson, G. A., Kobus, H., & Ellis, A. V. (2011, December). Surface modification of poly (dimethylsiloxane)(PDMS) microchannels with

- DNA capture-probes for potential use in microfluidic DNA analysis systems. In *Smart Nano-Micro Materials and Devices* (Vol. 8204, p. 82040J). International Society for Optics and Photonics.
- [98] Nootchanat, S., Jaikeandee, W., Yaiwong, P., Lertvachirapaiboon, C., Shinbo, K., Kato, K.,... & Baba, A. (2019). Fabrication of Miniature Surface Plasmon Resonance Sensor Chips by Using Confined Sessile Drop Technique. *ACS applied materials & interfaces*, 11(12), 11954-11960.
- [99] Zhang, W., Lin, S., Wang, C., Hu, J., Li, C., Zhuang, Z.,... & Yang, C. J. (2009). PMMA/PDMS valves and pumps for disposable microfluidics. *Lab on a Chip*, 9(21), 3088-3094.
- [100] Weibel, D. B., & Whitesides, G. M. (2006). Applications of microfluidics in chemical biology. *Current opinion in chemical biology*, 10(6), 584-591.
- [101] Unger, M. A., Chou, H. P., Thorsen, T., Scherer, A., & Quake, S. R. (2000). Monolithic microfabricated valves and pumps by multilayer soft lithography. *Science*, 288(5463), 113-.
- [102] Wang, Z., Wilkop, T., Xu, D., Dong, Y., Ma, G., & Cheng, Q. (2007). Surface plasmon resonance imaging for affinity analysis of aptamer-protein interactions with PDMS microfluidic chips. *Analytical and bioanalytical chemistry*, 389(3), 819-825.
- [103] Jiang, X., Xu, Q., Dertinger, S. K., Stroock, A. D., Fu, T. M., & Whitesides, G. M. (2005). A general method for patterning gradients of biomolecules on surfaces using microfluidic networks. *Analytical chemistry*, 77(8), 2338-2347.
- [104] Dertinger, S. K., Chiu, D. T., Jeon, N. L., & Whitesides, G. M. (2001). Generation of gradients having complex shapes using microfluidic networks. *Analytical Chemistry*, 73(6), 1240-1246.
- [105] Pihl, J., Sinclair, J., Sahlin, E., Karlsson, M., Petterson, F., Olofsson, J., & Orwar, O. (2005). Microfluidic gradient-generating device for pharmacological profiling. *Analytical Chemistry*, 77(13), 3897-3903.
- [106] Paguirigan, A., & Beebe, D. J. (2006). Gelatin based microfluidic devices for cell culture. *Lab on a Chip*, 6(3), 407-413.

- [107] Gunawan, R. C., Silvestre, J., Gaskins, H. R., Kenis, P. J., & Leckband, D. E. (2006). Cell migration and polarity on microfabricated gradients of extracellular matrix proteins. *Langmuir*, 22(9), 4250-4258.
- [108] MichelleáGrandin, H. (2007). Micro-well arrays for 3D shape control and high resolution analysis of single cells. *Lab on a Chip*, 7(8), 1074-1077.
- [109] Gao, X., Stoecklin, C., Zhang, Y., Weng, Z., De Mets, R., Greci, G., & Viasnoff, V. (2018). Artificial microniche array with spatially structured biochemical cues. In *Cell-Based Microarrays* (pp. 55-66). Humana Press, New York, NY.
- [110] Hu, K. H., Bruce, M. A., Liu, J., & Butte, M. J. (2019). Biochemical Stimulation of Immune Cells and Measurement of Mechanical Responses Using Atomic Force Microscopy. *Current protocols in chemical biology*, e63.
- [111] Serruys, P. W., Kutryk, M. J., & Ong, A. T. (2006). Coronary-artery stents. *New England Journal of Medicine*, 354(5), 483-495.
- [112] Simmons, A., Padsalgikar, A. D., Ferris, L. M., & Poole-Warren, L. A. (2008). Biostability and biological performance of a PDMS-based polyurethane for controlled drug release. *Biomaterials*, 29(20), 2987-2995.
- [113] Scott, A., Gupta, R., & Kulkarni, G. U. (2010). A Simple Water-Based Synthesis of Au Nanoparticle/PDMS Composites for Water Purification and Targeted Drug Release. *Macromolecular Chemistry and Physics*, 211(15), 1640-1647.
- [114] Holländer, J., Hakala, R., Suominen, J., Moritz, N., Yliruusi, J., & Sandler, N. (2018). 3D printed UV light cured polydimethylsiloxane devices for drug delivery. *International journal of pharmaceuticals*, 544(2), 433-442.
- [115] Nagai, N., Saijo, S., Song, Y., Kaji, H., & Abe, T. (2019). A drug refillable device for transscleral sustained drug delivery to the retina. *European Journal of Pharmaceuticals and Biopharmaceutics*, 136, 184-191.

- [116] Jiang, J., Kojima, N., Guo, L., Naruse, K., Makuuchi, M., Miyajima, A.,... & Sakai, Y. (2004). Efficacy of engineered liver tissue based on poly-L-lactic acid scaffolds and fetal mouse liver cells cultured with oncostatin M, nicotinamide, and dimethyl sulfoxide. *Tissue engineering*, 10(9-10), 1577-1586.
- [117] Griffith, L. G., & Naughton, G. (2002). Tissue engineering--current challenges and expanding opportunities. *Science*, 295(5557), 1009-1014.
- [118] Mata, A., Boehm, C., Fleischman, A. J., Muschler, G., & Roy, S. (2002). Growth of connective tissue progenitor cells on microtextured polydimethylsiloxane surfaces. *Journal of Biomedical Materials Research: An Official Journal of The Society for Biomaterials, The Japanese Society for Biomaterials, and The Australian Society for Biomaterials and the Korean Society for Biomaterials*, 62(4), 499-506.
- [119] Shi, D., Ma, D., Dong, F., Zong, C., Liu, L., Shen, D.,... & Wang, J. (2010). Proliferation and multi-differentiation potentials of human mesenchymal stem cells on thermoresponsive PDMS surfaces grafted with PNIPAAm. *Bioscience reports*, 30(3), 149-158.
- [120] Bédurier, A., Vaysse, L., Flahaut, E., Seichepine, F., Loubinoux, I., & Vieu, C. (2011). Multi-scale engineering for neuronal cell growth and differentiation. *Microelectronic Engineering*, 88(8), 1668-1671.
- [121] Paranjape, M., Garra, J., Brida, S., Schneider, T., White, R., & Currie, J. (2002, June). Dermal thermo-poration with a PDMS-based patch for transdermal biomolecular detection. In *Solid-State Sensor and Actuator Workshop, Hilton Head* (pp. 73-76).
- [122] Leyerle, B. J., LoBue, M., & Shabot, M. M. (1988). The PDMS as a focal point for distributed patient data. *International Journal of Clinical Monitoring and Computing*, 5(3), 155-161.
- [123] Alves, C. B., Loughran, S., MacGregor, F. B., Dey, J. I. R., & Bowie, L. J. (2002). Bioplastique™ medialization therapy improves the quality of life in terminally ill patients with vocal cord palsy. *Clinical Otolaryngology & Allied Sciences*, 27(5), 387-391.

- [124] Asadishad, T., Sohrabi, F., Ghazimoradi, M. H., Hamidi, S. M., Anaghizi, S. J., & Farivar, S. (2020). Detection of Nicotine Effect on Colon Cells in a Plasmonic Platform. *Journal of Lasers in Medical Sciences*, 11(1), 8-13.
- [125] Asadishad, T., Sohrabi, F., Hamidi, S. M., Farivar, S., & Hakimi M. (2020). Impact of methadone and tramadol opioids on cellular activity of stem cells. *Under review in Optics communication*.
- [126] Costner, E. A., Lin, M. W., Jen, W. L., & Willson, C. G. (2009). Nanoimprint lithography materials development for semiconductor device fabrication. *Annual review of materials research*, 39, 155-180.
- [127] Traub, M. C., Longsine, W., & Truskett, V. N. (2016). Advances in nanoimprint lithography. *Annual review of chemical and biomolecular engineering*, 7, 583-604.
- [128] Zeng, S., Liang, G., Gheno, A., Vedraïne, S., & Yu, N. (2019, May). 2D Perovskite-Based Metasurfaces for Enhanced Plasmonic Sensing. In *CLEO: QELS_Fundamental Science* (pp. FTh4C-5). Optical Society of America.
- [129] Lee, K. L., Tsai, P. C., You, M. L., & Wei, P. K. (2019, May). 96-well capped gold nanoslits for backside-reflection plasmonic biosensing. In *Advanced Environmental, Chemical, and Biological Sensing Technologies XV* (Vol. 11007, p. 1100704). International Society for Optics and Photonics.
- [130] Hou, H. S., Lee, K. L., Wang, C. H., Hsieh, T. H., Sun, J. J., Wei, P. K., & Cheng, J. Y. (2019). Simultaneous assessment of cell morphology and adhesion using aluminum nanoslit-based plasmonic biosensing chips. *Scientific reports*, 9(1), 7204.
- [131] Han, X., Liu, K., & Sun, C. (2019). Plasmonics for Biosensing. *Materials*, 12(9), 1411.
- [132] Rahmandoust, M., & Ayatollahi, M. R. (Eds.). (2019). *Nanomaterials for Advanced Biological Applications* (Vol. 104). Springer.
- [133] Ali, M. R., Wu, Y., & El-Sayed, M. A. (2019). Gold Nanoparticle-Assisted Plasmonic Photothermal Therapy Advances Towards Clinical Application. *The Journal of Physical Chemistry C*.

- [134] He, Y., Laugesen, K., Kamp, D., Sultan, S. A., Oddershede, L. B., & Jauffred, L. (2019). Effects and side effects of plasmonic photothermal therapy in brain tissue. *Cancer Nanotechnology*, 10(1), 1-11.
- [135] Soni, S., & Sinha, R. K. (2019). Tumor blood perfusion-based requirement of nanoparticle dose-loadings for plasmonic photothermal therapy. *Nanomedicine*, 14(14), 1841-1855.
- [136] Padervand, M., Asgarpour, F., Akbari, A., Sis, B. E., & Lammel, G. (2019). Hexagonal Core–Shell SiO₂ [–MOYI] Cl– Ag Nanoframeworks for Efficient Photodegradation of the Environmental Pollutants and Pathogenic Bacteria. *Journal of Inorganic and Organometallic Polymers and Materials*, 29(4), 1314-1323.
- [137] Furletov, A. A., Apyari, V. V., Garshev, A. V., Volkov, P. A., & Dmitrienko, S. G. (2019). Silver triangular nanoplates as a colorimetric probe for sensing thiols: Characterization in the interaction with structurally related thiols of different functionality. *Microchemical Journal*, 147, 979-984.
- [138] Sharifi, M., Attar, F., Saboury, A. A., Akhtari, K., Hooshmand, N., Hasan, A.,... & Falahati, M. (2019). Plasmonic gold nanoparticles: Optical manipulation, imaging, drug delivery and therapy. *Journal of Controlled Release*.
- [139] Veloso, S. R. S., Cardoso, B. D., Rodrigues, A. R. O., Martins, J. A., Ferreira, P. M., Coutinho, P. J., & Castanheira, E. (2019). Magnetogels based on magnetic/plasmonic nanoparticles and self-assembled peptide hydrogels as drug nanocarriers. In *I Jornadas da Ciência-Concentra o Conhecimento*. Universidade do Minho. Escola de Ciências (EC).
- [140] Marangoni, V. S., Cancino Bernardi, J., Reis, I. B., Fávoro, W. J., & Zucolotto, V. (2019). Photothermia and Activated Drug Release of Natural Cell Membrane Coated Plasmonic Gold Nanorods and β -Lapachone. *ACS Applied Bio Materials*, 2(2), 728-736.
- [141] Crawford, B. M., Strobbia, P., Wang, H. N., Zentella, R., Boyanov, M. I., Odion, R.,... & Vo-Dinh, T. (2019, May). *In vivo* nucleic acid

- detection and imaging within whole plants using plasmonic nanosensors. In *Advanced Environmental, Chemical, and Biological Sensing Technologies XV* (Vol. 11007, p. 1100708). International Society for Optics and Photonics.
- [142] Zeng, J., Gong, M., Wang, D., Li, M., Xu, W., Li, Z.,... & Yin, Y. (2019). Direct Synthesis of Water-Dispersible Magnetic/Plasmonic Heteronanostructures for Multimodality Biomedical Imaging. *Nano letters*, 19(5), 3011-3018.
- [143] Cheng, Y. H., Tam, T. S. C., Chau, S. L., Lai, S. K. M., Tang, H. W., Lok, C. N.,... & Ng, K. M. (2019). Plasmonic gold nanoparticles as multifaceted probe for tissue imaging. *Chemical Communications*, 55(19), 2761-2764.
- [144] Wu, Q., Jia, H., Xiao, S., & Zhang, D. (2019). Plasmonic color filters fabricated by soft-X-ray lithography. In *9th International Conference on Surface Plasmon Photonics*.
- [145] Gupta, V., Probst, P. T., Goßler, F. R., Steiner, A. M., Schubert, J., Brasse, Y.,... & Fery, A. (2019). Mechanotunable Surface Lattice Resonances in the Visible Optical Range by Soft Lithography Templates and Directed Self-Assembly. *ACS applied materials & interfaces*, 11(31), 28189-28196.
- [146] Diaz-Valencia, B. F., Mejía-Salazar, J. R., Oliveira Jr, O. N., Porrás-Montenegro, N., & Albella, P. (2017). Enhanced transverse magneto-optical Kerr effect in magnetoplasmonic crystals for the design of highly sensitive plasmonic (bio) sensing platforms. *ACS omega*, 2(11), 7682-7685.
- [147] Sharma, A. K., & Pandey, A. K. (2019). Design and analysis of plasmonic sensor in communication band with gold grating on nitride substrate. *Superlattices and Microstructures*, 130, 369-376.
- [148] Tawa, K., Kondo, F., Sasakawa, C., Nagae, K., Nakamura, Y., Nozaki, A., & Kaya, T. (2015). Sensitive detection of a tumor marker, α -fetoprotein, with a sandwich assay on a plasmonic chip. *Analytical chemistry*, 87(7), 3871-3876.
- [149] Matsuura, R., Tawa, K., Kitayama, Y., & Takeuchi, T. (2016). A plasmonic chip-based bio/chemical hybrid sensing system for the

- highly sensitive detection of C-reactive protein. *Chemical Communications*, 52(20), 3883-3886.
- [150] Crawley, D., Nikolic, K., & Forshaw, M. (2004). *3D Nanoelectronic Computer Architecture and Implementation*. CRC Press.
- [151] Barbillon, G. (2012). Plasmonic nanostructures prepared by soft UV nanoimprint lithography and their application in biological sensing. *Micromachines*, 3(1), 21-27.
- [152] Borile, G., Rossi, S., Filippi, A., Gazzola, E., Capaldo, P., Tregnago, C.,... & Romanato, F. (2019). Label-free, real-time on-chip sensing of living cells via grating-coupled surface plasmon resonance. *Biophysical Chemistry*, 254, 106262.
- [153] Wood, A., Barizuddin, S., Darr, C. M., Mathai, C. J., Ball, A., Minch, K.,... & Andama, A. (2019). Ultrasensitive detection of lipoarabinomannan with plasmonic grating biosensors in clinical samples of HIV negative patients with tuberculosis. *PloS one*, 14(3), e0214161.
- [154] Kahraman, M., & Wachsmann-Hogiu, S. (2016, April). Plasmonic nanostructures for bioanalytical applications of SERS. In *Plasmonics in Biology and Medicine XIII* (Vol. 9724, p. 972405). International Society for Optics and Photonics.
- [155] Fortenbaugh, R. J., & Lear, B. J. (2017). On-demand curing of polydimethylsiloxane (PDMS) using the photothermal effect of gold nanoparticles. *Nanoscale*, 9(25), 8555-8559.
- [156] Liu, G. L., Kim, J., Lu, Y. U., & Lee, L. P. (2006). Optofluidic control using photothermal nanoparticles. *Nature materials*, 5(1), 27.
- [157] Hong, J., Hwang, D. K., Park, C., & Kim, Y. (2019). Photothermal performance of plasmonic patch with gold nanoparticles embedded on polymer matrix. *Korean Journal of Chemical Engineering*, 36(10), 1746-1751.
- [158] Li, Y., Verbiest, T., & Vankelecom, I. (2013). Improving the flux of PDMS membranes via localized heating through incorporation of gold nanoparticles. *Journal of membrane science*, 428, 63-69.
- [159] Zhou, W., Chen, M., Liu, X., Zhang, W., Cai, F., Li, F.,... & Lin, Z. (2019). Selective photothermal ablation of cancer cells by patterned

- gold nanocages using surface acoustic waves. *Lab on a Chip*, 19(20), 3387-3396.
- [160] Gatea, M. A., Jawad, H. A., & Hamidi, S. M. (2019). Detecting the thermoplasmonic effect using ellipsometry parameters for self-assembled gold nanoparticles within a polydimethylsiloxane matrix. *Applied Physics A*, 125(2), 103.
- [161] Sohrabi, F., Etezadi, D., Perin, R. D. C., Jahani, Y., Mohammadi, E. & Hamidi, S. M. (2020). Phase-Sensitive Optical Neural Recording of Cerebellum Tissue on a Flexible Interface. *Under review in Journal of Applied Physics*.
- [162] Asadishad, T., Sohrabi, F., Ghazimoradi, M. H., Saeidifard, S., Hamidi, S. M., Farivar, S. (2020). Plasmophore Enhancement in Fibroblast GFP-Positive Cell Excited by Nicotine. *Under review in Optica*

Chapter 5

**STUDY OF TiO₂-PDMS AS AN ADSORBENT
IN SOLID PHASE MICROEXTRACTION
OF AROMATIC COMPOUNDS**

***Erbin G. Uc-Cayetano, Ilse Ileana Cárdenas-Bates,
Pablo Acereto-Escoffié and Cristian Carrera-Figueiras****

Cuerpo Académico de Química Fundamental y Aplicada,
Facultad de Ingeniería Química, Universidad Autónoma de Yucatán,
Mérida, Yucatán, México

ABSTRACT

In this study, a hybrid material of titanium dioxide and polydimethylsiloxane (TiO₂-PDMS) was obtained and characterized using a sol-gel and electro spraying method. The micrographs revealed the formation of spherical microparticles 3.8 μm in diameter. Infrared spectroscopy (FTIR) showed bands at 920 and 612 cm⁻¹, indicating the formation of Ti-O-Si and Ti-O-Ti-O bonds. The contact angle was 103°, which corresponds to a nonpolar material. TiO₂-PDMS presented a decomposition start temperature at 240°C, obtained by thermogravimetric analysis (TGA). Subsequently, its adsorption capacity was evaluated for

* Corresponding Author's E-mail: cristian.carrera@correo.uady.mx.

the removal of benzene and naphthalene using solid-phase microextraction (SPME) with a liquid chromatography-ultraviolet detector (HPLC-UV). Different polarity elution solvents were compared, and the adsorption capacity was determined at different concentrations while maintaining a fixed amount of adsorbing material. The micrographs revealed the formation of uniform spherical microparticles of 3.8 ± 0.7 μm . The FTIR analysis of the hybrid composite material showed bands at 920 and 612 cm^{-1} , indicating the formation of Ti-O-Si and Ti-O-Ti bonds. The highest extraction percentages for benzene and naphthalene were 47 and 84%, respectively, with a relationship of analytes to synthesized absorbent material of 2 ppm in 25 mg. These results indicate that the hybrid material obtained could be viable as an adsorbent and that the optimization of the process could reduce both cost and analysis time.

Keywords: electrospraying, polydimethylsiloxane, titanium dioxide, benzene, naphthalene

INTRODUCTION

Polycyclic aromatic hydrocarbons (PAHs) are important industrial chemicals used worldwide and are involved in various chemical reactions. Recently, their presence has become ubiquitous as pollutants in outdoor and indoor environments. In terms of their toxicological properties, many countries have introduced legislation about their maximum concentration in drinking water (Qi et al. 2008).

Naphthalene and benzene are priority pollutants because of their high human toxicity at even low concentrations. Naphthalene is extensively used in 2-naphthol synthesis, pigments and precursors for various dyestuffs (Olmez-Hanci, Kartal, and Arslan-Alaton 2012), and benzene is a powerful industrial solvent used in the manufacture of explosives, rubber, lubricants, paints and dyes, among others (E. Popek 2017). Both naphthalene and benzene exposure may damage or destroy red blood cells and the central nervous system and cause hemolytic anemia, acute leukemia and cancer in humans (Smith 2010; Tavakoly Sany et al. 2014). Therefore, there is

increasing interest in the development of a specific analytical procedure to measure these aromatic hydrocarbons in environmental water.

Many techniques have been investigated for naphthalene and benzene removal from water, including chemical oxidation, reverse osmosis, microbial degradation, biofiltration, bioreactors, solvent extraction, adsorption and photocatalytic processes (Andas et al. 2014; Rubio-Clemente, Torres-Palma, and Peñuela 2014). For commercialization of organic compound removal/degradation, adsorption by solid phase microextraction (SPME) is the most appropriate system, as this technique offers several advantages, such as high selectivity, applicability to trace levels and good reproducibility. However, solid phase microextraction is still laborious, time-consuming, and expensive, and a concentration step through solvent evaporation is often required, which can result in the loss of volatile components (Qi et al. 2008). In addition, despite the existing technological development, today's commercial coatings for SPME do not cover the full range of requirements for the separation and extraction of analytes of interest, which makes it necessary to continuously search for new adsorbents for this technique that improve efficiency and optimize both cost and analysis time.

That is why synthesized coatings have gained interest among researchers. Polymeric nanomaterials are one type of coating that can be synthesized by different techniques, such as drawing, template synthesis, phase separation, self-assembly, and electrohydrodynamic techniques.

These electrohydrodynamic techniques, namely, electrospinning and electrospraying, are powerful approaches for developing materials with morphological features suitable for several applications. The incorporation of nanoparticles allows the generation of multifunctional materials that can be used in different applications ranging from filters for pollutant removal to wound dressings. Regarding pollutants, metal oxides (mainly ZnO and TiO₂) are the most promising nanoparticles (Rodríguez-Tobías, Morales, and Grande 2016).

Comparing electrohydrodynamic techniques, the electrospraying process enables a higher nanoparticle surface area prone to act as antibacterial agents or degrading materials, regardless of the presence of aggregates obtained in most cases. On the other hand, certain nanoparticles promote other specific properties, such as thermal stability, original crystallization behavior, and enhanced mechanical properties, which can lead to the diversification of polymeric/nanoparticle-based materials (Korina et al. 2013; Rodríguez-Tobías, Morales, and Grande 2016).

TiO₂ has been extensively used as an adsorbent for aromatic compound removal due to its photocatalytic properties, low cost, improved activity over a large pH range, and long-term stability (Rubio-Clemente, Torres-Palma, and Peñuela 2014; Wang et al. 2014). As an example, carbon nanotube-doped titanate nanotubes have been used as catalysts for the degradation of benzene (Tang et al. 2011). Titanium-based nanocomposites and metal oxide nanoparticles with large surface areas are advantageous for adsorbing and degrading organics at even low concentrations (Tunçal and Uslu 2015). In addition, TiO₂ can not only decompose organics but also kill bacteria and other microorganisms (Yang et al. 2016).

Zhang et al. 2008 designed a solid phase extraction system (SPME) that replaces the conventional cartridge with a micropipette tip, in which a bed of fibers obtained by electrospinning from polystyrene and polymethyl methacrylate is deposited. The system was used to investigate the extraction of hydrocortisone, cortisone acetate, ethinylestradiol and estradiol in human hair samples. In this work, it was found that when the tip was used for the detection of cortisol in human hair, the pretreatment efficiency of the biological sample was better than that of the traditional method of SPME (Zhang et al. 2008). Based on the above, this work focuses on the study of the physicochemical properties of a hybrid material based on titanium dioxide and polydimethylsiloxane (TiO₂-PDMS) and its capacity to adsorb two aromatic compounds (benzene and naphthalene) from water by using the micropipette tip method described by Zhang et al. 2008.

MATERIALS AND METHODS

Materials

The following analytical grade reagents were used: titanium tetrahydrofuran (TIPT, Sigma Aldrich), polydimethylsiloxane with terminal hydroxyls (PDMS-OH, Sigma Aldrich, MW: 550 g / mol), tetrahydrofuran (THF, JT Baker), nitric acid (HNO₃, Sigma Aldrich), ethanol (EtOH, Sigma Aldrich), HPLC grade acetonitrile (C₂H₃N, Sigma Aldrich), benzene (C₆H₆, Sigma Aldrich), naphthalene (C₁₀H₈, Sigma Aldrich), and hexane (HEX, Sigma Aldrich). Distilled water was used to prepare all solutions.

Synthesis of TiO₂-PDMS

A solution of THF-PDMS and a solution of EtOH-TIPT at a ratio of 1:0.37 and 1:0.75 by volume, respectively, were prepared individually. Subsequently, the two solutions were mixed, and the resulting solution was magnetically stirred for 5 min at 80°C. Immediately, without stirring and heating, 500 µL of concentrated HNO₃ was added. After 20 min another 200 µL of concentrated HNO₃ was added, and then, after 8 min, 100 µL more was added. Finally, the mixture was kept for 5 min under stirring and heating to achieve better curing before being used in the electrospinning system.

The polymeric solution was introduced into a 10 mL syringe equipped with a luer needle OD= 8 mm, L= 15 mm flat tip (NEL_0815, Linari Engineering). The solution was electrospun using vertical TL-1 electrospinning and spray equipment, as shown in Figure 1, with a metallic fixed collector plate.

The electrospaying conditions used for the experiments were as follows: voltage, 14-15.5 kV and feed rate, 1 mL/h for the first two hours and then at 1.5 mL/h, and the distance between the needle and collector was 12 cm.

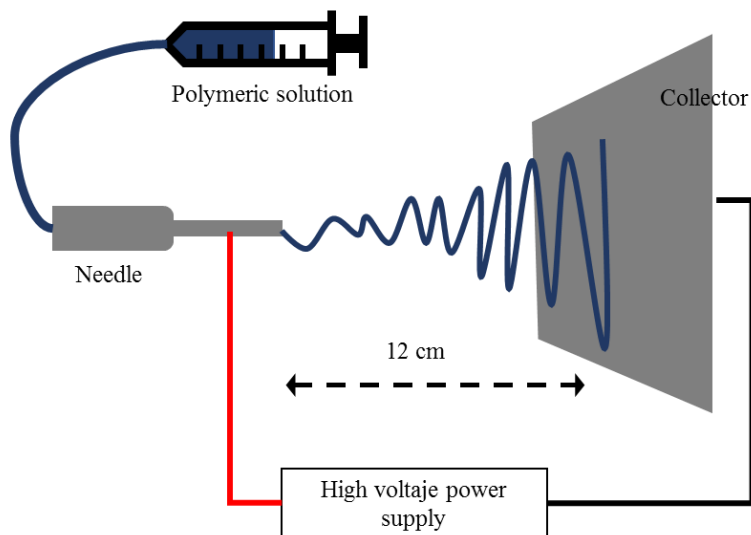


Figure 1. Illustration of the electrospinning technique.

CHARACTERIZATION OF TiO₂-PDMS

Scanning Electron Microscopy (SEM)

To study the morphology a Nova NanoSEM 200, FEI brand scanning electron microscope. A small portion of the material was dispersed in THF by means of ultrasound energy for 4 hours. A drop of the previous dispersion was placed in the equipment sample holder, and the solvent was allowed to evaporate. Finally, the sample was coated with a gold layer in the metallizing of the sorbent, images of the material at different magnifications were taken using equipment for 60 seconds. The samples were analyzed at an acceleration voltage of 10 kV under high vacuum. The average diameter of the particles was measured using image processing software (ImageJ, developed by the National Institute of Health) by taking a minimum of 100 particles per sample.

Contact Angle

On a tablet of the material to be analyzed, a drop of water with a volume of 2 μL was placed at room temperature (23°C). As soon as the drop was placed, a photo of it was captured to measure its angles, both on the left and right sides. This procedure was performed six times to calculate an average of the angles and obtain an accurate result. The images were obtained from a Nikon camera, model D5100, and the angle was also determined through ImageJ processing software.

Fourier Transformed Infrared Spectroscopy (FTIR)

With a completely homogenized mixture of 120 mg of previously dried KBr and 3 mg of sample, a tablet was made in a Carver hydraulic press applying a pressure of 90 psi. The spectrum was obtained with the Omnic Spectral Files program using the Thermo Nicolet 380 FTIR infrared spectrophotometer, with 64 scans in the spectral range of 4000-400 cm^{-1} with a resolution of 4 cm^{-1} .

Thermogravimetric Analysis (TGA)

Samples (5 to 15 mg) were taken from the polymeric material and deposited in equipment sample cups. The measurements were carried out in a Perkin Elmer TGA 7 thermogravimetric analyzer. The analysis conditions were as follows: temperature sweep from 40 to 600°C, heating rate of 10°C/min in an inert nitrogen atmosphere and flow rate of 20 mL/min.

Nitrogen Adsorption-Desorption Isotherms (BET)

The specific surface area and pore volume were calculated using the Brunauer-Emmett-Teller (BET) method using a Quantachrome Nova Station A surface area and porosity analyzer. A sample mass of 40 mg was first degassed for 6 h at 120°C to remove any residual material before BET analysis. Each characterization was performed in triplicate.

Evaluation of TiO₂-PDMS as an SPME Adsorbent

It has been known for many years that titanium dioxide has a strong ability to adsorb PAHs (Nagao and Suda 1989; Yuzawa et al. 2011; Sharma and Lee 2015). Therefore, benzene and naphthalene solutions at desired concentrations were prepared individually using acetonitrile as the solvent. Calibration curves were obtained by high-performance liquid chromatography (HPLC). Subsequently, SPME tests were performed by packing 25 mg of the obtained powder material into 1000 µL micropipette tips that contained filter paper in the lower part to avoid loss of the material when exerting pressure when passing the solution. Finally, 3 mL of the standard solutions was passed through the sorbent material at concentrations of 2, 4, 6 and 8 ppm, and the solutions were collected in Eppendorf tubes and centrifuged at 13,000 rpm for 10 min. The amount of adsorbed analyte was quantified by HPLC according to the following conditions: column Fenomex 5U model Jupiter, reversed-phase C18 with a particle size of 10 µm and length and internal diameter of 250 x 4.60 mm. A UV-Vis detector was used at a wavelength of 214 nm. Eluent flow: 1 mL/min, mobile phase A: water, mobile phase B: acetonitrile, injection volume 20 µL, gradient elution. The gradient programming was as follows: initially 40% of B, at minute 20, B reached 80%, and at minute 22, the percentage of B returned to 40%. This percentage was maintained for 5 min up to 27 min.

After saturation, the absorbed analytes were eluted with 1 mL of solvent (tests were performed with acetonitrile/water 60:40 and hexane HPLC grade). All experiments were carried out in triplicate.

RESULTS AND DISCUSSION

Scanning Electron Microscopy

The morphological characteristics of the TiO₂-PDMS electrospayed material are presented in Figure 2. SEM images show that spherical, homogeneous, smooth, and monodispersed nanoparticles were obtained with an average diameter of $3.65 \pm 1.25 \mu\text{m}$. This small diameter means a high specific surface area, with more active sites on the surface, which should lead to a high adsorption capacity.

The concentration of the polymeric solution was the main factor that influenced the resulting morphology of the material. The formation of particles is attributed to the fact that a solution of low concentration was used to control the increase in viscosity and the tension of the solution.

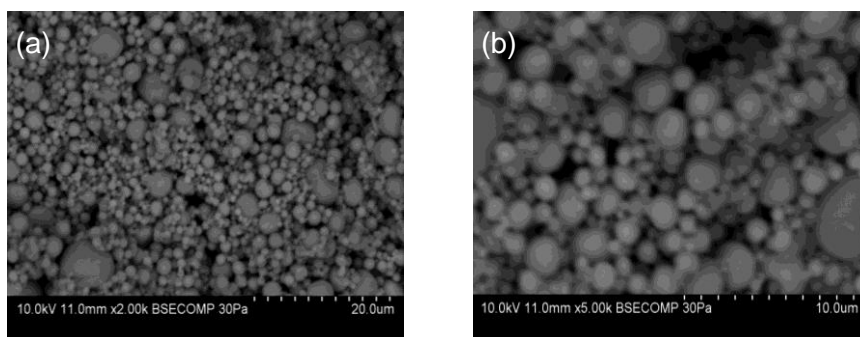


Figure 2. (a) Scanning electron micrograph at 10 kV, magnification = x2000 and (b) at 10 kV, magnification = x5000 of spherical TiO₂-PDMS particles obtained by electrospaying.

During the electrohydrodynamic process, when the number of chain crossings of the polymeric solution that modify the viscosity is exceeded,

the molecular surface tension leads to the formation of spherical particles (Al-Qadhi et al. 2015).

Contact Angle

The contact angle measurement was carried out by making 6 measurements in different areas and taking the average value. The results obtained (see Table 1) reveal that there is a small variation in the polar character for each sample; however, as expected, the 3 samples were found to have an angle greater than 90° (average angle of 103°), indicating nonpolar behavior because most of the structure contains methyl groups that are nonpolar. On the other hand, this nonpolar behavior is also influenced by the induction of charges in the material, as during the electro spraying process, the Ti-O and Si-O bonds are reoriented towards the interior of the material, giving it a hydrophobic character in the surface.

Table 1. Average contact angle for each sample indicating the degree of polarity

| Sample | Average polarity degree | Standard deviation of triplicates | Polarity |
|--------|-------------------------|-----------------------------------|----------|
| 1 | 103° | 4.52 | Nonpolar |
| 2 | 113° | 3.74 | Nonpolar |
| 3 | 98° | 0.89 | Nonpolar |

Fourier Transformed Infrared Spectroscopy (FTIR)

Figure 3 shows the infrared spectrum of the hybrid product TiO₂-PMDS compared to the precursor compound PDMS-OH. In the spectrum corresponding to the hybrid material, a band located between 3000-3500 cm⁻¹ and the band near 1750 cm⁻¹ correspond to the vibrations of the OH group and surface adsorbed molecular water, respectively (Sharma and Lee 2015). Characteristic infrared bands for PDMS can be seen at 2958 cm⁻¹ (asymmetric CH₃ stretch), 1392 cm⁻¹ (asymmetric CH₃ bending), 1100 and

1010 cm^{-1} doublet (Si-O stretch) and 797 cm^{-1} (Si- CH_3) (Sadeghi and Mollahosseini 2018). Several studies have revealed that a peak near 920 cm^{-1} corresponds to the Si-O-Ti vibration (Franc et al. 2006; Wallidge et al. 2004; Tada et al. 2011; Haitao Wang, Sheng Meng, Peng Xu, Wei Zhong 2006).

The formation of the Si-O-Ti bond indicates the interactions of covalent bonds between the structures of silica and titania, which shows that the correct hybridization was carried out. The band located at 612 cm^{-1} corresponds to the vibration of Ti-O-Ti (Mauritz and Jones 1990; Sadeghi and Mollahosseini 2018), and these links can only be observed in the spectrum of the hybrid material, indicating its presence.

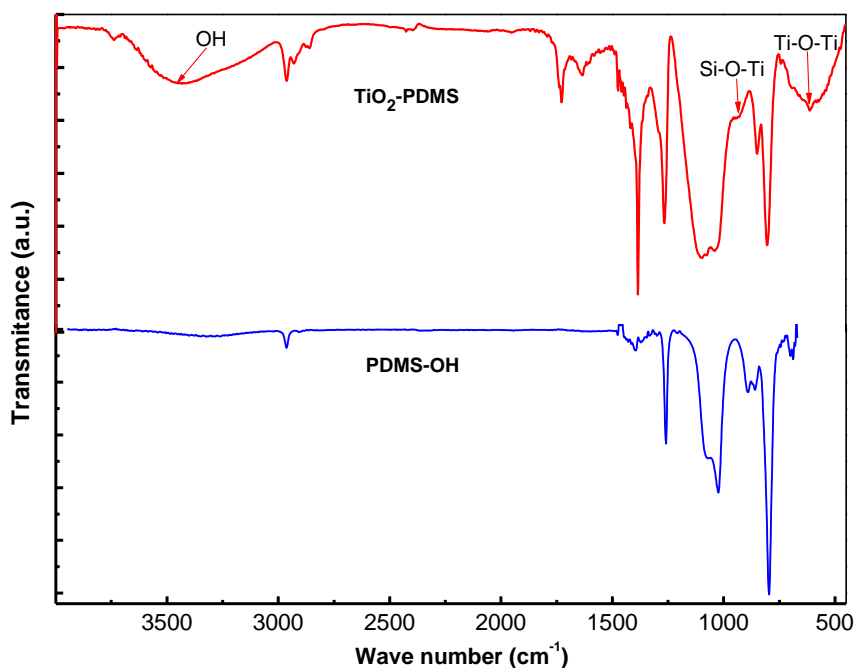


Figure 3. FTIR spectra of hybrid and nonhybridized material.

Thermogravimetric Analysis (TGA)

The results of the thermogravimetric analysis of the TiO₂-PDMS hybrid material shown in Figure 4 allow the proportion between the organic and inorganic parts, as well as the thermal stability of this material, to be determined.

In Figure 4, there are two inflection points in the graph before the PDMS-OH decomposes. The first fall begins at approximately 70 °C, and the second occurs at approximately 205 °C and ends at 250 °C. This may be due to the presence of residual volatile solvents, nonhydrolyzed alkoxy groups, low molecular weight PDMS-OH contained in the sample and moisture that may have been trapped in the network of the particles.

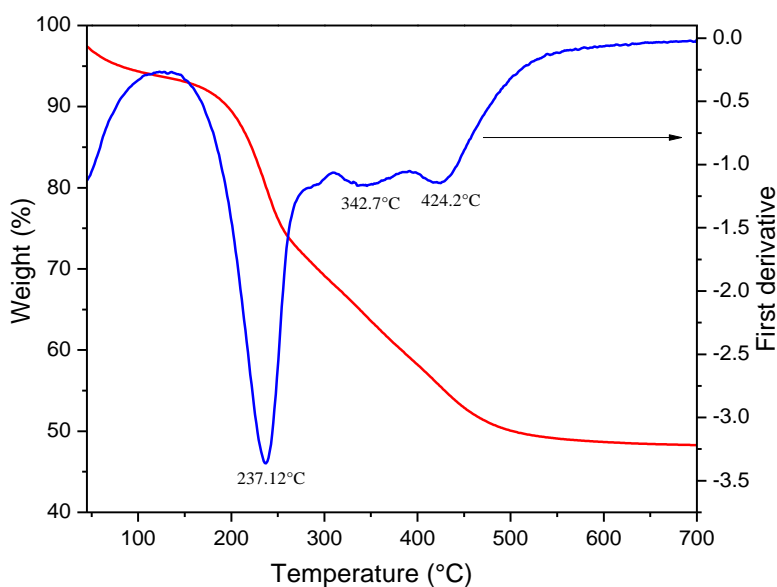


Figure 4. TGA curves of the hybrid TiO₂-PDMS material.

Concerning PDMS-OH, (Tomer et al. 2012) reported its decomposition temperature at 340°C, reaching its maximum close to 550°C. However, according to the report by (Vera-Graziano, Hernandez-Sanchez, and Cauch-Rodriguez 1995), noncrosslinked PDMS loses weight near 100°C due to the presence of low molecular weight

siloxane, while for cross-linked PDMS, it starts close to 425°C. The more crosslinked the material is, the higher the temperature at which the mass loss begins.

Because the solution of precursor is transferred to the electrospinning system before it reaches a complete cure, complete crosslinking in the polymer does not occur, and therefore, the material decomposes at lower temperatures. Therefore, the second decrease that begins at approximately 240°C can be attributed to the decomposition. Likewise, the residual content (once the last plateau is established) corresponds to the inorganic part of the material (silicon and titanium).

When analyzing the thermogram in a quantitative way, it can be observed that the weight loss of the solvents and humidity represents approximately 7%, the low molecular weight TIPT and PDMS approximately 20%, the high molecular weight PDMS hybrid polymer approximately 25% and the inorganic part of the particles 48% by weight.

These results are consistent with the stoichiometry of the reaction. It was expected that the inorganic part was 48% by weight, corresponding to SiO₂ and TiO₂, and the remaining 28% corresponded to the methyl groups coming from the PDMS.

Nitrogen Adsorption-Desorption Isotherms (BET)

Nitrogen adsorption-desorption isotherms for this material (Figure 5) demonstrate sigmoidal-shaped behavior with narrow hysteresis loops of the H3 type. This behavior indicates the formation of aggregates with initially nonporous particles that are characterized by textural porosity (Kruk and Jaroniec 2001). The sigmoidal-shaped isotherms observed for the sample correspond to type III in the IUPAC classification of pores. This behavior can be observed when lateral interactions between adsorbed molecules are strong in comparison to the interactions between the adsorbent surface and adsorbate. Type III adsorption isotherms have been reported for water adsorption on certain organic-inorganic nanocomposites with hydrophobic surfaces. The surface characterization allowed us to determine that the

hybrid material obtained presented a specific surface area of 13.02 m²/g and a pore volume V_p (voids between TiO₂-PDMS particles in their aggregates) of 48 cm³/g.

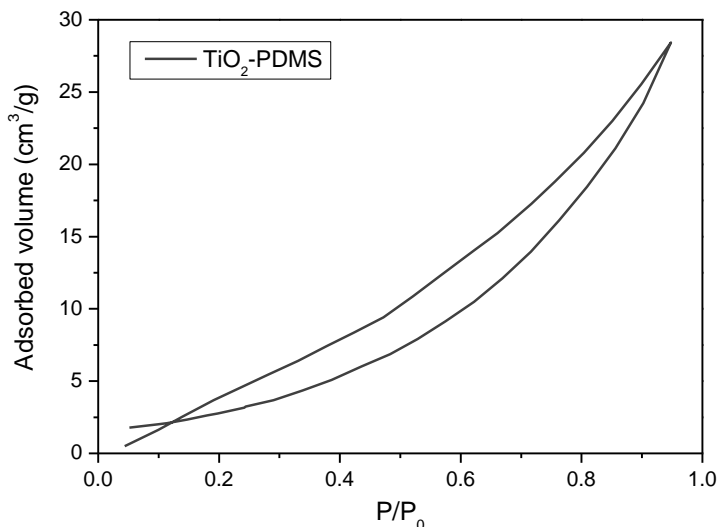


Figure 5. BET nitrogen adsorption isotherm plot for TiO₂-PDMS material.

Evaluation as an Adsorbent Material

Table 2 shows the percentages of adsorption of benzene and naphthalene on the TiO₂-PDMS particles. Naphthalene has a higher affinity towards the synthesized particles since the percentages of adsorption of this compound are higher.

The standard deviation values observed for the data are due to the slight variation of both the initial concentration that each point presents and the mass amount of particles in each cartridge. (Qi et al. 2008) obtained similar values of standard deviation to those in this report, working in the same way with both nano- and microscale polymeric hybrid materials as adsorbents of aromatic compounds by solid phase microextraction.

In general, for naphthalene, an inverse correlation of the percentage of adsorption with respect to the initial concentration of the sample can be observed, where the adsorption percentage decreases with increasing concentration of aromatic compounds. However, for benzene, despite the increase in its concentration, the percentage of adsorption did not decrease significantly.

Table 2. Adsorption percentages and standard deviations of benzene and naphthalene on TiO₂-PDMS

| Concentration (ppm) | Adsorption capacity (%) | |
|---------------------|-------------------------|---------------|
| | Benzene | Naphthalene |
| 2.5 | 46.73 ± 7.73 | 83.89 ± 5.84 |
| 4.5 | 48.56 ± 9.08 | 68.66 ± 16.38 |
| 6.5 | 45.54 ± 8.92 | 62.93 ± 16.25 |
| 8.5 | 43.75 ± 6.16 | 58.41 ± 11.40 |

Comparison of Elution Solvents

Figure 6 shows the percentages of elution obtained by comparing two solvent systems, one of nonpolar character (hexane) and the other of polar character (water-acetonitrile) in cartridges with 25 mg of microparticles. The elution percentages were calculated with respect to the concentration of analytes retained in the extraction process.

The previous results show that hexane with nonpolar behavior has a greater elution capacity for the analytes, since these are also nonpolar. It can be observed that the water-acetonitrile mixture failed to elute even half of what hexane was able to elute, even when there was a lower concentration of analytes for the first solvent. Hexane is considered a good option for the elution process because although other nonpolar solvents such as diethyl ether, toluene and chloroform may have an equal or better entrainment of these analytes, these are more expensive, harmful to health or dangerous.

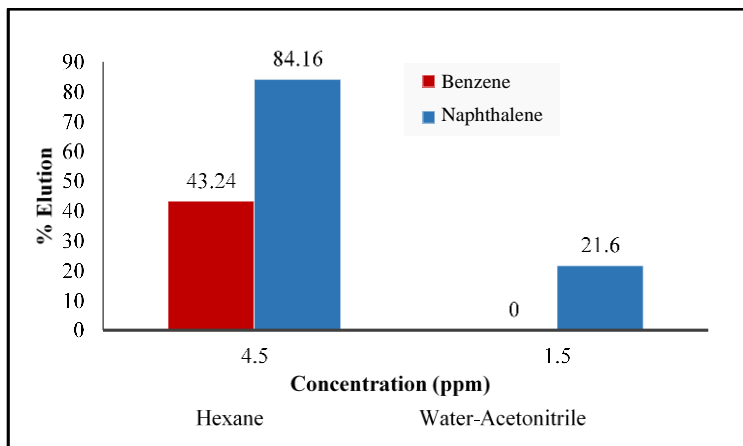


Figure 6. Percentages of elution of benzene and naphthalene with hexane and water-acetonitrile.

CONCLUSION

Spherical particles of TiO_2 -PDMS approximately $3.5 \mu\text{m} \pm 1.2$ in diameter were obtained. From the FTIR spectra, the presence of the characteristic vibrations of the hybrid polymer (Si-O-Si, $1100\text{-}1010 \text{ cm}^{-1}$) was observed, and the Si-O-Ti bond was formed (920 cm^{-1}). The percentages of organic and inorganic material obtained by TGA analysis were 45% and 48%, respectively; the contact angle analyses show that a nonpolar material was obtained ($>90^\circ$).

The hybrid particles were evaluated as an adsorbent material for SPME using 0.025 g of SPME in the extraction of benzene and naphthalene. For a concentration of 3 ppm of both analytes, the analytical signal was higher for naphthalene, achieving extraction percentages of up to 83% and 84% for its elution using hexane as the solvent. The material has high potential as an adsorbent for aromatic compounds similar to naphthalene in structure and polarity.

REFERENCES

- Al-Qadhi, M., N. Merah, A. Matin, N. Abu-Dheir, M. Khaled, and K. Youcef-Toumi. 2015. "Preparation of Superhydrophobic and Self-Cleaning Polysulfone Non-Wovens by Electrospinning: Influence of Process Parameters on Morphology and Hydrophobicity." *Journal of Polymer Research* 22 (11). <https://doi.org/10.1007/s10965-015-0844-x>.
- Andas, Jeyashelly, Farook Adam, Ismail Ab Rahman, and Yun Hin Taufiq-Yap. 2014. "Optimization and Mechanistic Study of the Liquid-Phase Oxidation of Naphthalene over Biomass-Derived Iron Catalyst." *Chemical Engineering Journal* 252: 382–92. <https://doi.org/10.1016/j.cej.2014.04.113>.
- E. Popok. 2017. "Environmental Chemical Pollutants." In *Sampling and Analysis of Environmental Chemical Pollutants*, 13–69. Elsevier; 2 edition.
- Franc, J., D. Blanc, A. Zerroukhi, Y. Chalamet, A. Last, and N. Destouches. 2006. "Organo-Silica-Titania Nanocomposite Elaborated by Sol-Gel Processing with Tunable Optical Properties." *Materials Science and Engineering B: Solid-State Materials for Advanced Technology* 129 (1–3): 180–85. <https://doi.org/10.1016/j.mseb.2006.01.011>.
- Haitao Wang, Sheng Meng, Peng Xu, Wei Zhong, Qiangguo Du. 2006. "Effect of Traces of Inorganic Content on Thermal Stability of Poly(Methyl Methacrylate) Nanocomposites." *Society*. <https://doi.org/10.1002/pen>.
- Korina, Elena, Olya Stoilova, Nevena Manolova, and Iliya Rashkov. 2013. "Multifunctional Hybrid Materials from Poly(3-Hydroxybutyrate), TiO₂ Nanoparticles, and Chitosan Oligomers by Combining Electrospinning/Electrospraying and Impregnation." *Macromolecular Bioscience* 13 (6): 707–16. <https://doi.org/10.1002/mabi.201200410>.
- Kruk, M., and M. Jaroniec. 2001. "Gas Adsorption Characterization of Ordered Organic-Inorganic Nanocomposite Materials." *Chemistry of Materials* 13 (10): 3169–83. <https://doi.org/10.1021/cm0101069>.

- Mauritz, K. A., and C. K. Jones. 1990. "Novel Poly(N-butyl Methacrylate)/Titanium Oxide Alloys Produced by Te Sol–Gel Process for Titanium Alkoxides." *Journal of Applied Polymer Science* 40 (7–8): 1401–20. <https://doi.org/10.1002/app.1990.070400726>.
- Nagao, Mahiko, and Yasuharu Suda. 1989. "Adsorption of Benzene, Toluene, and Chlorobenzene on Titanium Dioxide." *Langmuir* 5 (1): 42–47. <https://doi.org/10.1021/la00085a009>.
- Olmez-Hanci, Tugba, Zeynepf Kartal, and Idil Arslan-Alaton. 2012. "Electrocoagulation of Commercial Naphthalene Sulfonates: Process Optimization and Assessment of Implementation Potential." *Journal of Environmental Management* 99: 44–51. <https://doi.org/10.1016/j.jenvman.2012.01.006>.
- Qi, Dongjin, Xuejun Kang, Liqin Chen, Yiyun Zhang, Hongmei Wei, and Zhongze Gu. 2008. "Electrospun Polymer Nanofibers as a Solid-Phase Extraction Sorbent for the Determination of Trace Pollutants in Environmental Water." *Analytical and Bioanalytical Chemistry* 390 (3): 929–38. <https://doi.org/10.1007/s00216-007-1747-4>.
- Rodríguez-Tobías, Heriberto, Graciela Morales, and Daniel Grande. 2016. "Electrospinning and Electro spraying Techniques for Designing Antimicrobial Polymeric Biocomposite Mats." *Nanofiber Research - Reaching New Heights*. <https://doi.org/10.5772/63470>.
- Rubio-Clemente, Ainhoa, Ricardo A. Torres-Palma, and Gustavo A. Peñuela. 2014. "Removal of Polycyclic Aromatic Hydrocarbons in Aqueous Environment by Chemical Treatments: A Review." *Science of the Total Environment* 478: 201–25. <https://doi.org/10.1016/j.scitotenv.2013.12.126>.
- Sadeghi, Sahar, and Afsaneh Mollahosseini. 2018. "Electrospun Polydimethylsiloxane/Polyacrylonitrile/Titanium Dioxide Nanofibers as a New Coating for Determination of Alpha-Linolenic Acid in Milk by Direct Immersion-Solid Phase Nanoextraction." *Journal of Chromatography B: Analytical Technologies in the Biomedical and Life Sciences* 1073: 43–50. <https://doi.org/10.1016/j.jchromb.2017.11.042>.

- Sharma, Ajit, and Byeong Kyu Lee. 2015. "Adsorptive/Photo-Catalytic Process for Naphthalene Removal from Aqueous Media Using in-Situ Nickel Doped Titanium Nanocomposite." *Journal of Environmental Management* 155: 114–22. <https://doi.org/10.1016/j.jenvman.2015.03.008>.
- Smith, Martyn T. 2010. "Advances in Understanding Benzene Health Effects and Susceptibility." *Annual Review of Public Health* 31 (1): 133–48. <https://doi.org/10.1146/annurev.publhealth.012809.103646>.
- Tada, Hiroaki, Qiliang Jin, Hiroaki Nishijima, Hironori Yamamoto, Musashi Fujishima, Shin Ichi Okuoka, Takanori Hattori, Yasutaka Sumida, and Hisayoshi Kobayashi. 2011. "Titanium(IV) Dioxide Surface-Modified with Iron Oxide as a Visible Light Photocatalyst." *Angewandte Chemie - International Edition* 50 (15): 3501–5. <https://doi.org/10.1002/anie.201007869>.
- Tang, Zi Rong, Fan Li, Yanhui Zhang, Xianzhi Fu, and Yi Jun Xu. 2011. "Composites of Titanate Nanotube and Carbon Nanotube as Photocatalyst with High Mineralization Ratio for Gas-Phase Degradation of Volatile Aromatic Pollutant." *Journal of Physical Chemistry C* 115 (16): 7880–86. <https://doi.org/10.1021/jp1115838>.
- Tavakoly Sany, Seyedeh Belin, Rosli Hashim, Majid Rezayi, Aishah Salleh, Mohammad Azizur Rahman, Omid Safari, and A. Sasekumar. 2014. "Human Health Risk of Polycyclic Aromatic Hydrocarbons from Consumption of Blood Cockle and Exposure to Contaminated Sediments and Water along the Klang Strait, Malaysia." *Marine Pollution Bulletin* 84 (1–2): 268–79. <https://doi.org/10.1016/j.marpolbul.2014.05.004>.
- Tomer, Namrata S., Florence Delor-Jestin, Lawrence Frezet, and Jacques Lacoste. 2012. "Oxidation, Chain Scission and Cross-Linking Studies of Polysiloxanes upon Ageings." *Open Journal of Organic Polymer Materials* 02 (02): 13–22. <https://doi.org/10.4236/ojopm.2012.22003>.
- Tunçal, Tolga, and Orhan Uslu. 2015. "Industrial Sludge Remediation with Photonic Treatment Using Ti-Ag Nano-Composite Thin Films: Persistent Organic Pollutant Removal from Sludge Matrix." *Journal of*

- Environmental Management* 149: 37–45. <https://doi.org/10.1016/j.jenvman.2014.07.040>.
- Vera-Graziano, R., F. Hernandez-Sanchez, and J. V. Cauich-Rodriguez. 1995. “Study of Crosslinking Density in Polydimethylsiloxane Networks by DSC.” *Journal of Applied Polymer Science* 55 (9): 1317–27. <https://doi.org/10.1002/app.1995.070550905>.
- Wallidge, G. W., R. Anderson, G. Mountjoy, D. M. Pickup, P. Gunawidjaja, R. J. Newport, and M. E. Smith. 2004. “Advanced Physical Characterisation of the Structural Evolution of Amorphous $(\text{TiO}_2)_x(\text{SiO}_2)_{1-x}$ Sol-Gel Materials.” *Journal of Materials Science* 39 (22): 6743–55. <https://doi.org/10.1023/B:JMSE.0000045604.02983.96>.
- Wang, Yan, Yiming He, Qinghua Lai, and Maohong Fan. 2014. “Review of the Progress in Preparing Nano TiO_2 : An Important Environmental Engineering Material.” *Journal of Environmental Sciences (China)* 26 (11): 2139–77. <https://doi.org/10.1016/j.jes.2014.09.023>.
- Yang, Shu Jing, Xin Chen, Bing Yu, Hai Lin Cong, Qiao Hong Peng, and Ming Ming Jiao. 2016. “Self-Cleaning Superhydrophobic Coatings Based on PDMS and $\text{TiO}_2/\text{SiO}_2$ Nanoparticles.” *Integrated Ferroelectrics* 169 (1): 29–34. <https://doi.org/10.1080/10584587.2016.1162604>.
- Yuzawa, Hayato, Masanori Aoki, Hideaki Itoh, and Hisao Yoshida. 2011. “Adsorption and Photoadsorption States of Benzene Derivatives on Titanium Oxide Studied by NMR.” *Journal of Physical Chemistry Letters* 2 (15): 1868–73. <https://doi.org/10.1021/jz200621w>.
- Zhang, Yiyun, Xuejun Kang, Liqin Chen, Chao Pan, Yingfang Yao, and Zhong Ze Gu. 2008. “Fiber-Packed SPE Tips Based on Electrospun Fibers.” *Analytical and Bioanalytical Chemistry* 391 (6): 2189–97. <https://doi.org/10.1007/s00216-008-2145-2>.

Chapter 6

**POLYDIMETHYLSILOXANE (PDMS):
A FAVORABLE MATERIAL FOR ACTIVE
PLASMONIC APPLICATIONS**

H. Mbarak, S. M. Hamidi
and E. Mohajerani*

Magneto-plasmonic lab, Laser and Plasma Research Institute,
Shahid Beheshti University, Tehran, Iran

ABSTRACT

Polydimethylsiloxane (PDMS), as a common silicone polymer, has attracted the attention of many researchers due to its own characteristics that make it desirable for use in different applications. This promising material is applied in a variety of fields including mechanics, electronics, medicines, cosmetics and fibers. According to its flexibility, low cost, optical transparency, long service life, good dielectric properties and ease of fabrication, the use of PDMS is expanded to new and exciting applications, especially in active plasmonic devices. The fabrication of PDMS-based 2D plasmonic grating switch is realized in a straightforward method, enabling the active control over the plasmonic properties. In order to advance the applications of PDMS, a significant part of this

* Corresponding Author's E-mail: m_hamidi@sbu.ac.ir.

chapter is devoted to introduce first the polymer (PDMS) and its properties, then describes the design steps of fabrication of the plasmonic structure and finally presents the switching effect of the sample showing the relevance of PDMS in this application.

Keywords: PDMS substrate, 2D plasmonic grating, active plasmonic system, switching effects, active control

INTRODUCTION

The scientific field of active plasmonics, which exploits the active control of surface plasmon resonance, has attracted significant attention for plenty of applications such as plasmonic switches [1-3], active color filter [4-6], modulators [7-9] plasmonic waveguides [10] and polarizers [11-14]. In the same context, the important need to have effective instruments for chemical and biological detection is also booming and developing considerably due to the high demand for medicine or for food control, to name just two. Among the large number of existing detection devices, also called “switches”, one of them is based on a physical phenomenon of surface lattice resonance (SLR). This type of active plasmonic component is particularly used today because it has proven its ability to provide high response speeds under external controlled methods. The working principle can be derived from the singular surface plasmon property of guiding light along a metal / dielectric interface as well as the properties of the dielectric medium. More specifically, surface plasmons are surface waves whose characteristics are very sensitive to the surrounding medium, which is in contact with the surface of the metal. A small variation in the refractive index of this medium causes a change in the so-called “resonance” conditions. By measuring this change, it is then possible to detect, in real time, the presence of chemical and / or biochemical species in the vicinity of the metal surface and thus to produce very sensitive sensors for quantitative analyzes of biomolecular reactions as an example.

In fact, the design of an active plasmonic structure must take into account the type of material in which the structure is based on. Among

different soft polymers, polydimethylsiloxane (PDMS) is chosen to be used here in this research to open a new window in plasmonic switching applications.

Due to its promising properties which are presented below in detail, many articles have been published on soft polymer systems made in PDMS and their applications. Its currently used for example as flexible substrates of E-skin [15] and other stretchable electronics [16-17], as the mechanical interconnection layer between two silicon wafers [18], in medical devices [19-20], in biomaterial science [15,21] as well as it was integrated in microfluidic systems [22], etc. Whereas a few are successfully reported about the integration of PDMS in active plasmonics devices [23].

With the development of active plasmonics devices, we have demonstrated that the fabrication of plasmonic switches in PDMS-based systems can be successfully realized.

For this purpose, this chapter briefly introduces a clear picture about the important properties of PDMS. Afterwards, it provides how active plasmonic switch in PDMS-based system can be fabricated as well as describes how the active control of this system can be achieved. Finally, the last section presents an example about the characterization of the switching effect of the PDMS-based structure under different external fields.

PROPERTIES OF PDMS AND ITS APPLICATIONS

Materials based on silicones have been commercialized in the United States in the early 1940s, and have been used in numerous applications in civil engineering, construction, electricity, transport, aeronautics, defense, textiles and cosmetic industry [24]. The main product in the silicone series is polydimethylsiloxane (PDMS). PDMS is a linear polymer that has repeating units of $-O-Si(CH_3)_2-$ groups consisting of two methyl groups attached to the silicon atom [25]. It is by the presence of silicon and by the existence of the Si-O bond that silicones are distinguished with from other organic polymers, giving the rise for polydimethylsiloxanes (PDMS)

properties of excellent temperature resistance, weather resistance, biocompatibility and lubricity [26]. The flexibility and high mobility of the PDMS chain results in a small change in physical properties such as viscosity, temperature, relatively high solubility and permeability to gases (in particular to water vapor) [27]. Consequently, PDMS has low glass transition temperature [26], unique flexibility [28], high dielectric strength [29] low boiling point (oligomers), low freezing point and high compressibility.

The structural formula and a 3D model of the fundamental chemical structure of a polydimethylsiloxane (PDMS) are shown in Figure 1(a, b) [30].

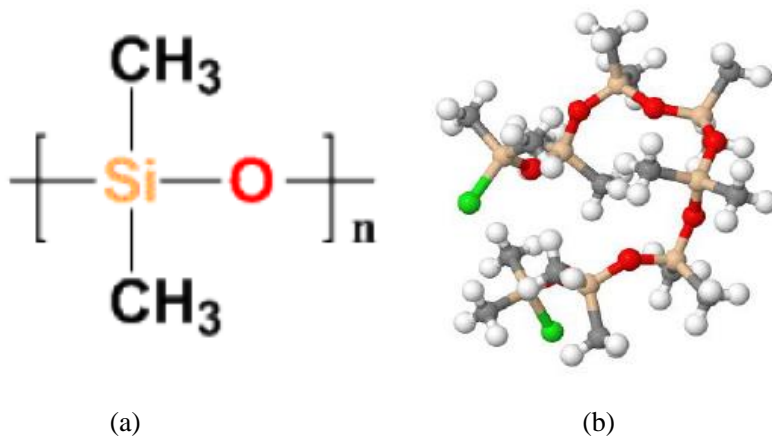


Figure 1. (a) Chemical structure of PDMS, (b) Spatial representation.

The main characteristics that make these kinds of materials interesting and applicable in many different applications are its elastomeric properties, easy to fabricate, optical transparency and inexpensive [31]. In addition to this, PDMS is differentiated by its low surface energy, no surface viscosity, low reactivity, inertly, toxicity and combustibility [28]. Also, PDMS is considered water insoluble, good dielectric insulator [24] and non-flammable [32]. Since PDMS is a quite flexible macromolecule, it occurs in a semi-crystalline state and therefore has characteristics halfway between solid and liquid materials [33]. Thus, all these physical and

chemical properties of the PDMS mentioned above open numerous opportunities for applications, ranging from cosmetic industry to medical field as well as from chemical and biological applications to the production of microfluidic devices [34], and nowadays in active plasmonics.

Thanks to its good biocompatibility, low toxicity, chemical stability, transparency and mechanical elasticity, PDMS was used in biomaterials science such as implants, contact lenses and tissue engineering [21, 35], in which the response of biological cells and tissues can be affected by its mechanical properties [31]. On the other hand, PDMS was appeared in biomedical devices such as catheter and drainage tubing, dialysis membrane, micro pumps and micro valves [36]. Furthermore, since its surface undergoes the plasma modification it was used also in both medicine and medical diagnostic [20]. Thanks also to its low cost, good microstructural characteristics and good manufacturing ability, polymeric systems will displace glass and silicon based systems for fabricating microfluidic devices, involving simpler and less expensive manufacturing processes [22]. Other possible applications are its use in aero-space, electronics and semiconductor industry [25]. More and more, it can be used in sensor technology and radar absorbing materials [37].

At last, another important use which this chapter focuses on, is how to use PDMS to create a substrate and deposit different thin layers on its surface, such as gold layer [20]. Keeping in mind the following advantages of PDMS: long service life, flexibility, ease of fabrication into different shapes, good dielectric properties, optical transparency, high surface mobility, low reactivity and low environment hazard, PDMS is devoted to be used in a promising field in the development of active plasmonic devices, which is nothing that plasmonic switches.

PREPARATION OF PDMS-BASED 2D PLASMONIC GRATING

It is important to keep in mind, while the fabrication of a plasmonic structure, to be sure of two things, first, a convenient soft-polymer that can

realize the conditions of the plasmon resonances of the system, and second, a suitable active medium with tunable dielectric responses under external fields.

Our fabricated sample in active plasmonic field is focused primary on PDMS polymer [38]. As we mentioned above, owing to its characteristics, experiences have proved that PDMS is an interesting and desired material in wide fields of different applications, especially in active plasmonics.

In the present study, a 2D gold grating based on PDMS is fabricated using nanoimprint lithography method [39]. The preparation process of this sample is schematically shown in Figure 2.

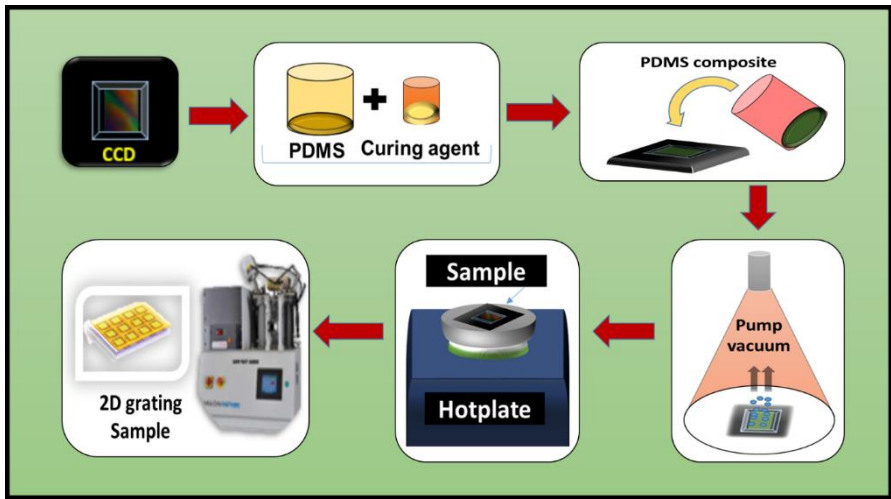


Figure 2. The fabrication process of the PDMS-based 2D plasmonic grating.

To create the sample, our first step was to separate a two dimensional (2D) charge coupled device (CCD) from a camera, in which each CCD is characterized by a unique code enabling specific dimensions of the grating obtained from the PDMS. Then, a plexiglas frame was placed on this CCD stamp and glued by thermal adhesive around it. After that, the silicone elastomer base (PDMS) and curing agent were mixed homogenously in a fixed ratio of 10:1 for 5 minutes. Then, a good quantity of approximately 1.4 mm thickness was infiltrated in the frame. In order to remove the trapped air bubbles from the PDMS composite, the sample was degassed

for 15 min using a vacuum pump and then kept at different temperatures (from 50 to 100 °C) for one hour on a hot plate. Actually, to assure a good drying of PDMS, the sample must take place at room temperature for one day and therefore the CCD stamp can be easily removed. Finally, the obtained 2D grating based on PDMS was coated by a thin gold layer with a thickness of 35nm using PVD device. Figure 3(a) and 3(b) show a representative SEM and AFM images of the 2D plasmonic grating in a simple cubic structure, having a unit cell size about 1.2 μm . Also, the figures show the nanowires between each cube and the displacement of the crystal period.

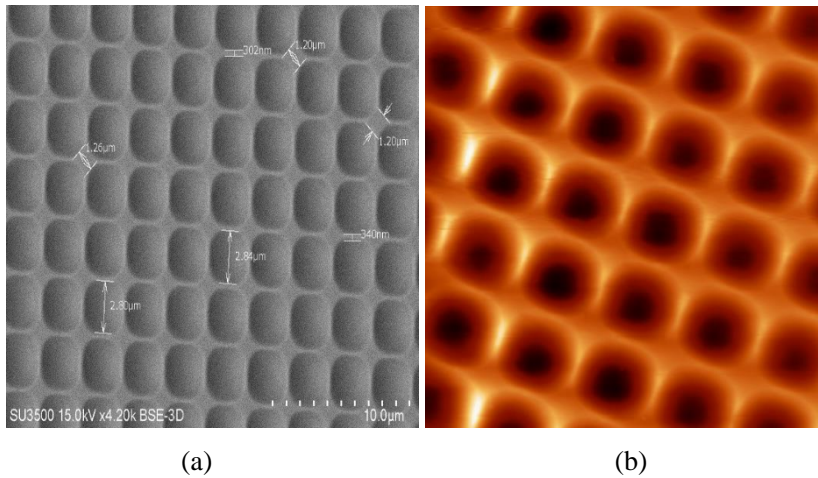


Figure 3. (a)The SEM image and (b) the SEM image of the sample [38].

By this manner, the fabricated plasmonic structure is ready now for depositing different tunable surrounding media on the gold surface enabling the switching effect under many external fields.

This sample has attracted other groups in different domains in plasmonics such as random lasing and biomedical substrate [40-41].

The goal of our first experimental work was focused on the realization of the electrically switching effect of the PDMS-based 2D plasmonic grating using nematic liquid crystal as an active medium.

For this reason, a typical ITO glass substrate was fixed on the 2D grating gold surface, using a spacer of 10 μm mixed with UV adhesive under a UV light for around 20 min, forming a cell as shown in Figure 4(a). The real picture of the flexible sample is shown in Figure 4(b).

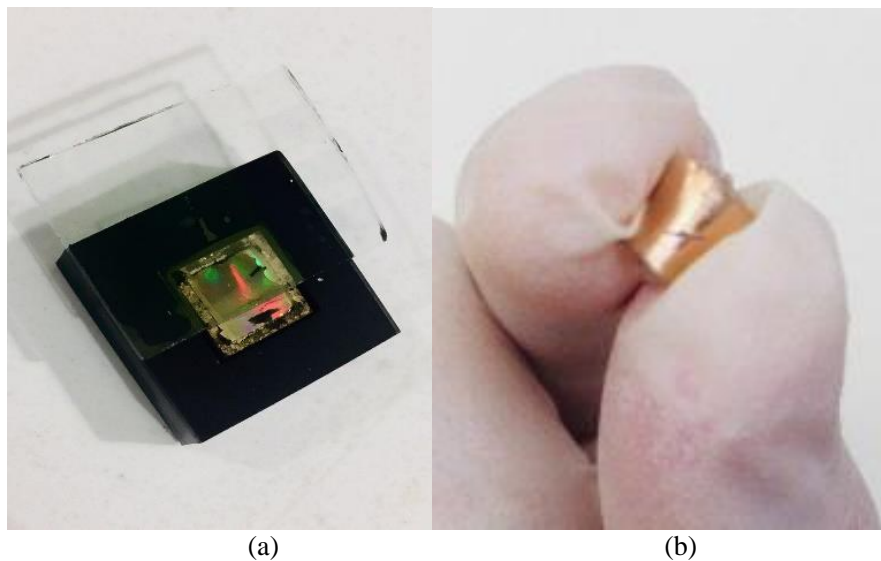


Figure 4. (a) Schematic of our main preparation cell, (b) Real picture of the flexible sample [38].

APPLICATION OF PDMS IN PLASMONIC SWITCHES

After the deposition of the gold thin layer on the PDMS substrate, a thin layer of E7 liquid crystal was typically injected between the gold surface and ITO glass achieving the tuning of optical plasmonic properties of the structure as well as the switching manner under external electric field.

Actually, an electric field was applied across the cell between the ITO substrate and the perforated Au film. Therefore, the director of the liquid crystal molecules can be oriented along the electric field direction driving

variation in the propagation constant of the SPR by changing the refractive index and accordingly modulating the reflected light [42].

The reflectance spectrum of the 2D gold grating array was recorded experimentally at different voltages for TM and TE polarization respectively Figure (5). As can be seen in this figure, a redshift associated with an amplitude change of the reflectance spectrum for both polarizations can take place for an increasing voltage from 0V to 20V. The outcomes of this work are discussed in details in this paper [38].

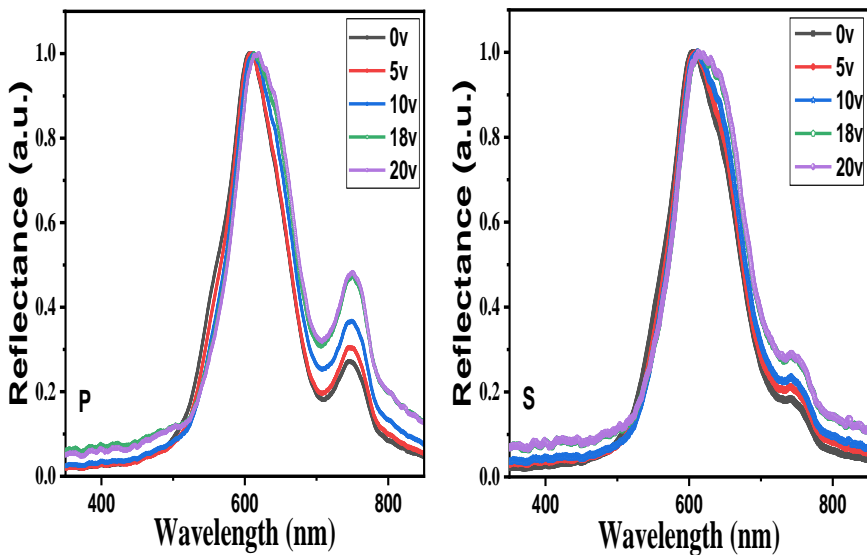


Figure 5. Reflectance spectra for p and s polarizations.

Finally, voltage-induced 2D-plasmonic grating switching time was realized by recording the variation of the reflection intensity between 0V and 20V. When we applied the voltage on the sample, the LC molecules start to align with each other causing a noticeable increasing in the reflectance intensity Figure (6). The reflectance decreases in the absence of voltage, indicating the random state of LC molecules. It means that the LC filled 2D-plasmonic array can reduce the intensity of the reflected light well without applying external voltage. This reversible switching was

repeated many times and the intensity change was approximately the same during many cycles, confirming that the change in the refractive index of the LC in the sample is reversible and reliable. The response time for the off voltage-switching process is estimated to be ~ 56 s.

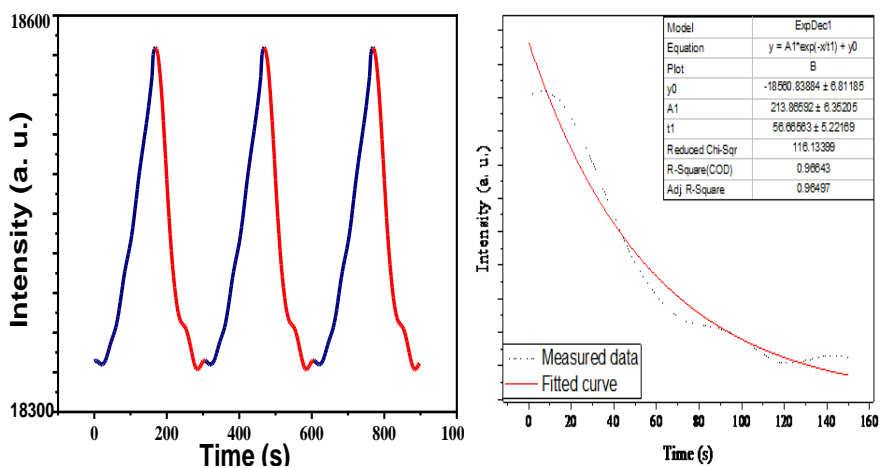


Figure 6. (a) The switching manner of the sample under external voltage and (b) the fitted decay graph [38].

In accordance with the first experimental work, we have been able to realize for the first time an all-optical plasmonic switch based on photochemical material (8-hydroxypyrene-1,3,6-trisulfonate, HPTS). We used this photoacid (HPTS) as an active surrounding medium that can be optically controlled enabling the switching effect and the modulation of plasmon resonances. The PDMS-based 2D-plasmonic grating was coated by thin film of HPTS exposed to UV irradiation. By tuning the UV light on and off, the HPTS thin film maintains an excited-state proton transfer (ESPT) process followed by green fluorescence resulting in a good switching manner of the system, accompanied with a plasmonic redshift of the reflection spectrum. The response time of the photoswitching process is considered to be 270 ms for S polarization. Actually, the results of this work are submitted in a new paper, which is under review state.

On the other hand, we have studied the switching effect of the same PDMS-based 2D plasmonic grating coated by NiFe thin film under an external magnetic field. The switching manner of the sample was measured under external magnetic field in “on” and “off” states, using UV-visible spectrometer and spectral longitudinal magneto-optical Kerr effect measurements. In fact, the results of this work are accomplished, just in need to be published. In summary, this PDMS-based 2D plasmonic sample is characterized by its simple fabrication, feasible price, good efficiency and the possibility to be reproduced easily at high scales. It has the ability to be coated by different materials that can be controlled by many external fields, enabling the active control of the plasmonic properties as well as the switching effects of the system. An improvement in the efficiency of this sample, is expected, and should be further investigated to obtain a promising tuning of the plasmonic properties, leading to high sensitivities, using other tunable optical materials.

CONCLUSION

The fabrication of a tunable 2D plasmonic structure in polydimethylsiloxane (PDMS) is realized for the first time, which is based on an array of gold nanoparticles. In this structure, the gold layer is deposited on a PDMS substrate using nanoimprint lithography method. As a first attempt, working with new application in active plasmonics, the PDMS-based system can act as an electrical plasmonic switch based on nematic liquid crystal. By applying an external field, the average orientation of the rod-like liquid crystal molecules can be reversibly switched, inducing a refractive index change, resulting in a spectral shift in the surface plasmons resonances. Since PDMS is flexible and inexpensive, the PDMS-based plasmonic structure possess high design flexibility as well as simplicity of fabrication, making it useful in important applications in switching and sensing.

In this chapter only the optical effect is mentioned, but by using other tunable optical materials accompanied with different external fields (all-

optical, thermo-optical and magneto-optical effects, etc.), an improvement of the sample's efficiency is expected, and it have to be further investigated.

REFERENCES

- [1] Lin, Y., Zhang, X., Fang, X., & Liang, S. (2016). A cross-stacked plasmonic nanowire network for high-contrast femtosecond optical switching. *Nanoscale*, 8(3), 1421-1429. doi:10.1039/c5nr06464c.
- [2] Chu, H., & How Gan, C. (2013). Active plasmonic switching at mid-infrared wavelengths with graphene ribbon arrays. *Applied Physics Letters*, 102(23), 231107. doi:10.1063/1.4810003.
- [3] Hsiao, V. K., Zheng, Y. B., Juluri, B. K., & Huang, T. J. (2008). Light-Driven Plasmonic Switches Based on Au Nanodisk Arrays and Photoresponsive Liquid Crystals. *Advanced Materials*, 20(18), 3528-3532. doi:10.1002/adma.200800045.
- [4] Si, G., Zhao, Y., Lv, J., Lu, M., Wang, F., Liu, H., ... Liu, Y. J. (2013). Reflective plasmonic color filters based on lithographically patterned silver nanorod arrays. *Nanoscale*, 5(14), 6243. doi:10.1039/c3nr01419c.
- [5] Si, G., Zhao, Y., Liu, H., Teo, S., Zhang, M., Jun Huang, T., ... Teng, J. (2011). Annular aperture array based color filter. *Applied Physics Letters*, 99(3), 033105. doi:10.1063/1.3608147.
- [6] Liu, Y. J., Si, G. Y., Leong, E. S., Xiang, N., Danner, A. J., & Teng, J. H. (2012). Light-Driven Plasmonic Color Filters by Overlaying Photoresponsive Liquid Crystals on Gold Annular Aperture Arrays. *Advanced Materials*, 24(23), OP131-OP135. doi:10.1002/adma.201104440.
- [7] Degl'Innocenti, Riccardo, David S. Jessop, Christian W. Sol, Long Xiao, Stephen J. Kindness, Hungyen Lin, J. A. Zeitler, et al. "Fast Modulation of Terahertz Quantum Cascade Lasers Using Graphene Loaded Plasmonic Antennas." *ACS Photonics* 3, no. 3 (2016): 464-470. doi:10.1021/acsp Photonics.5b00672.

- [8] Ansell, D., I. P. Radko, Z. Han, F. J. Rodriguez, S. I. Bozhevolnyi, and A. N. Grigorenko. "Hybrid graphene plasmonic waveguide modulators." *Nature Communications* 6, no. 1 (2015). doi:10.1038/ncomms9846.
- [9] Cai, Wenshan, Justin S. White, and Mark L. Brongersma. "Compact, High-Speed and Power-Efficient Electrooptic Plasmonic Modulators." *Nano Letters* 9, no. 12 (2009): 4403-4411. doi:10.1021/nl902701b.
- [10] Zografopoulos, D. C., & Beccherelli, R. (2013). Liquid-crystal-tunable metal-insulator-metal plasmonic waveguides and Bragg resonators. *Journal of Optics*, 15(5), 055009. doi:10.1088/2040-8978/15/5/055009.
- [11] Shrestha, Raj, V., Lee, S., Kim, E., & Choi, D. (2015). Polarization-tuned Dynamic Color Filters Incorporating a Dielectric-loaded Aluminum Nanowire Array. *Scientific Reports*, 5(1). doi:10.1038/srep12450.
- [12] Duempelmann, L., Luu-Dinh, A., Gallinet, B., & Novotny, L. (2015). Four-Fold Color Filter Based on Plasmonic Phase Retarder. *ACS Photonics*, 3(2), 190-196. doi:10.1021/acsphotonics.5b00604.
- [13] Ellenbogen, T., Seo, K., & Crozier, K. B. (2012). Chromatic Plasmonic Polarizers for Active Visible Color Filtering and Polarimetry. *Nano Letters*, 12(2), 1026-1031. doi:10.1021/nl204257g.
- [14] Li, Z., Clark, A. W., & Cooper, J. M. (2016). Dual Color Plasmonic Pixels Create a Polarization Controlled Nano Color Palette. *ACS Nano*, 10(1), 492-498. doi:10.1021/acsnano.5b05411.
- [15] Gu, Yumao, Yuanzhen Dai, Yang Liu, and Xiaoping Chen. "Electronic Artificial Skin for Application in Pressure Sensor." *Advances in Intelligent Systems and Computing*, 2015, 433-439. doi:10.1007/978-3-319-16841-8_40.
- [16] Liu, C. "Recent Developments in Polymer MEMS." *Advanced Materials* 19, no. 22 (2007): 3783-3790. doi:10.1002/adma.200701709.

- [17] Ahn, Jong-Hyun, and Jung H. Je. "Stretchable electronics: materials, architectures and integrations." *Journal of Physics D: Applied Physics* 45, no. 10 (2012): 103001. doi:10.1088/0022-3727/45/10/103001.
- [18] Arquint, P., P.D. Van der Wal, B.H. Van der Schoot, and N.F. De Rooij. "Flexible polysiloxane Interconnection Between Two Substrates For Microsystem Assembly." *Proceedings of the International Solid-State Sensors and Actuators Conference - TRANSDUCERS '95* (n.d.). doi:10.1109/sensor.1995.717164.
- [19] Xia, Younan, and George M. Whitesides. "SOFT LITHOGRAPHY." *Annual Review of Materials Science* 28, no. 1 (1998): 153-184. doi:10.1146/annurev.matsci.28.1.153.
- [20] Jofre-Reche, José A., Jérôme Pulpytel, Houssam Fakhouri, Farzaneh Arefi-Khonsari, and José M. Martín-Martínez. "Surface Treatment of Polydimethylsiloxane (PDMS) with Atmospheric Pressure Rotating Plasma Jet. Modeling and Optimization of the Surface Treatment Conditions." *Plasma Processes and Polymers* 13, no. 4 (2015): 459-469. doi:10.1002/ppap.201500118.
- [21] Kim, J.Y., J.Y. Baek, K.A. Lee, and S.H. Lee. "Automatic aligning and bonding system of PDMS layer for the fabrication of 3D microfluidic channels." *Sensors and Actuators A: Physical* 119, no. 2 (2005): 593-598. doi:10.1016/j.sna.2004.09.023.
- [22] Ng, Jessamine M., Irina Gitlin, Abraham D. Stroock, and George M. Whitesides. "Components for integrated poly(dimethylsiloxane) microfluidic systems." *ELECTROPHORESIS* 23, no. 20 (2002): 3461-3473. doi:10.1002/1522-2683(200210)23:20<3461::aid-elps3461>3.0.co;2-8.
- [23] Lu, Wenzheng, Nina Jiang, and Jianfang Wang. "Plasmon Switching: Active Electrochemical Plasmonic Switching on Polyaniline-Coated Gold Nanocrystals (Adv. Mater. 8/2017)." *Advanced Materials* 29, no. 8 (2017). doi:10.1002/adma.201770051.
- [24] Belovickis, Jaroslavas R., Jan Macutkevicius, Šarūnas Svirskas, Vytautas Samulionis, Jūras Banys, Olga Shenderova, and Vesna Borjanovic. "Ultrasonic and dielectric relaxations in PDMS/ZnO

- nanocomposite.” *physica status solidi (b)* 252, no. 12 (2015): 2778-2783. doi:10.1002/pssb.201552383.
- [25] Bistričić, L., V. Borjanović, L. Mikac, and V. Dananić. “Vibrational spectroscopic study of poly(dimethylsiloxane)-ZnO nanocomposites.” *Vibrational Spectroscopy* 68 (2013): 1-10. doi:10.1016/j.vibspec.2013.05.005.
- [26] Anoop, V., S. Subramani, S. N. Jaisankar, C. Sohini, and N. L. Mary. “Mechanical, dielectric, and thermal properties of polydimethylsiloxane/polysilsesquioxane nanocomposite for sealant application.” *Journal of Applied Polymer Science* 136, no. 12 (2018): 47228. doi:10.1002/app.47228.
- [27] R. Reddy, Boreddy S., and D. Gnanasekar. “Structure-Gas Transport Property Relationships of Poly(dimethylsiloxane-urethane) Nanocomposite Membranes.” *Advances in Nanocomposites - Synthesis, Characterization and Industrial Applications*, 2011. doi:10.5772/14718.
- [28] Kim, J., M.K. Chaudhury, and M.J. Owen. “Hydrophobicity loss and recovery of silicone HV insulation.” *IEEE Transactions on Dielectrics and Electrical Insulation* 6, no. 5 (1999): 695-702. doi:10.1109/94.798126.
- [29] Lötters, J. C., W. Olthuis, P. H. Veltink, and P. Bergveld. “The mechanical properties of the rubber elastic polymer polydimethylsiloxane for sensor applications.” *Journal of Micromechanics and Microengineering* 7, no. 3 (1997): 145-147. doi:10.1088/0960-1317/7/3/017.
- [30] Kuncova-Kallio, J., & Kallio, P. J. (2006). PDMS and its Suitability for Analytical Microfluidic Devices. *2006 International Conference of the IEEE Engineering in Medicine and Biology Society*. doi:10.1109/iembs.2006.260465.
- [31] Sharfeddin, Asma D., Alex A. Volinsky, Greeshma Mohan, and Nathan D. Gallant. “Comparison of the macroscale and microscale tests for measuring elastic properties of polydimethyl siloxane.” *Journal of Applied Polymer Science* 132, no. 42 (2015): n/a-n/a. doi:10.1002/app.42680.

- [32] Peng, Qingrong, and Dehua He. "Hydroformylation of mixed octenes over immobilized Co-Ph₃PO/PDMS/SiO₂ catalyst." *Catalysis Letters* 115, no. 1-2 (2007): 19-22. doi:10.1007/s10562-007-9050-8.
- [33] Schönhals, A., H. Goering, Ch. Schick, B. Frick, and R. Zorn. "Polymers in nanoconfinement: What can be learned from relaxation and scattering experiments?" *Journal of Non-Crystalline Solids* 351, no. 33-36 (2005): 2668-2677. doi:10.1016/j.jnoncrysol.2005.03.062.
- [34] Fischer-Cripps, Anthony C. "Other Techniques in Nanoindentation." *Nanoindentation*, 2011, 163-180. doi:10.1007/978-1-4419-9872-9_9.
- [35] Schneider, Florian C., Jan Draheim, Robert Kamberger, and Ulrike Wallrabe. "Process and material properties of polydimethylsiloxane (PDMS) for Optical MEMS." *Sensors and Actuators A: Physical* 151, no. 2 (2009): 95-99. doi:10.1016/j.sna.2009.01.026.
- [36] Victor, Andrews C., João Ribeiro, and Fernando F. Araújo. "Study of PDMS characterization and its applications in biomedicine: A review." *Journal of Mechanical Engineering and Biomechanics* 4, no. 1 (2019): 1-9. doi:10.24243/jmeb/4.1.163.
- [37] Sagar, Sadia, Nadeem Iqbal, and Asghari Maqsood. "Dielectric, electric and thermal properties of carboxylic functionalized multiwalled carbon nanotubes impregnated polydimethylsiloxane nanocomposite." *Journal of Physics: Conference Series* 439 (2013): 012024. doi:10.1088/1742-6596/439/1/012024.
- [38] Mbarak, H., S. M. Hamidi, E. Mohajerani, and Y. Zaatari. "Electrically driven flexible 2D plasmonic structure based on a nematic liquid crystal." *Journal of Physics D: Applied Physics* 52, no. 41 (2019): 415106. doi:10.1088/1361-6463/ab2fea.
- [39] Asgari, N., & Hamidi, S. (2018). Exciton-plasmon coupling in two-dimensional plexitonic nano grating. *Optical Materials*, 81, 45-54. doi:10.1016/j.optmat.2018.05.011.
- [40] SF Haddawi, M Mirahmadi, H Mbarak, AK Kodeary, M Ghasemi, "Footprint of plexcitonic states in low-power green-blue plasmonic random laser", *Applied Physics A* 125 (12), 843, 2019.

- [41] Sajede Saeidifard, Foozieh Sohrabi, Mohammad Hossein Ghazimoradi, S. M. Hamidi, Shirin Farivar, and Mohammad Ali Ansari, “Two-Dimensional Plasmonic Biosensing Platform: Cellular Activity Detection under Laser Stimulation”, *Journal of Applied Physics*, 126 (10), 104701, 2019.
- [42] Lu, Naiyan, Wei Zhang, Yuyan Weng, Xiaoxia Chen, Yao Cheng, and Peng Zhou. “Fabrication of PDMS surfaces with micro patterns and the effect of pattern sizes on bacteria adhesion.” *Food Control* 68 (2016): 344-351. doi:10.1016/j.foodcont.2016.04.014.

INDEX

#

2D plasmonic grating, xi, 199, 200, 204, 205, 209
3T3-L1, 31, 42, 56, 61

A

acetone, 44, 47, 51, 168
acetonitrile, 183, 186, 187, 193, 194
acid, 96, 104, 107, 109, 110, 163, 183
acrylate, 107, 112, 138, 139
acrylic acid, 114
activation energy, 22
active control, xi, 199, 200, 201, 209
active plasmonic devices, xi, 199, 203
active plasmonic system, 200
active plasmonics, 200, 201, 204, 209
adhesion, vii, x, 57, 72, 73, 74, 77, 78, 81, 88, 90, 96, 97, 98, 99, 102, 103, 104, 106, 107, 108, 109, 111, 112, 113, 115, 116, 117, 118, 120, 121, 122, 123, 124, 125, 126, 127, 129, 130, 134, 135, 136,

137, 138, 139, 140, 142, 143, 144, 148, 153, 156, 158, 170, 174, 215
adhesives, 39, 40, 41, 46
adsorption, xi, 106, 107, 137, 153, 179, 181, 187, 191, 192, 193
adsorption isotherms, 191
albumin, ix, 30, 48
albumin aqueous solution, 48, 49, 81
allergic reaction, 99
alpha-MEM, 31
antibiofilm coatings, 96, 108, 115, 116, 117, 130
antibiotic, 108, 136, 144
anticancer drug, 166
aqueous solutions, 153
aromatic compounds, 182, 192, 193, 194
aromatic hydrocarbons, 180, 181
ascorbic acid, 152
aspect ratio, 36, 57, 85, 89
atomic force microscope, 155
attachment, 102, 105, 106, 110, 114, 115, 116, 117, 125, 170

B

bacteremia, 100, 132
 bacteria, 103, 105, 106, 107, 109, 110, 111,
 112, 114, 116, 123, 124, 134, 135, 142,
 143, 149, 182, 215
 bacterial adhesion, vii, x, 96, 97, 98, 99,
 102, 103, 104, 106, 107, 108, 109, 111,
 112, 113, 115, 116, 117, 121, 122, 130,
 134, 137, 138, 139, 143, 144
 bacterial cells, 116
 base, ix, 29, 30, 37, 43, 44, 47, 49, 51, 52,
 76, 204
 benzene, xi, 180, 181, 182, 183, 186, 192,
 193, 194, 196, 197, 198
 biochemistry, 155, 160, 169
 biocompatibility, vii, x, 97, 98, 99, 145,
 148, 153, 156, 159, 160, 202, 203
 biodegradation, 97
 biofilm, vii, x, 96, 97, 98, 99, 102, 103, 104,
 105, 106, 107, 108, 110, 111, 114, 115,
 116, 117, 118, 119, 120, 121, 122, 126,
 127, 128, 129, 130, 134, 135, 136, 137,
 138, 139, 140, 141, 142, 143, 144
 biological behavior, vii, x, 145
 biological cell, v, vii, ix, 29, 30, 31, 32, 38,
 39, 41, 42, 45, 48, 49, 53, 71, 72, 76, 80,
 83, 84, 86, 147, 148, 203
 biological processes, 102
 biomass, 129
 biomaterials, 97, 98, 134, 163, 203
 biomedical applications, 149, 161
 biomolecules, x, 145, 148, 151, 152, 153,
 155, 167, 171
 biosafety, 131
 biosensors, x, 146, 148, 154, 158, 162, 163,
 166, 177
 biosurfactant, 143
 biotechnology, 152, 158, 162, 170
 blood, 79, 83, 87, 132, 157, 162, 175
 blood cultures, 132

blood flow, 83
 blood vessels, 79
 bonding, 43, 143, 147, 153, 212

C

C2C12, 31, 33, 36, 37, 39, 41, 42, 44, 46,
 48, 49, 53, 55, 56, 58, 59, 60, 61, 62, 64,
 66, 67, 68, 69, 70, 71, 73, 74, 75, 81, 82,
 83, 90, 92
 calcium, 98, 99, 103
 calcium carbonate, 98, 99
 cancer, 76, 77, 81, 89, 156, 157, 177, 180
 cancer cells, 76, 89, 177
 capillary, 37, 72, 76, 79, 163
 carbon, vii, viii, 1, 7, 11, 16, 25, 26, 27, 33,
 157, 182
 catheter, 96, 99, 101, 102, 103, 104, 105,
 106, 107, 110, 111, 116, 132, 134, 136,
 137, 138, 139, 140, 142, 203
 cell biology, 159, 161, 164
 cell culture, 30, 33, 35, 36, 37, 44, 58, 72,
 146, 147, 148, 149, 157, 160, 167, 171
 cell cycle, 74
 cell differentiation, x, 146, 160
 cell line, 31, 149, 157
 cell size, 84, 205
 central nervous system, 180
 centrifugal force, 35, 56, 57, 73, 74, 75
 changing environment, 71
 charge coupled device, 204
 checkered convexo-concave pattern, 36, 57
 chemical, ix, x, 2, 3, 26, 71, 98, 99, 102,
 146, 149, 153, 158, 160, 161, 164, 168,
 171, 172, 174, 176, 180, 181, 200, 202,
 203
 chemical characteristics, 149
 chemical properties, 160, 203
 chemical reactions, 180
 chemical stability, 203
 chemical vapor deposition, 153

cleaning, viii, 1, 3, 47, 117
 clusters, viii, 2, 10, 11, 12, 13, 15
 coatings, viii, ix, 1, 2, 3, 96, 97, 99, 104,
 105, 106, 107, 108, 113, 115, 116, 117,
 130, 132, 135, 139, 140, 161, 181
 cochlear implant, 148
 colonisation, 110, 136
 colonization, 100, 101, 102, 103, 105, 113,
 115, 117, 133, 135
 combustibility, 202
 commercial, 123, 181
 communication, 102, 166, 176
 communities, 103
 compatibility, ix, 2, 98
 compliance, 76, 78, 79, 84
 complications, vii, x, 96, 97, 100, 103, 130
 composites, vii, viii, ix, 1, 2, 3, 4, 8, 9, 10,
 11, 12, 13, 14, 15, 16, 17, 18, 19, 20, 21,
 22, 23, 24, 25, 26, 27
 composition, 6, 143, 160
 compounds, 13, 149, 159
 computational fluid dynamics, 96, 120
 condensation, 156, 157
 conductivity, 8, 9, 10, 11, 12, 13, 14, 16, 24,
 25, 146
 confinement, 27, 159
 conjugation, 113, 164
 connective tissue, 31, 173
 construction, 97, 118, 157, 201
 contact angle, xi, 33, 53, 54, 72, 123, 124,
 143, 144, 153, 179, 185, 188, 194
 cooling, 13, 18, 19, 20, 21, 22, 23, 147
 copolymer, 107, 111, 138, 154, 167
 cost, viii, ix, xi, 2, 101, 146, 151, 166, 180,
 181, 182, 199, 203
 crystallization, 18, 19, 23, 27, 182
 crystals, 103, 176
 culture, 31, 33, 36, 37, 42, 57, 125, 126,
 147, 149, 160, 165, 167, 169
 culture media, 149
 culture medium, 31, 125, 126, 149

| |
|----------|
| D |
|----------|

decomposition, xi, 179, 190, 191
 decomposition temperature, 190
 deformability, 45, 77, 78, 79, 83, 86, 91
 deformation, 33, 53, 56, 67, 69, 70, 71, 74,
 78, 79, 80, 81, 83, 84, 85, 87, 88, 91
 degradation, 116, 130, 181, 182
 depolarization, 156, 160
 deposition, 47, 51, 52, 146, 150, 163, 168,
 206
 depth, 34, 38, 39, 40, 41, 42, 43, 46, 50, 56,
 61, 63, 77
 detachment, 103, 125, 141, 143
 detection, 148, 152, 156, 158, 159, 160,
 162, 163, 166, 167, 169, 173, 176, 177,
 182, 200
 dielectric permittivity, viii, 2, 7, 8, 17, 18,
 19, 22
 dielectric relaxations, 212
 dielectric strength, 202
 differential scanning, 19
 differential scanning calorimetry, 19
 dispersion, 3, 5, 6, 18, 24, 28, 184
 distilled water, 32, 34, 38, 40, 45, 47
 distribution, viii, 1, 3, 4, 5, 6, 7, 54, 78
 D-MEM, 31, 33
 DNA, 154, 155, 156, 157, 162, 163, 166,
 170, 171
 DNA sequencing, 162, 170
 drainage, 98, 99, 203
 drawing, 32, 34, 38, 40, 41, 45, 47, 51, 181
 drug delivery, x, 119, 146, 156, 159, 160,
 172, 175
 drug discovery, 162
 drug release, 172
 durotactic migration, 36, 58, 75, 85

E

E. coli, 104, 105, 106, 107, 108, 109, 110, 111, 112, 113, 114, 115, 116, 117, 121, 124, 125, 126, 127, 128, 136, 142

EBM-2, 31

elastomers, 146, 147, 148

electrical conductivity, viii, 2, 7, 8, 10, 11, 12, 13, 15

electrical properties, viii, 2

electromagnetic, ix, 2, 159

electromagnetic fields, 159

electron, viii, 2, 12, 14, 15, 35, 46, 47, 49, 51, 52, 64, 124, 134, 135, 151, 184, 187

electron microscopy, 135

electrospinning, 181, 182, 183, 184, 191

electrospraying, viii, xi, 179, 180, 181, 182, 183, 187, 188, 195, 196

E-MEM, 31

endothelial cells, 31, 71, 87, 155, 170

energy, 14, 22, 124, 184

engineering, x, 30, 84, 87, 161, 169, 173, 174, 201

environment, 31, 76, 88, 155, 169, 203

environmental factors, 102

etching, x, 30, 31, 32, 33, 34, 35, 36, 38, 43, 45, 47, 51, 52, 84, 163

ethanol, 47, 123, 149, 183

ethylene, 106, 107, 111, 112, 114

ethylene glycol, 106, 107, 111, 112, 114

ethylene oxide, 107, 111

exposure, 57, 79, 101, 112, 147, 150, 180

external electric field, 206

external magnetic field, 209

extracellular matrix, 155, 172

extraction, xi, 170, 180, 181, 182, 193, 194

F

fabrication, viii, x, xi, 91, 95, 140, 146, 147, 151, 158, 160, 161, 162, 169, 174, 199, 201, 203, 204, 209, 212

FBS, 31, 33

fibers, xi, 26, 71, 182, 199

fillers, viii, ix, 1, 2, 3, 18, 23

films, 104, 107, 108, 112, 113, 152, 156, 163, 170

flexibility, vii, viii, x, xi, 1, 3, 18, 79, 99, 145, 152, 160, 199, 202, 203, 209

flow systems, 96, 98, 118, 121

fluid, ix, 30, 73, 76, 80, 82, 102, 118, 119, 120, 129, 143, 150

fluorescence, 89, 160, 170, 208

force, 35, 56, 57, 73, 74, 75, 78, 79, 81, 84, 86, 88, 103, 147

formamide, 123, 124

formation, vii, x, xi, 96, 97, 98, 99, 102, 103, 104, 105, 106, 107, 108, 110, 111, 114, 116, 117, 118, 120, 121, 122, 126, 127, 130, 135, 136, 137, 139, 141, 142, 143, 144, 179, 187, 188, 189, 191

fouling, 107, 113, 117, 140, 142, 161

free energy, 123, 124

freezing, 27, 202

friction, 68, 83

FTIR, xi, 179, 185, 188, 189, 194

functionalization, 137, 146, 160

fungal infection, 137

G

glass transition, ix, 2, 17, 18, 22, 23, 26, 27, 147, 202

glass transition temperature, ix, 2, 18, 22, 23, 27, 147, 202

glucose, 152, 158

glycol, 24, 96, 106, 113, 114, 115, 117, 137

gold nanoparticles, 175, 176, 177, 178, 209

groove, 30, 33, 38, 41, 43, 50, 54, 59, 61, 62, 63, 67, 72, 76, 77, 78, 84, 86
 growth, 17, 23, 88, 102, 104, 114, 116, 120, 126, 129, 130, 135, 136, 141, 146, 149, 157, 173

H

half cylindrical holes, 40
 hardness, 82, 146
 health, 99, 133, 158, 193
 health care, 133
 health condition, 158
 health risks, 158
 heating rate, 185
 height, 15, 32, 33, 34, 35, 43, 44, 46, 48, 49, 50, 54, 55, 56, 57, 59, 60, 63, 68, 69, 70, 73, 75, 76, 78, 81, 82, 84
 Hepa1-6, 31, 46, 48, 49, 53, 67, 68, 69, 70, 81, 82, 83
 hexane, 183, 187, 193, 194
 history, 132, 134
 HMDS, 34, 47
 human, ix, 2, 31, 91, 118, 122, 135, 155, 160, 170, 173, 180, 182
 human body, 118, 122
 HUVEC, 31, 53, 69, 82, 83, 93
 hybrid, vii, xi, 114, 116, 158, 162, 168, 176, 179, 182, 188, 189, 190, 191, 192, 194
 hydrogels, 106, 162, 165, 175
 hydrogen, 32, 38
 hydrogen peroxide, 32, 38
 hydrophilic, x, 33, 35, 36, 37, 38, 41, 53, 72, 78, 87, 90, 115, 117, 123, 124, 136, 145, 147, 153, 154
 hydrophobic properties, 104
 hydrophobicity, 123, 149, 153
 hysteresis, 19, 21, 23, 35, 57, 74, 84, 191
 hysteresis effect, 35, 84

I

immune response, 165
 immunogenicity, 107
 immunoglobulin, 160
 in vitro, 31, 44, 46, 72, 73, 75, 76, 85, 88, 114, 116, 118, 121, 130, 135, 138, 139, 142, 143
 in vivo, 45, 71, 77, 79, 80, 83, 99, 114, 116, 141, 148
 incidence, x, 95, 98, 99, 100, 101, 132, 134, 138
 incubator, 33, 37, 44, 48, 62, 81
 industrial chemicals, 180
 industry, x, 145, 146, 158, 201, 203
 infection, 96, 100, 101, 102, 134
 intensive care unit, 101
 interface, 91, 141, 154, 160, 200
 ions, 104, 107, 113
 IPA, 37, 43, 45, 47, 51, 52
 isolation, 89, 149, 154

L

lactic acid, 173
 light scattering, 57
 lipids, 104, 108, 110
 liquid chromatography, xi, 180, 186
 liquid phase, 76, 119
 liquids, 27, 123, 144, 146
 lithography, 36, 151, 158, 160, 166, 167, 169, 174, 176, 177, 204, 209
 longitudinal magneto-optical Kerr effect, 209
 low temperatures, 13, 16, 17, 18

M

magnetic field, 209
 magnitude, ix, 2, 22

- manipulation, 119, 151, 154, 175
- marker, 30, 35, 44, 63, 75, 78, 84, 176
- materials, viii, ix, 1, 2, 3, 13, 25, 26, 28, 36, 97, 98, 100, 102, 103, 106, 118, 121, 128, 137, 138, 143, 144, 146, 147, 149, 150, 151, 154, 162, 163, 164, 165, 166, 169, 171, 174, 176, 177, 181, 192, 202, 203, 209, 212
- materials science, 166
- matrix, viii, 1, 3, 5, 11, 12, 13, 18, 23, 71, 102, 103, 114, 116, 130, 134, 178
- MC3T3-E1, 31, 35, 41, 53, 60, 71, 88
- mechanical properties, ix, 2, 90, 137, 182, 203, 213
- medical, x, 30, 84, 97, 98, 101, 102, 117, 118, 120, 128, 129, 131, 134, 145, 146, 148, 151, 161, 201, 203
- mesenchymal stem cells, 157, 162, 173
- methodology, vii, 31, 71, 72, 160
- methyl groups, 188, 191, 201
- micro cylindrical columns, 45, 65, 66
- micro slit, 45, 46, 48, 65, 66, 69, 70, 79, 83, 84, 85, 86, 87, 93
- microbial communities, 102
- micro-checked pattern, 36, 57, 75
- microcirculation, 91
- microenvironments, 91, 142, 155
- microfabrication, 148, 167
- microgravity, 75, 88
- micro-grooves, vii, ix, 30, 33, 34, 38, 42, 84
- micro-machining, ix, 29, 30, 45, 84
- micrometer, ix, 29, 30, 72, 73, 79, 81, 88, 117, 146
- microorganisms, 102, 104, 182
- microparticles, xi, 5, 179, 193
- micropatterns, 76, 88, 90, 117, 157, 167
- micro-protrusions, 44, 78, 84
- micro-ridge, vii, ix, 30, 32, 34, 35, 53, 54, 55, 56, 72, 84
- microscope, 30, 33, 34, 37, 38, 39, 41, 42, 46, 47, 48, 49, 53, 54, 56, 57, 60, 64, 65, 68, 79, 121, 123, 125, 184
- microscopy, 96, 113, 121, 126, 127
- micro-slit between rectangular ridge and plate, 50
- micro-slits, vii, ix, 30, 31, 45, 84
- microspheres, 164
- migration, 36, 37, 56, 58, 74, 76, 85, 90, 97, 155, 172
- mold, 32, 33, 34, 35, 36, 37, 38, 40, 41, 42, 43, 44, 45, 46, 47, 49, 51, 56, 57, 59, 60, 63, 147
- molecular dynamics, 24
- molecular mobility, 18
- molecular weight, 26, 148, 190, 191
- molecules, 23, 102, 139, 152, 155, 162, 169, 170, 191, 206, 207, 209
- morphology, vii, ix, 29, 30, 31, 32, 34, 37, 47, 49, 56, 59, 60, 65, 66, 71, 72, 73, 74, 76, 79, 81, 84, 159, 174, 184, 187
- myoblasts, 64, 67, 72, 74, 89

| |
|----------|
| N |
|----------|

- nanocomposites, viii, 2, 19, 24, 26, 27, 105, 109, 156, 182, 191, 213
- nanoimprint, 151, 158, 160, 165, 174, 177, 204, 209
- nanomaterials, 181
- nanometer, 72, 88, 117
- nanoparticles, viii, 2, 7, 18, 19, 21, 22, 23, 24, 27, 96, 104, 108, 110, 131, 156, 157, 159, 166, 175, 177, 181, 187
- nanoscale structures, 151
- nanostructures, 140, 148, 152, 159, 162, 166, 177
- naphthalene, xi, 180, 181, 182, 183, 186, 192, 193, 194, 195, 196, 197
- nematic liquid crystal, 168, 205, 209, 214
- Neuro-2a, 31, 53, 56, 67, 69
- neuronal cells, 157
- NiFe thin film, 209
- nitrogen, 150, 168, 185, 192

NMD-3, 32, 34, 45, 47, 51
 nontoxicity, vii, x, 145
 nucleation, 18
 nuclei, 21, 23
 nucleic acid, 102, 129, 175
 nutrients, vii, x, 120, 145, 146, 149

O

oblique groove, 42, 43, 62, 77
 observed behavior, 59
 OFPR-800, 32, 34, 44, 45, 47, 51
 opportunities, 149, 173, 203
 optical properties, 153
 oxygen, vii, ix, x, 30, 32, 33, 34, 35, 36, 37, 38, 39, 40, 41, 43, 44, 47, 48, 49, 51, 52, 54, 78, 84, 120, 145, 146, 153, 165
 oxygen plasma, ix, 30, 32, 33, 37, 39, 40, 43, 44, 47, 48, 49, 51, 52, 54, 84, 153
 oxygen plasma ashing, ix, 30, 32, 33, 37, 39, 40, 43, 44, 47, 48, 49, 51, 52, 54, 84

P

parallel, 32, 34, 35, 38, 41, 46, 48, 54, 57, 65, 73, 74, 80, 81, 82, 97, 118, 120, 121, 140, 143, 144, 159
 parallel plate flow chamber, 97, 118, 121, 143
 pathogens, 101, 102, 103, 106, 135
 PDMS substrate, 157, 200, 206, 209
 PDMS-based 2D plasmonic grating, xi, 199, 204, 205, 209
 PDMS-based surfaces, 96, 98, 100, 103, 130
 penicillin, 31, 108
 peptide, 96, 106, 110, 111, 137, 143, 175
 percolation, viii, 1, 2, 3, 7, 9, 11, 12, 16, 25
 permeability, vii, x, 77, 145, 160, 202
 permittivity, 7, 9, 10, 11, 13
 phosphate, 31, 98, 99, 103, 113, 116, 140
 photochemical material, 208

photoelectron spectroscopy, 150
 photolithography, x, 30, 31, 32, 34, 35, 36, 38, 40, 43, 44, 46, 48, 72, 76, 78, 80, 81, 84, 87, 93, 156, 158, 165
 photomasks, 36
 photoresist material, 32, 34, 36, 37, 38, 40, 41, 42, 43, 45, 47, 51, 52
 physical properties, 71, 147, 202
 physicochemical characteristics, 102
 physicochemical properties, 98, 104, 106, 182
 platform, vii, x, 96, 120, 121, 156, 158, 159, 160, 166, 169
 polar, 124, 144, 188, 193
 polarity, xi, 155, 172, 180, 188, 194
 polycyclic aromatic hydrocarbon, 24
 polydimethylsiloxane, v, vi, vii, viii, ix, xi, 1, 3, 26, 27, 29, 30, 90, 145, 147, 162, 165, 167, 168, 172, 173, 177, 178, 179, 180, 182, 183, 196, 198, 199, 201, 202, 209, 212, 213, 214
 polyimide, 33, 36, 42, 43, 49, 52
 polymer, ix, xi, 2, 4, 7, 9, 11, 13, 18, 20, 22, 24, 25, 27, 72, 87, 97, 98, 106, 111, 113, 114, 116, 136, 137, 138, 152, 154, 159, 160, 163, 169, 177, 191, 194, 199, 201, 203, 204, 213
 polymer matrix, ix, 2, 7, 9, 11, 13, 18, 177
 polymer nanocomposites, 25
 polymer systems, 201
 polymeric materials, 98
 polymerization, 107, 112
 polymers, x, 3, 4, 6, 24, 95, 97, 106, 113, 114, 115, 116, 117, 143, 146, 147, 148, 153, 156, 159, 201
 polystyrene, 24, 26, 144, 147, 182
 polyurethane, 98, 137, 138, 156, 172
 polyurethanes, 98, 111, 137
 preparation, iv, 72, 78, 81, 204, 206
 prevention, 99, 104, 107, 134
 proliferation, 56, 57, 71, 72, 73, 74, 88, 157, 162

proteins, 48, 102, 106, 116, 150, 151, 154,
155, 159, 160, 168, 170, 172
protrusions, 44, 63, 64, 78
Pseudomonas aeruginosa, 102, 139, 142
pumps, 120, 171, 203
pure water, 37, 44, 47

R

reactive ion etching system, 32, 33, 34, 35,
36, 38, 43, 45, 47, 51, 52
refractive index, 160, 200, 207, 208, 209
regenerative medicine, x, 30, 77, 84
relaxation, 3, 4, 5, 6, 7, 17, 18, 20, 21, 22,
23, 24, 25, 26, 214
relaxation process, 6, 23
relaxation times, 4, 6, 7
resistance, ix, 2, 81, 82, 83, 98, 99, 100,
103, 105, 106, 107, 109, 113, 117, 135,
142, 143, 146, 202
resolution, 159, 172, 185
response, 4, 6, 9, 75, 76, 87, 155, 200, 203,
208
reverse osmosis, 181
Reynolds number, 80
ridge, 30, 32, 34, 35, 50, 54, 55, 57, 68, 69,
72, 74, 75, 80, 82, 83, 93, 167
room temperature, 7, 8, 13, 19, 39, 41, 185,
205
roughness, 82, 106, 128, 129, 149
rubber, 28, 39, 41, 42, 46, 68, 136, 140, 143,
180, 213

S

semiconductor, 158, 163, 174, 203
sensing, xi, 102, 116, 130, 146, 158, 160,
166, 175, 176, 177, 209
sensor, 148, 169, 176, 203, 212, 213
shape, 9, 13, 14, 35, 40, 41, 44, 64, 81, 83,
147, 172

shear, 22, 39, 41, 42, 71, 79, 80, 81, 87, 91,
118, 119, 120, 121, 122, 125, 140, 141,
143
silicon, 32, 34, 38, 40, 41, 45, 100, 147,
148, 149, 151, 157, 191, 201, 203
silver, 96, 97, 104, 108, 110, 115, 116, 131,
132, 135, 136, 138, 140, 210
single walled carbon nanotube, 26
slit, 30, 45, 46, 47, 48, 49, 50, 52, 53, 65,
66, 67, 68, 69, 70, 79, 80, 81, 82, 83, 85,
87
soft lithography, 148, 155, 156, 159, 160,
170, 171
software, 125, 128, 129, 184, 185
solution, 31, 32, 38, 39, 41, 44, 45, 48, 49,
51, 52, 53, 67, 81, 84, 122, 123, 150,
183, 186, 187, 191
solvents, xi, 180, 190, 191, 193
sort biological cells, 45, 76
species, 103, 104, 116, 140, 150, 151, 200
specific gravity, 77
specific surface, 186, 187, 192
spectroscopy, ix, xi, 2, 25, 27, 179
spin, 27, 32, 34, 37, 38, 40, 41, 43, 44, 45,
47, 49, 51, 52, 123
standard deviation, 54, 55, 97, 126, 192, 193
stent, 101, 102, 103, 132, 133, 143, 156
stimulation, 44, 57, 71, 74, 75, 79, 87, 88,
156, 160, 169
stress, 38, 40, 71, 79, 81, 87, 118, 119, 120,
121, 140, 143, 147, 167
structure, viii, xii, 6, 25, 72, 83, 89, 117,
118, 121, 149, 151, 167, 168, 188, 194,
200, 201, 202, 203, 205, 206, 209, 214
SU-8, 36, 37, 47, 51, 52, 58, 59, 76, 89
substrate, 90, 121, 139, 148, 157, 159, 176,
200, 203, 205, 206, 209
substrates, 88, 90, 91, 114, 147, 148,
surface area, 120, 182, 186
surface component, 124
surface energy, 202
surface hardness, 36, 58

surface lattice resonance (SLR), 176, 200
 surface modification, 156, 157, 169
 surface plasmon resonance, 155, 156, 171,
 177, 200
 surface properties, 140, 149
 surface structure, 30, 102
 surface tension, 98, 99, 123, 124, 134, 143,
 144, 188
 surrounding medium, 200, 208
 switching effect, viii, xii, 200, 201, 205,
 208, 209

T

taper-alternative-stripe pattern, 36, 58
 techniques, x, 81, 102, 134, 145, 146, 155,
 156, 158, 169, 181
 temperature, vii, viii, xi, 1, 2, 6, 9, 10, 11,
 12, 13, 14, 18, 19, 21, 22, 23, 27, 33,
 102, 122, 150, 161, 164, 168, 179, 185,
 191, 202
 temperature dependence, ix, 2, 14, 19, 21,
 22, 23
 therapy, xi, 146, 157, 159, 173, 175
 thermal expansion, 11
 thermal properties, 213, 214
 thermal stability, 182, 190
 tissue, ix, 2, 31, 71, 72, 73, 75, 78, 81, 84,
 87, 90, 91, 98, 99, 146, 150, 155, 160,
 162, 167, 173, 175, 176, 203
 tissue engineering, 146, 162, 203
 titanium, vii, xi, 47, 51, 52, 65, 88, 179,
 180, 182, 183, 186, 191
 titanium dioxide, vii, xi, 179, 180, 182, 186,
 196
 toxicity, 150, 180, 202, 203
 transition temperature, viii, 2, 9, 10, 12, 13,
 22
 transparency, vii, x, xi, 30, 63, 145, 147,
 148, 151, 160, 199, 202, 203
 transport, 12, 15, 26, 120, 125, 201

treatment, 100, 101, 102, 123, 153, 154
 tunable dielectric responses, 204
 tunable optical materials, 209
 tunneling, viii, 2, 12, 13, 14, 15

U

ultrasonic frequency, 90
 ultrasound, 18, 123, 184
 umbilical cord, 157, 162
 ureteral stents, vii, x, 95, 96, 97, 98, 100,
 101, 103, 115, 116, 121, 122, 126, 127,
 128, 129, 130, 132, 133, 134, 143
 urethane, 213
 urethra, 111, 114, 116
 urinary catheters, vii, x, 95, 96, 97, 98, 99,
 101, 103, 105, 106, 108, 111, 116, 121,
 122, 126, 127, 128, 129, 130, 131, 132,
 134, 135, 136, 138, 139
 urinary tract, vii, x, 95, 96, 97, 98, 99, 100,
 101, 104, 118, 120, 129, 130, 132, 133,
 134, 135, 137, 138, 142
 urinary tract infection, x, 95, 96, 97, 98,
 101, 104, 132, 133, 134, 135, 138, 142
 urinary tract infections, x, 95, 96, 98, 101,
 104, 132, 134, 135, 142
 urine, 126, 129, 135, 137, 140
 UV irradiation, 208
 UV light, 172, 206, 208

V

velocity, ix, 2, 18, 20, 21, 22, 53, 62, 63, 65,
 68, 69, 70, 71, 77, 80, 81, 83, 87, 144
 viral pathogens, 158
 viscosity, ix, 2, 19, 27, 37, 40, 41, 47, 51,
 52, 80, 150, 151, 187, 202
 visualization, 118, 128

W

wall shear rate, 39, 41, 80
water, 32, 33, 35, 38, 42, 47, 51, 52, 122,
123, 124, 153, 156, 181, 182, 183, 185,
186, 187, 188, 191, 193, 194, 202
weight loss, 191
weight ratio, 149

workers, 100, 105, 107, 117
worldwide, 180

Z

zinc oxide, 18, 26
ZnO, viii, 2, 17, 18, 19, 20, 21, 22, 23, 26,
27, 181, 212, 213